

QUANTUM SYSTEMS  
IN COLD ATOMS  
AND  
SUPERCONDUCTING CIRCUITS

NIELS JAKOB SØE LOFT

PHD DISSERTATION  
AUGUST 2019

MAIN SUPERVISOR: NIKOLAJ T. ZINNER  
CO-SUPERVISOR: GEORG M. BRUUN

DEPARTMENT OF PHYSICS AND ASTRONOMY  
AARHUS UNIVERSITY

# English summary

Quantum mechanics has fascinated physicists and the general public alike since its introduction about a century ago. The theory successfully explained many phenomena occurring in Nature, including few-body systems like atoms and many-body effects like magnetism. These new insights paved the way for technological breakthroughs such as the transistor and laser. Within the recent decades, experimental techniques have become so sophisticated that scientists are now able to engineer and control the individual quantum states of a physical system; an accomplishment thought impossible by the founding fathers of quantum mechanics. In addition to providing a better understanding of our world, the advances has opened the frontier of quantum technology, including quantum computing.

This dissertation explores several avenues opened up by these advances in experimental capability. Specifically, it studies the recent theoretical spin chain model of a system of strongly interacting ultracold atoms trapped in a one-dimensional laser field, and presents a new powerful tool for computing this model. The interplay between particles confined to different spatial dimensions is also considered, as a two-dimensional polaron in a three-dimensional Bose-Einstein condensate is characterized. Moreover, several superconducting devices and their applications in quantum computing is proposed. Here the highlight is the detailed description and analysis of a fast high-fidelity four-qubit gate between four superconducting transmon qubits.

# Dansk resumé

Kvantemekanikken har fascineret fysikere, folk og fæ siden dens fremkomst for omkring hundrede år siden. Teorien forklarede med stor nøjagtighed mange naturligt forekommende fænomener, heriblandt få-legeme-systemer som atomer og kollektive effekter som magnetisme. Den nye forståelse af verden banede vejen for teknologiske landvindinger som transistoren og laseren. Indenfor de seneste årtier er de eksperimentelle teknikker blevet så sofistikerede, at videnskabsfolk nu er i stand til at kreere og manipulere de enkelte kvantetilstande i et fysisk system; en bedrift, der blev anset som umulig af kvantemekanikkens fædre. Ud over at forøge vores grundlæggende forståelse af verden åbner det også op for fremtidens kvanteteknologi, herunder kvantecomputeren.

I denne afhandling behandles en række af de forskningsområder, som disse eksperimentelle fremskridt giver anledning til at studere. Specifikt undersøges en nyligt fremsat teoretisk spinkædebeskrivelse af stærkt vekselvirkende atomer i en en-dimensionel laserfælde, og et kraftfuldt nyt værktøj til at beregne modellen præsenteres. Samspillet mellem partikler i forskellige rumlige dimensioner betragtes også, idet en to-dimensionel polaron i et tre-dimensionelt Bose-Einstein-kondensat karakteriseres. Derudover foreslåes også en række superledende mikrochips samt deres mulige anvendelse i en kvantecomputer. Her er højdepunktet en detaljeret beskrivelse og analyse af en hurtig og pålidelig fire-qubit-gate mellem fire superledende transmon-qubits.

# Preface

This thesis concludes my PhD studies at the Department of Physics and Astronomy at Aarhus University. It covers many different research topics in modern quantum physics which I had the pleasure to delve into during my time as a PhD student. Be prepared to read about one-dimensional few-body systems and mixed-dimensional many-body systems. Some systems are implemented in ultracold trapped atoms, others in superconducting circuits. Sometimes we will think a scientists trying to understand Nature at a deeper level, sometimes as programmers trying to optimize software and other times as engineers trying to build components for a quantum computer. As Robert A. Heinlein puts it: *Specialization is for insects.*

\* \* \*

My supervisors, Nikolaj T. Zinner and Georg M. Bruun, deserve a big thanks for their support. I learned a lot from each and their different approaches to physics. I am especially grateful to Nikolaj for teaching me about the scientific community and for letting me visit four different continents of our planet. I would like to thank everyone at the EQuS group at MIT for their hospitality and engagement during my stay, in particular to Benjamin Lienhard, Bharath Kannan, Mirabella Pulido, Roni Winik and Morten Kjaergaard. My work days in Aarhus would have been boring was it not for Jonatan Midtgaard, Lasse Bjørn Kristensen, Jesper Halkjær Jensen, Søren Møller, Jeppe Christiansen, Michael Munch, Jacob Søgaard and everyone else from Frokostgruppen. Thank you. For reading and commenting on parts of my thesis, I wish to thank Kristian Knakkegaard Nielsen, Lasse Bjørn Kristensen, Jesper Halkjær Jensen, Søren Møller, Thor Inuk Sander Holm, Chris Risager and Anna Nygaard Andersen. A special thanks goes to my family for their continuous support and understanding through my entire PhD life.

# Publications

This thesis is based in parts on the following scientific papers:

- I N. J. S. Loft, L. B. Kristensen, A. E. Thomsen, A. G. Volosniev, and N. T. Zinner. “CONAN – The cruncher of local exchange coefficients for strongly interacting confined systems in one dimension”. In: *Computer Physics Communications* 209 (2016), pp. 171–182
- II N. J. S. Loft, L. B. Kristensen, A. E. Thomsen, and N. T. Zinner. “Comparing models for the ground state energy of a trapped one-dimensional Fermi gas with a single impurity”. In: *Journal of Physics B Atomic Molecular Physics* 49.12, 125305 (June 2016), p. 125305
- III N. J. S. Loft, O. V. Marchukov, D. Petrosyan, and N. T. Zinner. “Tunable self-assembled spin chains of strongly interacting cold atoms for demonstration of reliable quantum state transfer”. In: *New Journal of Physics* 18.4, 045011 (Apr. 2016), p. 045011
- IV C. W. Duncan, N. J. S. Loft, P. Öhberg, N. T. Zinner, and M. Valiente. “Spin Localization of a Fermi Polaron in a Quasirandom Optical Lattice”. In: *Few-Body Systems* 58.2 (2017), p. 50
- V N. J. S. Loft, Z. Wu, and G. M. Bruun. “Mixed-dimensional Bose polaron”. In: *Physical Review A* 96.3 (2017), p. 033625
- VI N. J. S. Loft, L. B. Kristensen, C. K. Andersen, and N. T. Zinner. “Quantum spin transistors in superconducting circuits”. In: *arXiv preprint arXiv:1802.04292* (2018)
- VII T. Bækkegaard, L. B. Kristensen, N. J. S. Loft, C. K. Andersen, D. Petrosyan, and N. T. Zinner. “Realization of efficient quantum

gates with a superconducting qubit-qutrit circuit". In: *Scientific Reports (accepted for publication)* (2019)

- VIII N. J. S. Loft, M. Kjaergaard, L. B. Kristensen, C. K. Andersen, T. W. Larsen, S. Gustavsson, W. D. Oliver, and N. T. Zinner. "Quantum interference device for controlled two-qubit operations". In: *arXiv preprint arXiv:1809.09049 (submitted to npj Quantum Information)* (2018)

The thesis also discusses work from the following patent application and software package:

- IX L. B. Kristensen, N. J. S. Loft, C. K. Andersen, and N. T. Zinner. *Quantum logic gate and quantum spin transistors*. European Patent Office application no. EPO 17185721.2–1879. Aug. 10, 2017
- X N. J. S. Loft. *SonPy – Python interface for Sonnet*. Version 1.1. Available here: <https://github.com/QMIT/sonpy>. Sept. 16, 2018

In addition to the work presented in this this thesis, I have published the following scientific paper:

- XI N. J. S. Loft, A. S. Dehkarghani, N. P. Mehta, A. G. Volosniev, and N. T. Zinner. "A variational approach to repulsively interacting three-fermion systems in a one-dimensional harmonic trap". In: *The European Physical Journal D* 69 (2015)

During my PhD, I also published the following outreach articles:

- XII A. S. Dehkarghani, N. J. S. Loft, and N. T. Zinner. "Kvantemagneter – Magneter når de er allermindst". In: *Aktuel Naturvidenskab* 5-2016 (2016)
- XIII N. J. S. Loft. "På jagt efter computerens næste kvantespring". In: *videnskab.dk* (Mar. 24, 2017)
- XIV N. J. S. Loft. "Vi får aldrig eksakt viden om verden". In: *videnskab.dk* (Aug. 10, 2017)
- XV N. J. S. Loft. "Tyngdekraften findes kun i dit hoved". In: *videnskab.dk* (Jan. 27, 2018)
- XVI N. J. S. Loft. "Matematikken kan bryde sammen i morgen". In: *videnskab.dk* (Jan. 6, 2019)

# Contents

<b>1</b>	<b>Strongly interacting cold atoms in one dimension</b>	<b>1</b>
1.1	One-dimensional systems	1
1.1.1	Experimental realization	3
1.1.2	The role of confinement	4
1.2	Effective spin chain model	5
1.2.1	The strongly interacting regime	7
1.2.2	Heisenberg XXZ model	9
1.3	CONAN	12
1.3.1	Algorithm for computing the coefficients	13
1.3.2	Numerical implementation	15
1.3.3	Benchmark results	18
1.3.4	Outlook	19
1.4	Comparing models: what is many and what is strong?	20
1.4.1	Model and theory landscape	21
1.4.2	Mapping to the strongly interacting trapped case	23
1.4.3	Results and discussion	29
1.5	State transfer in a chain of atoms	31
1.5.1	Optimizing the potential	32
1.5.2	Including noise in the potential	34
1.6	Fermi polaron in an quasirandom potential	38
<b>2</b>	<b>Confined polaron in a Bose-Einstein condensate</b>	<b>42</b>
2.1	Bose-Einstein condensation	43
2.1.1	Bogoliubov theory	44
2.2	Green's functions	47
2.2.1	Correlation functions in many-body physics	48
2.2.2	Green's function for a BEC boson	50
2.3	Polarons	52
2.4	Mixed-dimensional Bose polaron	55

2.4.1	Model	55
2.4.2	Self-energy	57
2.4.3	Quasiparticle properties	60
2.4.4	Numerical calculation	60
2.4.5	Results	61
2.4.6	Conclusions	66
<b>3</b>	<b>Superconducting circuits and quantum transistor</b>	<b>67</b>
3.1	Quantum transistor: controlled state transfer	67
3.2	Superconducting qubits: artificial atoms	70
3.2.1	Back-of-the-envelope characterization	71
3.2.2	Basic qubit control and readout	71
3.3	Superconducting circuits	74
3.4	The transmon qubit	76
3.5	The C-shunted flux qubit	80
3.6	The quantum transistor revisited	81
3.7	Heisenberg XXZ coupler	85
3.7.1	Effective circuit Hamiltonian	86
3.7.2	Method	88
3.7.3	Results and discussion	88
3.7.4	Conclusion and outlook	94
3.8	Programmatic chip design with SonPy	94
<b>4</b>	<b>Quantum computing and four-qubit diamond gate</b>	<b>98</b>
4.1	Quantum computing	98
4.1.1	Quantum logic gates	99
4.1.2	Quantum algorithms	104
4.1.3	Advantages	105
4.1.4	Challenges	106
4.2	Four-qubit diamond gate	109
4.2.1	System and unitary gates	110
4.2.2	Extensible quantum computer	114
4.2.3	Numerical simulations	116
4.2.4	Higher-energy states	121
4.2.5	Discussion	126
4.3	Qubit-qutrit based gates	127
4.3.1	Hardware supported gates	128
<b>5</b>	<b>Geometric phases and holonomic gate</b>	<b>131</b>
5.1	Geometric phases	133

5.1.1	Derivation of the geometric phase . . . . .	134
5.2	Two-qubit holonomic gate . . . . .	137
5.2.1	Quaternionic representation . . . . .	139
5.2.2	Holonomy as a quantum gate . . . . .	140
5.2.3	Gauge potential and holonomy . . . . .	141
5.2.4	Final remarks . . . . .	143
<b>A</b>	<b>Mixed-dimensional Bose polaron</b>	<b>144</b>
A.1	$\Sigma_0$ and its derivatives . . . . .	144
A.2	$\Sigma_1$ and its derivatives . . . . .	148
<b>B</b>	<b>Four-qubit diamond gate</b>	<b>151</b>
B.1	Unitary dynamics in the qubit model . . . . .	151
B.1.1	The case of $J_C = 0$ . . . . .	153
B.1.2	The case of non-zero $J_C$ . . . . .	156
B.1.3	Equivalent gate diagram for the diamond gate .	158
B.2	Superconducting circuit analysis . . . . .	160
B.2.1	Derivation of the qutrit model Hamiltonian . .	160
B.2.2	Redefinition of the control states . . . . .	167
B.2.3	Engineering crosstalk . . . . .	168
	<b>Bibliography</b>	<b>171</b>

---

# Strongly interacting cold atoms in one dimension

*My earliest scientific work was about the theoretical description of strongly interacting atoms confined by a one-dimensional potential. I will open this chapter with an introduction to the field and then present a computational method we developed in the group, based on Ref. [1]. This served as a vital tool for the subsequent works published in Refs. [2–4], that I will discuss in the remainder of the chapter.*

## 1.1 One-dimensional systems

Strongly interacting quantum particles are responsible for many physical phenomena. Take for instance superconductivity, superfluidity and magnetism, which all arise due to strong correlations between electrons in certain materials. In 1926, in the early days of quantum mechanics, Heisenberg and Dirac discovered that ferromagnetism was a consequence of an effective correlation between the spin degree of freedom of electrons located at neighboring atoms in a piece of metal[17, 18]. The model, now known as the Heisenberg model, can be expressed in terms of the Hamiltonian

$$H = -J \sum_{i,j} \mathbf{S}_i \cdot \mathbf{S}_j, \quad (1.1)$$

where  $J$  is the effective spin-spin interaction strength and  $\mathbf{S}_i$  is the spin-vector operator for electron  $i$ . The sum is taken over neighboring electrons, typically modeled as sitting at the vertices (atoms) in a three-dimensional lattice. The orientation of the spins with respect to each other is quantified in the dot product, making it energetically favorable for them to either align in the same direction ( $J > 0$ ), or alternating directions ( $J < 0$ ), as observed in ferromagnets and antiferromagnets, respectively.

A simple case of the Heisenberg model is when the lattice is one-dimensional. Of course, this is far away from the three-dimensional scenario arising in Nature, but studying crudely simplified ‘toy models’ often captures the essential physics and guides intuition. Onsager[19] solved the two-dimensional Ising model in 1944, but most models have only been solved in one dimension. For instance, the one-dimensional Heisenberg model was solved in 1931 by Bethe[20], who assumed a specific form of the wavefunctions – known as the Bethe ansatz – in order to find analytic expressions for the eigenstates and energies of the Hamiltonian. Since then, the Bethe ansatz and variations thereof have been employed to solve a broad range of one-dimensional models[21].

Even though the important physics is often retained when the model dimensionality is reduced, some phenomena are unique to one dimension due to the restrictive geometry. Consider a collection of particles arranging themselves in a configuration in order to lower the system energy. In two or more dimensions, a pair of particles can exchange their positions without physically occupying the same space, but in one dimension, they cannot. If the particles have a strong short-range interaction, the fact that particles have to touch in order to swap positions makes one-dimensional systems very special. In particular, if the interaction is strongly repulsive, coming into contact with one another is energetically unfavorable, making the particles behave like hard spheres. As a consequence, even bosons will refuse to occupy the same space, making them obey an exclusion principle similar to Pauli’s exclusion principle for fermions[22, 23]. Thus, the process is called fermionization. The system of strongly repulsive bosons in one dimension is known as a Tonks-Girardeau gas[22, 24].

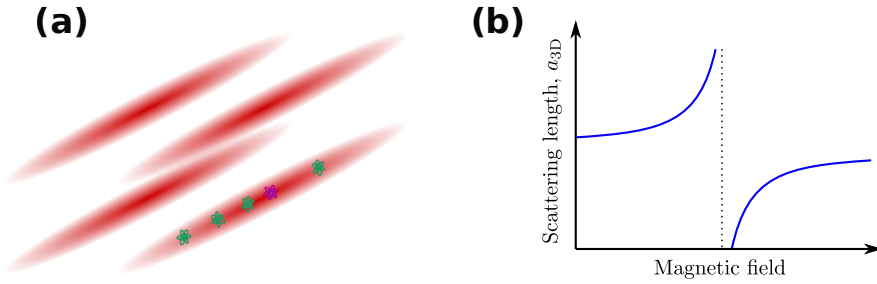


Figure 1.1: (a) Few-body one-dimensional system created by trapping atoms (green and purple) in laser fields (red). (b) Sketch of the scattering length as a function of the external magnetic field, which diverges at the Feshbach resonance, allowing for a tunable inter-particle interaction of both large attractive and repulsive nature.

### 1.1.1 Experimental realization

For many years, one-dimensional systems was purely a theoretical game, as experimentalists were limited to studying what Nature provided them. However, within the recent 10 to 20 years, progress in experimental techniques have made it possible to realize a wide range of one-dimensional systems[25–32], including the Tonks-Girardeau gas[33, 34]. These systems are realized by trapping a gas of atoms in a potential well created by a laser field. By tuning the laser frequency, one can slow down the average speed of the atoms via Doppler cooling, while a magnetic quadrupole field confines them to a small volume. Additional cooling of the gas cloud is ensured by lowering the side walls of the confining potential, allowing the most excited atoms to escape the trap. This technique, called evaporative cooling, allows the temperature to become just a few  $\mu\text{K}$ , and the cloud is referred to as an ultracold atomic gas. At this stage, bosons condensate into a single coherent ground state, known as a Bose-Einstein condensate, while fermions populate a Fermi sea of the lowest available states. To create one-dimensional systems, a two-dimensional optical lattice is superimposed into the three-dimensional cloud, forming elongated cigar-shaped tubes that traps a few atoms each, as illustrated in Figure 1.1a.

The effective interaction strength between the atoms can be controlled through a Feshbach resonance, which occurs when the energy

of two scattering atoms is close to the energy of a two-body bound state[35, 36]. Often, the relevant states are hyperfine states with an energy controlled by an external magnetic field due to the Zeeman effect, which makes it possible to tune the system in and out of the Feshbach resonance at will. This gives experimentalists a handle on the scattering length between the atoms that depends on the applied magnetic field as shown in Figure 1.1b. The effective contact interaction between the atoms has a coupling strength[37]

$$g = -\frac{2\hbar^2}{ma_{1D}}, \quad (1.2)$$

that depends on the effective one-dimensional scattering length,  $a_{1D}$ , and the atomic mass,  $m$ . Here, and in the remainder of this dissertation,  $\hbar$  is Planck's reduced constant. The one-dimensional scattering length is directly related to the three-dimensional scattering length,  $a_{3D}$ , through[38]

$$a_{1D} = -\frac{l_{\perp}^2}{a_{3D}} \left( 1 - 1.0326 \frac{a_{3D}}{l_{\perp}} \right). \quad (1.3)$$

Here it is assumed that the perpendicular confinement is due to a harmonic oscillator potential with frequency  $\omega_{\perp}$  and oscillator length  $l_{\perp} = \sqrt{\hbar/(m\omega_{\perp})}$ . Thus, by controlling the three-dimensional scattering length and the perpendicular confinement, one can tune the interaction strength,  $g$ , from weakly interacting systems to strongly attractive or repulsive systems.

So far, we have imagined a system consisting of identical particles. Mixed systems can be created using different atoms or atoms of the same species in different hyperfine states. A typical example is a two-component mixture, often denoted as  $A$  and  $B$  particles or spin up ( $\uparrow$ ) and spin down ( $\downarrow$ ) states. In this way, one have realized multi-component Bose gases, Fermi gases and even Bose-Fermi mixtures; see Ref. [37] for a recent review.

### 1.1.2 The role of confinement

During the 1960's the Bethe ansatz method proved very useful in solving several paradigmatic one-dimensional models[23, 39–42]. The advent of experimental one-dimensional physics and the possibility of testing the textbook solutions sparked renewed interest in one-dimensional systems. As these models were invented in order to

understand many-body condensed matter systems, open or periodic boundary conditions were assumed, which made them solvable by the Bethe ansatz. In general, the Bethe ansatz cannot be applied to particles confined by potential, which is nonetheless the case in the experiments described above. This short-coming motivated theoreticians to understand the role of the confining potential, and take it into account.

In 2006, Girardeau demonstrated that a one-dimensional strongly interacting atomic system could be mapped to a spin model akin to the Heisenberg model described in the opening of this chapter[43]. Although it was first believed that the strength of the exchange couplings between neighboring sites were all identical as in Eq. (1.1), this turned out not to be the case[44, 45]. For non-homogeneous confining potentials, such as a harmonic oscillator trap, the exchange coupling strengths must reflect the potential energy landscape, and thus be site-dependent. Volosniev *et al.* derived a confinement-dependent spin model in 2014[46]. Here it was also shown that, as long as the interaction is strong and the atomic masses equal, the exchange coefficients are independent of the system composition, i.e. whether the atoms are bosons, fermions, a Bose-Fermi mixture.

Although Ref. [46] provided an explicit expression for the spin model exchange coefficients, it did not scale favorably with the system size from a computational point of view. For a system of  $N$  atoms, each coefficient had to be computed as an  $(N - 1)$ -dimensional integral over an  $N$ -body Slater determinant wavefunction. Two similar methods that bypass the numerical complexity of the integral and Slater determinant were published simultaneously in 2016[1, 47]. In the following, I shall elaborate on the effective spin model for strongly interacting one-dimensional systems, and our method for efficiently computing the exchange coefficients, published in Ref. [1].

## 1.2 Effective spin chain model

The spin model mapping for strongly interacting atoms in one-dimension was given by Deuretzbacher *et al.* for a harmonic confining potential[48], and by Volosniev *et al.* for an arbitrary confining potential[49]. Here, I follow Ref. [49].

Consider a two-component quantum gas confined to a one-dimensional potential,  $V(x)$ . We refer to the two species as ‘spin up’ and

‘spin down’. Denote by  $N_\uparrow$  the number of spin up particles and their coordinates by  $x_1, x_2, \dots, x_{N_\uparrow}$ . The total number of particles is  $N = N_\uparrow + N_\downarrow$ , where  $N_\downarrow$  is the number of spin down particles, located at the positions  $x_{N_\uparrow+1}, \dots, x_N$ . We assume that the particles interact through a repulsive short-range interaction, which we model with Dirac delta functions, which only contribute when particles share position coordinates. The strength of interspecies interaction is  $g \geq 0$ , while intraspecies interaction is modulated by a dimensionless parameter  $\kappa \geq 0$ . Thus, the  $N$ -body system can be described with the Hamiltonian,

$$\begin{aligned}
 H = & \sum_{i=1}^N H_0(x_i) + \underbrace{g \frac{\hbar^2}{m\ell} \sum_{i=1}^{N_\uparrow} \sum_{j=N_\uparrow+1}^N \delta(x_i - x_j)}_{\uparrow\downarrow \text{ interaction}} \\
 & + \underbrace{\kappa g \frac{\hbar^2}{m\ell} \sum_{i=1}^{N_\uparrow} \sum_{j>i}^{N_\uparrow} \delta(x_i - x_j)}_{\uparrow\uparrow \text{ interaction}} + \underbrace{\kappa g \frac{\hbar^2}{m\ell} \sum_{i=N_\uparrow+1}^N \sum_{j>i}^N \delta(x_i - x_j)}_{\downarrow\downarrow \text{ interaction}}, \tag{1.4}
 \end{aligned}$$

where  $H_0(x_i)$  is the one-body Hamiltonian for particle  $i$ ,

$$H_0(x) = -\frac{\hbar^2}{2m} \frac{\partial^2}{\partial x^2} + V(x). \tag{1.5}$$

In the interaction terms above, I have included the factor  $\hbar^2/(m\ell)$ , where  $\ell$  is a characteristic length scale of the potential, in order to render  $g$  dimensionless. However, this factor is sometimes omitted, or expressed in units where it is one.

The Hamiltonian of Eq. (1.4) may both describe bosons and fermions, but the particle type must be reflected in the symmetry of the total wavefunction, which should be symmetric (anti-symmetric) under the exchange of coordinates of identical bosons (fermions). In particular, this means that the wavefunction for fermions must vanish whenever two particles in the same spin state come into contact. This can be enforced by letting  $\kappa \rightarrow \infty$  since the energy would receive diverging contributions, scaling with  $\kappa g$ , unless the wavefunction vanishes at the contact line,  $x_i = x_j$ . Thus, in this limit, with proper antisymmetrization, we can retrieve a fermionic system from a bosonic system.

### 1.2.1 The strongly interacting regime

The requirement of finite energy also has interesting consequences for the Tonks-Girardeau limit of infinitely strong interaction,  $g \rightarrow \infty$ . In this limit, the  $N$ -body wavefunction must vanish whenever any two particles meet,  $x_i = x_j$  for any  $i$  and  $j \neq i$ , no matter their spin statistics. This is satisfied for Slater determinant wavefunction,  $\Phi_0(x_1, \dots, x_N)$ , composed of the  $N$  lowest-energy solutions to the one-body Schrödinger equation,

$$H_0(x)\psi_i(x) = \epsilon_i\psi_i(x), \quad i = 1, 2, \dots \quad (1.6)$$

Explicitly, the Slater determinant wavefunction is obtained by considering all possible ways to fill the  $N$  particles in the  $N$  lowest-energy orbitals, then adding these product states in an antisymmetric fashion,

$$\begin{aligned} \Phi_0(x_1, \dots, x_N) &= \begin{vmatrix} \psi_1(x_1) & \psi_2(x_1) & \cdots & \psi_N(x_1) \\ \psi_1(x_2) & \psi_2(x_2) & \cdots & \psi_N(x_2) \\ \vdots & \vdots & \ddots & \vdots \\ \psi_1(x_N) & \psi_2(x_N) & \cdots & \psi_N(x_N) \end{vmatrix} \\ &= \sum_{\sigma \in S_N} \text{sign}(\sigma) \prod_{i=1}^N \psi_{\sigma(i)}(x_i), \end{aligned} \quad (1.7)$$

where  $\sigma$  is a permutation operator acting on the set  $\{1, 2, \dots, N\}$ , the symmetric group,  $S_N$ , being the set of these. This wavefunction is antisymmetric in the exchange of any pair of coordinates,  $x_i \leftrightarrow x_j$ , and is normalized according to

$$\int_{x_1 < x_2 < \dots < x_N} dx_1 dx_2 \dots dx_N |\Phi_0|^2 = 1. \quad (1.8)$$

In the Tonks-Girardeau limit, the Slater determinant solves the  $N$ -body Schrödinger equation,  $H\Phi_0 = E_0\Phi_0$ , with the energy  $E_0 = \sum_{i=1}^N \epsilon_i$ . In fact, the ground state energy  $E_0$  is degenerate, as a general ground state can be written on the form [22, 46, 49]

$$\Psi(x_1, \dots, x_N) = \sum_{n=1}^{N!/(N_\uparrow!N_\downarrow!)} a_n \Pi_n \Phi_0(x_1 < x_2 < \dots < x_N), \quad (1.9)$$

which is a sum over all permutations  $\Pi_n$  of coordinates. Each coefficient,  $a_n$ , scales the Slater determinant in a region of the  $N$ -dimensional position space defined by a specific ordering of the

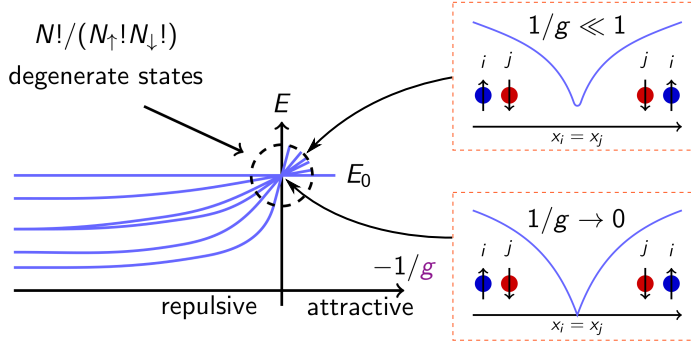


Figure 1.2: The low-energy states become degenerate in the limit of infinitely strong interaction, and the  $N$ -body wavefunction must vanish at particle intersection lines. When the interaction is strong, but finite, the degeneracy is lifted and the wavefunction becomes non-zero.

particles. There are  $N!/(N_\uparrow!N_\downarrow!)$  regions of distinct particle orderings, giving rise to just as many independent ground states with energy  $E_0$ .

For strong – but not infinitely strong – interactions,  $1/g \ll 1$ , the degeneracy of the ground state manifold is lifted, as illustrated in Figure 1.2. The finite interaction strength will in general no longer pin the wavefunction to zero at  $x_i = x_j$ , but it will gain a small finite value (unless they are identical fermions). This allows neighboring particles to exchange positions, and we can intuitively understand that the system can be described in terms of spins with neighbor-neighbor exchange interactions. Technically, the spin model arises as a perturbative expansion to linear order in  $1/g$ .

Consider  $\Psi$  in the vicinity of the degeneracy point, where its energy  $E = \langle \Psi | H | \Psi \rangle / \langle \Psi | \Psi \rangle$  depends on  $g$ . From the Hellman-Feynman theorem,

$$\begin{aligned} \frac{\partial E}{\partial g} = & \frac{\hbar^2}{m\ell} \sum_{i=1}^{N_\uparrow} \sum_{j=N_\uparrow+1}^N \langle \Psi | \delta(x_i - x_j) | \Psi \rangle \\ & + \frac{\kappa \hbar^2}{m\ell} \left( \sum_{i=1}^{N_\uparrow} \sum_{j>i}^{N_\uparrow} \langle \Psi | \delta(x_i - x_j) | \Psi \rangle + \sum_{i=N_\uparrow+1}^N \sum_{j>i}^N \langle \Psi | \delta(x_i - x_j) | \Psi \rangle \right) \end{aligned} \quad (1.10)$$

Furthermore, the delta function interactions yields the following boundary condition at the contact position,  $x_i = x_j$ , of any two particles[49]:

$$\left( \frac{\partial \Psi}{\partial x_i} - \frac{\partial \Psi}{\partial x_j} \right) \Big|_{x_i - x_j = 0^-}^{x_i - x_j = 0^+} = 2\tilde{g} \Psi(x_1, \dots, x_N) \Big|_{x_i = x_j}, \quad (1.11)$$

where  $\tilde{g} = g/\ell$  if particle  $i$  and  $j$  are from different species, and  $\tilde{g} = \kappa g/\ell$  if they are identical (same spin). Combining Eqs. (1.10) and (1.11), one can obtain an expression for  $\partial E/\partial g$  as an expansion in  $1/g$ , and subsequently, to first order in  $1/g$ ,

$$E = E_0 - \frac{\hbar^2 \ell}{m} \sum_{k=1}^{N-1} \frac{\alpha_k}{g} \left( \beta_k + \frac{1}{\kappa} \gamma_k \right), \quad (1.12)$$

where  $\beta_k$  and  $\gamma_k$  are sums involving only the wavefunction coefficients  $a_n$  from Eq. (1.9). On the other hand, the coefficients  $\alpha_k$  does not depend on the specific eigenstate, but solely on the confining potential,  $V(x)$ , through  $\Phi_0$ , and are henceforth known as *geometric coefficients*:

$$\alpha_k = \int_{x_1 < x_2 < \dots < x_{N-1}} dx_1 dx_2 \dots dx_{N-1} \left| \frac{\partial \Phi_0}{\partial x_N} \right|_{x_N = x_k}^2. \quad (1.13)$$

### 1.2.2 Heisenberg XXZ model

In Ref. [49], Volosniev *et al.* map the  $N!/(N_\uparrow!N_\downarrow!)$  particle configurations to spin states, i.e.

$$|\Psi\rangle = \sum_{n=1}^{N!/(N_\uparrow!N_\downarrow!)} a_n \Pi_n \left| \uparrow_1 \dots \uparrow_{N_\uparrow} \downarrow_{N_\uparrow+1} \dots \downarrow_N \right\rangle, \quad (1.14)$$

and construct the following spin model Hamiltonian with the states of Eq. (1.14) as eigenstates with energies given by Eq. (1.12):

$$H_s = E_0 - \frac{\hbar^2 \ell}{m} \sum_{k=1}^{N-1} \frac{\alpha_k}{g} \left[ \frac{1}{2} (1 - \sigma_k \cdot \sigma_{k+1}) + \frac{1}{\kappa} (1 + \sigma_z^k \sigma_z^{k+1}) \right]. \quad (1.15)$$

This Hamiltonian is an effective description of the low-energy spectrum in the strongly interacting regime, based on a linearization in

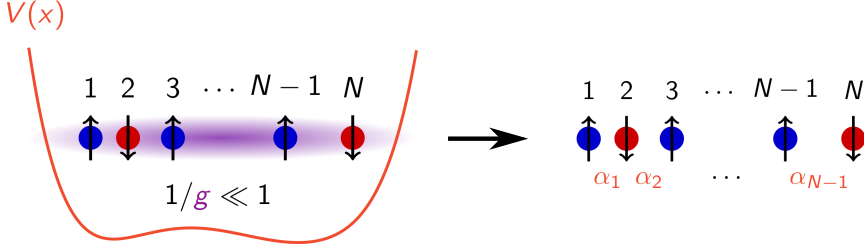


Figure 1.3: A system of  $N$  strongly interacting particles confined in a one-dimensional potential  $V(x)$  (left) can be mapped onto a lattice spin model with local exchange couplings proportional to  $\alpha_1, \dots, \alpha_{N-1}$  (right).

$1/g$  near the degenerate ground state manifold depicted in Figure 1.2. The mapping from a continuous model of atoms in a confining potential to a lattice spin model is illustrated in Figure 1.3. In the spin picture, we imagine a chain of  $N$  sites, where each site is populated by a spin-down or spin-up particle. Two neighboring particles exchanging position can equivalently be regarded as two neighboring sites in the chain exchanging spin states, i.e. flipping spins, if one is spin up and the other spin down. As is evident from Eq. (1.15), the coupling strength between site  $k$  and  $k+1$  is proportional to the local geometric coefficient,  $\alpha_k$ .

The Hamiltonian  $H_s$  is expressed in terms of Pauli spin operators,  $\sigma_k = (\sigma_x^k, \sigma_y^k, \sigma_z^k)$ , acting on site number  $k$ , given by

$$\sigma_x^k = |\uparrow_k\rangle\langle\downarrow_k| + |\downarrow_k\rangle\langle\uparrow_k|, \quad (1.16)$$

$$\sigma_y^k = -i|\uparrow_k\rangle\langle\downarrow_k| + i|\downarrow_k\rangle\langle\uparrow_k|, \quad (1.17)$$

$$\sigma_z^k = |\uparrow_k\rangle\langle\uparrow_k| - |\downarrow_k\rangle\langle\downarrow_k|. \quad (1.18)$$

Re-arranging the terms, we can express

$$H_s = \sum_{k=1}^{N-1} \frac{1}{2} J_x^k (\sigma_x^k \sigma_x^{k+1} + \sigma_y^k \sigma_y^{k+1}) + J_z^k \sigma_z^k \sigma_z^{k+1}, \quad (1.19)$$

with  $J_x^k = \hbar^2 \ell \alpha_k / (mg)$  and  $J_z^k = J_x^k (1/2 - 1/\kappa)$ . This is known as a Heisenberg XXZ model due to the similarity with Eq. (1.1); the spin-1/2 operators can be expressed as  $\mathbf{S}_k = (\hbar/2)\sigma_k$ . The two

models coincide when the sum in Eq. (1.1) is considered over a one-dimensional lattice of  $N$  sites and all couplings in  $H_s$  are identical,  $J_x^k/2 = J_z^k = -J\hbar^2/4$ .

Heisenberg models are typically given a label on the form 'XYZ'; these three letters refer to the coupling coefficients on the  $\sigma_x^k\sigma_x^{k+1}$ -term (XX coupling),  $\sigma_y^k\sigma_y^{k+1}$ -term (YY coupling) and  $\sigma_z^k\sigma_z^{k+1}$ -term (ZZ coupling), respectively. When they are identical, as in Eq. (1.1), the model is known as a Heisenberg XXX model. In  $H_s$ , the XX and YY coupling are identical, but different from the ZZ coupling, hence the label XXZ. When the ZZ coupling is zero,  $J_z^k = 0$ , which occurs when  $\kappa = 2$ , it reduces to a Heisenberg XX model.

One typically only encounters systems, where the XX and YY couplings are identical, since these couplings in combination are responsible for spin flip. In fact, by defining the raising and lowering operators for site  $k$ , respectively,

$$\sigma_+^k = |\downarrow_k\rangle\langle\uparrow_k|, \quad (1.20)$$

$$\sigma_-^k = |\uparrow_k\rangle\langle\downarrow_k|, \quad (1.21)$$

we can express

$$H_s = \sum_{k=1}^{N-1} J_x^k (\sigma_+^k \sigma_-^{k+1} + \sigma_-^k \sigma_+^{k+1}) + J_z^k \sigma_z^k \sigma_z^{k+1}. \quad (1.22)$$

In this form, we see directly that  $J_x^k = \hbar^2 \ell \alpha_k / (mg)$  is the strength of the local exchange (spin flip) coupling between site  $k$  and  $k + 1$  in the chain. In addition to the model parameters  $g$ ,  $\kappa$ ,  $m$ , and  $\ell$ , which appear in the original Hamiltonian of Eq. (1.4), the Heisenberg XXZ model is uniquely specified by the geometric coefficients  $\alpha_k$ . However, as is evident from the  $(N - 1)$ -dimensional integral over an  $N$ -body Slater determinant wavefunction in Eq. (1.13), a brute force computation of  $\alpha_k$  using this equation is only feasible for very small systems. The next section will introduce an algorithm that was developed and implemented in the group in order to compute the geometric coefficients in an efficient way.

## 1.3 CONAN

In this section, I will account for the algorithm and software implementation for computing the geometric coefficients, that I contributed to developing. Our results were published in Ref. [1], which forms the basis for this section. The paper is highly technical, containing involved mathematical proofs and instructions for the use of our software implementation, but here I will abstain from going into these details. I will instead give a qualitative explanation of our computational method and present some benchmark results for the efficiency of the code, which we released as open source software under the name CONAN (Coefficients of One-dimensional  $N$ -Atom Networks).

As shown in Ref. [1], one can get rid of the  $(N - 1)$ -dimensional integral and the Slater determinant of Eq. (1.13) by expressing the  $k$ 'th geometric coefficient as

$$\begin{aligned}
 \alpha_k &= \frac{4m}{\hbar^2} \sum_{i=1}^N \sum_{j=1}^N \sum_{l=0}^{N-1-k} \frac{(-1)^{i+j+N-k}}{l!} \binom{N-l-2}{k-1} \\
 &\times \int_a^b dx (V(x) - \epsilon_i) \psi_i(x) \frac{d\psi_j}{dx} \\
 &\times \left[ \frac{\partial^l}{\partial \lambda^l} \det \left[ (B(x) - \lambda \mathbb{1})^{(ij)} \right] \right]_{\lambda=0} \\
 &+ \sum_{i=1}^N \left[ \frac{d\psi_i}{dx} \right]_{x=b}^2.
 \end{aligned} \tag{1.23}$$

The first line begins a triple sum with  $\sim N^3$  terms with alternating signs and a binomial coefficient. The second line is an integral involving the single-particle solutions from Eq. (1.6) over the interval  $[a; b]$ , which denote the support of  $V(x)$ . For instance, a hard box from  $x = 0$  to  $x = L$  has  $[a; b] = [0; L]$ , and a harmonic oscillator has  $[a; b] = ] - \infty, \infty[$ . In the third line,  $\mathbb{1}$  denotes the  $N \times N$  identity matrix and  $(\ )^{(ij)}$  denotes the  $ij$ 'th submatrix, i.e. the matrix with the  $i$ 'th column and  $j$ 'th row removed. The  $N \times N$  symmetric matrix  $B(x)$  contains partial overlaps of single-particle wavefunction, with the  $mn$ 'th entry defined as

$$[B(x)]_{m,n} = \int_a^x dy \psi_m(y) \psi_n(y). \tag{1.24}$$

The fourth and final line is a boundary term.

When Lasse B. Kristensen, Anders E. Thomsen and I joined the project, Artem G. Volosniev had derived Eq. (1.23) without the boundary term, which I realized was necessary to include. LBK, AET and I then developed an efficient algorithm for computing the  $l$ 'th order derivative of the determinant in the third line above, which constituted the main obstacle for an efficient implementation. The final algorithm for  $\alpha_k$  was implemented in the C programmatic language as the open source software CONAN, which was developed by LBK, AET and myself, with LBK as lead programmer. The initial source code was turned into a user-friendly software program with the help of two student programmers, which I organized, and I wrote the documentation for CONAN. I tested and benchmarked the software, see Sec. 1.3.3. Finally, I had the main responsibility for writing the paper[1], but all authors contributed.

### 1.3.1 Algorithm for computing the coefficients

This subsection is quoted from Ref. [1] Secs. 3.1–3.2 with minor changes to fit the context here.

From the standpoint of an effective numerical implementation of Eq. (1.23) the complicated part is the evaluation of the derivatives of the determinant,

$$\left[ \frac{\partial^l}{\partial \lambda^l} \det \left[ (B(x) - \lambda \mathbf{1})^{(ij)} \right] \right]_{\lambda=0}. \quad (1.25)$$

Our method for evaluating this expression is due to the fact that  $B$  is symmetric (and real as we can choose real wavefunctions  $\psi_i$ ), and, hence, diagonalizable using an orthogonal matrix  $U = (\mathbf{u}_1 \dots \mathbf{u}_N)$  such that  $B = U^T D U$ , where  $D$  is a diagonal matrix composed of the eigenvalues of  $B$ . We note that taking the  $ij$ 'th submatrix of  $B$  is equivalent to removing a row and a column from  $U^T$  and  $U$  respectively. This observation allow us to show that the expression in Eq. (1.25) can be written as

$$(-1)^{i+j} l! \mathbf{u}_j^T \left( \sum_{n=0}^l p_{l-n} D^{-(n+1)} \right) \mathbf{u}_i, \quad (1.26)$$

where  $p_k$  are the coefficients of the polynomial

$$\det(D - \lambda \mathbf{I}) = p_N \lambda^N + \dots + p_1 \lambda + p_0. \quad (1.27)$$

Several comments are in order here. First of all, as  $D$  is diagonal, it can be easily inverted as long as its entries are nonzero. It can be proved that this is in fact the case. Secondly, the coefficients  $p_k$  are easily computable because  $\det(D - \lambda \mathbf{I})$  is a determinant of a diagonal matrix. Thirdly, a further reduction in computation requirements can be achieved by doing the sum over  $l$  inside the integral. Then we diagonalize  $B$  only once, rather than once for each  $l$ . Therefore, to evaluate the integrand we need to compute the expression

$$\begin{aligned} & (-1)^{i+j} \sum_{l=0}^{N-1-k} \binom{N-2-l}{k-1} \frac{1}{l!} \left[ \frac{\partial^l}{\partial \lambda^l} \det \left[ (B(x) - \lambda \mathbf{I})^{(ij)} \right] \right]_{\lambda=0} \\ &= \mathbf{u}_j^T \left[ \sum_{l=0}^{N-1-k} \binom{N-2-l}{k-1} \sum_{n=0}^l p_{l-n} D^{-(n+1)} \right] \mathbf{u}_i. \end{aligned} \quad (1.28)$$

Finally, and perhaps most interestingly, the expression in Eq. (1.28) depends on  $i$  and  $j$  only through  $\mathbf{u}_i$  and  $\mathbf{u}_j$ . Hence, the vast majority of the computations are independent on  $i$  and  $j$  which prompts us to take the sum over  $i$  and  $j$  inside the integral in Eq. (1.23) as well, and reuse the result for the derivatives of the determinant. The procedure reduces the computation time as the derivatives have to be computed only once for each  $x$  rather than computing it  $\sim N^2$  times.

We now outline our method for computing the coefficients  $\alpha_k$  from Eq. (1.23), where we first take all the sums for a given  $x$  and then perform the integration. To take the sums the following is done:

1. The entries of  $B(x)$  are evaluated.
2. The matrix  $B(x)$  is diagonalized.
3. The coefficients  $p_k$  are computed.
4. The matrices  $D^{-(n+1)}$  are computed for all  $0 \leq n \leq N-1-k$  utilizing that  $D$  is diagonal.
5. The (diagonal) matrix inside the square brackets of Eq. (1.28) is evaluated.
6. The sum over  $i$  and  $j$  is taken. For this the product in Eq. (1.28) is multiplied by the appropriate factors of  $\psi_i$ ,  $d\psi_j/dx$ , and  $(V - \epsilon_j)$ .

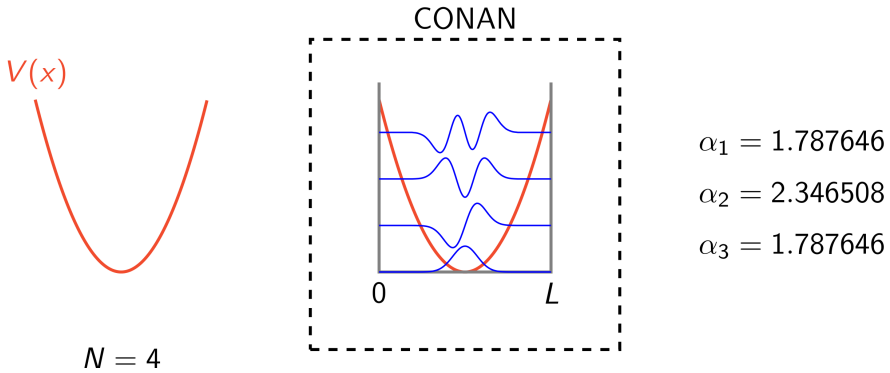


Figure 1.4: The software CONAN takes an input potential,  $V(x)$ , and particle number,  $N$ , and places the system in a hard wall box of length  $L$  in order to find the  $N$  lowest single-particle energy states, from which the geometric coefficients,  $\alpha_k$ , for  $k = 1, \dots, N - 1$  are computed and returned to the user.

From the procedure sketched above we can estimate how the computation time scales with the number of particles,  $N$ . It seems that the steps 2, 5, and 6 are the most demanding for large  $N$ , because the computation time of all these steps scales roughly as  $O(N^3)$ . Still, this scaling is surprisingly good.

### 1.3.2 Numerical implementation

The algorithm above works for a general system defined on the interval  $[a; b]$ , which may be  $\mathbb{R}$ . However, in order to achieve a feasible numerical implementation, we will truncate the physical extend of the system by placing the system in a hard wall box on  $[0; L]$ , i.e. such that  $V(0) = V(L) = \infty$ , as illustrated in Figure 1.4. Since the computation of the geometric coefficients require us to find the  $N$  lowest single-particle energy-states in  $V(x)$ , the box length,  $L$ , should be chose large enough to ensure that the hard walls do not influence these states.

Placing the system in a box allow us to express the required single-particle eigenstates,  $\psi_i(x)$ , in the basis of hard box eigenstates,

$$\phi_n(x) = \sqrt{\frac{2}{L}} \sin\left(\frac{n\pi x}{L}\right), \quad n = 1, \dots, N_b. \quad (1.29)$$

Here  $N_b$  is number of hard box eigenstates that we use in the expansion. It should be chosen sufficiently large,  $N_b \gg N$ , such that  $\psi_i(x)$  for  $i = 1, \dots, N$  can accurately be decomposed in the finitely sized hard box basis. Expressing the single-particle Hamiltonian,  $H_0(x)$ , as a  $N_b \times N_b$  matrix in the basis of hard box states, we diagonalize the it numerically and obtain the  $N$  lowest-energy eigenstates and corresponding energies. Then, we define a  $N \times N_b$  matrix  $C$  composed of the expansion coefficients,

$$[C]_{i,m} = \int_0^L dx \phi_m(x) \psi_i(x), \quad (1.30)$$

and the matrix  $f(x)$  with matrix elements

$$[f(x)]_{m,n} = \begin{cases} \frac{\sin((m-n)\pi x/L)}{\pi(m-n)} - \frac{\sin((m+n)\pi x/L)}{\pi(m+n)} & \text{for } m \neq n \\ \frac{x}{L} - \frac{1}{2\pi m} \sin(2m\pi x/L) & \text{for } m = n. \end{cases} \quad (1.31)$$

Then the starting point of the algorithm, the matrix  $B(x)$ , can be computed as

$$B(x) = C f(x) C^T. \quad (1.32)$$

Computing  $B(x)$  this way, the  $x$ -dependence lies only in the analytically known matrix  $f(x)$ , and the numerical integrals in  $C$  only have to be computed once. This is significantly faster than numerically performing the integrals in Eq. (1.24) for each  $x$ -point.

The success of the implementation hinges on an accurate numerical diagonalization of  $B(x)$ . Since some of the partial overlap integrals in  $B(x)$  can be very small – spanning several orders of magnitude – it can become numerically demanding to compute high powers of its inverse eigenvalues,  $D^{-(n+1)}$ , in Eq. (1.28). The usual floating point machine precision becomes insufficient for  $N \gtrsim 7$ , and we therefore had to implement the diagonalization of  $B(x)$  using an arbitrary precision library, which increases the computation time. In order to get a numerically stable computation, the bit-precision,  $p$ , has to be increased with  $N$ . The machine default precision is  $p = 64$ , which we increased by factors of two,  $p = 64, 128, 256, 512, 1024, \dots$ , when necessary, impacting the scaling of the computation time to more than  $O(N^3)$ . The next subsection will show a scaling of  $O(N^{3.5 \pm 0.4})$ .

Finally, the computation of each coefficient,  $\alpha_k$  for  $k = 1, \dots, N-1$ , can be performed independently, which lead us to parallelize the computation on multiple threads, thereby saving overall computation time.

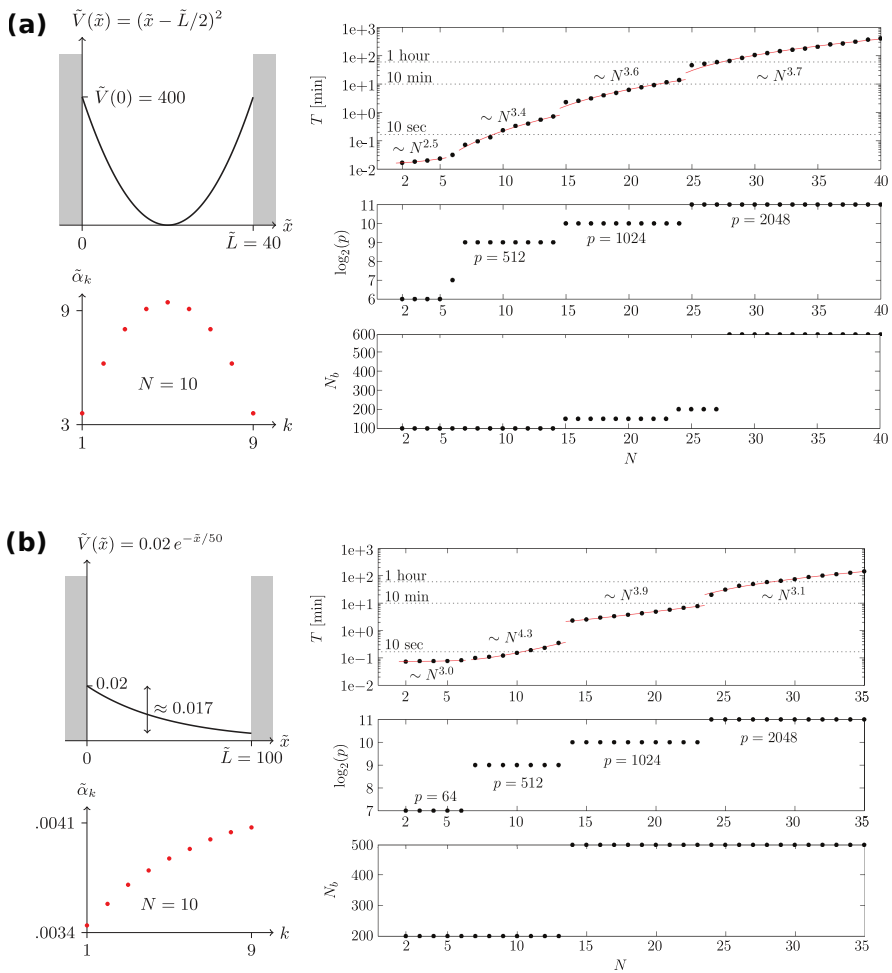


Figure 1.5: Example usage of CONAN for (a) a harmonic potential and (b) an asymmetric tilted potential, see the main text for details. The figure is adapted from Ref. [1].

### 1.3.3 Benchmark results

Ref. [1] presented examples of the use of CONAN for two different potentials over a wide range of system sizes,  $N$ . This was done in order to determine the scaling of the computation time, and to understand the typical precision settings such as the basis size,  $N_b$ , and bit-precision,  $p$ , required to obtain accurate results. Here, I summarize the results.

Every physical quantity in CONAN must be expressed in terms of the length  $\ell$  and energy  $\epsilon = \hbar^2 / (2m\ell^2)$ . In this subsection, a tilde will denote a unitless physical quantity, e.g.  $\tilde{V}(\tilde{x}) = V(x/\ell)/\epsilon$  and  $\tilde{\alpha}_k = \ell^3 \alpha_k$ .

We focus on the following two potentials: A harmonic oscillator,

$$\tilde{V}(\tilde{x}) = (\tilde{x} - \tilde{L}/2)^2 \quad \text{with box length } \tilde{L} = 40, \quad (1.33)$$

and an asymmetric tilted potential in a box,

$$\tilde{V}(\tilde{x}) = \begin{cases} 0.02e^{-\tilde{x}/50} & \text{for } 0 < \tilde{x} < \tilde{L} = 100 \\ \infty & \text{otherwise.} \end{cases} \quad (1.34)$$

These potential are sketched in Figure 1.5a and Figure 1.5b, respectively, which also show the resulting geometric coefficients for  $N = 10$ , and plots of the computation time  $T$ , bit-precision,  $p$ , and basis size,  $N_b$ , over a wide range of  $N$ .

The geometric coefficients reflect the potential shape, as they seems to mimic  $-V(x)$ . This can intuitively be understood from the following consideration: Whenever  $-V(x)$  is large, the spatial overlap of the wavefunctions for neighboring particles tends to be large, as more particles seek towards the local potential minima. This leads to a large exchange coefficient,  $\alpha_k$ , between the  $k$ 'th and  $(k + 1)$ 'th particle, where  $k$  translates to a discretized position coordinate in the spin chain.

Since the geometric coefficients are generally unknown, it is difficult to estimate the accuracy of the calculated geometric coefficients. One method is to increase  $p$  or  $N_b$  until the variation in the resulting coefficients is within a desired error bound. Furthermore, symmetric potentials, such as the harmonic oscillator, produces symmetric coefficients,  $\alpha_k = \alpha_{N-k}$ . Since  $\alpha_k$  and  $\alpha_{N-k}$  are computed in CONAN independently and using different routines, we can estimate the accuracy by inspecting symmetric pairs of coefficients. Since the use

of CONAN depends highly on the specific potential, it is difficult to give a general error estimate. However, in the examples in Figure 1.5, we estimate that the error is less than 0.0001% for  $N < 29$ , which increases to about 0.01% for  $N = 35$ . For larger  $N$ , the error is generally a few percent, but individual coefficients deviate from the rest as the system size increases to  $N = 40$ , leading us to conclude that CONAN should be restricted to at most  $N \sim 35$ .

As the value of  $N$  is increase, it becomes necessary to adjust the bit-precision,  $p$ , and the basis size,  $N_b$ , in order to ensure numerical stability and accurate results. Figure 1.5 shows how they were picked, and the resulting computation time,  $T$ . Sudden jumps in  $T$  are seen whenever  $p$  is doubled. We estimate the scaling of  $T$  with  $N$  by fitting the data points to a power law on the plateaus with constant  $p$ , which leads us to a scaling on the order  $O(N^{3.5 \pm 0.4})$ . Computation time is around 10 seconds for  $N \sim 10$ , and less than 10 minutes for  $N \sim 20$ . For the many-particle regime,  $N \sim 30$ , one or several hours has to be expected.

### 1.3.4 Outlook

CONAN provides a valuable tool for investigating effective spin chain models of one-dimensional strongly interacting quantum gases. Since it is capable of handling very large systems, with up to  $N \sim 35$  particles, it can be used to study the crossover from few-body physics to many-body physics. Comparing the exact results from CONAN with previous theories obtained in the thermodynamic limit, this may help answer the question of how many particles constitute a many-body system[2].

A great strength of CONAN is its ability to explore systems confined in arbitrary potentials. This can be exploited to find a specific potential that realizes a given spin model, for instance a model that is known to allow perfect quantum state transfer[3]. Furthermore, random noise can be included in the confining potential, allowing one to study model sensitivity to variations in the optical lattice[3] or spin localization in a quasi-random lattice[4].

In Ref. [50], Duncan *et al.* used CONAN to compute the spin model for  $N = 30$  particles in a periodic cosine lattice, showing that it was possible to realize various models, such as the Su-Schrieffer-Heeger model, by changing the number of particles per potential minimum (lattice site).

Very recently, Decamp *et al.* studied effective spin chain models from a graph theoretical point of view, using CONAN to compute the geometric coefficients for  $N = 2, \dots, 20$  particles in a quartic potential[51].

On the curious side, Chinese scientists working to prevent gas explosions in coal mines recently mentioned CONAN as one of the state-of-the-art intelligent data algorithms available today, stating that it can “describe the influence of gas concentration on the possible height of gas explosion in confined space (Loft N J S et al 2016)”[52]. I was delighted to learn about the vast impact of our research.

The remainder of this chapter will discuss those of the above project I were involved in.

## 1.4 Comparing models: what is many and what is strong?

In the experimental paper[53] from 2013 Wenz *et al.* studies a system of interacting fermions confined in a one-dimensional harmonic trap with a varying contact interaction strength,  $g$ . High degree of control allowed them to initialize the system with a single atom in the trap. Adding atoms of a different species one at a time, the total number of atoms in the trap gradually increased from  $N = 1$  to  $N = 6$ . Remarkably, agreement with theories assuming an infinite number of particles suggested that already a system of  $N = 6$  atoms could be considered a true many-body system with only five majority atoms constituting a Fermi sea[39, 53, 54].

In the light of these results, and since CONAN allowed us to probe the few-to-many-body crossover, we wanted to compare different models for calculating the ground state energy of the Fermi impurity system. Comparing with theories valid for finite  $g$  also allowed us to investigate what can be considered ‘strong’ interaction. Our findings were published in Ref. [2]. I carried out the project and wrote the paper under the supervision of Nikolaj T. Zinner. Lasse B. Kristensen and Anders E. Thomsen were instrumental in creating CONAN, which was used to compute the geometric coefficients for  $N = 2, \dots, 30$  particles in a harmonic trap. The coefficients were published as an appendix to the paper. This section is based on Ref. [2] and a follow-up corrigendum, which fixed a sign error in the original publication.

### 1.4.1 Model and theory landscape

The system under consideration consists of  $N$  spin-1/2 fermions with a repulsive contact interaction of strength  $g$ , confined in a one-dimensional harmonic trap with oscillation frequency  $\omega$ . The fermions are spin-polarized with a single atom (impurity) in the spin down state, while the remaining  $N_\uparrow = N - 1$  atoms are in the spin up state. The Hamiltonian of the system is a special case of Eq. (1.4),

$$H = \sum_{i=1}^N \left( -\frac{\hbar^2}{2m} \frac{\partial^2}{\partial x_i^2} + \frac{1}{2} m \omega^2 x_i^2 \right) + g \frac{\hbar^2}{m\ell} \sum_{i=1}^{N-1} \delta(x_i - x_N) \quad (1.35)$$

with  $\kappa \rightarrow \infty$  (here the same-spin interaction terms have been omitted in the Hamiltonian due to the Pauli principle). In this section, I use harmonic oscillator units  $\omega = m = \hbar = 1$ , which renders the harmonic oscillator length  $\ell = \sqrt{\hbar/(m\omega)} = 1$ .

The experiment performed by Wenz *et al.* realized the system with  $N = 2, \dots, 6$  (omitting the trivial single-particle case) and  $g = 0.36, 1.14, 2.80$ , and measured the ground state energy. In the present study, we compare the experimental data with numerically exact diagonalization results for up to  $N = 11$  obtained for  $g = 0.36, 1.14, 2.80, 10, 10000$ . Exact diagonalization becomes unfeasible for larger system sizes, but here CONAN will provide results for up to  $N = 30$  particles, which are valid in strongly interacting regime,  $1/g \approx 0$ . Thus, comparing results obtained for finite  $g$ , we can also shed light upon what constitute strong interaction. In the strongly interacting regime, the ground state energy to linear order in  $1/g$  is

$$E_g^t = E_\infty^t - \frac{1}{g} \mathcal{C}, \quad (1.36)$$

where  $E_\infty^t$  is the  $N$ -fold degenerate ground state energy in the Tonks-Girardeau limit (compare this equation with Eq. (1.12)). The superscript 't' denotes the energy in the (harmonically) trapped system, to distinguish it from the case of a free system, denoted with 'f'. The constant  $\mathcal{C}$  is known as the *contact coefficient*. From the spin model Hamiltonian of Eq. (1.15) we see that  $\mathcal{C}$  is given as the largest eigenvalue of

$$\sum_{k=1}^{N-1} \frac{\alpha_k}{2} (1 - \sigma_k \cdot \sigma_{k+1}), \quad (1.37)$$

Reference	Trapped	BC	$g$	$N$
McGuire [39]	No	PBC	any	$N \rightarrow \infty$
Astrakharchik <i>et al.</i> [54]	Yes	PBC	any	$N \rightarrow \infty$
Oelkers <i>et al.</i> [55]	No	PBC	$g \rightarrow \infty$	even
Oelkers <i>et al.</i> [55]	No	HWC	$g \rightarrow \infty$	even

Table 1.1: Summary of some previous results.

which can be computed given the geometric coefficients  $\alpha_k$  from CONAN.

We will compare the ground state energy predicted by various models, by comparing the predicted contact coefficients,  $\mathcal{C}$ . This also means bringing the expressions for the ground state energy into the form of Eq. (1.36), which means

- Harmonically trapped system,
- Strongly interacting regime (linear expansion in  $1/g$ ),
- Arbitrary system size,  $N$ .

McGuire provided the theoretical starting point in 1965, where he computed the ground state energy of one-dimensional Fermi gas with a single impurity[39]. His calculation is valid for an arbitrary value of  $g$ , however, he considered the limit of large (and even)  $N$  and assumed a free system with periodic boundary conditions (PBC). The harmonic trap was taken into account by Astrakharchik and Brouzos in 2013[54], who mapped McGuire’s result to a trapped system using the local density approximation (LDA) and extrapolated the result to small  $N$ . Thus, in order to find the contact coefficient, we must consider Astrakharchik and Brouzos’ expression in the strongly interacting regime in an expansion in  $1/g$ .

Finally, an expression for the ground state energy in the strongly interacting regime was given in 2006 by Oelkers *et al.*, who considered a finitely sized system with even  $N$ [55]. Since they considered a free system with periodic and hard wall boundary conditions (HWC), we must apply the LDA in order to obtain an expression for the trapped system.

However, one caveat should be noted when LDA is applied to a system of finite  $N$ . The procedure requires that we map one Fermi

level (chemical potential) to another, but since the Fermi level can be picked anywhere between the energy of the highest occupied state and lowest non-occupied state, it is not well-defined for finite  $N$ . This introduces a variable parameter,  $0 \leq \lambda \leq 1$ , on which the ground state energy will depend.

Table 1.1 provides an overview over the domains of these previous theories. In the next section, we will map these theories to the strongly interacting trapped case, and extract the contact coefficient as a function of  $N$ .

### 1.4.2 Mapping to the strongly interacting trapped case

This subsection is quoted from Ref. [2] Secs. 3.2–3.4 with minor changes to fit the context here.

The strategy to map a result from the free case to the trapped case is by applying LDA. Therefore, we will briefly discuss LDA, and most importantly the weakness in the method for small values of  $N$  mentioned above.

Denote by  $E_0^f$  ( $E_0^t$ ) the energy of the *free (trapped), non-interacting* system. Suppose that we know the energy states of these two systems, and that we therefore can associate with them Fermi levels and Fermi momenta, denoted  $E_F^f$  ( $E_F^t$ ) and  $k_F^f$  ( $k_F^t$ ), respectively. Suppose furthermore that we know an expression for the energy of the *interacting* system, but only in the *free* case. Denote this energy by

$$E_g^f = E_0^f + \Delta E_g^f(k_F^f), \quad (1.38)$$

where  $\Delta E_g^f$  is the correction due to interaction, which will generally depend on  $k_F^f$ . Now, the quantity sought after is the energy for the *interacting and trapped* system. Within LDA, this is found by mapping

$$E_0^f \mapsto E_0^t \quad \text{and} \quad k_F^f \mapsto k_F^t. \quad (1.39)$$

The interaction correction in the trapped case retain its functional form from the free case, but is now evaluated at the trapped Fermi momentum instead of the free Fermi momentum. Thus the LDA expression for the *interacting and trapped* system is

$$E_g^t \approx E_0^t + \Delta E_g^f(k_F^t). \quad (1.40)$$

An illustrative sketch of the LDA procedure is shown on Figure 1.6.

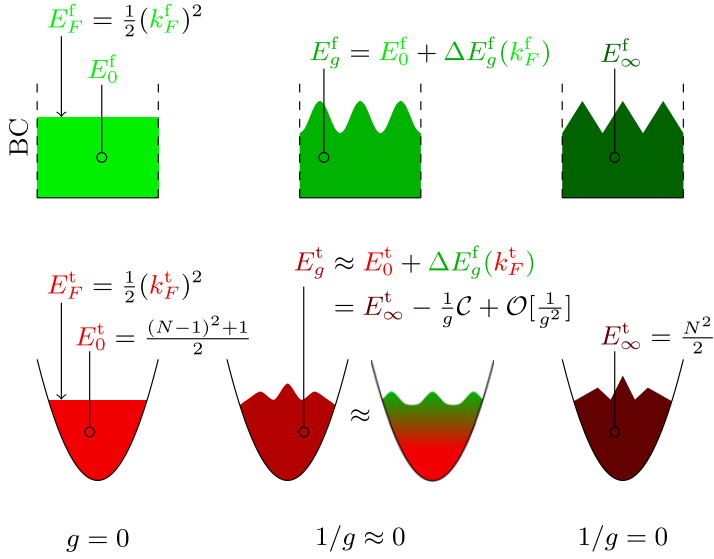


Figure 1.6: Illustration of the local density approximation, where the energy of a free system (upper row) can be mapped to a trapped system (lower row). The figure is adapted from Ref. [2].

We have just described the LDA method if our starting point was the known non-interacting limit for both the free and trapped system. If, however, we approached a finite interaction starting from the infinitely strong interacting case,  $1/g = 0$ , we would instead have mapped

$$E_\infty^f \mapsto E_\infty^t \quad \text{and} \quad k_F^f \mapsto k_F^t, \quad (1.41)$$

where  $E_\infty^f$  ( $E_\infty^t$ ) is the energy of the free (trapped) infinitely strongly interacting system, both assumed to be known. We use this approach in later.

The employment of LDA relies on the knowledge of the Fermi momenta,  $k_F^{f,t}$ , for the free and trapped (non-interacting) systems, or equivalently the Fermi levels,  $E_F^{f,t}$ . Now the problem is that the Fermi level (also called the chemical potential) is not well-defined if the systems contains a finite number of particles. We know that the Fermi level should lie between the highest energy of the occupied states and the lowest energy of the unoccupied states. But exactly where between these two energies is irrelevant for the occupancy of

the states. In the non-interacting limit, the  $N - 1$  identical fermions fill up the  $N - 1$  states of lowest energy. The impurity is occupying the state of lowest energy, but this is irrelevant for the determination of the Fermi level. Recall that the momentum for a particle subject to PBC, HWC or in a harmonic oscillator (HO) is given as

$$\begin{aligned} k_i^{\text{PBC}} &= \frac{2\pi}{L}i, & i &= 0, \pm 1, \pm 2, \dots \\ k_i^{\text{HWC}} &= \frac{\pi}{L}i, & i &= 1, 2, 3, \dots \\ k_i^{\text{HO}} &= \ell^{-1}\sqrt{2i+1}, & i &= 0, 1, 2, \dots \end{aligned}$$

where  $L$  is the length of the system and  $\ell = \sqrt{\hbar/m\omega}$  is the standard oscillator length,  $\ell = 1$  in our units. Then the energy at the Fermi levels can be described using the following expressions for the Fermi momenta:

$$\begin{aligned} k_F^{\text{PBC}} &= \begin{cases} \frac{\pi}{L}(N - 2 + 2\lambda^{\text{PBC}}) & \text{if } N \text{ is even} \\ \frac{\pi}{L}(N - 1) & \text{if } N \text{ is odd} \end{cases} \\ k_F^{\text{HWC}} &= \frac{\pi}{L}(N - 1 + \lambda^{\text{HWC}}), \\ k_F^{\text{HO}} &= \ell^{-1}\sqrt{2(N - \frac{3}{2} + \lambda^{\text{HO}})}. \end{aligned}$$

Here  $\lambda^\alpha \in [0, 1]$  with  $\alpha = \text{PBC, HWC, HO}$  is some tuning parameter that allow us to probe the energies between that of the highest occupied state and the lowest unoccupied state. Picking  $\lambda^\alpha = 0$  corresponds to picking the Fermi level at the highest occupied state and  $\lambda^\alpha = 1$  corresponds to taking the Fermi level at the lowest unoccupied state. Another appealing choice is  $\lambda^\alpha = 1/2$ , corresponding to taking the Fermi level right in the middle. For the time being, we will carry around the tuning parameters, but at some point we would like to pick specific values.

Note in particular that the ambiguity of the Fermi momentum disappears in the thermodynamic limit, because the difference between the highest occupied state and lowest unoccupied state becomes insignificant when  $N \rightarrow \infty$ . This is reflected in the fact that the ambiguity of the Fermi momentum is not discussed in Ref. [54], where also the concepts of the Fermi level and Fermi energy, which only equal each other in the thermodynamic limit, are used somewhat

interchangeably. But if we want to derive energy expressions that apply to finite  $N$ , we should be careful when choosing the Fermi momentum.

In Ref. [39] McGuire finds the following expression for the ground state energy of the interacting, free system subject to PBC:

$$\Delta E_g^f = \frac{(k_F^{\text{PBC}})^2}{2} \frac{\gamma}{\pi^2} \left[ 1 - \frac{\gamma}{4} + \left( \frac{\gamma}{2\pi} + \frac{2\pi}{\gamma} \right) \tan^{-1} \frac{\gamma}{2\pi} \right], \quad (1.42)$$

where  $\gamma = g\pi/k_F^{\text{PBC}}$ . The result applies to all values of the interaction strength  $g$ , but in deriving Eq. (1.42) McGuire converts a sum to an integral letting  $N \rightarrow \infty$  and  $L \rightarrow \infty$  with the density  $N/L$  held constant. This sum to integral conversion can be done in several ways introducing some degree of freedom in  $k_F^{\text{PBC}}$  consistent with the discussion in the previous section. Notice that picking  $\lambda^{\text{PBC}} = 1/2$  would set  $k_F^{\text{PBC}} = (N-1)\pi/L$  for all  $N$ . This would imply a vanishing interaction correction for  $N \rightarrow 1$  as it should.

We now sketch how Astrakharchik and Brouzos implement LDA on McGuire's free energy expression of Eq. (1.42) to find the energy of the trapped system[54]. The LDA expression for the energy of the trapped system of Eq. (1.40) yields

$$\begin{aligned} E_g^t &\approx E_0^t + \Delta E_g^f(k_F^{\text{HO}}) \\ &= \frac{(N-1)^2 + 1}{2} \\ &\quad + \frac{(k_F^{\text{HO}})^2}{2} \frac{\gamma^t}{\pi^2} \left[ 1 - \frac{\gamma^t}{4} + \left( \frac{\gamma^t}{2\pi} + \frac{2\pi}{\gamma^t} \right) \tan^{-1} \frac{\gamma^t}{2\pi} \right], \end{aligned} \quad (1.43)$$

with  $\gamma^t = g\pi/k_F^{\text{HO}}$ . As before, we have to pick  $\lambda^{\text{HO}} = 1/2$  and thus  $k_F^{\text{HO}} = \sqrt{2(N-1)}$  in order to ensure that the energy correction vanishes for  $N \rightarrow 1$ . Since we are interested in the energy in the case of strong interaction, we expand the above general expression to first order in  $1/g$ :

$$E_g^t \approx \frac{N^2}{2} - \frac{1}{g} \mathcal{C}, \quad (1.44)$$

where the desired contact coefficient is given as

$$\mathcal{C} = \frac{8\sqrt{2}}{3\pi} (N-1)^{3/2}. \quad (1.45)$$

The above LDA expression is directly comparable to our exact results. Notice that the LDA method introduced ambiguities in the choice of the Fermi momenta, but that known physics could be used to restrict the choice and get an unambiguous final result. Unfortunately, this cannot be done in the calculations based on the free results of Oelkers *et al.* for a finite  $N$  in PBC and HWC.

Before we compare the approximated expression in Eq. (1.45) with our exact calculations, we wish to derive two other approximated expression for the contact coefficient. These two expressions will rely on the results derived by Oelkers *et al.* in Ref. [55]. In this reference, the authors calculate the energy of a free strongly interacting system using PBC and HWC. Contrary to McGuire who assumed large  $N$ , these results are valid for finite (but even)  $N$ , which is what we ultimately are interested in. Our plan is now to apply the LDA method in order to get expressions for the trapped systems. We start by considering the case of PBC.

*Periodic boundary condition.* To first order in  $1/g$ , we find the free ground state energy to be

$$E_g^f = \frac{\pi^2}{6L^2} (N^3 + 2N) \left[ 1 - \frac{8}{gL} \right] = E_\infty^f - \frac{1}{g} \frac{4\pi^2}{3L^3} (N^3 + 2N). \quad (1.46)$$

We now follow the mapping prescription (1.41) and map  $E_\infty^f \mapsto E_\infty^t = N^2/2$  and  $k_F^{\text{PBC}} \mapsto k_F^{\text{HO}}$ . Using the expressions for  $k_F^{\text{PBC}}$  and  $k_F^{\text{HO}}$ , we can rewrite the mapping as

$$\frac{1}{L} \mapsto \frac{\sqrt{2(N - \frac{3}{2} + \lambda^{\text{HO}})}}{\pi(N - 2 + 2\lambda^{\text{PBC}})}, \quad (1.47)$$

where we have kept the tuning parameters unspecified. Applying the above substitution to the result in (1.46), we obtain the energy of the trapped system within LDA:

$$E_g^t \approx \frac{N^2}{2} - \frac{1}{g} \frac{8\sqrt{2}}{3\pi} (N^3 + 2N) \frac{(N - \frac{3}{2} + \lambda^{\text{HO}})^{3/2}}{(N - 2 + 2\lambda^{\text{PBC}})^3}. \quad (1.48)$$

In the thermodynamic limit,  $N \rightarrow \infty$ , the contact coefficient read off Eq. (1.48) and the one in Eq. (1.45) tend towards the same asymptote given by

$$\mathcal{C}_\infty = \frac{8\sqrt{2}}{3\pi} N^{3/2}, \quad (1.49)$$

regardless of the choice of the tuning parameters. This is indeed reassuring, but we are mostly interested in results for small  $N$ . Eq. (1.48) is derived for even  $N$ , but let us extend the domain also to odd  $N$  in order to restrict the tuning parameters by requiring the vanishing of the contact coefficient for  $N = 1$ . Since we also require  $\mathcal{C}$  to be non-divergent for finite  $N$ , we end up with  $\lambda^{\text{HO}} = 1/2$  and  $\lambda^{\text{PBC}} \in ]0; 1/2[ \cup ]1/2; 1]$ . While this fixes  $\lambda^{\text{HO}}$ , there is still ambiguity in  $\lambda^{\text{PBC}}$ . Choosing  $\lambda^{\text{PBC}} = 1$  yields

$$\mathcal{C} = \frac{8\sqrt{2}}{3\pi} (N^3 + 2N) \frac{(N-1)^{3/2}}{N^3}. \quad (1.50)$$

*Hard wall condition.* The ground state energy with HWC is found in Ref. [55]:

$$E_g^f = \frac{\pi^2}{12L^2} (2N^3 + 3N^2 + N) \left[ 1 - \frac{8}{gL} \cos^2 \left( \frac{\pi}{2N} \right) \right]. \quad (1.51)$$

This result is consistent with the energy found in Ref. [56] in the thermodynamic limit ( $N, L \rightarrow \infty$  and  $N/L$  constant). In a completely similar way as before, mapping  $E_\infty^f \mapsto E_\infty^t = N^2/2$  and  $k_F^{\text{HWC}} \mapsto k_F^{\text{HO}}$  yields the energy of the trapped system:

$$E_g^t = \frac{N^2}{2} - \frac{1}{g} \frac{8\sqrt{2}}{3\pi} (N^3 - \frac{3}{2}N^2 + \frac{1}{2}N) \frac{(N + \frac{3}{2} + \lambda^{\text{HO}})^{3/2}}{(N-1 + \lambda^{\text{HWC}})^3} \cos^2 \left( \frac{\pi}{2N} \right). \quad (1.52)$$

As expected, the contact coefficient goes towards the common asymptote  $\mathcal{C}_\infty$  in the limit  $N \rightarrow \infty$ . Again we wish to extend the result to odd  $N$ , not just even  $N$ . To ensure that the contact coefficient is real and well-defined for any integer  $N \geq 1$  and zero at  $N = 1$ , we should pick *either*  $\lambda^{\text{HO}} = 1/2$  and  $\lambda^{\text{HWC}} = 0$  *or*  $\lambda^{\text{HO}} \in [1/2; 1]$  and  $\lambda^{\text{HWC}} \in ]0; 1]$ . For the choices  $\lambda^{\text{HO}} = \lambda^{\text{HWC}} = 1/2$ , we get

$$\mathcal{C} = \frac{8\sqrt{2}}{3\pi} (N^3 + \frac{3}{2}N^2 + \frac{1}{2}N) \frac{(N-1)^{3/2}}{(N - \frac{1}{2})^3} \cos^2 \left( \frac{\pi}{2N} \right). \quad (1.53)$$

In deriving Eqs. (1.50) and (1.53), we had to specify values for the tuning parameters, but notice that we could just as well have chosen other values within certain bounds.

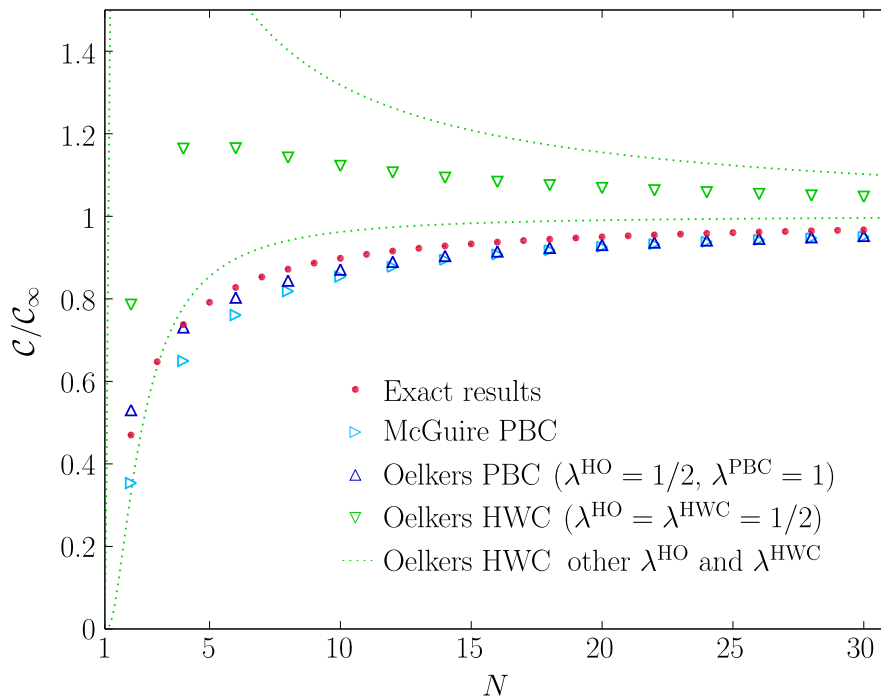


Figure 1.7: Contact coefficients computed from CONAN (red dots) and using the theoretical expressions derived in the previous subsection. The green dotted lines are computed using  $\lambda^{\text{HO}} = 1$  and  $\lambda^{\text{HWC}} = 1/4$  (upper curve) and  $\lambda^{\text{HO}} = 1/2$  and  $\lambda^{\text{HWC}} = 1$  (lower curve), where  $N$  has been taken as a continuous parameter for clarity. The figure is adapted from Ref. [2].

### 1.4.3 Results and discussion

Firstly, we compare the contact coefficients using the LDA expressions in Eqs. (1.45), (1.50) and (1.53) with the exact results from CONAN. This is shown in Figure 1.7, where we also show green dashed lines to illustrate the degree of tunability in the HWC results through the choice of Fermi levels. Notice that the PBC results (blue) of McGuire and Oelkers *et al.* are in good agreement with the exact results (red) for all  $N$ , whereas the HWC results (green) are generally not as good. This is somewhat surprising, as one might expect that HWC more closely resembles the harmonic oscillator confinement

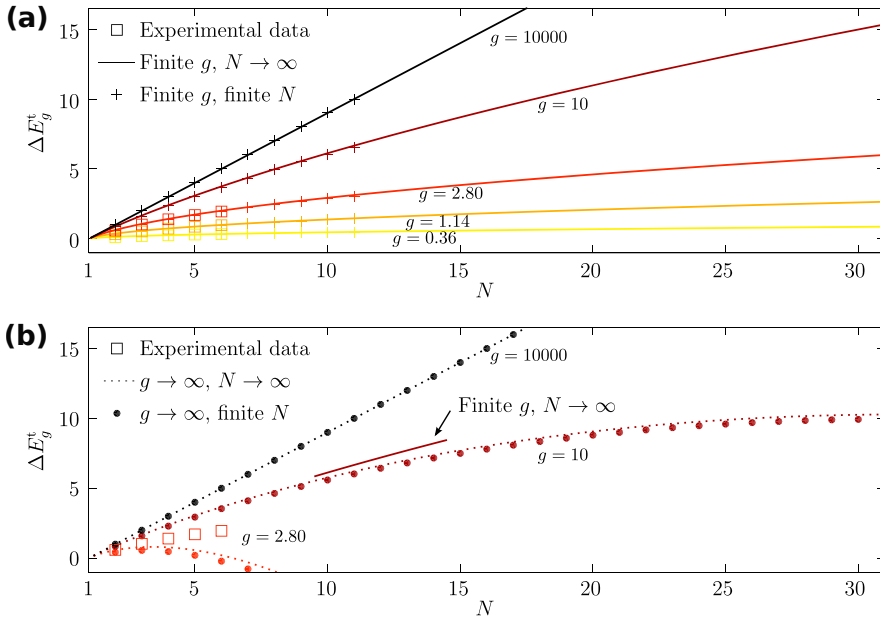


Figure 1.8: The correction to the ground state energy due to interaction versus the number of particles,  $N$ . Experimental data is compared to theories assuming (a) finite  $g$  and (b) strong interaction,  $1/g \approx 0$ . The figure is adapted from Ref. [2].

compared to PBC. However, the most striking observation from the data is the large degree of tunability in the LDA results stemming from the ambiguity in the choice of the Fermi levels. This arbitrary choice plays the biggest role for small systems,  $N < 10$ , but even for  $N \sim 30$  there is some degree of tunability in the contact coefficient, and eventually, all theories do converge when  $N \rightarrow \infty$ . In this regard,  $N \sim 10$  cannot be considered infinity, and it seems like an improbable stroke of luck that result of McGuire computed in the thermodynamic limit works so well when extrapolated to finite  $N$ .

Secondly, we wish to study compare the experimental data of Ref. [53] obtained for  $g = 0.36, 1.14, 2.80$  and  $N = 2, \dots, 6$  with theories in different regimes of  $g$  and  $N$ . There are four theoretical domains of finite/infinite  $g$  and finite/infinite  $N$ , which constitute a landscape of theories. We consider first the case of finite  $g$ , where the interaction energy,  $\Delta E_g^t$ , in the  $N \rightarrow \infty$  regime is calculated from the

McGuire result in Eq. (1.43). This is compared to the experimental data and numerically exact data for  $N \leq 11$  in Figure 1.8a. As expected, the numerically exact data matches the experimental data very well, but it is surprising that also McGuire’s thermodynamic result also matches very well for these small systems.

However, when we consider theories in the strongly interacting regime, the agreement with experimental data is not as good. In this regime,  $g \rightarrow \infty$ , we find the interaction energy in the  $N \rightarrow \infty$  case from Eq. (1.44), and use CONAN to cover the case of finite  $N \leq 30$ . As we see in Figure 1.8b, McGuire’s thermodynamic theory matches well with the finite  $N$  results, but these theories do not capture the  $g = 2.80$  experimental data. Thus,  $g = 2.80$  cannot be considered strong interacting. If we go up to  $g = 10$ , we find a better theoretical agreement for systems up to  $N \sim 12$ , but the theories for finite and large  $g$  deviates for larger  $N$ . This is not surprising, since the interaction correction goes like  $\Delta E_g^t \sim -N^{3/2}/g$  for large  $N$  and  $g$ , so a breakdown of the strongly interacting theory will occur for sufficiently large  $N$  and/or small  $g$ . This also means that we cannot answer the question ‘what is strong interaction?’ without referencing the system size. From Figure 1.8b, we may say that  $g = 2.80$  is strong for  $N < 3$  and  $g = 10$  is strong for  $N < 12$ .

## 1.5 State transfer in a chain of atoms

Quantum state transfer is an important aspect of quantum information theory, as it allows one to transfer quantum information coherently from one location to another. In a chain of  $N$  atoms, we prepare the atom at the first site in a given state, and let the spin model Hamiltonian unitarily evolve the system in time. Perfect state transfer is obtained when the state of the first atom has been transferred to the other end of the chain, at site  $N$ , without altering the states of the bulk atoms. In 2004, several groups showed independently that a one-dimensional Heisenberg XX model can accommodate perfect state transfer given a specific form of the Heisenberg exchange couplings[57–61]. Only in a classical system of coupled optical waveguides was this protocol experimentally tested[62, 63].

The ability to compute spin chain Hamiltonians with CONAN allowed us to study a realization in a real many-body quantum system. The idea was to optimize the functional form of the confining

potential in order to achieve the correct form of exchange coefficients that would allow perfect state transfer. Furthermore, we studied how noise on the potential present in an actual setup affected the system's ability to perform perfect state transfer. We published the results in Ref. [3] on which this section is based. I suggested and optimized the trial potential, computed the resulting spin chain model using CONAN, performed the statistical analysis of the noise-influenced data and wrote the paper with input from the remaining authors. Oleksandr V. Marchukov performed the unitary time-evolution of the system and computed the state transfer fidelities. David Petrosyan and Nikolaj T. Zinner suggested and supervised the project.

### 1.5.1 Optimizing the potential

The  $N$ -body one-dimensional Heisenberg XX model has the Hamiltonian,

$$H_s = \sum_{k=1}^{N-1} \frac{1}{2} J_x^k (\sigma_x^k \sigma_x^{k+1} + \sigma_y^k \sigma_y^{k+1}), \quad (1.54)$$

which is a special case of the effective spin chain model of Eq. (1.19) with  $\kappa = 2$ . In the implementation with strongly interacting atoms, recall the relationship between geometric coefficients and the coupling strengths,  $J_x^k = \hbar^2 \ell \alpha_k / (mg)$ .

The notion of perfect state transfer is defined in the following way. Assume the the system is initialized at time  $t = 0$  in the state  $|1\rangle \equiv |\uparrow\downarrow\downarrow \cdots \downarrow\downarrow\rangle$ , i.e. where the spin at the first site is up, while the remaining  $N - 1$  spins are down. Since  $H_s$  conserves the total spin project, unitary time-evolution will evolve the initial state into a superposition of the  $N$  basis states, where the spin up is located at various sites along the chain. The probability for observing the state  $|N\rangle \equiv |\downarrow\downarrow \cdots \downarrow\uparrow\rangle$ , i.e. the spin up at site  $N$ , is given by

$$F(t) = \left| \langle N | e^{-iH_s t / \hbar} | 1 \rangle \right|^2. \quad (1.55)$$

Perfect state transfer is achieved at time  $t$ , if this quantity, known as the fidelity, is unity,  $F(t) = 1$ .

It was shown in Ref. [57–61] that the Heisenberg XX model above permits perfect state transfer if the exchange couplings,  $J_x^k$ , or equivalently the geometric coefficients,  $\alpha_k$ , follow a semicircular form,

$$\alpha_k \propto \sqrt{k(N-k)}, \quad (1.56)$$

with a transfer time  $t_0 = \hbar\pi\sqrt{N-1}/(2|J_x^1|)$ .

In order to find an implementation of the system in strongly interacting cold atoms, we must find a confining potential that reproduces the above geometric coefficients. As discussed in Section 1.3.3, the  $\alpha_k$ 's mimic  $-V(x)$ , and we therefore employ the following 'bowl-shaped' trial potential,

$$V(x) = 100\epsilon \cdot \left| \frac{L/2 - x}{L/2} \right|^\tau. \quad (1.57)$$

As in Section 1.3.3  $\ell$  and  $\epsilon = \hbar^2/(2m\ell^2)$  are our length and energy unit, respectively, and  $L = 100\ell$  is the hard box length in which CONAN places the system. The potential has a variable parameter,  $\tau$ , that we will adjust in order to reproduce the desired geometric coefficients. We fit the resulting  $N - 1$  geometric coefficients to

$$\alpha_k \propto [k(N - k)]^\beta, \quad (1.58)$$

where  $\beta$  is a fit parameter;  $\beta = 1/2$  corresponding to the desired semicircular form. We do not expect the simple potential of Eq. (1.57) with only a single tunable parameter,  $\tau$ , to be able to perfectly produce the desired geometric coefficients. Even though the computed coefficients do not fit perfectly to Eq. (1.58), the fit will produce a value of  $\beta$ , and we can optimize  $\tau$  such that the fit returns  $\beta = 1/2$ . This will give us the trial potential that most faithfully produces the desired geometric coefficients, and presumably the best state transfer fidelity. Figure 1.9 shows the optimized  $\tau$  values and the goodness of the fit versus  $N$ . We see that it is possible to achieve good fits with the simple trial potential. Unsurprisingly, the quality of the potential decreases with  $N$ , as an increasing number of geometric coefficients has to fulfill the semicircular relationship.

Using the optimized potentials and the resulting spin models, we compute the state transfer fidelity from Eq. (1.55). If the optimized potential perfectly produces the desired model, the fidelity reaches unity at  $t = t_0$ . However, we cannot expect this to be the case, and maximum fidelity will in general be reached at another time, denoted  $t_{\text{out}}$ . Figure 1.10 shows the fidelities at  $t_0$  and  $t_{\text{out}}$ , and the relationship between these times, for  $N = 4, \dots, 20$ . We see that it is possible to obtain a high-fidelity state transfer,  $F(t_{\text{out}}) > 0.95$ , even for large systems with  $N = 20$  particles. The transfer fidelity decreases with the system size, which is to be expected due to a

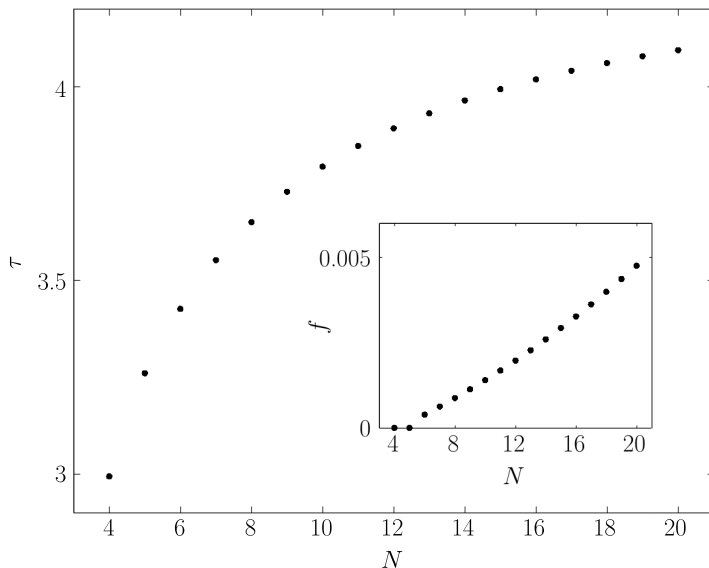


Figure 1.9: Optimal value of  $\tau$  for different  $N$ . The inset shows the goodness of the fit, defined as  $f = n^{-1} \sum_{i=1}^n (y(x_i) - y_i)^2$ , where  $(y_i, x_i)$  are  $n$  data points fitted to the model  $y(x)$ . A perfect fit has  $f = 0$ . The figure is adapted from Ref. [3].

decreasing fit quality. In addition, another explanation may be that the number of undesired states in the Hilbert space increases, and an increasing number of exchanges is required for the spin to reach the other side of the chain. We also note that the maximum fidelity is reached slightly before the predicted transfer time,  $t_0$ , resulting in a dramatically reduced  $F(t_0)$ , especially for systems larger than  $N \sim 10$  particles.

### 1.5.2 Including noise in the potential

The usual approach to studying the effects of noise in a lattice model is by including uniform, Gaussian or colored noise in the interaction parameters[64–68]. However, this approach does not specify the original source of noise, which in a real experiment arises from, e.g., random fluctuations in the confining potential. With CONAN we can include uniform noise directly in the confining potential, and we can determine whether the noise on resulting exchange coefficients

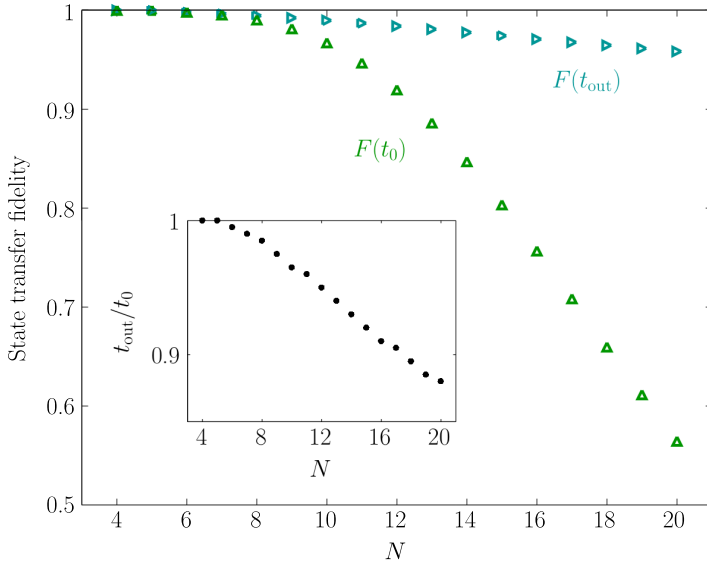


Figure 1.10: State transfer fidelity at  $t_0$  and  $t_{\text{out}}$  versus  $N$ . The inset shows the relationship between the two readout times. The figure is adapted from Ref. [3].

is uniform or not.

To the optimized potential,  $V(x)$ , we add the following quasirandom noise term,

$$\delta V(x) = V_0 \left[ \cos \left( \frac{x}{\ell} + \phi_1 \right) + \cos \left( \frac{\zeta x}{\ell} + \phi_2 \right) \right], \quad (1.59)$$

where  $V_0$  is the noise strength,  $\zeta = 2/(1 + \sqrt{5}) \approx 0.618$  is an irrational number, and  $\phi_1$  and  $\phi_2$  are random phases uniformly drawn from the interval  $[0; 2\pi[$ . For each value of  $V_0$ , we consider  $M = 200$  realizations of the noisy potential with random phases and compute the geometric coefficients and maximum fidelity,  $F(t_{\text{out}})$ . Due to the increased computation time for CONAN with  $N$ , we consider  $N \leq 10$ .

Figure 1.11 shows  $F(t_{\text{out}})$  averaged over  $M$  random realizations versus  $V_0$ . Not surprisingly, the transfer fidelity decreases with the noise strength. We note that close to perfect state transfer is achieved if  $V_0 < 0.02\epsilon$ . For a typical experimental setup with  $\ell$  being several micrometers and  $\epsilon \sim 500\text{Hz}$ , this leads to  $V_0 < 10\text{Hz}$ , which is

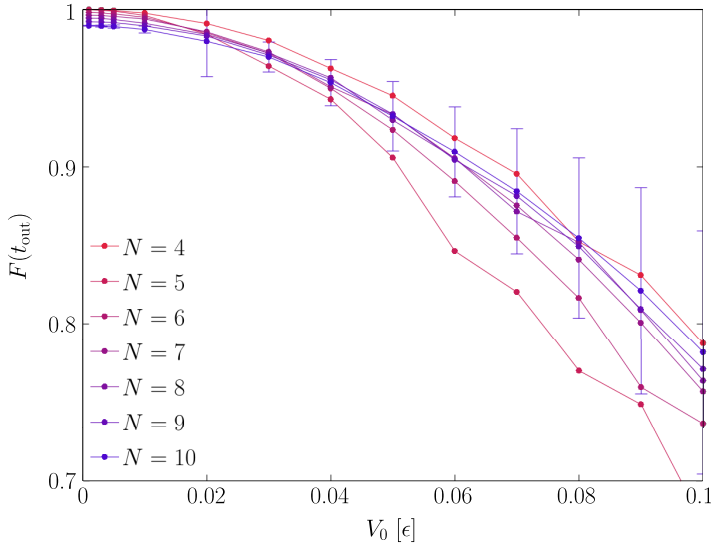


Figure 1.11: Fidelity versus noise strength. For better readability the error bars (one standard deviation) are only shown for  $N = 10$ . The figure is adapted from Ref. [3].

realistic, but not trivial. Expect for the case  $N = 4$ , which produces the best fidelity, the system seems to be more robust towards noise the longer the chain gets, probably because potential fluctuations are better averaged out for larger systems.

We now turn towards the question of whether uniform fluctuations in the potential create uniform noise on the exchange couplings. We focus on the  $N = 10$  particle system. For a given value of  $V_0$  we denote by  $\alpha_k^\phi$  the  $k$ 'th geometric coefficient for a specific realization with random phases  $\phi = (\phi_1, \phi_2)$ . The  $k$ 'th coefficient in the noise-free case (i.e. those found from the optimized potentials discussed in the previous subsection) is denoted by  $\alpha_k$ . The deviation due to noise is for a single realization is  $\Delta\alpha_k^\phi \equiv \alpha_k - \alpha_k^\phi$ , and the average value of all  $M$  realizations is  $\Delta\alpha_k \equiv \text{mean}_\phi\{\Delta\alpha_k^\phi\}$ . An example of the average deviation is shown in the inset in Figure 1.12, showing that the noise on the coefficients is in fact uniformly distributed over the lattice sites. Error bars on  $\Delta\alpha_k$  in the inset are one standard deviation,  $\text{std}_\phi\{\Delta\alpha_k^\phi\}$ . The standard deviation quantifies how strongly the exchange coefficients respond to random fluctuations

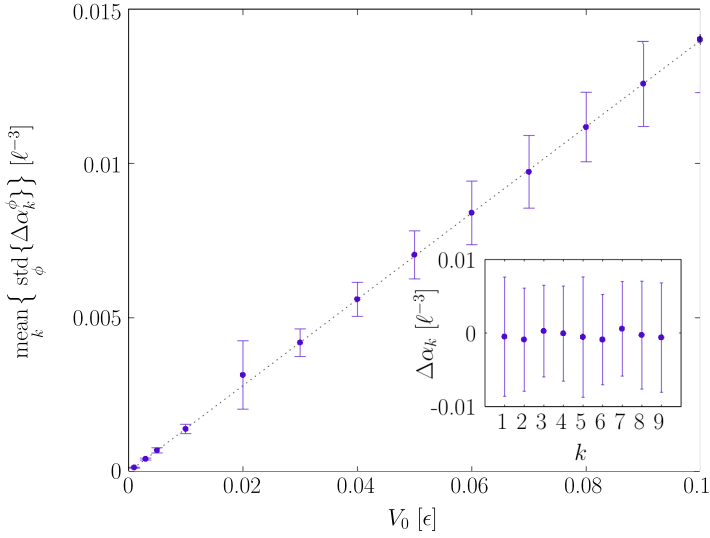


Figure 1.12: Mean response of the geometric coefficients to random fluctuations in the potential of strength  $V_0$  for  $N = 10$ . The inset shows site-dependent deviation due to noise for the case  $V_0 = 0.05\epsilon$ . The figure is adapted from Ref. [3].

in the potential, and it is therefore instructive to take the average over the  $N - 1$  neighbor pairs and see how it varies with the noise strength,  $V_0$ . This is exactly what is shown in Figure 1.12, where the error bars are one standard deviation. The dotted line is a linear fit with slope  $0.14\ell^{-3}\epsilon^{-1}$ , demonstrating a simple proportionality law between response of the exchange couplings and the noise strength. This relationship provides a very useful link between the experimental uncertainties and noise on the exchange couplings in the effective Heisenberg spin model.

In Ref. [3] we also considered how adding a small linear tilt on the potential affected the transfer fidelity, showing that a weak tilt improved the fidelity slightly, but in general suppressed the state transfer. However, since these results are rather uninteresting, I will not go into a further discussion here.

## 1.6 Fermi polaron in an quasirandom potential

In accordance with GSST rules, this section is quoted from Sec. 1.2 of my progress report for my qualifying exam, based on Ref. [4]. Minor changes has been made to fit the context here.

A great strength of CONAN is its capability to handle arbitrary confining potential, as opposed to considering, e.g., the important, but very special case of a harmonic confinement. As I demonstrated in the previous section, this makes CONAN an ideal tool for studying noise. We may consider a potential that is the sum of a fixed term  $V_0(x)$  and a quasi-random noise term  $\delta V(x)$ , and averaging the results from many realizations of the noise term, thus treating noise exactly at the level of the optical potential, before the lattice approximation is made. In this section I shall present some of the results from Ref. [4], from which parts of this section is taken. Calum Duncan was responsible for the project, and was the main force behind the project design, data analysis and scientific paper. I was responsible for designing and creating the very large data set (multiple computers where put to work night and day), and I participated in editing the manuscript from the first draft.

It is well-known that electrons in a periodic lattice, for instance in a metal, tend to be delocalized over many lattice points. However, as Anderson showed in 1958, the presence of random noise in the lattice could prevent an initially localized state to diffuse into a non-localized state[69]. In Ref. [4] we considered one and two spin impurities in a strongly interacting one-dimensional spin-1/2 Fermi system in a quasi-random lattice potential, and studied the emergence of spin localized and delocalized phases. In this brief review, I will focus on the single impurity case. The potential is given as the sum of two terms,  $V(x) = V_0(x) + \delta V(x)$ , the first being a periodic lattice with  $N_s$  sites:

$$V_0(x) = \tilde{V} \cos(2\pi N_s x) \quad (1.60)$$

where  $0 \leq x \leq 1$  is a unitless coordinate, and the potential strength  $\tilde{V} = 10N_s^2\epsilon$  scales with  $N_s^2$  to ensure a lattice that affects the particles without trapping them into single sites, and  $\epsilon$  is a unit of energy. The second term in the potential gives rise to noise, or disorder:

$$\delta V(x) = W\tilde{V} \cos(N_s x + \phi) , \quad (1.61)$$

where  $0 \leq W \leq 1$  is the disorder strength, and  $\phi$  a random phase picked uniformly from  $[0; 2\pi[$  at each realization of the quasi-random

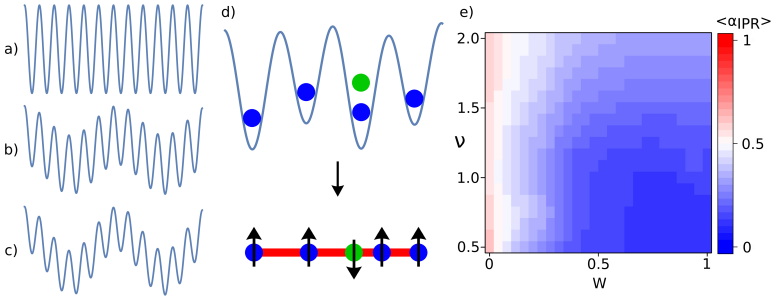


Figure 1.13: a) The quasi-random potential  $W = 0$ , b)  $W = 0.5$  and c)  $W = 1$ . d) Illustration of the mapping to an effective spin chain model for strong interactions. e) Average inverse participation ratio as a function of filling ratio  $\nu$  and disorder strength  $W$ .

potential. We shall be concerned with a lattice of  $N_s = 12$  sites, and independently vary the number of particles  $N = 6, 7, \dots, 24$ , corresponding to filling ratios  $\nu = N/N_s = 0.5, 0.583, \dots, 2$ , and the disorder strength  $W$  from 0 to 1. For each value of  $\nu$  and  $W$  we compute the measures of localization (as we shall define below) and average the results over for 19 randomly picked phases  $\phi$ . This totals to 6859 quasi-random realizations, and hence as many runs of CONAN. Figure 1.13a–c illustrate such quasi-random potentials for different strengths of the disorder.

The system of confined spin-1/2 fermions can be described with the effective Heisenberg XX model Hamiltonian of Eq. (1.15) with  $\kappa \rightarrow \infty$ , illustrated in Figure 1.13d. As we only require knowledge of the ordering of the energy eigenstates and relative energies to determine the localization properties, it is sufficient to compute the local exchange coefficients  $\alpha_k$  using CONAN. Doing so, we find the eigenstates of the spin chain system with a single spin impurity,

$$|\Psi\rangle = \sum_j^N C_j |\uparrow \dots \uparrow (\downarrow)_j \uparrow \dots \uparrow\rangle, \quad (1.62)$$

where the summation is over the different positions of the spin impurity along the chain, and the  $C_j$ 's are the expansion coefficients.

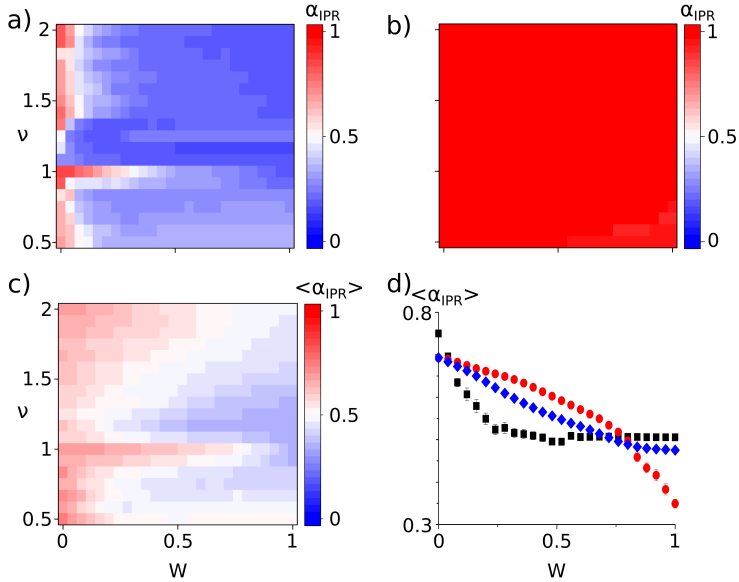


Figure 1.14: IPR for the single impurity spin chain for the a) ground state, b) highest energy state and c) the average IPR of the states in between. d) Cut-outs of c) for  $\nu = 0.5$  (black),  $\nu = 1$  (red), and  $\nu = 2$  (blue).

The onset of Anderson localization in the system can be observed by considering the inverse participation ratio (IPR)[70] of a certain state, given by

$$\alpha_{\text{IPR}} = \left\langle \left( N \sum_{j=1}^N |C_j|^4 \right)^{-1} \right\rangle, \quad (1.63)$$

where the average is taken over the 19 realizations of the quasirandom potential with randomly picked  $\phi$ . For instance, we may consider the IPR of the ground state from the ground states of all 19 realizations with fixed  $\nu$  and  $W$ .

For a fully delocalized state, the spin is evenly distributed over all the sites, and  $\alpha_{\text{IPR}} = 1$ . Conversely, a fully localized state with only one of the  $C_j$ 's non-zero has  $\alpha_{\text{IPR}} = 1/N \ll 1$ . In Figure 1.13e we show the average IPR over all the  $N$  states, denoted  $\langle \alpha_{\text{IPR}} \rangle$ , which gives an indication of the overall localization of the system. Consis-

tent with Anderson's localization, the system becomes increasingly localized with the disorder strength,  $W$ , independent of the filling  $\nu$ . The dependence of the filling becomes stronger once we look at the individual states. In Figure 1.14a–c we show the IPR for the ground state, the highest energy state, and the average over all the  $N - 2$  states in between.

The ground state of the spin is found to localize at small disorder, with strong localization for  $W > 0.1$ , for most  $\nu$ , with the exception of around unit filling, where we have a spin in each lattice site, resulting in an elongated transition to the localized state. The highest energy state is delocalized across the system over all disorder. Therefore, for our system we can never have a true many-body localized phase as all states will not localize. It is still useful to consider the localization properties of the rest of the states.

With the average IPR over all states in the system except the ground state and highest energy state (Figure 1.14c-d), we can gain an insight into the general localization properties of the system. We observe a defined transition from a majority of states being delocalized to heavily localized over a range of fillings from  $1 \leq \nu \leq 1.5$ . For small fillings,  $\nu < 1$ , we observe a trend towards localization with large disorder. The relatively weak localization of states at these fillings is due to the diluteness of the system: Each fermion (or groups of fermions) can be well separated from its neighbors, resulting in weak coupling coefficients, effectively resulting in the separation of the spin chain into sections. Hence we observe some localization of the state, but not due to disorder in the spin chain. For high filling,  $\nu > 1$ , the localization becomes progressively weaker as  $\nu$  is increased.

In Ref. [4] we also studied the case of two spin impurities, including some statistical analysis of the energy level spacing. We found that the localization properties followed the same trend as in the single impurity case discussed above, so I do not include this here.

---

# Confined polaron in a Bose-Einstein condensate

*In this chapter, I will describe the work I did on a polaron in a Bose-Einstein condensate in the group of Georg M. Bruun. I begin the chapter by a brief introduction to Bose-Einstein condensation and the theoretical foundation for the description of the polaron. Then, I present our original work based on Ref. [5].*

In the present chapter, we stay in the field of ultra-cold quantum gases, but the spatial dimension increases from one to two and three. In fact, the goal of this chapter is to describe a single atomic impurity confined to a two-dimensional (2D) space immersed in a three-dimensional (3D) Bose-Einstein condensate (BEC). The interplay between the 2D impurity and 3D BEC creates a mixed-dimensional Bose polaron.

While this sounds reminiscent of the impurity problems studied in Sections 1.4, 1.5 and 1.6, these were all few-body or mesoscopic problems that could be solved either directly from the geometric coefficients computed with CONAN or by numerical diagonalization of the resulting spin chain Hamiltonian. On the other hand, the number of atoms in a BEC is up to a million, and we must resort to a statistical description. For the interaction between the impurity and the BEC, we will take a diagrammatic approach within many-body quantum field theory.

## 2.1 Bose-Einstein condensation

In an ideal gas of classical particles the probability that an individual particle has a certain energy is given by the Maxwell-Boltzmann distribution. However, in a statistical ensemble of quantum particles, the Maxwell-Boltzmann distribution fails to describe the energy distribution for low temperatures. Instead, as Bose realized in 1924[71], the particles in an ideal gas of bosons follow the Bose-Einstein distribution,

$$f_{\mathbf{p}} = \frac{1}{e^{(\epsilon_{\mathbf{p}} - \mu)/(k_B T)} - 1}, \quad (2.1)$$

where  $\mu$  is the chemical potential,  $T$  is the temperature of the gas,  $k_B$  is Boltzmann's constant and  $\epsilon_{\mathbf{p}} = \mathbf{p}^2/(2m_B) > \mu$  is the energy of a free particle with mass  $m_B$  and momentum  $\mathbf{p}$ . In 1926, Fermi and Dirac introduced the Fermi-Dirac distribution for fermions[18, 72], obtained from Eq. (2.1) by changing  $-1$  to  $+1$  in the denominator, thereby completing the description of the quantum case.

Since multiple identical bosons can occupy the same quantum state, an increasing number of particles will occupy the ground state as the temperature decreases. According to Eq. (2.1) all particles reside in the ground state in the limit  $T \rightarrow 0$ . Immediately following Bose's discovery, Einstein predicted that this behavior would make the bosons condense into a new state of matter below a critical temperature[73], now known as a Bose-Einstein condensate. The condensation process can be qualitatively understood by considering the thermal de Broglie wavelength of the bosons,

$$\lambda = \sqrt{\frac{2\pi\hbar^2}{m_B k_B T}}. \quad (2.2)$$

When  $T$  is large, the particles have a short wavelength and behave as localized particles. However, when the temperature becomes sufficiently low, the de Broglie wavelength becomes comparable with the average particle distance, and the single-particle wavefunctions begin to overlap. In fact, an exact calculation for a 3D homogeneous gas yields  $n_B \lambda_c^3 \simeq 2.612$ , which links the particle density,  $n_B$ , to the critical wavelength,  $\lambda_c$ , and by Eq. (2.2) to the critical temperature,  $T_c$ . Below  $T_c$  the system condenses and can be described by a single 'macroscopic' many-body wavefunction.

Due to the technical difficulties of cooling an atomic gas below the critical temperature,  $T_c \sim \mu\text{K}$ , it was not until 1995 before scientists

experimentally realized the first Bose-Einstein condensates[74, 75], using the techniques described in Subsection 1.1.1. From an experimental point of view, a high  $T_c$  is favorable, which can be achieved by increasing the density,  $n_B$ . However, this also increases the number of atoms that escape the magneto-optical trap due to inelastic three-body collisions, and therefore BECs are typically formed in dilute Bose gases. This means that interactions between the bosons can be included perturbatively, using the approach first presented by Bogoliubov in 1947 in order to describe superfluidity[76]. Bogoliubov's theory was crucial in understanding properties of BECs, some of which are not correctly captured by the ideal Bose gas model.

### 2.1.1 Bogoliubov theory

The Bogoliubov theory of a weakly interacting Bose gas can be found in standard textbooks, for instance Ref. [77].

Consider a dilute ensemble of interacting bosons at low temperature, such that we may ignore three-body scattering processes. In terms of the bosonic quantum field operator,  $\psi(\mathbf{r})$ , we may express the system Hamiltonian as

$$H = \frac{\hbar^2}{2m_B} \int d\mathbf{r} \nabla \psi^\dagger(\mathbf{r}) \cdot \nabla \psi(\mathbf{r}) + \frac{1}{2} \int d\mathbf{r} d\mathbf{r}' \psi^\dagger(\mathbf{r}) \psi^\dagger(\mathbf{r}') V_B(\mathbf{r} - \mathbf{r}') \psi(\mathbf{r}) \psi(\mathbf{r}') , \quad (2.3)$$

where  $V_B(\mathbf{r} - \mathbf{r}')$  is the scattering potential. Assuming a uniform Bose gas in the volume  $\mathcal{V}$ , we may expand  $\psi(\mathbf{r})$  in plane waves,

$$\psi(\mathbf{r}) = \frac{1}{\sqrt{\mathcal{V}}} \sum_{\mathbf{p}} b_{\mathbf{p}} e^{i\mathbf{p} \cdot \mathbf{r} / \hbar} , \quad (2.4)$$

where  $b_{\mathbf{p}}$  denotes the annihilation operator of a plane wave mode with momentum  $\mathbf{p}$ , fulfilling the bosonic commutation relations

$$[b_{\mathbf{p}}, b_{\mathbf{p}'}^\dagger] = \delta_{\mathbf{p}, \mathbf{p}'} , \quad (2.5)$$

$$[b_{\mathbf{p}}, b_{\mathbf{p}'}] = [b_{\mathbf{p}}^\dagger, b_{\mathbf{p}'}^\dagger] = 0 . \quad (2.6)$$

Inserting the expansion for  $\psi(\mathbf{r})$  yields

$$H = \sum_{\mathbf{p}} \frac{\mathbf{p}^2}{2m_B} b_{\mathbf{p}}^\dagger b_{\mathbf{p}} + \frac{1}{2\mathcal{V}} \sum_{\mathbf{p}\mathbf{p}'\mathbf{q}} V_B(\mathbf{q}) b_{\mathbf{p}+\mathbf{q}}^\dagger b_{\mathbf{p}'-\mathbf{q}}^\dagger b_{\mathbf{p}} b_{\mathbf{p}'} , \quad (2.7)$$

where  $V_B(\mathbf{q})$  is the Fourier transform of the potential, i.e.

$$V_B(\mathbf{q}) = \int d\mathbf{r} V_B(\mathbf{r}) e^{-i\mathbf{q}\cdot\mathbf{r}/\hbar} . \quad (2.8)$$

Since we consider a weakly interacting Bose gas, we expect the collisions to be dominated by events with small momentum transfer,  $\mathbf{q}$ . Thus, we will substitute  $V_B(\mathbf{q})$  with an effective constant pseudo-potential,  $g_B$ , which can be related to the observable  $s$ -wave scattering length,  $a_B$ , as[77]

$$V_B(\mathbf{q}) \approx g_B = \frac{4\pi\hbar^2 a_B}{m_B} . \quad (2.9)$$

The assumption of diluteness means that the scattering length must be much smaller than the inter-particle distance, i.e.  $n_B^{1/3} a_B \ll 1$ .

In a BEC, a macroscopic number of bosons are in the ground state. We can therefore neglect fluctuations in the zero-momentum state, and replace  $b_0$  and  $b_0^\dagger$  with the constant number  $\sqrt{N_0}$ . The number operator becomes

$$N = N_0 + \sum_{\mathbf{p} \neq 0} b_{\mathbf{p}}^\dagger b_{\mathbf{p}} , \quad (2.10)$$

i.e.  $N_0$  is the number of zero-momentum bosons,  $N_0 \gg \langle N \rangle - N_0$ . Retaining only terms of order  $N_0$  and  $N_0^2$  in the interaction part, the Hamiltonian becomes

$$H = \sum_{\mathbf{p}} \epsilon_{\mathbf{p}} b_{\mathbf{p}}^\dagger b_{\mathbf{p}} + \frac{g}{2\mathcal{V}} \left[ N_0^2 + N_0 \sum_{\mathbf{p} \neq 0} \left( 4b_{\mathbf{p}}^\dagger b_{\mathbf{p}} + b_{\mathbf{p}}^\dagger b_{-\mathbf{p}}^\dagger + b_{\mathbf{p}} b_{-\mathbf{p}} \right) \right] , \quad (2.11)$$

where  $\epsilon_{\mathbf{p}} = \mathbf{p}^2/(2m_B)$  is the single-particle kinetic energy. In the truncated Hamiltonian above we have omitted four-body interactions that does not involve any bosons in the condensate, which is zeroth order in  $N_0$ , and not expected to contribute much to the energy. We have also omitted three-body interaction terms scaling with  $N_0^{1/2}$ , which can be justified by their vanishing expectation value and thus vanish on a mean field level. Finally, terms scaling with  $N_0^{3/2}$  has only a single annihilation or creation operator with non-zero momentum, which vanishes exactly due to momentum conservation. Another way to arrive at the quadratic Hamiltonian is by writing the real-space field operator of Eq. (2.4) as

$$\psi(\mathbf{r}) = \sqrt{\frac{N_0}{\mathcal{V}}} + \delta\psi(\mathbf{r}) , \quad (2.12)$$

and expand the Hamiltonian to second order in the fluctuations,  $\delta\psi(\mathbf{r})$ .

Next, by means of Eq. (2.10), under the assumption that the depletion  $\langle N - N_0 \rangle$  is small compared to the total number of particles, we eliminate  $N_0$  in favor of the total Bose gas density,  $n_B = \langle N \rangle / \mathcal{V}$ :

$$H = \frac{g_B \mathcal{V} n_B^2}{2} + \sum_{\mathbf{p} \neq 0} \left[ (\epsilon_{\mathbf{p}} + g_B n_B) b_{\mathbf{p}}^\dagger b_{\mathbf{p}} + \frac{g_B n_B}{2} (b_{\mathbf{p}}^\dagger b_{-\mathbf{p}}^\dagger + b_{\mathbf{p}} b_{-\mathbf{p}}) \right]. \quad (2.13)$$

Since the Hamiltonian is quadratic, it can be diagonalized by a canonical transformation of the annihilation and creation operators,

$$b_{\mathbf{p}} = u_{\mathbf{p}} \gamma_{\mathbf{p}} - v_{\mathbf{p}} \gamma_{-\mathbf{p}}^\dagger \quad (2.14)$$

$$b_{\mathbf{p}}^\dagger = u_{\mathbf{p}} \gamma_{\mathbf{p}}^\dagger - v_{\mathbf{p}} \gamma_{-\mathbf{p}}, \quad (2.15)$$

known as the Bogoliubov transformation. Imposing bosonic commutation relations on the new operators,  $\gamma_{\mathbf{p}}$  and  $\gamma_{\mathbf{p}}^\dagger$ , produces the restriction

$$u_{\mathbf{p}}^2 - v_{\mathbf{p}}^2 = 1. \quad (2.16)$$

Inserting the expressions of Eqs. (2.14)–(2.15) into Eq. (2.13), we find that the Hamiltonian is diagonalized in the new operator basis if the coefficients have the form

$$u_{\mathbf{p}} = \sqrt{\frac{1}{2} \left( \frac{\epsilon_{\mathbf{p}} + g_B n_B}{E_{\mathbf{p}}} + 1 \right)}, \quad (2.17)$$

$$v_{\mathbf{p}} = \sqrt{\frac{1}{2} \left( \frac{\epsilon_{\mathbf{p}} + g_B n_B}{E_{\mathbf{p}}} - 1 \right)}, \quad (2.18)$$

consistent with Eq. (2.16), and with  $E_{\mathbf{p}}$  given by

$$E_{\mathbf{p}} = \sqrt{\epsilon_{\mathbf{p}}(\epsilon_{\mathbf{p}} + 2g_B n_B)}. \quad (2.19)$$

The diagonalized Bogoliubov Hamiltonian takes the form

$$H = \underbrace{\frac{g_B \mathcal{V} n_B^2}{2} + \frac{1}{2} \sum_{\mathbf{p} \neq 0} (E_{\mathbf{p}} - \epsilon_{\mathbf{p}} - g_B n_B)}_{\text{ground state energy}} + \sum_{\mathbf{p}} E_{\mathbf{p}} \gamma_{\mathbf{p}}^\dagger \gamma_{\mathbf{p}}. \quad (2.20)$$

The apparent divergence of the ground state energy in the high-momentum limit can be treated by solving the Lippmann-Schwinger

equation to second order in the scattering length[78]. Alternatively, instead of replacing every Fourier component with the constant  $g_B$ , we could have considered a more realistic potential that also captures high momentum scattering. Then the Fourier components would fall off at high momentum, and the expression for the offset energy will be well-behaved[77].

The Hamiltonian of Eq. (2.20) describes a system of non-interacting quasiparticles – Bogoliubov modes – created and annihilated by  $\gamma_{\mathbf{p}}^{\dagger}$  and  $\gamma_{\mathbf{p}}$ , respectively. The energy dispersion,  $E_{\mathbf{p}}$ , reduces to that of free particles,  $\epsilon_{\mathbf{p}}$ , when the interaction strength between the bare bosons vanishes,  $g_B = 0$ . In the low momentum limit,  $u_{\mathbf{p}} \approx v_{\mathbf{p}} \gg 1$ , the real boson  $b_{\mathbf{p}} \approx u_{\mathbf{p}}(\gamma_{\mathbf{p}} - \gamma_{-\mathbf{p}}^{\dagger})$  is an even superposition of a forward-propagating quasiparticle and a backward-propagating anti-quasiparticle. In the high momentum limit,  $u_{\mathbf{p}} \approx 1$  and  $v_{\mathbf{p}} \approx 0$ , and the quasiparticles reduce to free bosons,  $b_{\mathbf{p}} \approx \gamma_{\mathbf{p}}$  as they no longer feel the effects of the low-energy condensate.

## 2.2 Green's functions

An important tool in many-body physics is the Green's function formalism, which I sketch briefly in this section. A detailed introduction can be found in textbooks such as Refs [77, 79].

Green's functions are known from the theory of differential equations. For instance, for the single-particle time-dependent Schrödinger equation,

$$\left(i\hbar \frac{\partial}{\partial t} - H(\mathbf{r})\right) \Psi(\mathbf{r}, t) = 0, \quad (2.21)$$

one defines the Green's function,  $G(\mathbf{r}, t; \mathbf{r}', t')$ , such that

$$\left(i\hbar \frac{\partial}{\partial t} - H(\mathbf{r})\right) G(\mathbf{r}, t; \mathbf{r}', t') = \hbar \delta(\mathbf{r} - \mathbf{r}') \delta(t - t'). \quad (2.22)$$

The Green's function is sometimes called a *propagator* because it propagates the wavefunction from one time,  $t'$ , to a later time,  $t$ :

$$\Psi(\mathbf{r}, t) = \int d\mathbf{r}' G(\mathbf{r}, t; \mathbf{r}', t') \Psi(\mathbf{r}', t'). \quad (2.23)$$

This identity can be verified by substituting it into Eq. (2.21) and using Eq. (2.22):

$$\begin{aligned} \left( i\hbar \frac{\partial}{\partial t} - H(\mathbf{r}) \right) \Psi(\mathbf{r}, t) &= \int d\mathbf{r}' \hbar \delta(\mathbf{r} - \mathbf{r}') \delta(t - t') \Psi(\mathbf{r}', t') \\ &= \hbar \delta(t - t') \Psi(\mathbf{r}, t') \\ &= 0 \quad \text{for } t > t' . \end{aligned} \quad (2.24)$$

Using the Heaviside step function,  $\theta(x)$ , we can express the Green's function as

$$G(\mathbf{r}, t; \mathbf{r}', t') = -i\theta(t - t') \langle \mathbf{r} | e^{-i(t-t')H/\hbar} | \mathbf{r}' \rangle . \quad (2.25)$$

In the case above, the Green's function is known as the retarded Green's function because the wavefunction at  $\mathbf{r}$  at time  $t$  depends on the position  $\mathbf{r}'$  at an earlier time,  $t'$ . Here it is expressed as an expectation value of the time-evolution operator on the domain  $t > t'$ , and the zero function for  $t \leq t'$ . A similar solution to Eq. (2.22), which is zero for  $t \geq t'$ , can be given, known as the advanced Green's function.

### 2.2.1 Correlation functions in many-body physics

The Green's function is a correlation function that expresses how the wave function or quantum field is correlated with itself in time and space. In general, the correlation function between two time-dependent quantum operators,  $A$  and  $B$ , is given as

$$C_{AB}(t, t') = - \langle A(t)B(t') \rangle . \quad (2.26)$$

The expectation value can be evaluated in terms of the density matrix of the system,  $\rho$ , as

$$C_{AB}(t, t') = -\text{Tr}(\rho A(t)B(t')) . \quad (2.27)$$

The density matrix is defined as

$$\rho = \sum_i p_i |\psi_i\rangle\langle\psi_i| , \quad (2.28)$$

where  $p_i$  is the probability to find the system in the state  $|\psi_i\rangle$ . In quantum many-body theory, we assume a thermal distribution: The

probability to find system in the eigenstate  $|\psi_i\rangle$  with energy  $E_i$  is given by the Boltzmann factor,  $p_i = e^{-\beta E_i} / \mathcal{Z}$ , where  $\beta = 1/(k_B T)$  with  $T$  the temperature and  $\mathcal{Z} = \sum_i e^{-\beta E_i}$  is the partition function that ensures normalization of the probability. Thus, the thermal density matrix becomes  $\rho = e^{-\beta H} / \mathcal{Z}$ , where  $H$  is the Hamiltonian, and the expectation value is the thermal average:

$$C_{AB}(t, t') = -\frac{1}{\mathcal{Z}} \text{Tr}(e^{-\beta H} A(t) B(t')) . \quad (2.29)$$

Time-evolution in quantum mechanics, e.g. for the operators  $A$  and  $B$ , is given by the time-evolution operator on the form  $e^{-itH/\hbar}$ . In the following, we set  $\hbar = 1$ . Being an exponential of the Hamiltonian, the time-evolution operator has a striking similarity to  $e^{-\beta H}$ . We can treat both operators on an equal footing if we define the imaginary time,  $\tau \equiv it$ , and define  $\tau$ -dependent operators in the imaginary time interaction picture as

$$A(\tau) = e^{\tau H_0} A e^{-\tau H_0} , \quad (2.30)$$

where  $H_0$  is the non-interacting part of the Hamiltonian  $H = H_0 + H_{\text{int}}$ . In the general case of a time-dependent Hamiltonian, the time-evolution operator in the imaginary time interaction picture is

$$U(\tau, \tau') = e^{\tau H_0} e^{-(\tau-\tau')H} e^{-\tau' H_0} = T_\tau \left\{ e^{-\int_{\tau'}^{\tau} d\tau'' H_{\text{int}}(\tau'')} \right\} , \quad (2.31)$$

where  $T_\tau$  is the time-ordering operator with respect to  $\tau$ . Then we can express

$$e^{-\beta H} = e^{-\beta H_0} U(\beta, 0) = e^{-\beta H_0} T_\tau \left\{ e^{-\int_0^\beta d\tau H_{\text{int}}(\tau)} \right\} , \quad (2.32)$$

and the partition function as

$$\mathcal{Z} = \text{Tr} \left( e^{-\beta H} \right) = \text{Tr} \left( e^{-\beta H_0} U(\beta, 0) \right) . \quad (2.33)$$

Thus, in the imaginary time formalism, the correlation function becomes

$$C_{AB}(\tau, \tau') = -\frac{1}{\mathcal{Z}} \text{Tr} \left( e^{-\beta H_0} T_\tau \left\{ U(\beta, 0) A(\tau) B(\tau') \right\} \right) . \quad (2.34)$$

One typically knows the solution to the non-interaction system which is enough to determine  $A(\tau)$  and  $B(\tau')$ . The only appearance of the

interaction Hamiltonian,  $H_{\text{int}}$ , is in  $U(\beta, 0)$ , which can be expanded as a Dyson series. Considering  $H_{\text{int}}$  a perturbation, we achieve a perturbative series for the correlation function in the characteristic interaction strength.

The correlation function depends only on the imaginary time difference,  $\tau - \tau'$ , which is restricted from  $-\beta$  to  $\beta$ , but can be defined outside this domain with a cyclic property:  $C_{AB}(\tau + \beta) = \pm C_{AB}(\tau)$  with  $+$  for bosons and  $-$  for fermions. The Fourier transformed correlation function can be expressed as<sup>[79]</sup>

$$C_{AB}(i\omega_n) = \int_0^\beta d\tau e^{i\omega_n\tau} C_{AB}(\tau), \quad (2.35)$$

where the Matsubara frequency is  $\omega_n = 2n\pi/\beta$  for bosons and  $\omega_n = (2n + 1)\pi/\beta$  for fermions for any integer  $n$ .

### 2.2.2 Green's function for a BEC boson

Let us now return to the single-particle Green's function. In the imaginary time formalism its real space representation is defined as

$$G(\mathbf{r}, \tau; \mathbf{r}', \tau') \equiv - \left\langle T_\tau \left\{ \Psi(\mathbf{r}, \tau) \Psi^\dagger(\mathbf{r}', \tau') \right\} \right\rangle. \quad (2.36)$$

As described above for the general correlation function, the Green's function for an interacting system can be evaluated perturbatively if the Green's function for the free (non-interacting) system is known. For a non-interacting bosonic gas the Hamiltonian is Eq. (2.7) without the interaction potential is

$$H_0 = \sum_{\mathbf{p}} \epsilon_{\mathbf{p}} b_{\mathbf{p}}^\dagger b_{\mathbf{p}}. \quad (2.37)$$

Due to translational invariance the Green's function depends only on the spatial difference,  $\mathbf{r} - \mathbf{r}'$ , and is thus naturally expressed in the momentum basis,

$$G_0(\mathbf{p}, \tau) = - \left\langle T_\tau \left\{ b_{\mathbf{p}}(\tau) b_{\mathbf{p}}^\dagger(0) \right\} \right\rangle, \quad (2.38)$$

which can be found from Fourier transforming Eq. (2.36) and expanding the field operators in creation and annihilation operators. Using

$b_{\mathbf{p}}(\tau) = e^{\tau H_0} b_{\mathbf{p}} e^{-\tau H_0} = e^{-\epsilon_{\mathbf{p}} \tau} b_{\mathbf{p}}$  the free boson Green's function is evaluated as

$$G_0(\mathbf{p}, \tau) = - \left\langle T_{\tau} \left\{ b_{\mathbf{p}}(\tau) b_{\mathbf{p}}^{\dagger}(0) \right\} \right\rangle \quad (2.39)$$

$$= -\theta(\tau) \left\langle b_{\mathbf{p}}(\tau) b_{\mathbf{p}}^{\dagger}(0) \right\rangle - \theta(-\tau) \left\langle b_{\mathbf{p}}^{\dagger}(0) b_{\mathbf{p}}(\tau) \right\rangle \quad (2.40)$$

$$= - \left( \theta(\tau) \left\langle b_{\mathbf{p}} b_{\mathbf{p}}^{\dagger} \right\rangle + \theta(-\tau) \left\langle b_{\mathbf{p}}^{\dagger} b_{\mathbf{p}} \right\rangle \right) e^{-\epsilon_{\mathbf{p}} \tau} \quad (2.41)$$

$$= - \left( \theta(\tau)(1 + f_{\mathbf{p}}) + \theta(-\tau)f_{\mathbf{p}} \right) e^{-\epsilon_{\mathbf{p}} \tau}, \quad (2.42)$$

where the time-ordering is evaluated using the Heaviside step function. In the last line we have written the expected number of bosons as the Bose-Einstein distribution function,

$$\left\langle b_{\mathbf{p}}^{\dagger} b_{\mathbf{p}} \right\rangle = f_{\mathbf{p}} = \frac{1}{e^{\beta \epsilon_{\mathbf{p}}} - 1}. \quad (2.43)$$

Going to the frequency representation according to Eq. (2.35) we achieve the usual expression,

$$G_0(\mathbf{p}, i\omega_n) = \int_0^{\beta} d\tau e^{i\omega_n \tau} G_0(\mathbf{p}, \tau) \quad (2.44)$$

$$= -(1 + f_{\mathbf{p}}) \int_0^{\beta} d\tau e^{i\omega_n \tau} e^{-\epsilon_{\mathbf{p}} \tau} \quad (2.45)$$

$$= -(1 + f_{\mathbf{p}}) \frac{1}{i\omega_n - \epsilon_{\mathbf{p}}} \left( e^{i\omega_n \tau} e^{-\epsilon_{\mathbf{p}} \tau} - 1 \right) \quad (2.46)$$

$$= \frac{1}{i\omega_n - \epsilon_{\mathbf{p}}}, \quad (2.47)$$

where  $\omega_n = 2n\pi/\beta$  is a bosonic Matsubara frequency. This result also holds for a free fermion if we take  $\omega_n$  to be a fermionic Matsubara frequency. This expression is also what could be expected from Eq. (2.22) and the interpretation of the Green's function as the inverse of  $i\partial/\partial t - H$ .

However, in order to compute the physical properties of the system we need to take the Green's function from the regime of discrete imaginary frequencies,  $i\omega_n$ , to a continuous real variable,  $\omega$ . This can be done by analytic continuation of the Green's function in the upper half complex plane,  $i\omega_n \rightarrow z$ . The (retarded) Green's function of the real frequency,  $\omega$ , is obtained by restricting the function to  $z = \omega + i0^+$ , i.e. just above the real axis. The infinitesimal positive

number  $0^+$  has to be included in order to ensure a well-defined continuation. The retarded Green's function for a free particle (bosonic or fermionic) is thus

$$G_0(\mathbf{p}, \omega) = \frac{1}{\omega - \epsilon_{\mathbf{p}} + i0^+}. \quad (2.48)$$

When we consider a gas of bosons, where the majority has condensed into a BEC, it is useful to express the free boson Green's function in terms of the Bogoliubov mode operators. Inserting Eqs. (2.14)–(2.15) into Eq. (2.38), we find

$$G_0(\mathbf{p}, \tau) = -u_{\mathbf{p}}^2 \left\langle T_{\tau} \left\{ \gamma_{\mathbf{p}}(\tau) \gamma_{\mathbf{p}}^{\dagger}(0) \right\} \right\rangle - v_{\mathbf{p}}^2 \left\langle T_{\tau} \left\{ \gamma_{-\mathbf{p}}^{\dagger}(\tau) \gamma_{-\mathbf{p}}(0) \right\} \right\rangle, \quad (2.49)$$

where we have used that the expectation value of two annihilation or creation operators vanish. Since the Bogoliubov mode operators diagonalizes the Bogoliubov Hamiltonian, we can write the expectation values above in terms of free particle Green's functions. In the frequency representation, the result is traditionally denoted by

$$G_{11}(\mathbf{p}, i\omega_n) = \frac{u_{\mathbf{p}}^2}{i\omega_n - E_{\mathbf{p}}} - \frac{v_{\mathbf{p}}^2}{i\omega_n + E_{\mathbf{p}}}. \quad (2.50)$$

This is known as the normal boson propagator. In addition, there are two anomalous boson propagators, which are proportional to  $v_{\mathbf{p}}$  and thus small for a weakly interacting gas. We will therefore ignore them when describing scattering processes involving bosons in a BEC.

## 2.3 Polarons

Feynman diagrams is a powerful tool for understanding scattering processes of quantum particles. The method is frequently used to calculate reaction cross sections in high-energy physics[80] and many-body dynamics and impurity scattering in condensed matter physics[77, 79]. While these two areas of physics are rather different – one concerning relativistic few-body systems, the other non-relativistic many-body systems – the quantum field theoretical formalisms are remarkably similar. One might say that condensed matter physicists create tiny universes where the elementary particles

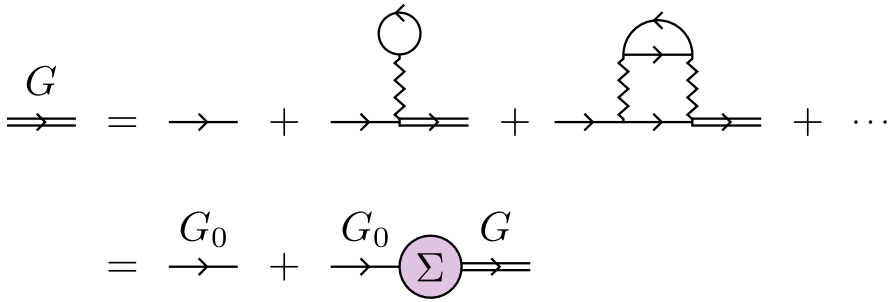


Figure 2.1: Dyson equation for the polaron propagator.

are the impurities in the otherwise homogeneous many-body world. In this analogy, physicists can tune the laws of physics in the universe via, e.g., the temperature, density or thermodynamic phase of the background medium, or its coupling to impurities. When an impurity interacts with the background medium, it may repel or attract neighboring particles according to the value of the coupling strength, which can be tuned at will using a Feshbach resonance, as explained previously. This alters the properties of the bare impurity, creating a dressed particle – a quasiparticle – known as a *polaron*. The concept of a collective polaron particle was introduced in 1933 by Landau, in the context of a phonon-dressed electron moving in a dielectric medium[81]. Since then the idea has been applied to many other condensed matter phenomena[82–84], but also to particles in nuclear physics[85] and as a way to understand how elementary particles acquire an effective mass through interactions with the surrounding Higgs field[86].

When an impurity interacts with a surrounding medium, its propagator (Green’s function) is altered from that of a bare particle. To take into account every possible scattering event, one defines the self-energy,  $\Sigma$ , of the polaron as the sum of irreducible Feynman diagrams (disregarding the external lines). This is illustrated in Figure 2.1, where a double line denotes the polaron propagator,  $G$ , and a single line is the bare impurity propagator,  $G_0$ . This yields the so-called Dyson equation for the polaron propagator,

$$G(\mathbf{p}, i\omega_n) = G_0(\mathbf{p}, i\omega_n) + G_0(\mathbf{p}, i\omega_n)\Sigma(\mathbf{p}, i\omega_n)G(\mathbf{p}, i\omega_n), \quad (2.51)$$

which is solved by

$$G(\mathbf{p}, i\omega_n) = \frac{1}{(G_0(\mathbf{p}, i\omega_n))^{-1} - \Sigma(\mathbf{p}, i\omega_n)}. \quad (2.52)$$

Taking  $i\omega_n \rightarrow \omega + i0^+$  and using Eq. (2.48) for the bare impurity propagator, we obtain the retarded Green's function for the polaron:

$$\begin{aligned} G(\mathbf{p}, \omega) &= \frac{1}{\omega - \frac{\mathbf{p}^2}{2m} - \Sigma(\mathbf{p}, \omega) + i0^+} \\ &= \frac{1}{\omega - \frac{\mathbf{p}^2}{2m} - \Re\Sigma(\mathbf{p}, \omega) - i\Im\Sigma(\mathbf{p}, \omega)}, \end{aligned} \quad (2.53)$$

where  $m$  is the bare mass of the impurity. Notice that this has the same form as the free particle Green's function, but with the free particle energy modified by the self-energy. From this Green's function, we can derive the physical properties of the polaron.

A well-defined polaron is characterized by a sharp peak in the Green's function, i.e. a small imaginary part of the self-energy. Assuming that a well-defined polaron exists for small momentum, we can determine its energy as the resonance frequency, found by self-consistently solving

$$\varepsilon_{\mathbf{p}} = \frac{\mathbf{p}^2}{2m} + \Re\Sigma(\mathbf{p}, \varepsilon_{\mathbf{p}}). \quad (2.54)$$

Consider the zero-momentum quasiparticle energy,  $\varepsilon_{\text{pol}} \equiv \varepsilon_{\mathbf{p}=0}$ . Expanding the Green's function around the resonance, we can write it on the form[87]

$$G(\mathbf{p}, \omega) \approx \frac{Z}{\omega - \varepsilon_{\text{pol}} - \frac{\mathbf{p}^2}{2m_{\mathbf{p}}^*} + \frac{i}{2\tau_{\mathbf{p}}(\omega)}}, \quad (2.55)$$

where  $m_{\mathbf{p}}^*$  is the effective mass,  $Z$  is the quasiparticle residue and  $\tau_{\mathbf{p}}(\omega)$  is the quasiparticle lifetime. Expressions for  $m_{\mathbf{p}}^*$  and  $Z$  will be given in the next section when treating the mixed-dimensional Bose polaron.

Near the resonance, the spectral function is a Lorentzian function,

$$A(\mathbf{p}, \omega) = -2\Im G(\mathbf{p}, \omega) \approx \frac{\frac{Z}{\tau_{\mathbf{p}}}}{\left(\omega - \varepsilon_{\text{pol}} - \frac{\mathbf{p}^2}{2m_{\mathbf{p}}^*}\right)^2 + \left(\frac{1}{2\tau_{\mathbf{p}}}\right)^2}, \quad (2.56)$$

with a characteristic peak width given by the lifetime,

$$\tau_{\mathbf{p}}(\omega) = -\frac{1}{2Z\Im\Sigma(\mathbf{p}, \omega)}. \quad (2.57)$$

In the limit of an infinite lifetime, we find the sharp resonance at  $\omega = \varepsilon_{\text{pol}}$  of a well-defined particle in the spectral function:

$$\lim_{\tau_{\mathbf{p}} \rightarrow \infty} A(\mathbf{p}, \omega) = 2\pi Z \delta(\omega - \varepsilon_{\mathbf{p}}). \quad (2.58)$$

This expression is the same as for a free particle only if  $Z = 1$ . The quasiparticle residue,  $Z \leq 1$ , determines how much of the spectrum can be associated with a distinct quasiparticle. Since the total spectral function fulfills the sum rule,

$$\int_{-\infty}^{\infty} \frac{d\omega}{2\pi} A_{\text{tot}}(\mathbf{p}, \omega) = 1, \quad (2.59)$$

we see by integrating Eq. (2.58) that the spectral function of the polaron only accounts for the fraction  $Z$  in the total spectrum. The remaining fraction,  $1 - Z$ , must be associated with non-quasiparticle state, i.e. a continuum of excited states.

## 2.4 Mixed-dimensional Bose polaron

This section is quoted from Ref. [5] (excluding the introduction and appendices) with minor changes in order to fit the context here. A misprint in Eq. (10) was corrected. I did the calculations, simulations and wrote the paper under the supervision of Georg M. Bruun and Zhigang Wu.

### 2.4.1 Model

We consider a single impurity atom of mass  $m$  confined in the 2D  $xy$ -plane by a strong harmonic trap  $m\omega_z^2 z^2/2$  along the  $z$ -direction. Since only one impurity is considered, our results of course do not depend on the statistics of the impurity. For concreteness, we take the impurity to be a fermion. The impurity atom is immersed in a weakly interacting 3D Bose gas of atoms with mass  $m_B$  (see Figure 2.2). The bosons form a BEC with density  $n_B$ , which is accurately described

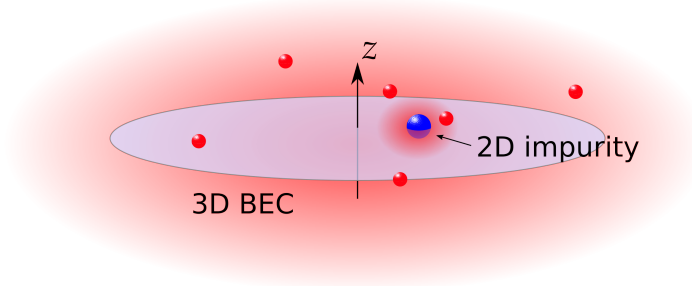


Figure 2.2: Sketch of the system: 2D impurity particle (blue) immersed in a 3D Bose-Einstein condensate (red). The Figure is adapted from Ref. [5].

by Bogoliubov theory since we assume  $n_B^{1/3} a_B \ll 1$ , where  $a_B$  is the boson scattering length. The Hamiltonian of the system is

$$H = \sum_{\mathbf{p}_\perp} \frac{\mathbf{p}_\perp^2}{2m} a_{\mathbf{p}_\perp}^\dagger a_{\mathbf{p}_\perp} + \sum_{\mathbf{p}} E_{\mathbf{p}} \gamma_{\mathbf{p}}^\dagger \gamma_{\mathbf{p}} + H_{\text{int}}, \quad (2.60)$$

where  $a_{\mathbf{p}_\perp}^\dagger$  creates an impurity with 2D momentum  $\mathbf{p}_\perp = (p_x, p_y)$ , and  $\gamma_{\mathbf{p}}^\dagger$  creates Bogoliubov mode in the BEC with 3D momentum  $\mathbf{p}$  and energy  $E_{\mathbf{p}} = \sqrt{\epsilon_{\mathbf{p}}(\epsilon_{\mathbf{p}} + 2n_B g_B)}$ . Here  $\epsilon_{\mathbf{p}} = \mathbf{p}^2/2m_B$  and  $g_B = 4\pi a_B/m_B$ . Throughout this paper, we set  $\hbar = k_B = 1$ . For clarity we will use the  $\perp$  sign to denote vectors in the plane in order to distinguish them from the 3D vectors. The interaction between the bosons and the impurity is

$$H_{\text{int}} = \frac{1}{\mathcal{V}} \sum_{\mathbf{p}\mathbf{p}'\mathbf{q}} e^{-(q_z l_z/2)^2} V(\mathbf{q}) b_{\mathbf{p}+\mathbf{q}}^\dagger a_{\mathbf{p}'-\mathbf{q}_\perp}^\dagger a_{\mathbf{p}'_\perp} b_{\mathbf{p}}, \quad (2.61)$$

where  $\mathbf{q} = (\mathbf{q}_\perp, q_z)$ ,  $l_z = 1/\sqrt{m\omega_z}$  is the harmonic oscillator length for the vertical trap and  $V(\mathbf{q})$  is the boson-fermion interaction potential. The latter will later be eliminated in favor of the effective 2D-3D scattering length  $a_{\text{eff}}$ . The operator  $b_{\mathbf{p}}^\dagger$  creates a boson with momentum  $\mathbf{p}$ , and it is related to the Bogoliubov mode creation operators by the usual relation  $b_{\mathbf{p}} = u_{\mathbf{p}} \gamma_{\mathbf{p}} - v_{\mathbf{p}} \gamma_{-\mathbf{p}}^\dagger$  with  $u_{\mathbf{p}}^2 = [(\epsilon_{\mathbf{p}} + g_B n_B)/E_{\mathbf{p}} + 1]/2$  and  $v_{\mathbf{p}}^2 = [(\epsilon_{\mathbf{p}} + g_B n_B)/E_{\mathbf{p}} - 1]/2$ . We have in Eq. (2.61) assumed that due to the strong confinement, the impurity resides in the lowest harmonic oscillator state  $\phi_0(z) =$

$\exp\{-z^2/2l_z^2\}/\pi^{1/4}\sqrt{l_z}$  in the  $z$ -direction. The exponential factor in Eq. (2.61) comes from the Fourier transform of  $\phi_0(z)$ . Note that only transverse momentum is conserved during boson-impurity collisions due to the confinement of the impurity in the vertical direction.

### 2.4.2 Self-energy

We employ the ladder approximation to calculate the self-energy of the Bose polaron [88]. For the Fermi polaron, this approximation has proven to be surprisingly accurate even for strong interactions [89–95]. The accuracy of the ladder approximation is less clear for the Bose polaron since there is no Pauli principle, which suppresses more than one fermion from being close to the impurity. The ladder approximation neglects such higher order correlations, which for instance can lead to the formation of a 3-body Efimov state consisting of the impurity atom and two bosons. In Ref. [96], it was shown that these Efimov correlations are important when the scattering length  $a_-$  for which the first Efimov trimer occurs, is comparable to or smaller than the interparticle distance in the BEC, whereas their effects are small for larger  $a_-$ . It has also been shown that the Efimov effect is suppressed in reduced dimensions as compared to the pure 3D case [97]. We therefore assume that higher order correlations are suppressed in the mixed dimensional geometry, and we resort to the ladder approximation in the following.

Within the ladder approximation, the polaron self-energy for momentum-frequency  $(\mathbf{k}_\perp, i\omega_n)$  is given by (see Figure 2.3a)

$$\Sigma(\mathbf{k}_\perp, i\omega_n) = \Sigma_0(\mathbf{k}_\perp, i\omega_n) + \Sigma_1(\mathbf{k}_\perp, i\omega_n) \quad (2.62)$$

where

$$\Sigma_0(\mathbf{k}_\perp, i\omega_n) = n_B \mathcal{T}(\mathbf{k}_\perp, i\omega_n) \quad (2.63)$$

describes the scattering of bosons out of the condensate by the impurity with  $\mathcal{T}$  the mixed dimension scattering matrix (see below). The calculations are all performed using finite temperature field theory with  $\omega_n = (2n + 1)\pi T$  a fermionic Matsubara frequency where  $T$  is the temperature and  $n$  is an integer. Once all frequency summations are performed, we let the temperature go to zero since this limit is the focus of the present paper. The self-energy coming from the

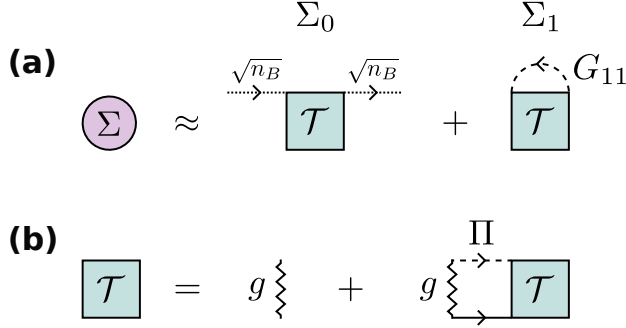


Figure 2.3: Diagrams used in the ladder approximation for the impurity. A solid line represents an impurity propagator, a dashed line denotes a boson propagator, and a dotted line denotes a boson emitted or absorbed by the BEC. (a) The polaron self-energy given by the sum of the diagrams  $\Sigma_0$  and  $\Sigma_1$ . (b) The  $\mathcal{T}$ -matrix giving the scattering between the impurity and a boson. The Figure is adapted from Ref. [5] and slightly modified.

scattering of bosons not in the condensate is

$$\Sigma_1(\mathbf{k}_\perp, i\omega_n) = -T \sum_\nu \int \frac{d^3 p}{(2\pi)^3} G_{11}(\mathbf{p}, i\omega_\nu) \mathcal{T}(\mathbf{k}_\perp + \mathbf{p}_\perp, i\omega_n + i\omega_\nu), \quad (2.64)$$

where  $\omega_\nu = 2\nu\pi T$  is a bosonic Matsubara frequency with  $\nu$  being an integer. The normal Bogoliubov Green's function for the bosons is

$$G_{11}(\mathbf{q}, i\omega_\nu) = \frac{u_{\mathbf{q}}^2}{i\omega_\nu - E_{\mathbf{q}}} - \frac{v_{\mathbf{q}}^2}{i\omega_\nu + E_{\mathbf{q}}}. \quad (2.65)$$

The 2D-3D scattering matrix between the impurity and a boson can be written as (see Figure 2.3b) [98]

$$\mathcal{T}(\mathbf{P}_\perp, i\omega_m) = \frac{1}{g^{-1} - \Pi(\mathbf{P}_\perp, i\omega_m)}. \quad (2.66)$$

Here  $g = 2\pi a_{\text{eff}}/\sqrt{m_B m_r}$ ,  $m_r = mm_B/(m + m_B)$  is the reduced mass,  $a_{\text{eff}}$  is the effective 2D-3D scattering length and  $\Pi(\mathbf{P}_\perp, i\omega_n)$  is the pair propagator. The effective scattering length is a function of the 3D boson-impurity scattering length and the trap harmonic oscillator

length  $l_z$  along the  $z$ -direction. This leads to several confinement induced resonances, which can be exploited to tune the 2D-3D interaction strength [99].

The mixed-dimensional pair propagator is given by

$$\Pi(\mathbf{P}_\perp, i\omega_m) = -T \sum_\nu \int \frac{d^3p}{(2\pi)^3} G_{11}(\mathbf{p}, i\omega_\nu) G_0(\mathbf{P}_\perp - \mathbf{p}_\perp, i\omega_m - i\omega_\nu), \quad (2.67)$$

where  $G_0(\mathbf{q}, i\omega_n) = [i\omega_n - \xi_{\mathbf{q}}]^{-1}$  is the bare impurity propagator with  $\xi_{\mathbf{q}} = \mathbf{q}^2/2m - \mu$  the bare energy relative to the impurity chemical potential. We keep a finite chemical potential  $\mu$  for the impurity when we derive the analytic expressions for all the relevant physical quantities. In the end, after all the Matsubara sums have been performed, we only retain those terms which survive the limit  $\mu \rightarrow \infty$ . Taking this limit ensures that the system has a vanishing concentration of impurities. This is a systematic way to obtain correct results relevant for a single impurity problem. Performing the Matsubara summation we arrive at

$$\begin{aligned} \Pi(\mathbf{P}_\perp, i\omega_m) = \int \frac{d^3p}{(2\pi)^3} & \left[ \frac{u_{\mathbf{p}}^2(1 + f_{\mathbf{p}})}{i\omega_m - E_{\mathbf{p}} - \xi_{\mathbf{P}_\perp - \mathbf{p}_\perp}} \right. \\ & \left. + \frac{v_{\mathbf{p}}^2 f_{\mathbf{p}}}{i\omega_m + E_{\mathbf{p}} - \xi_{\mathbf{P}_\perp - \mathbf{p}_\perp}} + \frac{2m_B}{p^2 + p_\perp^2/\alpha} \right], \end{aligned} \quad (2.68)$$

where  $f_{\mathbf{p}} = [\exp(E_{\mathbf{p}}/T) - 1]^{-1}$  is the Bose distribution function and  $\alpha = m/m_B$  is the ratio of the impurity and boson masses. The last term in the brackets in Eq. (2.68) comes from the regularization of the pair propagator by identifying the molecular pole of the  $\mathcal{T}$ -matrix at zero center-of-mass momentum in vacuum with  $\omega_M = -1/2m_r a_{\text{eff}}^2$  for  $a_{\text{eff}} > 0$  [98].

Eqs. (2.62)–(2.68) have the usual structure of the ladder approximation for a 3D Fermi polaron apart from two differences: First, the scattering medium is a BEC which involves processes describing the scattering of bosons into and out of the condensate; second, the mixed dimension 2D-3D scattering geometry has no intrinsic rotational symmetry, which complicates the evaluation of the resulting integrals significantly compared to the usual 3D case, as we shall discuss below.

### 2.4.3 Quasiparticle properties

The quasiparticle properties of the mixed dimension polaron are encapsulated in the single-particle retarded Green's function

$$G(\mathbf{k}_\perp, \omega) = \frac{1}{\omega - \frac{\mathbf{k}_\perp^2}{2m} - \Sigma(\mathbf{k}_\perp, \omega) + i0^+}, \quad (2.69)$$

where  $\Sigma(\mathbf{k}_\perp, \omega)$  is the retarded polaron self-energy obtained from performing the analytical continuation  $i\omega_n + \mu \rightarrow \omega + i0^+$ . To characterize the quasiparticle, we calculate its dispersion, residue, and effective mass. The quasiparticle dispersion  $\varepsilon_{\mathbf{k}_\perp}$  for a given momentum  $\mathbf{k}_\perp$  is found by solving the self-consistent equation

$$\varepsilon_{\mathbf{k}_\perp} = \frac{\mathbf{k}_\perp^2}{2m} + \Re \Sigma(\mathbf{k}_\perp, \varepsilon_{\mathbf{k}_\perp}), \quad (2.70)$$

where we assume that the damping (determined by the imaginary part of  $\Sigma$ ) of the polaron is small. The quasiparticle residue is

$$Z_{\mathbf{k}_\perp} = \frac{1}{1 - \partial_\omega \Re \Sigma(\mathbf{k}_\perp, \omega)|_{\omega=\varepsilon_{\mathbf{k}_\perp}}}, \quad (2.71)$$

and the effective mass is

$$m_{\mathbf{k}_\perp}^* = \frac{Z_{\mathbf{k}_\perp}^{-1}}{m^{-1} + k_\perp^{-1} \partial_{k_\perp} \Re \Sigma(\mathbf{k}_\perp, \omega)|_{\omega=\varepsilon_{\mathbf{k}_\perp}}}. \quad (2.72)$$

It should be noted that  $\Sigma$  only depends on the length of  $\mathbf{k}_\perp$ , denoted  $k_\perp$  above. We shall also calculate the spectral function of the polaron defined as

$$A(\mathbf{k}_\perp, \omega) = -2\Im m G(\mathbf{k}_\perp, \omega). \quad (2.73)$$

### 2.4.4 Numerical calculation

The mixed dimensional geometry turns out to significantly complicate the numerical calculation of the polaron self-energy. The reason is that the scattering of the impurity on a boson does not conserve momentum along the  $z$ -direction and therefore has no rotational symmetry, which can be used to reduce the number of convoluted integrals in the self-energy. This means that in order to make progress, we have to use simplifications for the calculation of  $\Sigma_1(\mathbf{k}_\perp, \omega)$  given

by Eq. (2.64), which involves six convoluted integrals. For  $\Sigma_1(\mathbf{k}_\perp, \omega)$  we shall approximate the mixed dimension pair propagator by that for a non-interacting Bose gas. Since we focus on the case of zero temperature, the pair propagator is then given by the vacuum expression

$$\Pi_{\text{vac}}(\mathbf{P}_\perp, i\omega_m) = -i \frac{\sqrt{m_B m_r}}{\sqrt{2\pi}} \sqrt{i\omega_m + \mu - \frac{\mathbf{P}_\perp^2}{2M}}, \quad (2.74)$$

where  $M = m + m_B$  and the complex square root is taken in the upper half plane. Physically, this approximation corresponds to assuming that the boson-impurity scattering is unaffected by the BEC medium, which is a good approximation for momenta  $p \gtrsim 1/\xi_B$ , where  $\xi_B = 1/\sqrt{8\pi n_B a_B}$  is the coherence length of the BEC. With this approximation, the numerical evaluation of  $\Sigma_1(\mathbf{k}_\perp, \omega)$  becomes feasible. In the following, we shall suppress the momentum label  $\mathbf{k}_\perp$  for the polaron, as we only consider the case of a zero momentum polaron  $\mathbf{k}_\perp = \mathbf{0}$ . We refer the reader to Appendix A for details of the numerical procedure.

### 2.4.5 Results

In this section, we present numerical results for the quasi-particle properties of the Bose polaron. In Figure 2.4, we plot the polaron energy  $\varepsilon/\varepsilon_n$  for zero momentum as a function of the inverse coupling strength  $1/k_n a_{\text{eff}}$  at zero temperature. We have defined the momentum and energy scales as  $k_n = (6\pi^2 n_B)^{1/3}$  and  $\varepsilon_n = k_n^2/2m_B$ , respectively. The energy is calculated for various gas parameters  $n_B^{1/3} a_B$  of the BEC, and for the mass ratios  $\alpha = m/m_B = 1$  and  $\alpha = 40/87$  relevant for the experiments in Refs. [100] and [70].

The corresponding quasiparticle residue and effective mass are plotted in Figs. 2.5–2.6. As for the 3D case, we see that there are two polaronic branches: One at negative energy  $\varepsilon < 0$ , which is called attractive polaron, and one at positive energy  $\varepsilon > 0$ , which is called the repulsive polaron.

For weak attractive interactions  $1/k_n a_{\text{eff}} \lesssim -4$ , the energy of the attractive polaron is close to the mean-field result  $g n_B$ , where  $n_B$  is the total density of the bosons, the residue is  $Z \simeq 1$ , and the effective mass is  $m^* \simeq m$ . As the attraction is increased, the polaron energy decreases, but it is significantly higher than the mean-field prediction. Contrary to the mean-field prediction, the polaron energy is finite

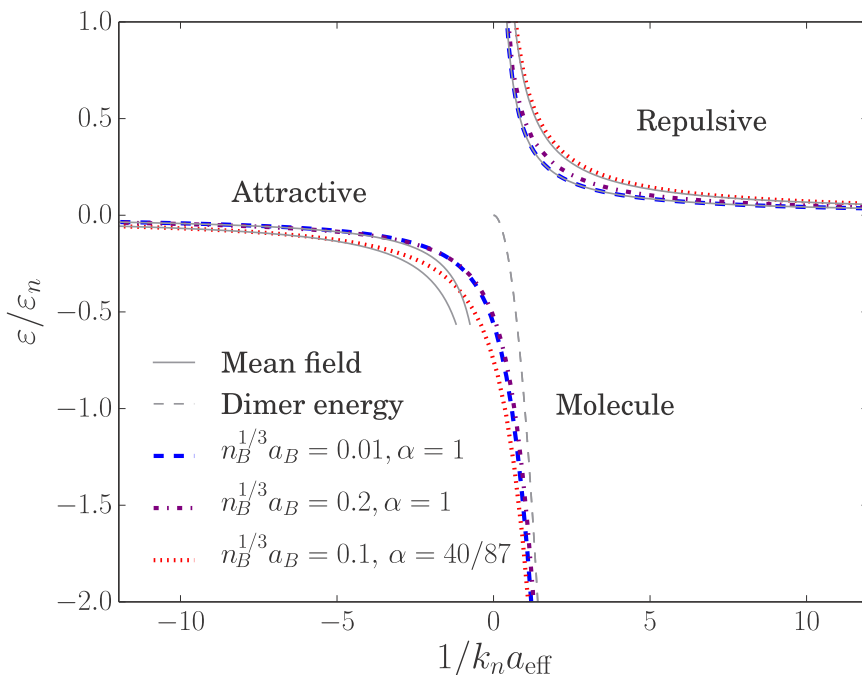


Figure 2.4: The quasiparticle energy for zero momentum as a function of the inverse Fermi-Bose interaction strength. The Figure is adapted from Ref. [5].

at unitarity  $1/k_n a_{\text{eff}} = 0$ , where we find the following quasiparticle properties:  $\varepsilon/\varepsilon_n \simeq -0.54$ ,  $Z \simeq 0.7$ ,  $m^*/m \simeq 1.17$  for  $\alpha = 1$  and  $\varepsilon/\varepsilon_n \simeq -0.75$ ,  $Z \simeq 0.7$ ,  $m^*/m \simeq 1.26$  for  $\alpha = 40/87$ . These results are *universal* in the sense that they depend only weakly on the BEC gas parameter in the range  $0.01 \leq n_B^{1/3} a_B \leq 0.2$  within the theory, as can be seen from Figs. 2.4–2.6. This should be contrasted with the case of a 3D Bose polaron, where a stronger dependence was found using the same ladder approximation [88]. The predicted universality of the polaron energy at unitarity could be an artifact of the ladder approximation. Indeed, there is presently no quantitatively reliable theory for whether the Bose polaron exists in the strongly correlated unitarity regime. In the pure 3D case, one particular variational ansatz including the dressing of the impurity with more than one Bogoliubov mode predicts that the Bose polaron does not exist at unitarity [101], whereas another variational ansatz, which

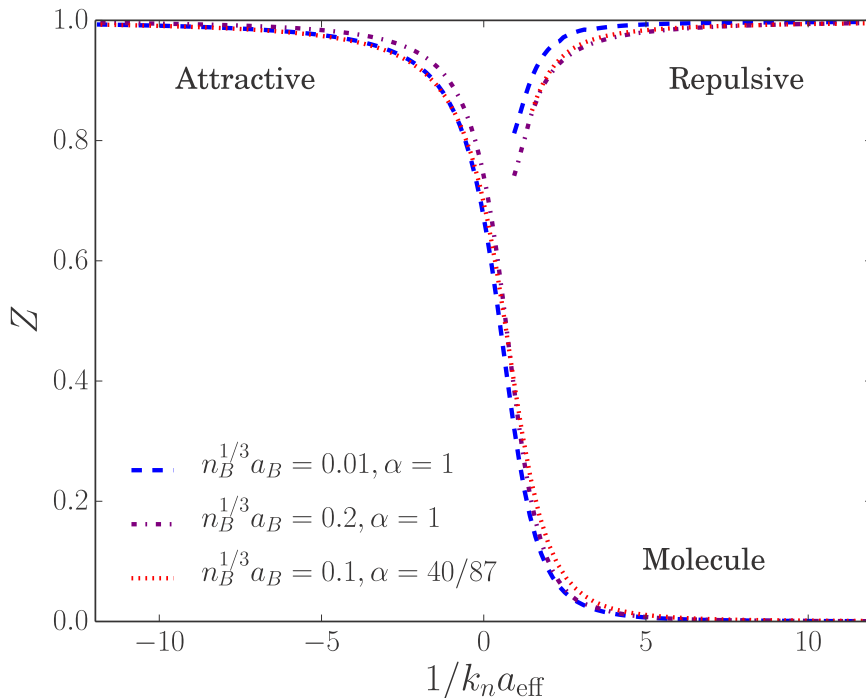


Figure 2.5: The quasiparticle residue for zero momentum as a function of the inverse Fermi-Bose interaction strength. The Figure is adapted from Ref. [5].

goes beyond the one Bogoliubov mode approximation including the correct 3-body Efimov correlations, predicts the polaron can be perfectly well-defined at unitarity provided the Efimov state is larger than the interparticle spacing [96]. So far, Monte-Carlo calculations have not provided an answer to this interesting question and the experimental results are ambiguous. We speculate that the results reported in this paper are more reliable, since the impurity living in 2D affects the bosons living in 3D less. Thus, higher order correlations neglected by the ladder approximation might be less important in the present mixed dimensional geometry. This is supported by the fact that 3-body Efimov physics is suppressed in mixed dimensional setups as noted above [97]. Our theory does not predict any instability as  $a_B \rightarrow 0$  in contrast to Monte-Carlo calculations for the 3D Bose polaron, where it was associated to the clustering of many bosons around to the impurity [102]. Similar effects for the 3D Bose polaron

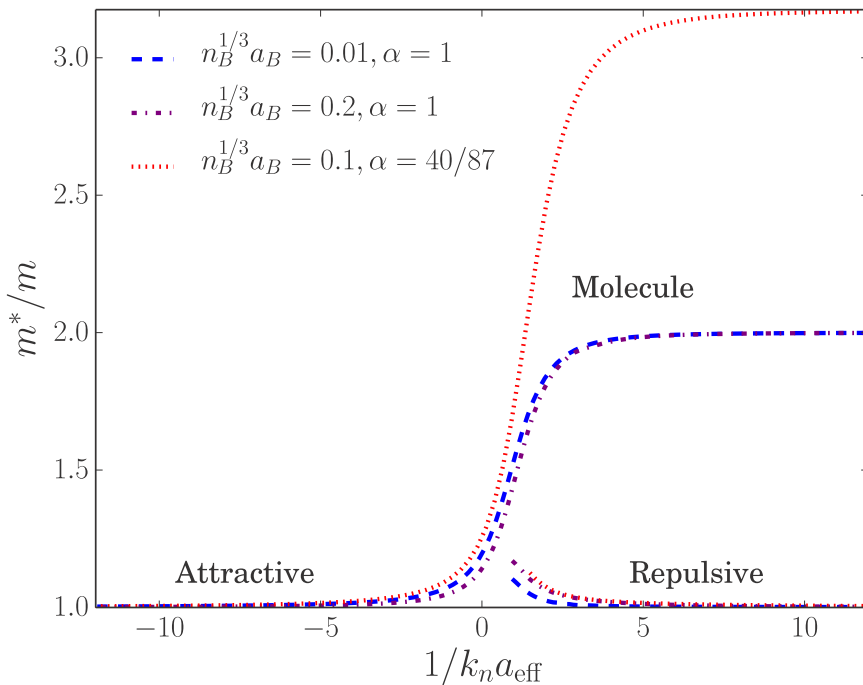


Figure 2.6: The effective mass for zero momentum as a function of the inverse Fermi-Bose interaction strength. The Figure is adapted from Ref. [5].

were found in Ref. [103]. Eventually, the attractive polaron energy approaches the dimer energy  $-1/2m_r a_{\text{eff}}^2$  on the BEC side ( $a_{\text{eff}} > 0$ ) of the resonance, the residue approaches zero, and the effective mass approaches  $m^* = m + m_B$ . This reflects the fact the impurity has formed a mixed dimensional dimer state with one boson from the BEC, in analogy with what happens for the 3D polaron.

The repulsive polaron is well defined for weak repulsive interactions  $1/k_n a_{\text{eff}} \gg 1$  with an energy close to the mean-field result  $gn_B$ , a residue  $Z \simeq 1$ , and an effective mass  $m^* \simeq m$ . As the repulsion increases, the energy and effective mass increase, whereas the residue decreases. We find that the polaron becomes ill defined for strong repulsion  $0 < 1/k_n a_{\text{eff}} \lesssim 0.8$ , where the numerics cannot find the residue and effective mass due to a large imaginary part of the self-energy.

To investigate this further, we plot in Figure 2.7 the spectral func-

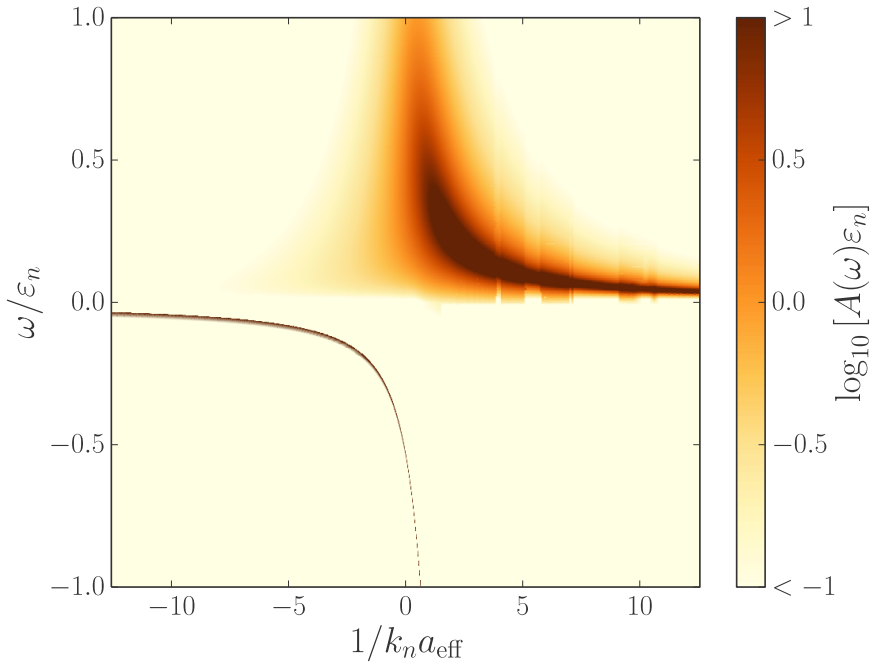


Figure 2.7: The spectral function of the zero momentum polaron as a function of frequency and inverse Fermi-Bose interaction strength. The Figure is adapted from Ref. [5].

tion  $A(\omega)$  of the polaron as a function of  $1/k_n a_{\text{eff}}$  for zero temperature and a BEC gas parameter  $n_B^{1/3} a_B = 0.1$ .

As expected, the attractive polaron gives rise to a sharp peak with a width given by the small imaginary part  $i\delta/\epsilon_n \leq i10^{-5}$ , which is added by hand to the frequency in the numerical calculations. We see that there is also a continuum of spectral weight for  $\omega > 0$ . This continuum corresponds to states consisting of an impurity with transverse momentum  $\mathbf{p}_\perp$  and a Bogoliubov mode with momentum  $\mathbf{p} = (-\mathbf{p}_\perp, p_z)$ . Since the ladder approximation treats the scattered impurity as a bare particle, the energy of these continuum states are predicted to be  $\omega = \mathbf{p}_\perp^2/2m + E_{\mathbf{p}}$  with a threshold at  $\omega = 0$ . This is, however, not physical since the scattered impurity also forms a polaron, and a more elaborate theory including self-consistent impurity propagators in all diagrams would yield a continuum starting just above the polaron quasiparticle peak on the attractive side  $a_{\text{eff}} < 0$  of the resonance [88].

We see from Figure 2.7 that the polaron peak on the repulsive side  $a_{\text{eff}} > 0$  is strongly damped as the interaction is increased towards the unitarity limit. This is because it sits right in the middle of the continuum described above. It is due to this strong damping that the repulsive polaron residue and effective mass cannot be calculated for  $1/k_n a_{\text{eff}} \lesssim 0.8$  as can be seen from Figs. 2.5–2.6. This result for the damping is, however, not quantitatively reliable since the continuum is not treated in a self-consistent manner as noted above. Also, we have not included 3-body decay of the repulsive polaron into the dimer state [94, 104, 105]. Nevertheless, we expect the non-zero damping of the repulsive polaron predicted by the ladder approximation to be qualitatively correct, since it does contain the 2-body decay into a Bogoliubov mode and a scattered impurity in an approximate way, which likely is dominant in analogy with the 3D case [94].

#### 2.4.6 Conclusions

In conclusion, we analyzed a mixed dimensional Bose polaron, where the impurity particle moves in a 2D plane immersed in a 3D BEC. Using a diagrammatic ladder approximation that includes the mixed dimensional 2D-3D vacuum scattering between the impurity and the bosons exactly, the mixed dimensional polaron was shown to exhibit the same qualitative features as the pure 3D Bose-polaron. In particular, there is a well defined polaron state for attractive impurity-boson interaction that smoothly develops into a mixed dimensional dimer for strong attraction, and there is a well defined polaron state for weak repulsive interaction, which becomes strongly damped as the repulsion increases. As opposed to the 3D case, our calculations predict that the properties of the polaron are almost independent of the gas parameter of the BEC as long as it is small so that Bogoliubov theory applies. It follows that the polaron has universal properties in the unitarity limit of the impurity-boson interaction. We speculate that higher order correlations, which could change this result, are suppressed in the mixed dimensional geometry. The fact that we predict well-defined quasiparticles in mixed dimensional systems indicates that these systems should be well described by Fermi liquid theory, which will be interesting to investigate in the future.

---

# Superconducting circuits and quantum transistor

*In 2016, Nikolaj T. Zinner's group made the transition from cold atoms to superconducting circuits. We were motivated by recent work in the group, which I will begin this chapter by describing. I will then give a general introduction to superconducting circuits, and conclude with my own work, based in parts on Refs. [6, 9, 10].*

In 2015–16, former PhD student in Nikolaj T. Zinner's group, Oleksandr Marchukov, developed the concept of a 'quantum transistor' in a few-body spin chain. This aligned well with the ongoing research in cold atoms in the group, and therefore an implementation of the quantum transistor in cold atoms trapped in one dimension was initially proposed [106]. However, as theoretical physicists, we are not limited by a specific platform, and at the time we were getting interested in a competitor for cold atoms: superconducting circuits. Before we turn to this platform, which is the main focus of this chapter, let me sketch the concept of a quantum transistor.

## 3.1 Quantum transistor: controlled state transfer

Consider the quantum state transfer problem discussed in Section 1.5: Suppose we have a spin chain with a single spin impurity located in

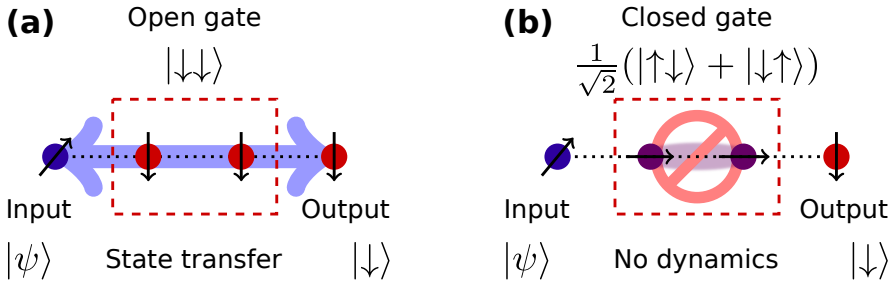


Figure 3.1: The quantum transistor: (a) State transfer between the input and output ports is permitted when the gate is open, and (b) not permitted when the gate is closed.

the right side of the chain, e.g. a spin up atom among a majority of spin down atoms,  $|\uparrow\downarrow\dots\downarrow\rangle$ . Then what must the model satisfy in order to ensure that the spin impurity is transferred to the left side,  $|\downarrow\dots\downarrow\uparrow\rangle$ , after some time  $t_g$ ?

The quantum transistor is the transfer problem with a twist. Like the transistor known from electric circuitry, the quantum transistor is a device capable of switching a current on and off. In the context of spin chains, the current is the spin impurity moving down the sites in the chain. Thus, transistor functionality is the ability to switch between a system configuration permitting perfect state transfer (open transistor) and freezing all dynamics (closed transistor). A classical transistor is comprised of an input port, an output port, and a gate (the switch). In the quantum transistor, the right spin plays the role of the input port, and the left spin is the output port, both coupled to the gate. The gate itself must be a quantum system accommodating the states  $|\text{open}\rangle$  and  $|\text{closed}\rangle$  for the two switch modes, satisfying

$$|\uparrow\rangle |\text{open}\rangle |\downarrow\rangle \rightarrow |\downarrow\rangle |\text{open}\rangle |\uparrow\rangle \quad \text{after some time } t_g, \quad (3.1)$$

$$|\uparrow\rangle |\text{closed}\rangle |\downarrow\rangle \rightarrow |\uparrow\rangle |\text{closed}\rangle |\downarrow\rangle \quad \text{for all times.} \quad (3.2)$$

Marchukov *et al.* showed in Ref. [106] that a Heisenberg XXZ chain could operate as a quantum spin transistor. In the simplest imaginable case, the gate is a single spin coupled to the input and output spin on each side. However, such a chain fails to prevent excitation leakage from the gate spin. Thus, the simplest realization is with four spins and no external magnetic fields, where the model

Hamiltonian takes the form

$$H_{\text{transistor}} = -\frac{1}{2} \sum_{k=1}^3 J_k \left( \sigma_x^k \sigma_x^{k+1} + \sigma_y^k \sigma_y^{k+1} - \sigma_z^k \sigma_z^{k+1} \right), \quad (3.3)$$

with symmetric couplings,  $J_3 = J_1$ . The left spin ( $k = 1$ ) is the input port, the right spin ( $k = 4$ ) is the output port, and the middle spins ( $k = 2, 3$ ) constitute the gate, provided that these are strongly bound, i.e.  $|J_2/J_1| \gg 1$ . The gate states controlling the state transfer between the ports are  $|\text{open}\rangle = |\downarrow\downarrow\rangle$  and  $|\text{closed}\rangle = (|\uparrow\downarrow\rangle + |\downarrow\uparrow\rangle)/\sqrt{2}$ . The functionality of the model extends the anticipated controlled transfer of a single spin excitation: In fact, Eqs. (3.1)–(3.2) hold if the state  $|\uparrow\rangle$  is replaced with an arbitrary spin state,  $|\psi\rangle = \alpha|\uparrow\rangle + \beta|\downarrow\rangle$ , with  $|\alpha|^2 + |\beta|^2 = 1$ :

$$|\psi\rangle |\downarrow\downarrow\rangle |\downarrow\rangle \rightarrow |\downarrow\rangle |\downarrow\downarrow\rangle |\psi\rangle \quad \text{after some time } t_g, \quad (3.4)$$

$$|\psi\rangle \frac{1}{\sqrt{2}} (|\uparrow\downarrow\rangle + |\downarrow\uparrow\rangle) |\downarrow\rangle \quad \text{is unchanged for all times.} \quad (3.5)$$

The transfer time is  $t_g = \pi/|J_1|$ , i.e. the natural time-scale set by the coupling between the gate and input/output ports. The functionality is illustrated in Figure 3.1.

The functionality can be qualitatively understood in the following way. The transfer in Eq. (3.4) happens via an intermediate resonant state, allowing the spin excited part of  $|\psi\rangle$  the exchange energy with its right neighbor, hence the  $|\uparrow\rangle$  travels to the output port. The  $|\downarrow\rangle$  part of  $|\psi\rangle$  does not contribute to any dynamics, as the state where all spins are down is an eigenstate of the system. The strongly bound middle spins can be understood as a single particle, and switching the state from  $|\text{open}\rangle$  to  $|\text{closed}\rangle$  can be interpreted as adding a excitation in the ‘gate particle’ with an energy of  $\sim 2J_2$ , effectively blocking state transfer. However, since this mechanism relies only on detuning the gate, there will be leakage across the closed gate on the time-scale  $1/J_2$ , preventing perfect blockade.

As described in Chapter 1, the Heisenberg XXZ Hamiltonian of Eq. (3.3) can be implemented with strongly interacting cold atoms in a one-dimensional optical trap. Marchukov *et al.* proposed a symmetric potential with three wells. The left and right wells are deep in order to trap a single atom each implementing the input and output spins, while the middle well traps the two strongly bound gate spins.

When the quantum transistor was developed in the group, it was framed in the language of atomic spin chains and state transfer. However, the spins we considered are nothing more than two-level systems, or in the terminology of quantum computing: *qubits*. The quantum computing aspect of the quantum transistor is already alluded to in the term *quantum transistor*, as the transistor is the backbone hardware device of classical computing. In quantum computing, the leading platforms are cold atoms and superconducting circuits. Having covered the cold atoms implementation, we thought also the superconducting circuit community could benefit from the quantum transistor. This meant we had to find a realistic superconducting circuit design that could implement  $H_{\text{transistor}}$ , or a Hamiltonian with similar properties. In general, superconducting circuits seemed like a promising platform for us, offering a large degree of freedom in system design and control. In particular, it gave us the opportunity to go beyond one-dimensional spin chains, as superconducting qubits can be wired together in different geometries on the chip, giving rise to quantum interference in a two-dimensional spin/qubit network. As we will see later in this chapter, this is a key aspect in the design of an improved quantum transistor.

## 3.2 Superconducting qubits: artificial atoms

Superconducting circuits, being macroscopic condensed matter systems, does not bear an immediate resemblance with the microscopic intrinsically quantum mechanical atoms. However, when built and operated properly, there is not much difference from a theoretical point of view. Superconducting circuit chips are fabricated in cleanrooms using lithographic and evaporation techniques developed for the production of integrated circuit used in modern electronics. The chip, usually a few millimeters to a centimeter in size, typically contains one or several qubits coupled to resonators or wave-guides, which connects the chip with classical electronics running the experiment. The energy-level spectrum of the qubit is characterized by the circuit parameters, and can be engineered by design, which is why superconducting qubits are sometimes referred to as artificial atoms[107].

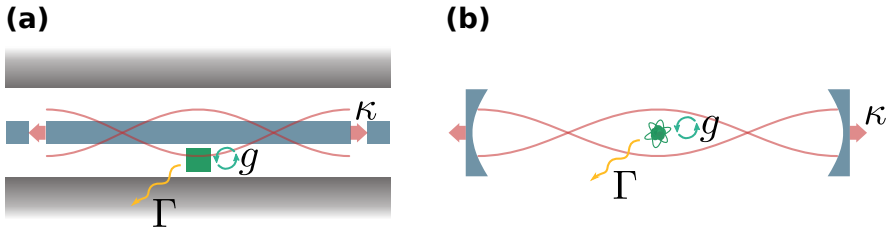


Figure 3.2: Two physical systems described by the Jaynes-Cummings model: (a) A superconducting qubit (green) coupled to a cavity resonator (blue). (b) A two-level atom (green) coupled to a light-field in a photon cavity (blue).

### 3.2.1 Back-of-the-envelope characterization

A lot of insight into superconducting qubits can be gained just by considering the physical scales involved. A typical chip design involves a qubit coupled to cavity resonator, such as in Figure 3.2a. The resonator length is comparable to the chip dimensions,  $L \sim 1$  cm, supporting photon modes with wavelength  $\lambda \sim 10L$ , i.e. with frequency in the microwave regime,  $\nu = c/\lambda \sim 3$  GHz[108]. The qubit can be addressed with microwaves if its characteristic energy-scale equals the photon energy,  $E = h\nu \sim 10^{-5}$  eV. This corresponds to a thermal energy at a temperature  $T = E/k \sim 0.1$  K. Thus, by cooling the chip in a dilution refrigerator to much lower temperatures, usually 0.01 K, the system will relax to its ground state, and the lowest two energy levels of the ‘artificial atom’ constitute our two-level qubit. At this temperature, metals such aluminum, which is often used in chip fabrication, becomes superconducting, providing the distinctive name of the platform.

We can also estimate the time it requires to perform a gate operation on a quantum computer based on superconducting qubits. The qubit frequency provides a characteristic time-scale for qubit dynamics,  $t = 1/\nu \sim 30$  ns. This matches well typical single-qubit gate times of 5–40 ns[109].

### 3.2.2 Basic qubit control and readout

The role of a superconducting qubit as an artificial atom is most clearly illustrated if we couple it to a cavity resonator. In this case, the physics is identical to an atom in a light-field (photon cavity).

The physics that describe this light-matter interaction is known as cavity quantum electrodynamics (cQED), and in the context of superconducting circuits: circuit QED. Both systems as illustrated in Figure 3.2.

Since many different designs for superconducting qubits exists, I simply illustrate the the qubit in Figure 3.2a as a generic superconducting island in green. In proceeding sections, I will give a detailed account of the most popular type of superconducting qubit, the transmon qubit, and give a short description of another type known as a C-shunted flux qubit. So, for the time being, let us describe the generic superconducting qubit in terms of a ground state,  $|0\rangle$ , and an excited state,  $|1\rangle$ . The qubit dynamics is governed by the Hamiltonian

$$H_q = -\frac{1}{2}\hbar\omega_q\sigma_z, \quad (3.6)$$

where  $\sigma_z = |0\rangle\langle 0| - |1\rangle\langle 1|$ , and  $\omega_q > 0$  is the qubit frequency.

Denote by  $\omega_r$  the cavity resonance frequency, and by  $g$  the coupling strength between the photon mode and qubit. Take  $g \ll \omega_r, \omega_q$  such that the resonator and qubit are well-defined quantum object perturbed by the resonator-qubit interaction.

The quality of the resonator is quantified by  $Q = \omega_r/\kappa$ , where  $\kappa$  is the photon loss rate. The quality of a qubit is typically characterized by two rates[107]:

- Longitudinal relaxation rate  $\Gamma_1$ , i.e. the rate of depolarization  $|0\rangle \leftrightarrow |1\rangle$ ,
- Transverse relaxation rate  $\Gamma_2 = \frac{\Gamma_1}{2} + \Gamma_\phi$ , where  $\Gamma_\phi$  is rate of pure dephasing  $|0\rangle + |1\rangle \rightarrow |0\rangle + e^{i\phi}|1\rangle$ .

The names ‘longitudinal’ and ‘transverse’ derive from the Bloch sphere picture of the qubit state. These two rates characterize the system dynamics within the Bloch-Redfield model of a qubit weakly coupled to a noise source with short correlation times and exponential qubit decay[107]. Here, let us for simplicity characterize the quality of the qubit with an overall decoherence rate,  $\Gamma$ .

We assume  $g \gg \kappa, \Gamma$  such that we can neglect photon loss and qubit decoherence on the time-scale of the qubit-resonator interaction. Today, high-quality resonators ( $Q > 10^6$ ) with the capability of trapping individual photons in the cavity can be constructed[110]. Qubit decoherence will always limit the fidelity of qubit operations,

but improvements in fabrication and control constantly increase the qubit lifetime. Typical lifetimes today are  $T \sim 1/\Gamma \sim 50\text{--}90\ \mu\text{s}$ [107, 109, 111]. The advancements in design, fabrication and control all together means that single-qubit operations are routinely performed with a fidelity  $F_{1\text{qb}} > 0.999$ [112–118], and several two-qubit gates have been demonstrated with a fidelity  $F_{2\text{qb}} > 0.99$ [118–123].

Under the above assumptions of perturbative coupling and high coherence, one can model the system as a single photon mode with an electric dipole interaction, known as the Jaynes-Cummings model[124]. The system Hamiltonian is typically cast as:

$$H_{\text{JC}} = \underbrace{\hbar\omega_r a^\dagger a}_{\text{photons}} - \underbrace{\frac{1}{2}\hbar\omega_q \sigma_z}_{\text{qubit}} + \underbrace{\hbar g (\sigma_+ a + \sigma_- a^\dagger)}_{\text{excitation exchange}}, \quad (3.7)$$

where  $a$  ( $a^\dagger$ ) is the single photon mode annihilation (creation) operator. When the resonator and qubit are close to resonance, the interaction term allow them to exchange excitations coherently, generating Rabi oscillations between the qubit states  $|0\rangle$  and  $|1\rangle$ . Thus, we can intuitively understand that one can control the qubit dynamics through the resonator. Using an arbitrary waveform generator, one can send tailored microwave pulses through the resonator (sometimes called feed-line or drive-line) to perform arbitrary single-qubit rotations. In this way, physicists can implement e.g. the Pauli gates, which rotate the qubit on the Bloch sphere around the axes. For an introductory discussion of qubit driving see Ref. [107].

Coupling the qubit to a resonator does not only allow us to control the qubit, it also allow us to measure the qubit state in a non-destructive way. The idea is to measure the resonance frequency of the resonator, which shifts according to the qubit state due to back-action from the qubit. This is known as quantum non-demolition dispersive readout. In the dispersive regime the qubit and resonator are far detuned,  $g/\Delta \ll 1$ , denoting by  $\Delta = \omega_q - \omega_r$  the detuning. In this limit, a unitary transformation to second order in  $g/\Delta$  takes  $H_{\text{JC}}$  to[124]

$$H_{\text{JC, disp}} = \hbar \left( \omega_r - \frac{g^2}{\Delta} \sigma_z \right) a^\dagger a - \frac{1}{2} \hbar \left( \omega_q + \frac{g^2}{\Delta} \right) \sigma_z. \quad (3.8)$$

Notice that the resonator frequency depends on the qubit state. Thus by measuring the amplitude of reflected microwave signal through

the resonator over a range of frequencies, we can determine the resonance frequency and hence infer whether the qubit is in its ground state,  $|0\rangle$ , or excited state,  $|1\rangle$ . On the other hand, back-action from the resonator induced by vacuum fluctuations in the resonator also shifts the qubit frequency by  $g^2/\Delta$ . This is analogous to the situation in atomic physics, where QED vacuum fluctuations perturb the electronic energies, lending the term ‘Lamb shift’.

### 3.3 Superconducting circuits

The quantum mechanical description of a superconducting circuit can be obtained from a classical description, using the standard method of canonical quantization. This process is explained in detail in Refs. [125, 126]. Here I simply sketch the method and provide the important example of the transmon qubit in the following section.

A good description of a classical circuit is provided by the lumped element model. Here the circuit is considered as a collection of circuit elements (capacitors, resistors, inductors etc.) connected through one-dimensional homogeneous and lossless wires. This reduces the continuous model based on the full apparatus of Maxwell’s equations to a finite set of nodes governed by Kirchhoff’s laws.

In superconducting circuit theory, lumped element diagrams are composed of capacitors, inductors and Josephson junctions. Resistors can be omitted due to the superconducting nature of chip. This also eliminates a major source of energy dissipation, allowing for unitary quantum dynamics. The Josephson junction, on the other hand, is unique to superconducting systems.

Given a lumped element diagram, we can construct a Lagrangian, for which Kirchhoff’s laws are the equations of motion. The Lagrangian is not uniquely determined, but requires a choice of generalized coordinates. One determines the number of independent nodes in the circuit and picks a ‘spanning tree’, i.e. a path from each node across the circuit elements to a ground node. Typically, one picks the fluxes  $\phi_1, \dots, \phi_N$  at the nodes as the generalized coordinates, with the ground node having zero flux. Another choice is the charges  $q_1, \dots, q_N$ . However, since the flux and charge are conjugate variables, satisfying the Poisson bracket,

$$\{\phi_i, q_j\} = \delta_{ij}, \quad (3.9)$$

the two choices are physically equivalent.

In order to construct the Lagrangian, we must express the energy stored in each lumped element in terms of the flux  $\phi$  or its time-derivative,  $\dot{\phi}$ . The flux is defined as the integral of the voltage across the element,

$$\phi(t) = \int_{-\infty}^t dt' V(t'), \quad (3.10)$$

assuming no voltages or currents are present in the infinite past. It follows from elementary electrodynamics that the energy stored in a capacitor with capacitance  $C$  is given by

$$\mathcal{T}_C = \frac{1}{2} C \dot{\phi}^2, \quad (3.11)$$

and the energy stored in an inductor with inductance  $L$  is

$$\mathcal{U}_L = \frac{1}{2L} \phi^2. \quad (3.12)$$

The third type of lumped element is the Josephson junction. It consists of two superconductors separated by a thin insulating layer, allowing Cooper pairs to tunnel across the junction. The energy stored in the electromagnetic field over the junction is

$$\mathcal{U}_J = -E_J \cos\left(\frac{2\pi\phi}{\Phi_0}\right), \quad (3.13)$$

where  $E_J$  is the Josephson energy proportional to the junction's critical current, and  $\Phi_0 = h/(2e)$  is the magnetic flux quantum. Notice that, since

$$\mathcal{U}_J = -E_J + \frac{E_J}{2} \left(\frac{2\pi\phi}{\Phi_0}\right)^2 - \frac{E_J}{24} \left(\frac{2\pi\phi}{\Phi_0}\right)^4 + \dots, \quad (3.14)$$

its leading contribution (apart from an irrelevant constant) is a  $\phi^2$ -term as in Eq. (3.13). Thus, we can consider the Josephson junction as a non-linear inductor.

Thinking of  $\phi$  as a 'position variable' in a classical mechanical sense, we can think of  $\mathcal{U}_L$  and  $\mathcal{U}_J$  as potential energies and  $\mathcal{T}_C$  as a kinetic energy. Thus, the Lagrangian can be constructed by subtracting the inductive energies from the capacitive energies for all the elements in the circuit,

$$\mathcal{L} = \mathcal{T}_{\text{cap}} - \mathcal{U}_{\text{ind}}. \quad (3.15)$$

The generalized momenta (charge variables) are found as  $q_i = \partial\mathcal{L}/\partial\dot{\phi}_i$  for  $i = 1, \dots, N$ .

The classical Hamiltonian of the circuit is computed as the Legendre transformation of the Lagrangian,

$$\mathcal{H} = \sum_{i=1}^N \dot{\phi}_i q_i - \mathcal{L} . \quad (3.16)$$

Finally, in order to obtain the quantum Hamiltonian of the system, we employ the usual quantization rule: promoting the flux and charge variables to linear operators with the commutation relation

$$[\phi_i, q_j] = i\hbar\delta_{ij} \quad (3.17)$$

and  $[\phi_i, \phi_j] = [q_i, q_j] = 0$ . This process is straight-forward, but will typically result in complicated Hamiltonians with many degrees of freedom. To arrive at manageable effective Hamiltonian, one must make appropriate simplifications such as discarding center-of-mass-type degrees of freedom and truncating the Hilbert space to the relevant low-energy spectrum.

### 3.4 The transmon qubit

Most widely used today is a type of qubit called a ‘transmon’ and variations thereof. It was introduced by Koch *et al.* in 2007 as an improved version of the so-called Cooper pair box qubit, which experienced low coherence times due to charge noise[108]. The Cooper pair box is a superconducting island onto which Cooper pairs may tunnel via two Josephson junctions from a grounded bulk piece of superconductor, acting as a reservoir of Cooper pairs[127, 128]. By applying a voltage across the device one can bias Cooper pairs towards the island, increasing the energy depending on the number of excess Cooper pairs. By operating the device near the ground state, the lowest two energy states can be used as a qubit.

The transmon is a Cooper pair box shunted by a large capacitance. It can be modeled with the lumped element circuit shown in Figure 3.3a. The dashed orange box represents the two Josephson junctions in parallel, connecting the island (top part half of the circuit) with the grounded reservoir (lower half), creating a loop which can be threaded by an external magnetic flux, known as a SQUID

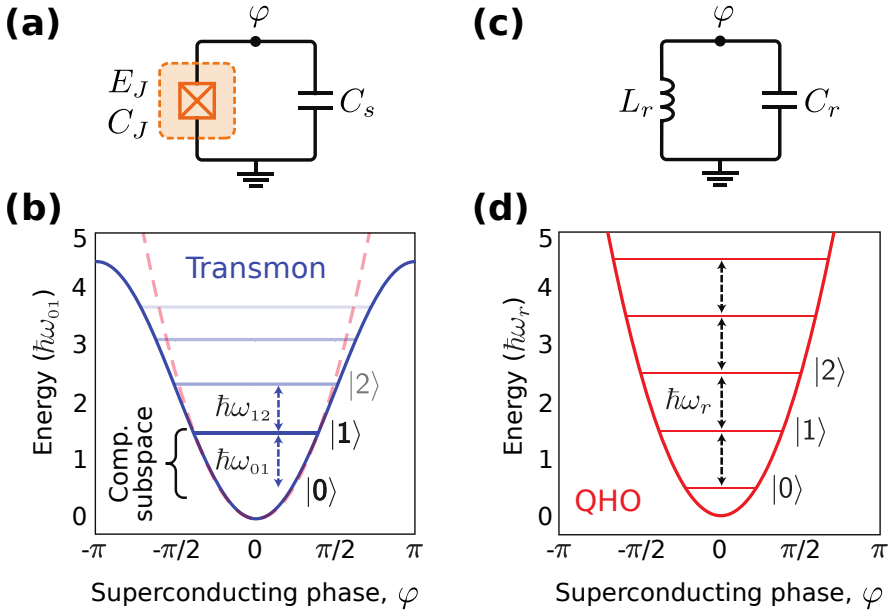


Figure 3.3: (a) Lumped element diagram of a transmon qubit with a non-linear inductive element in the orange box, here a single Josephson junction, achieving a (b) non-equidistant energy spectrum. (c) Lumped element diagram of an LC circuit in which the energy oscillates between the inductor and capacitor giving rise to (d) its quantum harmonic oscillator spectrum. Figure adapted from Ref. [107] and used with kind permission.

(superconducting quantum interference device). The SQUID acts as a single Josephson junction with a Josephson energy tunable by the external flux through the loop. We can therefore model it as a single Josephson junction with Josephson energy  $E_J$ , shown as the orange boxed cross in the circuit. A capacitance  $C_J$  can also be associated with the junction. This capacitance is much smaller than the shunt capacitance,  $C_s$ , and can either be ignored entirely, or included via the equivalent capacitance for the two capacitors in parallel,  $C = C_s + C_J$ . Since the Josephson junction can be thought of as a non-linear inductor, the transmon circuit is closely related to the LC circuit shown in Figure 3.3c. However, the non-linearity of the transmon is of crucial importance for its ability to function as a qubit. I will get back to this

point further in the analysis.

In terms of the flux node variable  $\phi$ , the classical Lagrangian of the transmon circuit is

$$\mathcal{L} = \frac{1}{2}C\dot{\phi}^2 + E_J \cos\left(\frac{2\pi\phi}{\Phi_0}\right), \quad (3.18)$$

from which we find the charge variable  $q = \partial\mathcal{L}/\partial\dot{\phi} = C\dot{\phi}$  and the Hamiltonian

$$\mathcal{H} = \frac{1}{2C}q^2 - E_J \cos\left(\frac{2\pi\phi}{\Phi_0}\right). \quad (3.19)$$

It is conventional to define the unitless coordinates  $\varphi = 2\pi\phi/\Phi_0$  and  $n = q/(-2e)$ , which can be interpreted as the superconducting phase across the junction and the number of excess Cooper pairs on the island, respectively. One often picks natural units where  $\hbar$  and  $2e$  are set to unity. In those units  $\phi$  and  $\varphi$  are identical, and  $q$  equals  $n$  up to a sign, which is irrelevant since the variable is squared in the Hamiltonian.

Quantizing the system in the operators  $\varphi$  and  $n$  with  $[\varphi, n] = -i$  produces the quantum Hamiltonian

$$H = 4E_C n^2 - E_J \cos \varphi. \quad (3.20)$$

Here  $E_C = e^2/(2C)$  is the charging energy, i.e. the energy cost of adding a charge  $e$  to the superconducting island. Crucial to the transmon design is the large shunt capacitance such that  $E_J/E_C \sim 50\text{--}100$ , which is in contrast to the Cooper pair box where the ratio is around unity. In this regime, the eigenenergies become insensitive to offset charge, providing protection from charge noise[108]. Since the kinetic energy is suppressed, we can assume the ‘position’ coordinate is near the potential minimum,  $\varphi \ll 1$ , in which case we can expand the cosine to fourth order in its argument:

$$H = \underbrace{4E_C n^2 + \frac{1}{2}E_J \varphi^2}_{\text{harmonic oscillator}} - \underbrace{\frac{1}{24}E_J \varphi^4}_{\text{anharmonicity}} - \underbrace{E_J}_{\text{offset}}. \quad (3.21)$$

If the Josephson junction had been replaced by an inductor, we would only have obtained the harmonic oscillator terms. That would be the LC resonator circuit shown in Figure 3.3c, where the energy oscillated between the capacitor of capacitance  $C_r$  and inductor with

inductance  $L_r$  with oscillation frequency  $\omega_r = 1/\sqrt{L_r C_r}$ , resulting in an equidistant spectrum with energy separation  $\hbar\omega_r$  shown in Figure 3.3d. However, this would be a poor qubit because we cannot address the transition between the lowest two (qubit) states without also driving excitations from the first excited state to the second, and so on. This is where the anharmonicity provided by the Josephson junction plays a crucial role, making it a key ingredient in every superconducting qubit design.

Defining the operator

$$b = \left(\frac{E_J}{32E_C}\right)^{\frac{1}{4}} \varphi - i \left(\frac{2E_C}{E_J}\right)^{\frac{1}{4}} n, \quad (3.22)$$

or equivalently,

$$\varphi = \left(\frac{2E_C}{E_J}\right)^{\frac{1}{4}} (b^\dagger + b) \quad \text{and} \quad n = -i \left(\frac{E_J}{32E_C}\right) (b^\dagger - b), \quad (3.23)$$

we can express the Hamiltonian as

$$H = \sqrt{8E_J E_C} \left(b^\dagger b + \frac{1}{2}\right) - \frac{1}{12} E_C (b^\dagger + b)^4 - E_J. \quad (3.24)$$

Thus,  $b$  and  $b^\dagger$  diagonalizes the harmonic oscillator part; they are the well-known step operators,

$$b = \sum_{k=1}^{\infty} \sqrt{k} |k-1\rangle\langle k|, \quad (3.25)$$

in the harmonic oscillator eigenbasis  $|0\rangle, |1\rangle, |2\rangle, \dots$ . Due to the anharmonic  $(b^\dagger + b)^4$ -term, these states are generally not eigenstates of  $H$ , and the energy spectrum becomes non-equidistant as shown in Figure 3.3b. This allows us to utilize the lowest two energy states as the computational subspace of our qubit. An effective Hamiltonian for the qubit is obtained by expressing  $H$  in the basis of harmonic oscillator states, and truncating the Hilbert space to the lowest two states,

$$H \approx -\frac{1}{2} \hbar\omega_q \sigma_z + \text{constant offset}, \quad (3.26)$$

with  $\sigma_z = |0\rangle\langle 0| - |1\rangle\langle 1|$  and  $\omega_q = (\sqrt{8E_J E_C} - E_C)/\hbar \sim 3\text{--}6\text{ GHz}$ . Notice that the harmonic oscillator states  $|0\rangle$  and  $|1\rangle$  remain eigenstates after the truncation. This is due to the fact that the anharmonic

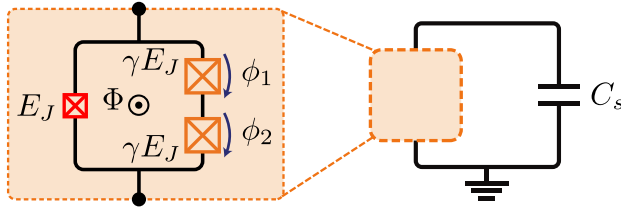


Figure 3.4: Lumped element diagram for a C-shunted flux qubit. The non-inductive element (orange box) consists of a superconducting loop with three Josephson junctions,  $\gamma$  being an asymmetry parameter for the Josephson energies. Figure adapted from Ref. [107] and used with kind permission.

term is quartic in step operators, and therefore does not couple states which are separated by an odd number of excitations. However, if the truncated Hilbert space included  $|2\rangle$ , a coupling between  $|2\rangle$  and  $|0\rangle$  would have made is necessary to diagonalize the truncated  $H$ .

Generally, one finds that transmon energies are shifted downwards compared to the harmonic oscillator. This is not surprising since the cosine potential is finite and dictates a maximum energy for any bound state, unlike the harmonic oscillator. The frequency difference between the lowest energy transitions,  $\alpha = \omega_{12} - \omega_{01}$ , is known as the anharmonicity of the qubit. For a transmon,  $-\alpha = E_C \sim 100\text{--}300$  MHz, which is typically a sufficient detuning to avoid excitations out of the computational subspace. However, it should be noted that a larger anharmonicity can be obtained with various types of flux qubits[107], where multi-dimensional energy landscapes can allow a positively valued anharmonicity.

### 3.5 The C-shunted flux qubit

Flux qubits are superconducting qubits consisting of a superconducting loop interrupted by a number of Josephson junctions[129–134]. When flux quanta penetrate the loop, persistent currents will run in the loop. The computational qubit states are superpositions of current states running clockwise and anti-clockwise. This is rather different from the transmon qubit, which is a so-called charge qubit due to the fact that its computational states are determined by the

number of Cooper pairs (charge) on the superconducting island.

Here I will briefly mention one type of flux qubit that will be relevant later: the C-shunted flux qubit[134]. The superconducting circuit for this qubit is shown in Figure 3.4. The shunt capacitance  $C_s$  of the transmon circuit is kept, hence the name ‘C-shunted’ flux qubit, but the inductive element is more complicated, counting three Josephson junctions. The Josephson junctions in series introduces additional flux variables  $\phi_1$  and  $\phi_2$ , giving rise to a two-dimensional potential energy landscape, as one variable can be eliminated by the fluxoid quantization condition. This complicates the analysis of the C-shunted flux qubit, and flux qubits in general, compared to the transmon. However, under the assumption of large array junctions,  $\gamma > 1$ , we can effectively treat the potential as quasi-one-dimensional in the sum variable,  $\phi = (\phi_1 + \phi_2)/2$ , assuming the same current direction across each junction[107]. In analogy with Eq. (3.20), we obtain the quantum Hamiltonian

$$H \approx 4E_C n^2 - E_J \cos(2\varphi + \varphi_{\text{ext}}) - 2\gamma E_J \cos \varphi, \quad (3.27)$$

where the  $n$  is the Cooper pair number operator and  $\varphi = 2\pi\phi/\Phi_0$  the dimensionless flux operator. We can treat the dimensionless external magnetic flux,  $\varphi_{\text{ext}} = 2\pi\Phi/\Phi_0$ , as a real continuous parameter, which is tunable in the experiment through flux lines on the chip. This provides a control knob for the shape of the well potential and the energy levels. Picking  $\varphi_{\text{ext}} = \pi$  renders the energy levels locally flat, making the qubit frequency  $\omega_q$  first-order insensitive to flux noise,  $\partial\omega_q/\partial\varphi_{\text{ext}} = 0$ . Operating the qubit at this flux bias point ensures long coherence times, while retaining a large anharmonicity  $\alpha \sim 500\text{--}900\text{ MHz}$ [134]. Unlike the transmon, the C-shunted flux qubit has a positive anharmonicity.

The landscape of superconducting qubits is diverse, and there are many innovative designs on the market. However, my goal here is not to give an overview of the field, but rather to introduce the two types of qubits – transmons and C-shunted flux qubits – which were relevant for my work.

## 3.6 The quantum transistor revisited

In 2016, a collaboration consisting of Lasse B. Kristensen, Christian K. Andersen, Nikolaj T. Zinner and I sought a superconducting

circuit implementation of the quantum transistor described in the beginning of this chapter. The idea was to substitute the spin-1/2 atoms with transmon qubits and engineer the couplings using the available circuit elements, i.e. capacitors, inductors and Josephson junctions. The efforts of our research is presented in Ref. [6] of which this section provides a brief summary.

While the original transistor proposal was a one-dimensional Heisenberg XXZ model implemented with atoms, we quickly realized that superconducting circuits offered both challenges and new possibilities. If we wanted to implement the same interaction Hamiltonian,  $H_{\text{transistor}}$  of Eq. (3.3), we would need to implement two-qubit XXZ couplings. As opposed to the situation in trapped cold atoms, the XXZ coupling does not arise naturally in superconducting qubits. However, the ingredients for an XXZ coupling is present: Two transmons coupled together via a capacitor produce the transverse (XX) coupling,  $J_x(\sigma_x^k\sigma_x^{k+1} + \sigma_y^k\sigma_y^{k+1})$ , and two inductively coupled flux qubits give rise to a longitudinal (ZZ) coupling,  $J_z\sigma_z^k\sigma_z^{k+1}$  [107]. However, these two couplings arise natively in different types of qubits. Creating a genuine XXZ coupling between two qubits, i.e. with the coupling strengths  $J_x$  and  $J_z$  of the same order of magnitude, would prove an engineering challenge, which we did overcome. However, from the way the transverse and longitudinal couplings arise natively, it is not surprising that the XXZ coupling can be achieved by combining capacitors and inductive elements (resonators/inductors and Josephson junctions). I will give an account of our XXZ coupler design in the proceeding section.

An obvious advantage of going to superconducting circuits is the possibility go beyond a one-dimensional ‘chain’ of atoms or qubits. This encouraged us to seek alternative geometries for the quantum transistor, while keeping the number of qubits fixed to four. We considered a general four-qubit Heisenberg Hamiltonian,

$$H_{\text{diamond}} = J_z^{23}\sigma_z^2\sigma_z^3 + \frac{1}{2}\sum_{i<j}^4 J_x^{ij}\left(\sigma_x^i\sigma_x^j + \sigma_y^i\sigma_y^j\right), \quad (3.28)$$

allowing XX couplings between any pair of qubits and a ZZ coupling between qubit 2 and 3. Figure 3.5a depicts the model, nicknamed *the diamond model* due to its geometry. As a quantum transistor, we considered qubit 1 and 4 as input and output ports, respectively, and qubits 2 and 3 as the gate. In order to reduce the parame-

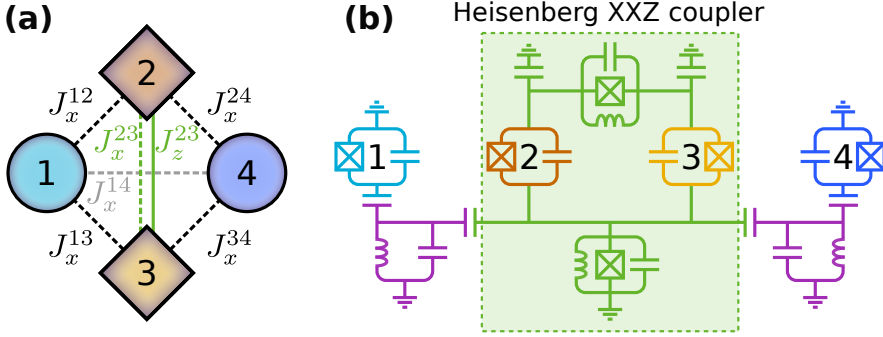


Figure 3.5: (a) Diamond model, denoting XX couplings with dashed lines and ZZ couplings with a solid line. (b) Lumped element diagram for the four-qubit transistor using transmon qubits. The Heisenberg coupler providing the XXZ coupling between qubit 2 and 3 is shown in the green box, which couples to qubit 1 and 4 through the purple resonator elements.

ter space, we asked the following question: Which restrictions are put on the model parameters if we require transistor functionality as defined in Eqs. (3.4)–(3.5)? In fact, we did allow for a more general closed gate state, but showed that it should be picked as  $|\text{closed}\rangle = (|\uparrow\downarrow\rangle \pm |\downarrow\uparrow\rangle)/\sqrt{2}$ , consistent with Ref. [106]. An analysis presented in Ref. [6] answered our question: Transistor functionality imposed horizontal symmetry,  $J_x^{13} = \mp J_x^{12}$  and  $J_x^{34} = \mp J_x^{24}$ , and prohibited any direct coupling between the input and output qubits,  $J_x^{14} = 0$ , as this would lead to leakage across the closed gate. For simplicity, we also imposed vertical symmetry,  $J_x^{12} = J_x^{24}$ , and abandoned the XX coupling in the gate,  $J_x^{23} = 0$ . With these restrictions, we proved that the diamond model would operate as a quantum transistor (up to a trivial single-qubit phase gate) with a transfer time of  $t_g = \pi/|J_z^{23}|$ , provided the ratio of coupling strengths fulfilled

$$\left| \frac{J_x^{12}}{J_z^{23}} \right| = \sqrt{n^2 - \frac{1}{4}}, \quad n = 1, 2, 3, \dots \quad (3.29)$$

The analysis assumed that  $J_z^{23} \neq 0$ . The reasoning behind this was the vital role the genuine XXZ coupling in the original transistor proposal of Ref. [106]. Here Marchukov *et al.* showed that the ZZ coupling between the gate constituents was necessary in order to

suppress second-order excitation exchange between the input and output ports, i.e. leakage across the gate. We believed this also to be case in the superconducting qubit model, which was why we engineered a circuit that implemented the XXZ coupling between the gate qubits. The superconducting circuit for the diamond model transistor is depicted in Figure 3.5b, showing four transmons connected through inductive couplers. On a superconducting chip, inductors (resonators) are the most space-consuming elements, and are avoided if possible. While our proposed circuit is readily built with today's technology, the presence of the inductive couplers involving four resonators makes the design slightly less appealing to experimentalists.

With this in mind, we were happy to learn from our continued research, that the model could be greatly simplified, removing the need for an XXZ coupling and inductors entirely. Furthermore, the improved four-qubit model has functionality that drastically extends the simple on/off state transfer switch of the transistor. I will omit a further analysis of the model in Figure 3.5 as chapter 4 will give an in-depth treatment of the improved model.

What made the XXZ coupling unnecessary in the diamond model compared to the linear chain model? The answer is exactly that: their different geometries. Unlike the linear model, the diamond model is a two-dimensional network, permitting quantum interference at the junctions. The requirements outlined above ensure that destructive interference cancels any state transfer when the gate is in its closed state, outperforming the linear model based on an energy blockade, which is only asymptotically closed. A similar analysis can be performed in the case  $J_z^{23} = 0$ . Constructive interference between the input and output ports ensure perfect state transfer when the gate is open. Thus, engineered quantum interference supersede the need for energetically suppressing certain transitions with the XXZ coupling.

Finally, I will mention that the work on the superconducting quantum transistor and Heisenberg XXZ coupler was sought patented by Aarhus University at the European Patent Office[9]. However, in 2018 Aarhus University decided not to continue the patenting process.

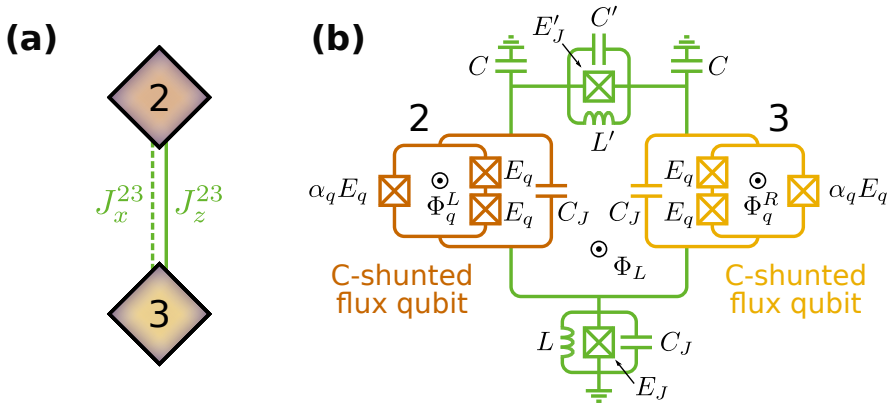


Figure 3.6: (a) XXZ-coupled qubits. (b) The Heisenberg XXZ coupler with C-shunted flux qubits. All the parameters describing the circuit are shown, but most relevant for our discussion are the magnetic fluxes through the central loop,  $\Phi_L$ , and the two qubits  $\Phi_q^L$  and  $\Phi_q^R$ , which can be controlled dynamically.

### 3.7 Heisenberg XXZ coupler

Although it turned out not to be necessary for the desired four-qubit dynamics, the work on the transistor project did bring about the development of the Heisenberg XXZ coupler, seen in Figure 3.5b coupling two transmon qubits. A Heisenberg XXZ coupler is a very useful tool when engineering Hamiltonians, e.g. for quantum annealing. In quantum annealing, one maps a specific (optimization) problem to a Hamiltonian, of which the ground state provides the solution. Getting access to Heisenberg XXZ interactions,

$$H_{\text{XXZ}} = \frac{1}{2} J_x (\sigma_x^i \sigma_x^j + \sigma_y^i \sigma_y^j) + J_z \sigma_z^i \sigma_z^j \quad (3.30)$$

$$= J_x (\sigma_-^i \sigma_+^j + \sigma_+^i \sigma_-^j) + J_z \sigma_z^i \sigma_z^j, \quad (3.31)$$

allows for a much broader class of problems to be solved compared to the the special cases of a Heisenberg XX model,  $J_z = 0$ , or the Ising model,  $J_x = 0$ , which are, as mentioned earlier, natively implemented in transmons or flux qubits, respectively. In order to cover as many optimization problems as possible on the same superconducting chip, a large degree of ‘on-the-fly’ tunability of the coupling strengths,  $J_x$

and  $J_z$ , is desired. While most of the circuit parameters (Josephson energies, capacitances and inductances) are fixed by the design, the external magnetic fluxes,  $\Phi_L$ ,  $\Phi_q^L$  and  $\Phi_q^R$ , can be controlled via flux-lines. We studied the degree of tunability for the Heisenberg XXZ coupler using C-shunted flux qubits, and not transmons as in the previous circuit in Figure 3.5b. However, we keep the indexes 2 and 3 for the coupled qubits in Figure 3.6a illustrating the resulting model and Figure 3.6b displaying the circuit diagram.

In the following, I will account for these unpublished results, using units where  $\hbar = 2e = 1$ . Lasse B. Kristensen analyzed the circuit in Figure 3.6b and derived the resulting qubit model, while I studied the dependency and tunability of the coupling strengths on the circuit parameters.

### 3.7.1 Effective circuit Hamiltonian

A careful analysis of the superconducting circuit in Figure 3.6b will show that the effective Hamiltonian of the system, when the degrees of freedom has be truncated to qubits, is

$$H = H_0 + H_I, \quad (3.32)$$

with a free evolution part

$$H_0 = -\frac{1}{2}\omega_2\sigma_z^2 - \frac{1}{2}\omega_3\sigma_z^3 - \frac{1}{2}\omega_{\text{CM}}\sigma_z^{\text{CM}}, \quad (3.33)$$

and the interaction part

$$H_I = J_{ZZ}^{2,3}\sigma_z^2\sigma_z^3 + J_{ZZ}^{2,\text{CM}}\sigma_z^2\sigma_z^{\text{CM}} + J_{ZZ}^{3,\text{CM}}\sigma_z^3\sigma_z^{\text{CM}} \\ + (J_{XXZ}^{2,3,\text{CM}}\sigma_z^{\text{CM}} + J_{YY}^{2,3} - J_{XX}^{2,3})(\sigma_-^2\sigma_+^3 + \sigma_+^2\sigma_-^3). \quad (3.34)$$

The model parameters above depend on the circuit parameters in a highly complicated fashion involving numerically found potential minima of the C-shunted flux qubits. For this reason, we do not give explicit expressions here, but resolve to numerical exploration of the parameter space.

This Hamiltonian describes the evolution of three independent degrees of freedom: the two qubits indexed 2 and 3, and a center-of-mass mode labeled CM. The center-of-mass degree arises from the fact that the circuit contains three independent fluxes nodes after the flux qubits has been defined, resulting in these three independent

modes. Here we are only interested in the two qubit modes, so we wish to get rid of the center-of-mass degree of freedom. To justify the way we do this, first notice that  $\sigma_{\text{CM}}^z$  commutes with the Hamiltonian. Thus the center-of-mass state is unchanged by the passing of time. Assuming it sits in the ground state, we replace  $\sigma_{\text{CM}}^z$  by its ground state expectation value  $\langle \sigma_{\text{CM}}^z \rangle = \text{sign}(\omega_{\text{CM}}) = 1$ . If the center-of-mass coordinate is far detuned from the two central qubits, we may address the qubits without accidentally exciting the center-of-mass coordinate. As we shall see later, this condition is fulfilled for the parameters studied here.

With the center-of-mass coordinate frozen to its ground state, we end up with the following two-qubit Hamiltonian:

$$H \approx H'_0 + H'_I + \text{constant offset} , \quad (3.35)$$

with a redefined free evolution part

$$H'_0 = -\frac{1}{2} \underbrace{(\omega_2 - 2J_{\text{ZZ}}^{2,\text{CM}})}_{\omega'_2} \sigma_z^2 - \frac{1}{2} \underbrace{(\omega_3 - 2J_{\text{ZZ}}^{3,\text{CM}})}_{\omega'_3} \sigma_z^3 \quad (3.36)$$

and interaction part

$$H'_I = \underbrace{(J_{\text{XXZ}}^{2,3,\text{CM}} + J_{\text{YY}}^{2,3} - J_{\text{XX}}^{2,3})}_{J_x} (\sigma_-^2 \sigma_+^3 + \sigma_+^2 \sigma_-^3) + \underbrace{J_{\text{ZZ}}^{2,3}}_{J_z} \sigma_z^2 \sigma_z^3 . \quad (3.37)$$

The interaction Hamiltonian,  $H'_I$ , is the desired two-qubit Heisenberg XXZ model of Eq. (3.30). The coupling strengths,  $J_x$  and  $J_z$ , depends on the circuit parameters in Figure 3.6b. While most of these are fixed by a specific realization of the circuit, the fluxes  $\Phi_L$ ,  $\Phi_q^L$  and  $\Phi_q^R$  can be controlled dynamically in the laboratory through flux lines producing local magnetic fields. Thus it is possible to change the values of the coupling strengths without resorting to a different physical circuit chip. Our idea is to pick a suitable set of chip specific circuit parameters (i.e. all but the fluxes), and then determine to which degree  $J_x$  and  $J_z$  can be tuned simply by means of varying the fluxes. Ideally, we will be able to tune them over a large range of models, from an XX model ( $|J_x/J_z| \gg 1$ ), over an XXZ model ( $|J_x/J_z| \sim 1$ ) to an Ising model ( $|J_x/J_z| = 0$ ).

### 3.7.2 Method

A good set of circuit parameters must be experimentally realistic and result in a set of Heisenberg model parameters that respect certain conditions. Firstly, we would like  $\omega_{\text{CM}}$  to be far away from  $\omega'_2$  and  $\omega'_3$ , as discussed earlier. Secondly, the C-shunted flux qubits functions best when  $E_{J,i}/E_{C,i} \sim 70\text{--}200$  and  $E_{L,i}/E_{J,i} \sim 1\text{--}5$ . Here  $E_{J,i}$ ,  $E_{C,i}$  and  $E_{L,i}$  are effective Josephson, capacitive and inductive energies, respectively, characterizing qubit  $i = 2, 3$ . Additionally, it is advantageous if the qubit frequencies  $\omega'_i/(2\pi)$  does not exceed 14 GHz, and if  $J_z/(2\pi) \sim 10\text{--}60$  MHz. Finally, we would like  $J_x/J_z$  to be highly tunable through the fluxes, and, if possible, include  $J_x/J_z = 0$ .

The circuit is characterized by nine parameters, therefore searching the parameter space for the best set of parameters, given the many constraints, is not an easy task. To do the job, we employ the machine learning tool M-LOOP[135]. We provide M-LOOP with experimentally realistic boundaries on the nine circuit parameters, and ask it to find a suitable point in parameters space that minimizes a given scalar function, known as the cost function. The cost function is defined in such a way that a small value corresponds to a good set of resulting spin model parameters, as defined by the conditions discussed above. Equivalently, if the spin model violates the requirements we wish to fulfill, we punish M-LOOP by returning a large cost function. As M-LOOP trawls through different points in parameter space, it gradually learns the landscape of the cost function, using the gained knowledge as the basis for the continued search. The search stops when M-LOOP has found a sufficiently good set of parameters, or alternatively, if it has run a certain number of search iterations.

### 3.7.3 Results and discussion

An example of a good set of circuit parameters and the resulting qubit and Heisenberg model parameters is presented in Table 3.1. Unless stated otherwise, the simulations and data presented here will rely on these circuit parameter values. However, these parameters should only be considered as an example, and there are many other parameter sets that would lead to similar results.

The qubit and Heisenberg XXZ model parameters are presented in intervals found from varying the fluxes  $\Phi_L$ ,  $\Phi_q^L$  and  $\Phi_q^R$ , but with

Circuit parameters		Resulting parameters ( $i = 2, 3$ )	
$L/\text{nH}$	13.47	$E_{J,i}/E_{C,i}$	[79.30; 132.4]
$L'/\text{nH}$	6.925	$E_{L,i}/E_{J,i}$	[1.412; 2.244]
$E_J/(2\pi \text{ GHz})$	156.9	$\omega'_i/(2\pi \text{ GHz})$	[12.66; 13.89]
$E'_J/(2\pi \text{ GHz})$	171.8	$\omega_{\text{CM}}/(2\pi \text{ GHz})$	[2.451; 6.140]
$E_q/(2\pi \text{ GHz})$	20.18	$J_z/(2\pi \text{ MHz})$	[-24.21; -21.32]
$C/\text{fF}$	97.41	$J_x/(2\pi \text{ MHz})$	[-592.7; 375.1]
$C_J/\text{fF}$	87.85	$J_x/J_z$	[-17.27; 24.92]
$C'/\text{fF}$	87.11		
$\alpha_q$	0.2465		

Table 3.1: Fixed circuit parameters and the resulting energy ratios and Hamiltonian parameters as intervals in which they are tunable through the magnetic fluxes.

the shown circuit parameters fixed. We parameterize the fluxes in the circuit in terms of  $f_L$ ,  $f_q$  and  $\Delta$  defined through

$$\Phi_L = \pi - 2\pi f_L \quad (3.38)$$

$$\Phi_q^L = \pi - 2\pi f_q \quad (3.39)$$

$$\Phi_q^R = \pi - 2\pi(f_q - \Delta) . \quad (3.40)$$

It suffices to let the flux variables  $f_L$  and  $\Delta$  take values from 0 to 0.5, and  $f_q$  from  $-0.5$  to 0.5. Notice that the case  $\Delta = 0$  corresponds to a symmetric circuit, with the qubits behaving identically.

Note that the ZZ coupling strength,  $J_z$ , is nearly constant compared to  $J_x$ . Letting the value of  $J_z$  set the energy scale of the Heisenberg XXZ coupler, we shall focus on the ratio  $J_x/J_z$ . When changing the three fluxes, this ratio can be tuned over a larger interval, allowing for a plethora of models.

Figure 3.7 shows  $J_x/J_z$  as a function of the qubit flux parameter  $f_q$ . The colors corresponds to different values of the central flux parameter  $f_L$ . It is seen that the effect of changing  $f_L$  is roughly just a shift of the  $J_x/J_z$  curve. Thus by tuning  $f_L$  we can achieve very large positive or negative values of  $J_x/J_z$ . The values  $f_L = 0$  and 0.5 used in the plot results in the lowest and highest curves, respectively, and cranking  $f_L$  from 0 to 0.5 smoothly evolves one curve into the other.

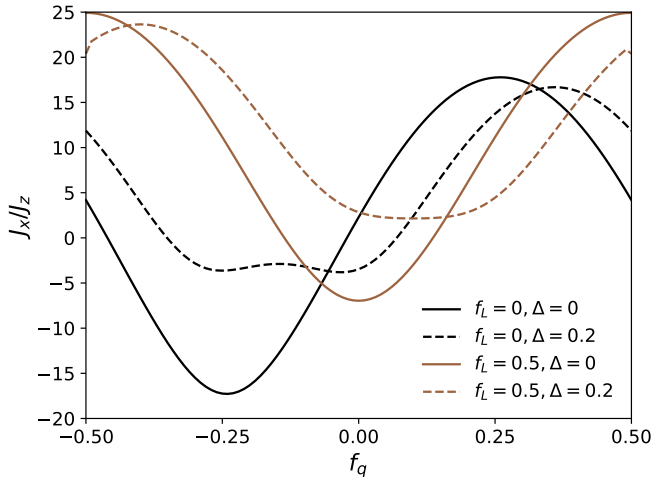


Figure 3.7: The ratio of the XXZ coupling strengths as a function of the fluxes in the circuit. Parameters are taken from Table 3.1.

Notice that the curves very closely resemble simple cosine function when the circuit is symmetric,  $\Delta = 0$ . When asymmetry is introduced, the minima are flattened out. A local flat curve reduces the need to fine-tune  $f_q$  to obtain a specific value of  $J_x/J_z$ . For instance, with  $\Delta = 0.2$  (the dashed curves), we can very precisely tune  $J_x/J_z$  from around  $-4$  to  $3$  by following the flat minimum as  $f_L$  goes from  $0$  to  $0.5$ . This allows for an XXZ model with both positive and negative relative sign of the coupling strengths (and hence also an Ising model at  $J_x/J_z = 0$ ). We may even achieve an XX model by following the curves to their maxima, where  $J_x/J_z \sim 17-24 \gg 1$ , without changing the asymmetry parameter  $\Delta$ .

As mentioned above,  $J_x/J_z$  as a function of  $f_q$  resembles cosine functions. This behavior must stem from the cosines in the potential,

$$U(x, y) = \alpha_q E_q [\cos(x - 2\pi f_q) + \cos(y - 2\pi(f_q - \Delta))] + \text{terms independent of } f_q. \quad (3.41)$$

Each variable  $x$  and  $y$  is associated with a qubit degree of freedom, and each cosine account for a part of the energy of that qubit (compare with the second term in Eq. (3.27)). Considered as a function of

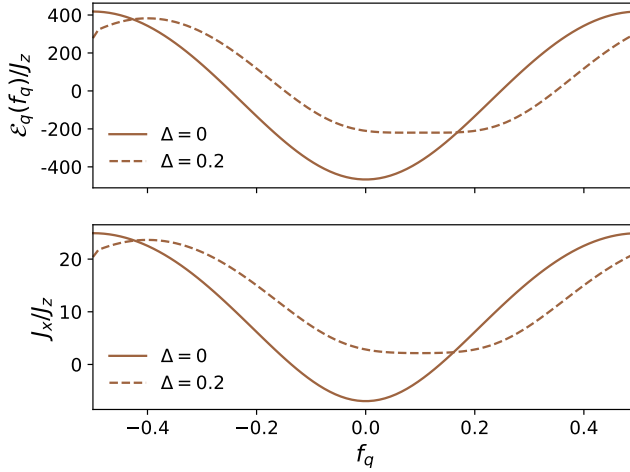


Figure 3.8: Comparison between the total qubit energy (upper) and XX coupling strength  $J_x$  (lower) for  $f_L = 0.5$ .

$f_q$ , the sum of cosine terms above expresses the total energy of the two C-shunted flux qubits (up to an additional constant). Since it is assumed that  $(x, y)$  is close to the minimum of the potential, denoted  $(x_0, y_0)$ , an approximate expression for the qubit energy is

$$\mathcal{E}_q(f_q) = \alpha_q E_q [\cos(x_0 - 2\pi f_q) + \cos(y_0 - 2\pi(f_q - \Delta))] , \quad (3.42)$$

The minimum  $(x_0, y_0)$  is found numerically, but an analytic approximate expression can also be derived.

In Figure 3.8 we compare the qubit energy and the strength of the XX coupling,  $J_x$ . Remarkably, the qubit energy and XX coupling are, up to a constant shift and scaling, almost indistinguishable. This can be justified by the following crude consideration: As can be seen from the full circuit analysis not presented here, both the qubit energies and the  $J_x$  coupling are related to the second derivatives of the potential, i.e.  $d^2U/dx^2$ ,  $d^2U/dy^2$  and  $d^2U/dxdy$ . It is not surprising that these derivatives (and hence the qubit energies and  $J_x$ ) scale similarly, and differently from  $J_z$  which scales with the fourth order derivatives.

The qubit energy  $\mathcal{E}_q$  scales linearly with  $\alpha_q$  and  $E_q$ . With the connection  $\mathcal{E}_q \sim J_x$  in mind, we wish to see if  $J_x$  scales in the same

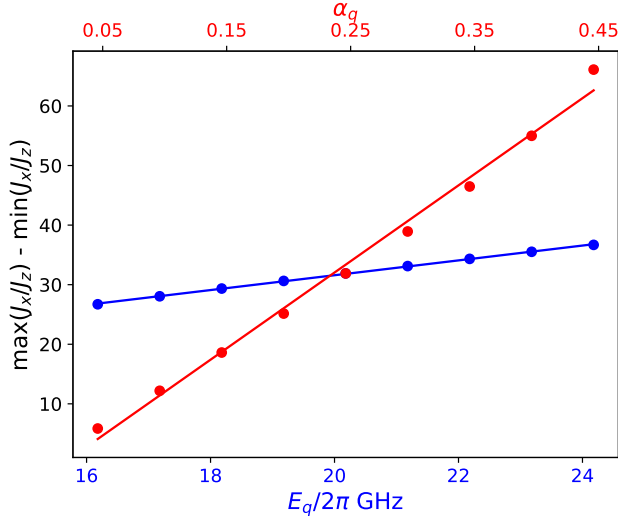


Figure 3.9: The width of the  $J_x/J_z$  curve for  $f_L = 0.5$  and  $\Delta = 0$  (i.e. the solid brown curve in Figure 3.7) scales linearly with  $\alpha_q$  and  $E_q$ . Dots are data points, lines are linear fits to the data.

way. We vary  $\alpha_q$  and  $E_q$ , one at a time, and find the width of the  $J_x/J_z$  curve (its maximum value minus its minimum value). As is evident from Figure 3.9,  $J_x/J_z$  scales linearly with both parameters.

Apart from the scaling of the width of the  $J_x/J_z$  curve with  $\alpha_q$  and  $E_q$ , we note the following trends when varying these two parameters.

Firstly, when  $\alpha_q$  is increased,  $J_x/J_z$  is allowed to take both larger positive and negative values. Thus the value of  $\alpha_q$  determines the overall tunability of the gate. A small  $\alpha_q$  ensures that variations in the fluxes does not drastically alter  $J_x/J_z$  and thereby setting aside the need to precisely control the fluxes to obtain a certain parameter ratio. An example with  $\alpha_q = 0.1$  can be seen in Figure 3.10, notice especially the scale compared to Figure 3.7. On the other hand, a large  $\alpha_q$  allows for very large values of  $J_x/J_z$  and hence surely the XX model. Above a certain threshold, it is even possible to get diverging parameter values, as seen in Figure 3.11. This behavior is in stark contrast to the simple relation  $\mathcal{E}_q \sim J_x$  suggested earlier, hence proving that there is more to  $J_x$  than just a one-to-one correspondence with the qubit energies. One might think that the divergence of  $J_x/J_z$  is caused by

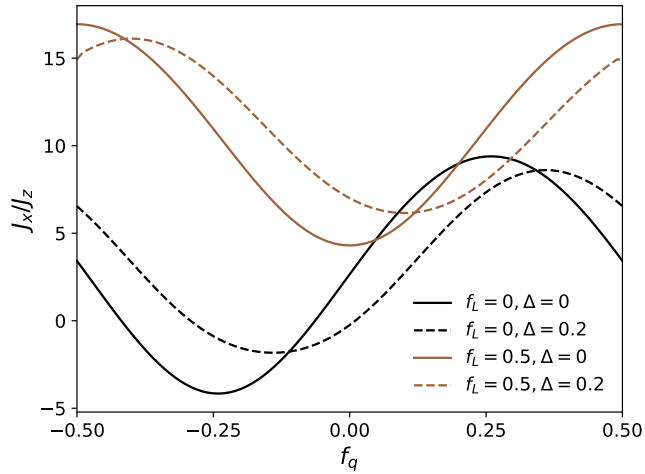


Figure 3.10: Same as Figure 3.7, but with  $\alpha_q = 0.1$ . The remaining parameters are taken from Table 3.1.

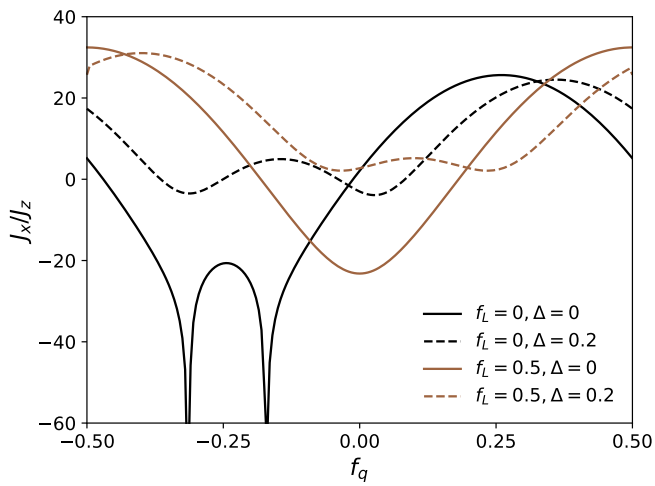


Figure 3.11: Same as Figure 3.7, but with  $\alpha_q = 0.4$ . The remaining parameters are taken from Table 3.1.

$J_z$  going towards zero, but this is not the case, as  $J_z$  remain nearly constant. Specifically we note that  $J_z/(2\pi) = (22.5 \pm 2.5)\text{MHz}$  in both Figure 3.10 and Figure 3.11. In fact, all parameters remain suitable for experimental realization. The only parameter which could potentially be worrisome is  $E_{J,i}/E_{C,i}$  whose minimum value decreases with increasing  $\alpha_q$ . However, we find  $E_{J,i}/E_{C,i} > 63.6$  for  $\alpha_q = 0.4$ , which should cause no serious trouble.

Secondly, when  $E_q$  is varied, the width of the  $J_x/J_z$  scales accordingly. Increasing  $E_q$  results in a scaling and a shift upwards along the ordinate, thereby reducing the possibility for negative values of  $J_x/J_z$ , but increasing the maximum value. Since the shape of the curves are unchanged, the effect of picking a different  $E_q$  is rather uninteresting, and we do not go into further investigations. But we do note that all experimental parameters are feasible over the range of  $E_q$  shown in Figure 3.9, so should we wish so, picking another  $E_q$  can be used to restrict or increase the range of  $J_x/J_z$ .

### 3.7.4 Conclusion and outlook

As we have seen, the fluxes permit a very large degree of tunability of  $J_x$ , and we can reach a variety of XXZ models including limiting cases such as the XX model and Ising model. On the other hand,  $J_z$  is nearly constant, which is fine as long as we consider a single two-qubit gate where the ratio  $J_x/J_z$  is enough to determine the physics. However, if we were to couple several two-qubit systems together, it would be advantageous to be able to tune  $J_z$  also, and for instance create a chain where the ZZ couplings vary along the chain for quantum annealing. Unfortunately, simulations indicate that the parameter space of the model considered here only permits limited tunability of the ZZ coupling. In fact, even when we allowed  $E_{J,i}/E_{C,i}$  to be as low as 15, all the acceptable parameter sets only allowed  $J_z/(2\pi)$  to be tuned over a range of approximately 10 MHz. In fact, all parameter sets considered resulted in  $J_z/(2\pi) = -(25 \pm 10)\text{MHz}$ , which seems to be inherent of the model.

## 3.8 Programmatic chip design with SonPy

Despite the power of the lumped element model in classical circuit theory, it does not capture stray magnetic fields, non-homogeneous accumulation of charge or three-dimensional effects present on the

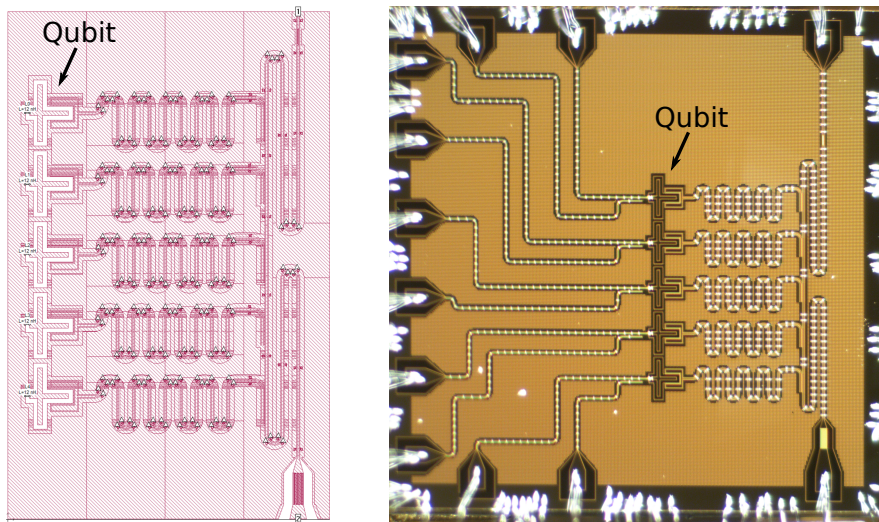


Figure 3.12: Superconducting chip designed using SonPy: Blueprint in the Sonnet GUI (left) and microscope picture of the final product (right). The chip contains five cross-shaped Xmon qubits (similar to transmons) with control lines to the left, coupled with resonators to a readout line to the right. Image by courtesy of Roni Winik.

actual chip. Therefore, it is often a good idea to simulate the chip design by numerically solving a discretized version of Maxwell's equations before it is manufactured in the clean-room. Thus, numerical simulations are a vital part of the chip design, and dedicated microwave simulation software has been developed. In this section, I will report on a software package named SonPy[10], that I developed during my stay at the Engineering Quantum Systems (EQuS) group at Massachusetts Institute of Technology in 2018, in order to automate the chip simulation process. SonPy is now in active use in the group, making the process of designing new chips easier and less time-consuming. An example of a chip designed using SonPy is shown in Figure 3.12.

In short, SonPy is an open source Python package that allows the user to control the commercial microwave simulation software, Sonnet. The name 'SonPy' is a contraction of 'Sonnet' and 'Python'. The package enables the user to set up simulations, change parameters,

start the simulation and retrieve data using nothing but a Python script – tasks that would otherwise have been done manually in the Sonnet GUI. While the geometric layout of the chip can be designed manually in Sonnet, the power of automation is fully unleashed if the chip is programmatically designed, for instance using the Python package ‘gdspy’ producing a GDSII file containing the layout. This combines chip design and simulation in a single Python script, allowing the user to iterate on the design based on the simulation results.

Consider this simple example: Suppose we wish to design a filter for a certain microwave frequency, using a resonator. Attaching ports to each end of the resonator, we input microwaves sweeping a range of frequencies and measure the amplitude of the transmitted signal at the output port, from which the resonance frequency can be determined. This experiment can be simulated in Sonnet. The resonance frequency and quality of the filter depend on the layout of the resonator, parameterized in e.g. the length and width of the resonator, whose numerical values can be changed in the Python script. In order to find the resonator length that produces the desired resonance frequency, we may construct a Python script with the following workflow:

1. gdspy: Create an initial parameterized chip design.
2. gdspy: Export the design as a GDSII file.
3. SonPy: Convert the GDSII file to a Sonnet project file (employs Sonnet’s own translator).
4. SonPy: Define the physical properties of the chip, such as setting metal properties and adding port. It is also possible to add lumped elements, define several metal and insulating layers and air bridges.
5. SonPy: Set up the simulation by specifying the frequency range and measurement parameters (e.g. the amplitude of the transmitted signal).
6. SonPy: Update the Sonnet project file with the changes made with SonPy and run the simulation (employs Sonnet’s simulator).

7. SonPy: When the simulation has completed, extract the data (signal amplitude vs. input frequency).
8. From the data we determine the resonance frequency and update the resonator length in step 1. We iterate this process until the resonance frequency has the desired value.

Since many aspects of Sonnet can be accessed through SonPy's functions, there is no need to open the Sonnet GUI, saving a lot of manual point-and-click labor. In the programmatic approach, standard metallic and dielectric properties of the chip materials can be set with a single function call, and elements such as ports and air bridges can be placed automatically at the desired locations if the chip layout is properly parameterized. Furthermore, microwave simulations can take from a few minutes to several hours. Automating the process of tweaking the design parameters as described above relieves the user to be around and wait for the simulation to complete, before the next manual iteration can take place.

The SonPy source code, extensive documentation and examples are available on GitHub[10].

---

# Quantum computing and four-qubit diamond gate

*I will begin this chapter by reviewing quantum computing, and then give a presentation of the proposal for a four-qubit gate from Ref. [8] and a brief account of the gate scheme proposed in Ref. [7].*

The diamond model shown in Figure 3.5 in the previous chapter was developed in order to operate as a quantum transistor using superconducting qubits. However, as I mentioned earlier, the continued research into the model revealed two remarkable facts: Firstly, that the model and superconducting circuit design could be greatly simplified, and secondly, that the computational capabilities far exceeded the quantum transistor functionality. From the point of view of *gate based quantum computing*, the improved diamond model realizes a four-qubit quantum gate.

## 4.1 Quantum computing

The basic computational quantity in a classical computer is a bit, which has two possible states: 0 and 1. Quantum computing is derived by considering the case where the bit is made a quantum object – a quantum bit or *qubit* – described by a quantum state,

$$|\psi\rangle = \alpha |0\rangle + \beta |1\rangle , \quad (4.1)$$

where  $|0\rangle$  and  $|1\rangle$  are orthonormal states, and  $\alpha$  and  $\beta$  complex coefficients fulfilling the normalization condition,  $|\alpha|^2 + |\beta|^2 = 1$ . In contrast to a classical bit, a qubit has an infinite amount of valid states as it requires two real numbers to fully specify its state (four reals from the complex coefficients; subtract one for the normalization condition and one for an immeasurable global phase).

Most classical computers today run on a 64-bit architecture, which means that they typically store the basic units of information, such as integers, in a string of 64 bits:  $0110 \cdots 10$ . The quantum version of a bit string is a multi-qubit state,  $|0110 \cdots 10\rangle$ , understood as a tensor product of single-qubit states. For instance, for a two-qubit register the computational space is the four-dimensional Hilbert space spanned by the two-qubit states  $|00\rangle$ ,  $|01\rangle$ ,  $|10\rangle$  and  $|11\rangle$ . For  $N$  qubits, the Hilbert space is  $2^N$ -dimensional, supporting states on the form

$$\begin{aligned} |\Psi\rangle &= \sum_{x=0}^{2^N-1} \alpha_{\tilde{x}} |\tilde{x}\rangle \\ &= \alpha_{0 \cdots 00} |0 \cdots 00\rangle + \alpha_{0 \cdots 01} |0 \cdots 01\rangle + \cdots + \alpha_{1 \cdots 11} |1 \cdots 11\rangle, \end{aligned} \quad (4.2)$$

where  $\tilde{x}$  denotes the binary form of  $x$ , and the complex coefficients normalizes the state,  $\sum_{x=0}^{2^N-1} |\alpha_{\tilde{x}}|^2 = 1$ . Thus, the size of the computational space increases exponentially with the physical resources, i.e. the number of qubits.

#### 4.1.1 Quantum logic gates

Classical computations are performed by manipulating bit strings into other bit strings. These bit-manipulating operations are performed as series of simple logic gate operations on a few bits at a time. Gate based quantum computing takes this approach into the quantum realm. A striking difference between classical logic gates and quantum logic gates is the requirement that quantum gates, being quantum operators on a Hilbert space, must be unitary operators, and hence reversible, with the same number of input and output qubits. Hence, some common classical gates, such as the AND or OR gate which have two input bits and one output bit, do not have a quantum analogue. However, non-unitary is present in the form of qubit readout (measurements), and in the hardware implementations as couplings to the environment causing decoherence and finite

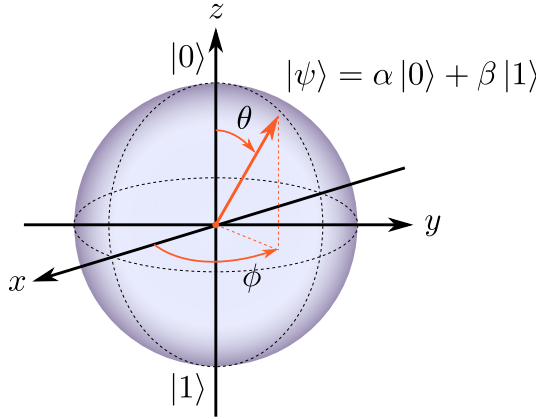


Figure 4.1: Bloch sphere picture of a single-qubit state.

qubit lifetimes. Usually, the qubits are screened from the environment as much as possible in order to avoid decoherence, although some scientists have proposed using highly dissipative qubits as an advantage[136], e.g. as an excitation sink.

Let us first consider quantum gates on a single (coherent) qubit. Since the overall phase of  $|\psi\rangle$  is physically irrelevant, the single-qubit state of Eq. (4.1) can be parameterized as

$$|\psi\rangle = \cos \frac{\theta}{2} |0\rangle + e^{i\phi} \sin \frac{\theta}{2} |1\rangle, \quad (4.3)$$

with  $0 \leq \theta \leq \pi$  and  $0 \leq \phi < 2\pi$ . Thinking of  $\theta$  and  $\phi$  as a polar and azimuthal angle, respectively, the qubit state can be mapped to point on a unit sphere, known as the Bloch sphere, as illustrated on Figure 4.1.

In order to perform arbitrary quantum computations, one must be able to change the initial qubit state  $|\psi\rangle$  into an arbitrary final state  $|\psi'\rangle$ . This can be accomplished by rotating the vector  $|\psi\rangle$  on the Bloch sphere to the position of the final state. As a unitary transformation, this can be expressed as

$$|\psi'\rangle = e^{i\gamma} R_{\hat{n}}(\Theta) |\psi\rangle, \quad (4.4)$$

where  $\gamma$  is some angle, and  $R_{\hat{n}}(\Theta)$  is a rotation about the unit vector  $\hat{n}$  by the angle  $\Theta$ . Parameterizing  $\hat{n} = (\sin \Xi \cos \Phi, \sin \Xi \sin \Phi, \cos \Xi)$  in a polar angle  $\Xi$  and an azimuthal angle  $\Phi$ , the rotation can be

decomposed into rotations about the Cartesian axes:

$$R_{\hat{n}}(\Theta) = \underbrace{R_z(\Phi)R_y(\Xi)}_{\text{rotate } \hat{n} \text{ back}} \underbrace{R_z(\Theta)}_{\text{rot. about } \hat{n}} \underbrace{R_y(-\Xi)R_z(-\Phi)}_{\text{align } \hat{n} \text{ with } z \text{ axis}} . \quad (4.5)$$

Rotations of angle  $\Theta$  about the Cartesian axes of the Bloch sphere are given by

$$R_x(\Theta) = e^{-i\frac{\Theta}{2}\sigma_x} , \quad (4.6)$$

$$R_y(\Theta) = e^{-i\frac{\Theta}{2}\sigma_y} , \quad (4.7)$$

$$R_z(\Theta) = e^{-i\frac{\Theta}{2}\sigma_z} , \quad (4.8)$$

which are unitary transformations generated by the Pauli matrices:

$$\sigma_x \equiv X = |1\rangle\langle 0| + |0\rangle\langle 1| , \quad (4.9)$$

$$\sigma_y \equiv Y = i|1\rangle\langle 0| - i|0\rangle\langle 1| , \quad (4.10)$$

$$\sigma_z \equiv Z = |0\rangle\langle 0| - |1\rangle\langle 1| . \quad (4.11)$$

Eq. (4.5) shows that any unitary single-qubit operation can be performed as a series of more manageable gate operations (rotations about the  $z$  and  $y$  axes). In quantum circuit notation, the gate sequence is written as

$$|\psi\rangle \text{ --- } \boxed{R_z(-\Phi)} \text{ --- } \boxed{R_y(-\Xi)} \text{ --- } \boxed{R_z(\Theta)} \text{ --- } \boxed{R_y(\Xi)} \text{ --- } \boxed{R_z(\Phi)} \text{ --- } |\psi'\rangle \quad (4.12)$$

Notice that the gates are applied from left to right, which is the reverse order compared to the matrix product in Eq. (4.5).

In order to perform any desired quantum computation, one has to be able to perform arbitrary unitary operations  $U$  on  $N$  qubits. This is in general not a simple task and the resulting state may be highly entangled. However, the implementation of  $U$  can be broken down into simpler gates that only operate on a few qubits at a time, analogous to the way a classical computer runs a complicated algorithm as a series of simple logic gates. It turns out that single-qubit gates supplemented with a two-qubit entangling gate provides the necessary computational complexity [137, 138]. Such a gate set is known as a *universal* gate set, as it allows for the construction of any  $U$ . One example of a two-qubit entangling gate is the ‘controlled-not’ gate,

$$\text{CNOT} = |00\rangle\langle 00| + |01\rangle\langle 01| + |11\rangle\langle 10| + |01\rangle\langle 11| , \quad (4.13)$$

which flips the second qubit (a ‘not’ operation) only if the first qubit is in  $|1\rangle$ . For this reason, the first qubit is called the control qubit, and the second qubit is called the target qubit. It is an entangling gate because it can create an entangled state from a product state:

$$\text{CNOT} \underbrace{\frac{1}{\sqrt{2}}(|0\rangle + |1\rangle)}_{\text{product state}} |0\rangle = \underbrace{\frac{1}{\sqrt{2}}(|00\rangle + |11\rangle)}_{\text{not a product state}} . \quad (4.14)$$

Thus, the CNOT combined with single-qubit rotations constitute a universal gate set. In gate circuit notation, the gate is expressed as

$$\text{CNOT} = \begin{array}{c} \text{---} \bullet \text{---} \\ | \\ \text{---} \oplus \text{---} \end{array} \quad (4.15)$$

The black dot on the first qubit wire denotes that the first qubit controls the ‘not’ operation ( $\oplus$ ) on the second qubit. Since a ‘not’ operation is identical to the Pauli X gate of Eq. (4.9), we can also think of the CNOT as a controlled-X:

$$\text{CNOT} = \begin{array}{c} \text{---} \bullet \text{---} \\ | \\ \text{---} \boxed{X} \text{---} \end{array} \quad (4.16)$$

The CNOT is not the only two-qubit entangling gate that may be picked for a universal gate set. Another choice is the ‘controlled-phase’ gate, also known as a controlled-Z or simply CZ,

$$\text{CZ} = |00\rangle\langle 00| + |01\rangle\langle 01| + |10\rangle\langle 10| - |11\rangle\langle 11| , \quad (4.17)$$

which changes the sign on the  $|11\rangle$  state with respect to the other computational states. Due to the symmetry of the operation, either qubit can be considered the control qubit or the target qubit, and it is thus given a symmetric symbol:

$$\text{CZ} = \begin{array}{c} \text{---} \bullet \text{---} \\ | \\ \text{---} \bullet \text{---} \end{array} \quad (4.18)$$

In order to show that the choice of CZ in the universal gate set is equivalent to CNOT, consider the single-qubit Hadamard gate,

$$\text{H} = \frac{1}{\sqrt{2}}(X + Z) = \frac{1}{\sqrt{2}}(|0\rangle\langle 0| + |0\rangle\langle 1| + |1\rangle\langle 0| - |1\rangle\langle 1|) , \quad (4.19)$$

which is useful for creating superposition states. The CNOT gate can be decomposed into two Hadamard gates and a CZ gate:

$$\begin{array}{c} \bullet \\ | \\ \oplus \end{array} = \begin{array}{c} \bullet \\ | \\ \text{H} \bullet \text{H} \end{array} \quad (4.20)$$

The CNOT and CZ are considered equivalent because they only differ by Hadamard gates, which can be constructed from the single-qubit gates in the gate set. Here the Hadamard gates are applied to the second qubit only, so if we wanted to write this as an operator or matrix equation, we should apply an identity operation on the first qubit like so:  $\text{CNOT} = \text{I} \otimes \text{H} \cdot \text{CZ} \cdot \text{I} \otimes \text{H}$ , with  $\text{I} \otimes \text{H}$  being the tensor product of the identity  $\text{I}$  and  $\text{H}$ . The equality can be shown with a straight-forward computation using the Dirac bracket expressions for the involved gates.

One final two-qubit gate worth mentioning is the SWAP gate,

$$\text{SWAP} = |00\rangle\langle 00| + |10\rangle\langle 01| + |01\rangle\langle 10| + |11\rangle\langle 11| , \quad (4.21)$$

which exchanges the states of the two qubits. This gate is neither a controlled operation, since both qubits are changed, nor an entangling gate, as product states are transformed into product states:

$$\text{SWAP} |\psi\rangle |\psi'\rangle = |\psi'\rangle |\psi\rangle , \quad (4.22)$$

for single-qubit states  $|\psi\rangle$  and  $|\psi'\rangle$ . It is denoted by

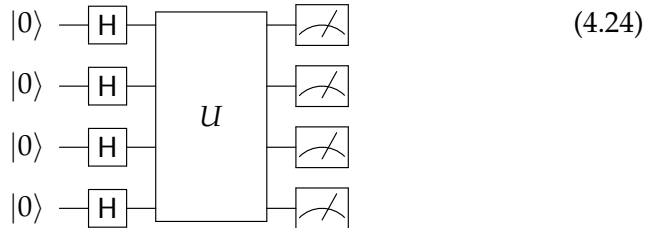
$$\text{SWAP} = \begin{array}{c} \times \\ | \\ \times \end{array} \quad (4.23)$$

The concept of quantum gates can be generalized to an arbitrary number of qubits, however, they can always be expressed in terms of two- and one-qubits gates from a universal gate set. Useful three-qubit gates can be constructed as controlled two-qubit gates, such as the CSWAP gate (Fredkin gate), which performs a SWAP gate on two target qubits controlled by a third (control) qubit. Another three-qubit gate is the CCNOT gate (Toffoli gate), which applies a 'not' operation on a target qubit only if both control qubits are in the  $|1\rangle$  state.

My goal here is not to give a comprehensive introduction to even the most common quantum gates. For this, I refer to textbooks such as Ref. [139] by Nielsen and Chuang or Ref. [140] by Mermin. Rather, I want to showcase some notation in the field and demonstrate how one can perform calculations with quantum gates.

### 4.1.2 Quantum algorithms

A typical quantum algorithm has the following structure:



First, all qubits are initialized in the  $|0\rangle$  state. Then, a Hadamard gate is applied to each qubit, creating an even superposition of all  $2^4 = 16$  computational states,

$$\text{HHHH } |0000\rangle = (\text{H } |0\rangle)(\text{H } |0\rangle)(\text{H } |0\rangle)(\text{H } |0\rangle) \quad (4.25)$$

$$= \frac{1}{4}(|0\rangle + |1\rangle)(|0\rangle + |1\rangle)(|0\rangle + |1\rangle)(|0\rangle + |1\rangle) \quad (4.26)$$

$$= \frac{1}{4}(|0000\rangle + |0001\rangle + |0010\rangle + \dots + |1111\rangle) \quad (4.27)$$

This puts us in a position to harvest the advantages of computing with superposition states unique to quantum computing. The bulk of the algorithm is the unitary operator  $U$ , which acts on the superposition above, distributing the transformation of  $U$  onto each computational state:  $(1/4)(U|0000\rangle + U|0001\rangle + \dots + U|1111\rangle)$ . This is sometimes referred to as parallelism in quantum computer. However, it should be noted that this type of parallelism is very different from classical parallel computing, where tasks can be distributed among several cores. In a quantum computing, the parallelism does not give the user access to results computed in parallel; rather the parallel results are kept in one big coherent quantum state. Only when the individual qubits are measured in the computational basis, as denoted by a measurement apparatus above, do we gain any knowledge of the result of the computation. Each computational state corresponds to a possible measurement outcome – a classical bit string – and it requires a great deal of ingenuity to design  $U$  in such a way that we measure the desired result with a probability of 100%. It is a matter of engineering interference between the computational states to ensure that the amplitudes of unwanted outcomes are diminished and the amplitudes of the desired outcomes are amplified.

The core of the algorithm is  $U$ , which in general is a highly specialized many-body operation that cannot be implemented ‘as is’ on the quantum computing hardware. However, assuming we have access to a universal gate set like CNOT and single-qubit operations, we can implement  $U$  as a series of  $m$  operations from this gate set  $U = U_m \cdot U_{m-1} \cdots U_2 \cdot U_1$ . Decomposing  $U$  into a suitable product is known as the quantum compilation problem, and it depends highly on the available gates in the quantum computing hardware[141–143].

### 4.1.3 Advantages

Quantum mechanics brings distinctive non-classical features to the field of computing, such as superpositions and entanglement. This enables quantum algorithms to solve certain problems more efficiently than their classical counterparts. An early example is Deutsch’s algorithm[144], originally published in 1985, and later improved[145, 146]. The algorithm determines whether an unknown function, that takes an  $N$ -bit string and produces a single-bit output, is constant (returns only 0 or 1) or balanced (returns 0 and 1 equally often). Deutsch’s algorithm has a provable exponential speed-up compared to any deterministic classical algorithm in the sense that the number of function evaluations scales more favorably with the problem size,  $N$ . This demonstrated that quantum mechanics could lead to exponentially faster computers, serving as the main motivation for continued research and development in the field.

Deutsch’s problem was constructed in order to be easier for a quantum computer to solve than for a classical computer. As a consequence, the problem itself is of limited practical use. The debate of whether real-world applications of a quantum computer existed was put to rest in 1994, where a prime-factorization algorithm was proposed by Shor[147]. Shor’s algorithm provides an almost exponential speed-up compared to any known classical algorithm, thereby posing a theoretical threat to encryption schemes based on products of large prime numbers, such as RSA encryption.

Shortly after, in 1996, Grover gave the quantum computer another useful application: database search[148, 149]. Grover’s algorithm exploits quantum amplitude amplification to find a specific element in an  $N$ -item database with  $O(\sqrt{N})$  queries to the database. The worst case scenario for any classical algorithm is when the correct element is looked up last, yielding  $O(N)$  queries.

In general, guaranteed quantum speed-up is difficult to prove. For instance, in the case of Shor's algorithm, a classical prime-factorizing algorithm solving the problem more efficiently can in principle be discovered in the future. This scenario did in fact occur for Kerentidis and Prakash's quantum recommendation system algorithm[150], which is a quantum machine learning algorithm. When the algorithm was published in 2016, it provided an exponential speed-up compared to any known classical algorithm. However, in 2018, Tang demonstrated a classical algorithm with only polynomially slower run-time, thereby denying the quantum algorithm its promised exponential speed-up[151]. Tang 'de-quantized' the algorithm in question by replacing quantum state preparation assumptions by classical stochastic sampling, thereby arriving at a quantum-inspired classical algorithm. Immediately after, the same technique was used[152, 153] to de-quantize quantum principal component analysis[154], quantum supervised clustering[155] and quantum matrix inversion[156], and it may leave a lasting impact on the field of quantum machine learning.

If a quantum algorithm is truly superior to any classical algorithm, the advantage must be traced back to inherently quantum mechanical effects. Bravyi, Gosset and Koenig did so in 2018, where they showed that quantum non-locality provided a computational advantage when solving a linear algebra problem known as the 2D hidden linear function problem[157]. Furthermore, they showed this result under the restriction that the quantum gate circuit is shallow, meaning that the number of successively applied gates must not increase with the problem size. This restriction was included in order to model the limits of current or near-future quantum computers, where system decoherence and finite qubit lifetimes prevent us from running long algorithms. Indeed, in order to fairly compare the computational capabilities between a quantum and a classical computer, we must take into account the physical limits of today's hardware.

#### 4.1.4 Challenges

As argued above, quantum computing does provide a computational advantage above classical computers. However, building a quantum computer is a hard task. DiVincenzo boiled down the necessary requirements for gate based quantum computing to five criteria, which I quote from Ref. [158]:

1. A scalable physical system with well characterized qubits.
2. The ability to initialize the state of the qubits to a simple fiducial state, such as  $|000\cdots\rangle$ .
3. Long relevant decoherence times, much longer than the gate operation time.
4. A ‘universal’ set of quantum gates.
5. A qubit-specific measurement capability.

Several architectures have been demonstrate to fulfill DiVincenzo’s criteria for a few qubits, most promisingly trapped cold ions and superconducting circuits. A major challenge lies in the first criteria – scalability – as the amount of necessary experimental control escalates when adding more qubits. Notice for instance the amount of wires on the five-qubit superconducting chip in Figure 3.12. Efforts can be made in order to couple several qubits to the same resonator, however, frequency crowding will at some point set a limit. So, while superconducting chips with  $\sim 10$ –70 qubits have be produced, one sacrifices qubit control compared to few-qubit devices.

Indeed, the number of qubits in itself is a poor measure for the computational capability of the quantum computer. A more sophisticated measure was proposed in 2017 by Bishop *et al.*, named the ‘quantum volume’[159]. It is a hardware-agnostic measure that tries to capture many factors that determine the computational power of a quantum computer, including:

1. The number of qubits.
2. The natively available gates.
3. The connectivity of the qubits; say, whether it is possible to perform operations between two arbitrary qubits.
4. The amount of possible parallelization of gates.
5. The number of gates that can be run consecutively before the computation is lost to decoherence.

One major limiting factor is the final point on the list above: the number of consecutive gates that can be run. This is determined by

the qubit lifetime compared to the gate operation time, and by the gate error.

Increasing the qubit lifetime is an everlasting struggle due to the frail nature of quantum coherence. For trapped ions and superconducting qubits, the lifetimes are  $\sim 50$ s and  $\sim 50\mu$ s, respectively[111]. A great deal of progress has been made on the hardware level in order to improve coherence times, but since the qubits cannot be completely screened from the environment – partly because we need to control and measure them – errors will occur. To combat this, several error correction schemes have been proposed[160–165]. This is analogous to classical error correction, where several physical bits comprise a single logical bit. Should a bit-flip error occur on one bit, it can be corrected using a ‘majority rule’ type of error correction. However, since even a slightly drifted, erroneous qubit state is a valid qubit state on the Bloch sphere, quantum error correction is much harder, typically requiring a large number of physical qubits in order to create one error-corrected logical qubit. Furthermore, when a single logical qubit consists of several physical qubits, it alters the way gate operations are performed, and performing a certain gate on each physical qubit cannot in general be expected to produce the corresponding gate on the logical qubit[166, 167].

The qubit lifetimes mentioned above should be compared with the time it takes to run a two-qubit gate. For trapped ions and superconducting qubits, these are  $\sim 50\mu$ s and  $\sim 50$ ns, respectively[111]. This produces a ‘gates per qubit life’ of  $10^6$  and  $10^3$ , respectively, although the actual number of gates that can be run successfully is much lower, as errors built up due to imperfect gate operations. However, a fault-tolerant architecture, i.e. where qubit errors do not cascade and corrupt the computation, can be achieved if the gate errors are kept below a certain threshold. For the promising error correcting surface codes, the threshold is around 0.01, i.e. requiring gate fidelities to be 0.99[168–171].

While single-qubit gates are routinely performed with fidelities  $F_{1\text{qb}} > 0.99$ [112–118, 172–175], it remains a challenge to achieve the same numbers for two-qubit gates. Nonetheless, several groups have reported doing so. In 2008, Benhelm *et al.* realized a Mølmer-Sørensen-type entangling gate[176, 177] in trapped calcium ions with a fidelity  $F_{2\text{qb}} = 0.993$ [178]. Since then, a range of high-fidelity two-qubit gates have been demonstrated in ion traps[179–183]. In superconducting qubits two different two-qubit gates have been

implemented with fidelities exceeding 0.99: the controlled-phase gate[118–122] and the cross-resonance gate[123], which is also a controlled one-qubit operation. Other superconducting two-qubit gates with fidelities in the 0.9's are the parametric controlled-phase gate[114, 184], the resonator induced phase gate[185], the *b*SWAP gate[186] and the *i*SWAP gate[114, 184, 187–189].

Whether the quantum computing community will overcome the challenges and build a universal, scalable, fault-tolerant quantum computer is still an open question. Another open question is whether it will be able to beat a classical computer by solving a problem that even the best classical computer cannot solve. And finally, it is an open question whether this problem will be of any practical relevance.

One thing is for certain; prime-factorization using Shor's algorithm will not be the first practical application of quantum computers, as it is estimated that it requires over a million qubits to factorize cryptographically relevant integers[111]. Rather, the first real-world applications will most likely run on the noisy, intermediate scale quantum computers of today and the near-future, using hardware devices optimized for certain tasks. One example of usage is quantum chemistry, for instance using a variational quantum eigensolver to find the ground states of molecules, something that has been demonstrated for small molecules[190].

## 4.2 Four-qubit diamond gate

We now return to the system of four qubits coupled in a diamond pattern discussed in Section 3.6. This model came about as a way to implement the quantum transistor, but we realized that we could drop the expensive XXZ coupling and at the same time control a much more sophisticated gate operation. In this section, I report on this work [8], which we recently submitted for publication in npj Quantum Information. The original diamond model of Section 3.6 was developed by Lasse B. Kristensen, Christian K. Andersen, Nikolaj T. Zinner and I. I lead the four-qubit gate project, including proposing the superconducting circuit, deriving the effective Hamiltonian and the corresponding unitary gates, performing numerical simulations and writing the manuscript. LBK found a method for suppressing state leakage via engineered crosstalk. During my visit to the group of William D. Oliver and Simon Gustavsson, I discussed the experi-

mental realization with Morten Kjaergaard with contributions from Thorvald W. Larsen. While writing the manuscript, I had many helpful discussions with Morten Kjaergaard and others. All authors commented on the manuscript. The remainder of this section is quoted from Ref. [8] Secs. II–III with minor changes to fit the context here.

### 4.2.1 System and unitary gates

Consider the four-qubit Hamiltonian being a sum of the non-interacting part

$$H_0 = -\frac{1}{2}(\Omega + \Delta)(\sigma_z^{T1} + \sigma_z^{T2}) - \frac{1}{2}\Omega(\sigma_z^{C1} + \sigma_z^{C2}), \quad (4.28)$$

where  $\Omega + \Delta$  ( $\Omega$ ) is the fixed frequency of the target (control) qubits, and the interaction terms

$$H_{\text{int}} = J_C \sigma_y^{C1} \sigma_y^{C2} + J(\sigma_y^{T1} + \sigma_y^{T2})(\sigma_y^{C1} + \sigma_y^{C2}). \quad (4.29)$$

Here  $\sigma_z^j = |0\rangle\langle 0|_j - |1\rangle\langle 1|_j$  and  $\sigma_y^j = i|1\rangle\langle 0|_j - i|0\rangle\langle 1|_j$  are Pauli operators on qubit  $j$ , and the qubit frequencies are assumed positive such that  $|0\rangle_j$  is the non-interacting qubit ground state. For simplicity we have assumed that the two target (control) qubits are on resonance, and that all the couplings between the target and control qubits have the same strength  $J$ , although, as we will show later, this constraint is not needed for high performance of the gate. The four-qubit system is sketched in Figure 4.2a. As we will discuss in the following, the system implements a four-qubit gate, which we will refer to as ‘the diamond gate’ due to the geometry of the system.

Superconducting circuits offer a natural platform for implementing this type of Hamiltonian[107]. Specifically, by truncating the Hilbert space for each degree of freedom to qubits, the circuit of four capacitively coupled transmon qubits in Figure 4.2b implements the Hamiltonian. Later, we analyze the model including the second excited state of the transmon qubits.

We now consider the interaction Hamiltonian,  $H_{\text{int}}$ , in the frame rotating with  $H_0$  and simplify the expression by assuming  $|2\Omega| \gg |J|$  (rotating wave approximation), which allows us to ignore the most rapidly oscillating terms. The system Hamiltonian is then

$$H = J_C \sigma_+^{C1} \sigma_-^{C2} + J e^{i\Delta t} (\sigma_+^{T1} + \sigma_+^{T2})(\sigma_-^{C1} + \sigma_-^{C2}) + \text{H.c.}, \quad (4.30)$$

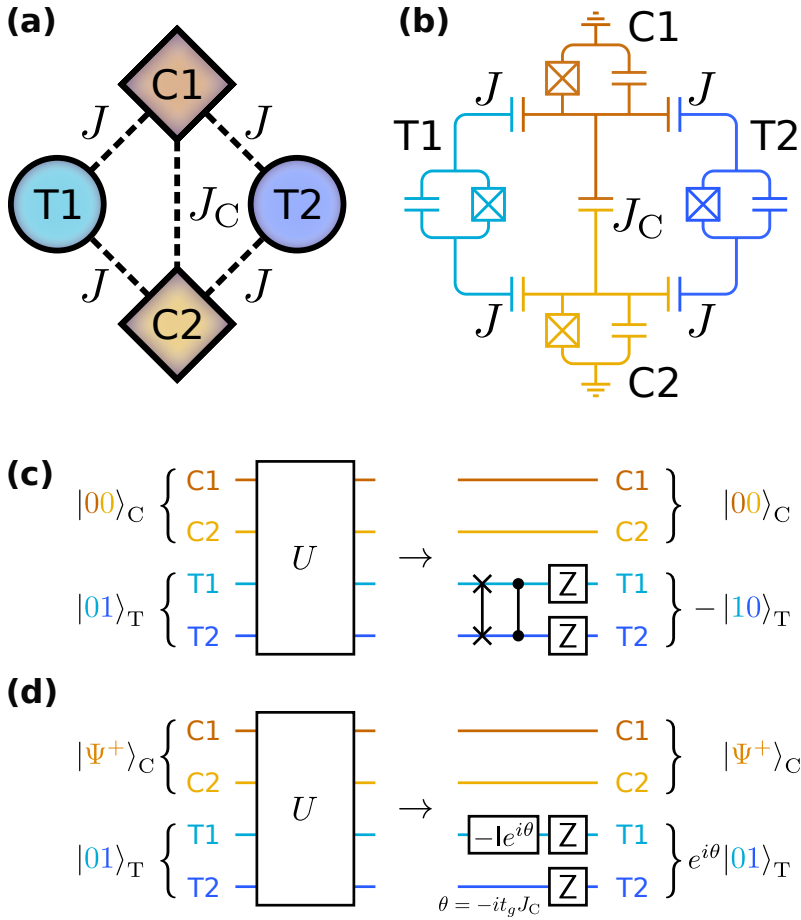


Figure 4.2: (a) The diamond gate: Four-qubit system consisting of two target qubits (T1 and T2) and control qubits (C1 and C2) coupled through exchange interactions (dashed lines) with the indicated strengths. (b) Lumped element superconducting circuit diagram of four capacitively coupled transmons, where each colored subcircuit corresponds to the same-colored qubit in (a). (c)–(d) Example transformations implemented by the diamond gate,  $U$ , of Eq. (4.36). The figure is adapted from Ref. [8].

with  $\sigma_+^j = |1\rangle\langle 0|_j$  and  $\sigma_-^j = |0\rangle\langle 1|_j$  on qubit  $j$ . This Hamiltonian governs the dynamics resulting from the interactions in the model. We show in Appendix B.1 that the effective unitary time-evolution of  $H$  gives rise to a four-qubit gate operating by means of controlled quantum interference (the diamond gate). The analysis is based on a Magnus expansion of  $H$  within Floquet theory, which assumes  $|\Delta| \gg |J|, |J_C|$ , i.e. a qubit detuning much larger than the coupling strengths.

The diamond gate is a four-way controlled two-qubit gate operation on the target qubits T1 and T2. Consider the following gates in the target qubit computational basis,  $\{|00\rangle_T, |01\rangle_T, |10\rangle_T, |11\rangle_T\}$ , where the superscripts refer to the control setting (discussed below):

$$U_T^{00} = \begin{pmatrix} 1 & 0 & 0 & 0 \\ 0 & 0 & -1 & 0 \\ 0 & -1 & 0 & 0 \\ 0 & 0 & 0 & -1 \end{pmatrix} = \text{ZZ} \cdot \text{CZ} \cdot \text{SWAP}, \quad (4.31)$$

$$U_T^{11} = \begin{pmatrix} -1 & 0 & 0 & 0 \\ 0 & 0 & -1 & 0 \\ 0 & -1 & 0 & 0 \\ 0 & 0 & 0 & 1 \end{pmatrix} = -\text{CZ} \cdot \text{SWAP}, \quad (4.32)$$

$$U_T^{\Psi+} = \begin{pmatrix} -1 & 0 & 0 & 0 \\ 0 & 1 & 0 & 0 \\ 0 & 0 & 1 & 0 \\ 0 & 0 & 0 & -1 \end{pmatrix} e^{-it_g J_C} = -\text{ZZ} e^{-it_g J_C}, \quad (4.33)$$

$$U_T^{\Psi-} = \begin{pmatrix} 1 & 0 & 0 & 0 \\ 0 & 1 & 0 & 0 \\ 0 & 0 & 1 & 0 \\ 0 & 0 & 0 & 1 \end{pmatrix} e^{+it_g J_C} = \mathbb{1} e^{+it_g J_C}. \quad (4.34)$$

Here  $t_g$  is the gate time given by

$$t_g = \frac{\pi|\Delta|}{4J^2}. \quad (4.35)$$

Eqs. (4.31)–(4.34) show the two-qubit operations in terms of well-known gates from the literature, see e.g. Ref. [139]. Here ZZ is understood as a Z gate on each target qubit. Thus we see that  $U_T^{00}$

and  $U_T^{11}$  are two different combined swap and phase operations. Access to just one of these entangling gates will facilitate universal quantum computing. The third gate,  $U_T^{\Psi^-}$ , is a phase operation distinguishing target states with different parity (addition of T1 and T2's bit value modulo 2) by application of a relative sign. The final gate,  $U_T^{\Psi^-}$ , which just adds a global phase, is the identity gate. We can therefore regard the preceding three gates as actual computational gates, while  $U_T^{\Psi^-}$  is the idle position of the device.

The above two-qubit gates are controlled by the state of the control qubits, which we describe in the following orthonormal basis:  $\{|00\rangle_C, |11\rangle_C, |\Psi^+\rangle_C, |\Psi^-\rangle_C\}$ . We refer to this basis, which mixes computational basis states and the Bell states  $|\Psi^\pm\rangle_C = (|01\rangle_C \pm |10\rangle_C)/\sqrt{2}$ , as the control basis. The full four-qubit unitary operation of the diamond gate is

$$U = |00\rangle\langle 00|_C U_T^{00} + |11\rangle\langle 11|_C U_T^{11} + |\Psi^+\rangle\langle \Psi^+|_C U_T^{\Psi^+} + |\Psi^-\rangle\langle \Psi^-|_C U_T^{\Psi^-}. \quad (4.36)$$

Cast this way, it is evident that  $U$  describes a four-way controlled operation on the target qubits. If the control qubits are initialized in one of the control basis states, only the corresponding gate among (4.31)–(4.34) is performed. The control state is unchanged after the gate operation. Figure 4.2c–d illustrate the gate operation on the target state  $|01\rangle_T$  in the cases where the control is  $|00\rangle_C$  and  $|\Psi^+\rangle_C$ , respectively. However, these gate diagrams only show the gate operation for these two control states, and in general the diamond gate performs a unitary operation on any initial four-qubit state. A more sophisticated decomposition of the full unitary  $U$  is given in Figure B.1 in Appendix B.1, where we note that the complexity in terms of number of CNOT gates is 42. Have access to four controlled two-qubit operations natively is useful for quantum simulation and may ease quantum gate compilation significantly.

As shown in Appendix B.1, the unitary time-evolution under the Hamiltonian of Eq. (4.30) approximately gives rise to  $U$ . Within the first order Magnus expansion, the approximation is exact when  $J_C = 0$ , however a non-zero coupling between the control qubits is needed in order to initialize the control Bell states. Such a coupling allows the triplet states  $\{|00\rangle_C, |11\rangle_C, |\Psi^+\rangle_C\}$  to mix slightly during the gate operation, in which case the separation of control states in Eq. (4.36) is no longer exact. This leads to small gate infidelities of the

order  $(2J/\Delta)^2 = \pi/(t_g\Delta)$  when then control qubits are initialized in  $|00\rangle_C$  or  $|11\rangle_C$ , and twice as large when the control is in  $|\Psi^+\rangle_C$ . For typical superconducting circuit parameter values, like the ones used in the following section, these infidelities are on the order  $10^{-3}$  to  $10^{-2}$ . Notice that the infidelity scales inversely with the gate time, leading to a trade-off between a fast gate and high-fidelity coherent operations. Since the singlet state  $|\Psi^-\rangle_C$  does not mix with the triplet states, the idle gate operation is not affected by the coupling  $J_C$ , and the gate fidelity is only limited by other factors, e.g. qubit decoherence.

As mentioned above, the performance of the gate is increased if  $J_C = 0$ , however a non-zero direct coupling between the control qubits is necessary if we wish to prepare the entangled Bell states. In the following, we will assume a fixed value of  $J_C$ , although ideally a tunable coupler[191] can be used to turn on the coupling only during control state preparation. If the control qubits are detuned from the target qubits,  $|\Delta| \gg |J|$ , we can initialize the control state without affecting the target qubits. This detuning can be achieved by flux tunable devices, or by fabricating single-junction qubits with different frequencies. Thus, ignoring the oscillating terms of Eq. 4.30, we have effectively decoupled the control and target qubits. We note that the effective Hamiltonian of the control qubits in the rotating frame,  $J_C(\sigma_+^{C1}\sigma_-^{C2} + \sigma_-^{C1}\sigma_+^{C2})$ , has a zero-energy subspace spanned by  $|00\rangle_C$  and  $|11\rangle_C$ , and eigenstates  $|\Psi^\pm\rangle_C$  of energy  $\pm J_C$ . An energy separation of  $J_C/2\pi \sim 20$  MHz allows us to initialize the control in  $|\Psi^\pm\rangle_C$  by driving energy transitions[123, 186]. To initialize the control in  $|00\rangle_C$  or  $|11\rangle_C$ , we can induce Rabi oscillations between these two states by driving the control qubits similarly to the procedure analyzed in Ref. [192].

### 4.2.2 Extensible quantum computer

The four-qubit quantum interference device can constitute a building block in an extensible quantum computer by connecting several copies. One possible architecture is illustrated in Figure 4.3a, where a 16-qubit quantum computer is constructed by connecting four copies of the four-qubit device, for instance through capacitive couplings. On the plaquettes labelled A the control qubits are oriented vertically (1, 2, 13 and 14) and the target qubits horizontally (3, 4, 15 and 16), while the diamond gate devices on the plaquettes B are rotated by

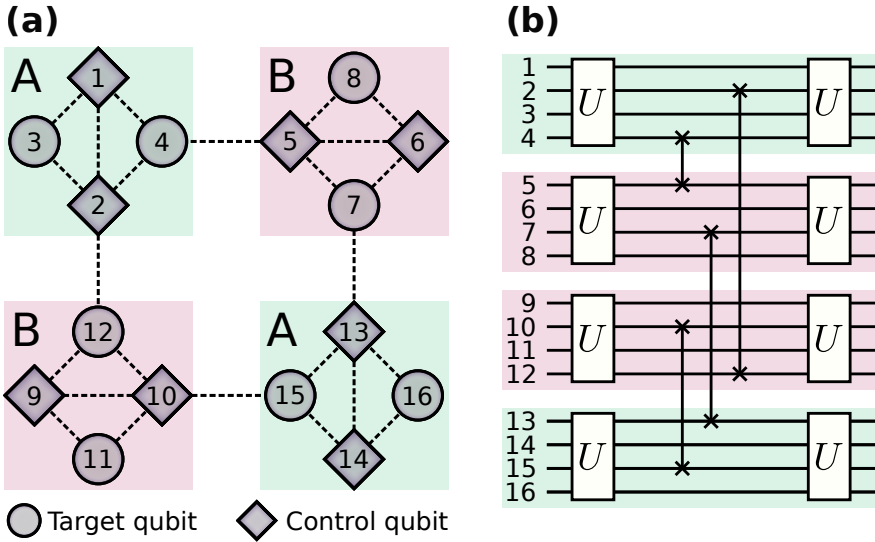


Figure 4.3: Proposed architecture for an extensible quantum computer. (a) Four connected copies of the four-qubit diamond gate device. Detuning the qubits on the plaquettes A from the qubits on the plaquettes B allows each four-qubit device to run the diamond gate independently, while tuning the connecting qubits into resonance allows swap operations between plaquettes A and B. (b) A sequence of diamond gates  $U$  of Eq. (4.36) in each plaquette and two-qubit swaps between the plaquettes running on the 16-qubit quantum computer. The figure is adapted from Ref. [8].

ninety degrees, such that control and target qubits from different plaquettes are connected. This design of alternating A and B plaquettes can be extended in a straight-forward manner in one or two dimensions.

The quantum algorithm shown in Figure 4.3b is a generic algorithm spreading entanglement in the computer. Supplemented with single-qubit rotations, it may serve as a variational quantum eigensolver[193]. The algorithm can be implemented in the following way. Initially, the plaquette A qubits are far detuned from the plaquette B qubits, allowing each four-qubit diamond gate device to run the unitary gate  $U$  of Eq. (4.36) independently. After the completion of the gates, we can prevent further dynamics within each plaquette by

switching the controls to the idle state. Then, by tuning pairs of connected qubits from different plaquettes into resonance, for instance 4 and 5, we can perform swap gates or use a suitable microwave driving to perform other desired two-qubit operations. Finally, by tuning the qubits out of resonance, and potentially switching certain controls, we are ready to run the diamond gate again.

### 4.2.3 Numerical simulations

Although the analytic results suggest a functioning four-qubit diamond gate, we use numerical simulations to quantify the performance of the gates for state-of-the-art superconducting qubit parameters [109, 194, 195]. Decoherence is included via the Lindblad master equation,

$$\dot{\rho} = -i[H, \rho] + \sum_n \left[ C_n \rho C_n^\dagger - \frac{1}{2} (\rho C_n^\dagger C_n + C_n^\dagger C_n \rho) \right]. \quad (4.37)$$

Here  $\rho$  is the density matrix,  $H$  is the Hamiltonian of Eq. (4.30), and the sum is taken over the following eight collapse operators,  $C_n$ :  $\sqrt{\gamma} \sigma_z^i$  inducing pure dephasing and  $\sqrt{\gamma} \sigma_-^i$  inducing qubit relaxation (photon loss), with  $i$  running over all four qubits, denoting by  $\gamma$  the decoherence rate. We solve the master equation numerically using the Python toolbox QuTiP [196].

As a quality measure of the gate, we consider the average fidelity [197] (or simply ‘fidelity’ in the following),

$$F(t) \equiv \int d\psi \langle \psi | U_{\text{target}}^\dagger \mathcal{E}_t(|\psi\rangle\langle\psi|) U_{\text{target}} |\psi\rangle, \quad (4.38)$$

which quantifies how well the quantum map  $\mathcal{E}_t$  approximates the target unitary gate  $U_{\text{target}}$  over a uniform distribution of input quantum states. If the diamond gate is run with an arbitrary initial state, the integral is taken over all possible four-qubit states, and can be reduced to a sum over a density matrix basis, as shown in Ref. [197]. Putting  $U_{\text{target}} = U$  from Eq. (4.36) and  $\mathcal{E}_t(\rho(0)) = \rho(t)$  found from solving Eq. (4.37), the computed fidelity quantifies the overall performance of the diamond gate with arbitrary initial states. We denote this fidelity by  $F$ . Its maximum value (the gate fidelity) defines the gate time, which generally matches the predicted value of Eq. (4.35) within a few percent. The sources of gate infidelity are qubit decoherence and state mixing accommodated by a non-zero  $J_C$ .

	Parameter set 1	Parameter set 2
$J_C/2\pi$ MHz	20	20
$J/2\pi$ MHz	65	45
$\Delta/2\pi$ GHz	2	0.5
$\gamma$ /MHz	0.01	0.01
Predicted $t_g$ /ns	59.2	30.9
Simulated $t_g$ /ns	59.3	31.5
$F_{00}(t_g)$	0.9943	0.9662
$F_{11}(t_g)$	0.9931	0.9668
$F_{\Psi^+}(t_g)$	0.9881	0.9348
$F_{\Psi^-}(t_g)$	0.9968	0.9983
$F(t_g)$	0.9923	0.9637

Table 4.1: Two sets of model parameters and their corresponding gate times and gate fidelities. The gate fidelities are found at the simulated  $t_g$ .

In order to study the performance of the four individual gates of Eqs. (4.31)–(4.33), we initialize the control qubits in

$$|\phi\rangle_C \in \{|00\rangle_C, |11\rangle_C, |\Psi^+\rangle_C, |\Psi^-\rangle_C\}. \quad (4.39)$$

In this case the target operation is a single term in Eq. (4.36),  $U_{\text{target}} = |\phi\rangle\langle\phi|_C U_T^\phi$ , and the integral is taken over all states on the form  $|\phi\rangle_C |\psi\rangle_T$ , i.e. only varying the target qubits' state,  $|\psi\rangle_T$ . These states span a subspace of the entire four-qubit Hilbert space characterized by the fixed control state, however couplings to other control states leads to leakage out of the subspace, which we take into account with the appropriate modification of the sum formula in Ref. [197]. The resulting fidelity is denoted  $F_\phi$ , and the value at the gate time is denoted the gate fidelity for the associated gate.

Two example parameter sets relevant for superconducting qubits are shown in Table 4.1. We use the state-of-the-art decoherence rate  $\gamma = 0.01$  MHz, corresponding to a qubit life-time of  $\gamma^{-1} = 100$  us[194]. Figure 4.4 shows the simulated fidelities as functions of time. As expected, there is a trade-off between a fast gate and high-fidelity operations. Parameter set 1 operates in 59.3 ns with gate fidelities  $\sim 0.99$ , which decreases to  $\sim 0.96$  for the very fast 31.5 ns

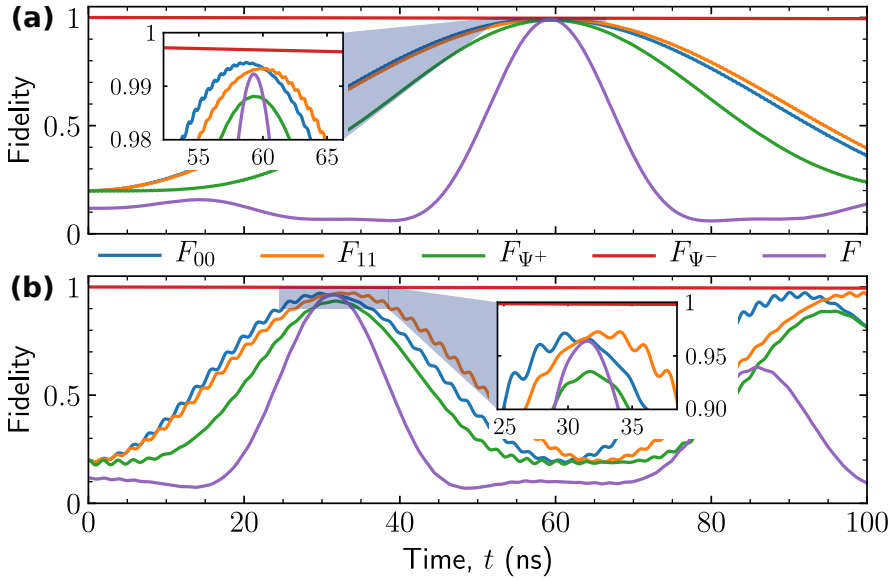


Figure 4.4: Fidelities versus time for the individually controlled gates ( $F_{00}$ ,  $F_{11}$ ,  $F_{\Psi+}$ ,  $F_{\Psi-}$ ) and the total diamond gate ( $F$ ). Insets show zooms around the gate time. The parameters used in (a) are set 1 from Table 4.1, and in (b) they are set 2. The figure is adapted from Ref. [8].

gate of parameter set 2. The gate infidelities for each controlled gate follow the expectations discussed in the previous section. In particular, the idle gate fidelity,  $F_{\Psi-}(t)$ , is only limited by qubit decoherence, reducing its value from 1 to 0.9983 and 0.9968, respectively, during the operation time in the two cases. For the remaining three controlled gates, a longer gate time can improve the gate fidelity, with the drawback of increased susceptibility to qubit decoherence. Ultimately this limits the number of computations the diamond gate device can run successfully. For the purpose of demonstrating the model, we will use parameter set 1 in the following, unless otherwise stated.

To probe the sensitivity to the model parameters, we vary each of  $\Delta$ ,  $J$  and  $J_C$ . As is evident from Figure 4.5a–c, the simulated gate times follow closely the prediction of Eq. (4.35). Specifically, the gate time is tunable through  $\Delta$  and  $J$ . The gate fidelities for the individually controlled gates and the total diamond gate are shown

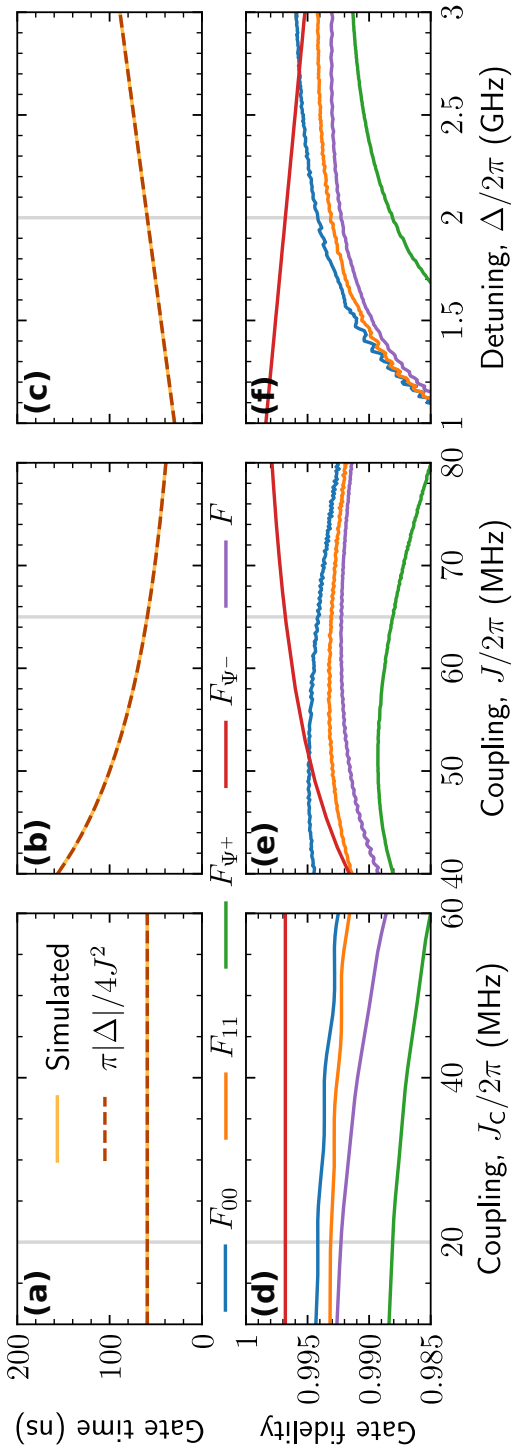


Figure 4.5: Simulations varying the model parameters  $J_C$ ,  $J$  and  $\Delta$ , with qubit decoherence of rate  $\gamma = 0.01$  MHz. While one parameter is varied, the remaining two are fixed at the values marked by the gray vertical lines (parameter set 1 of Table 4.1). (a)–(c) Gate times, also showing the prediction of Eq. (4.35) as the dashed line. (d)–(f) Gate fidelities, i.e. the fidelities at the simulated gate time. The figure is adapted from Ref. [8].

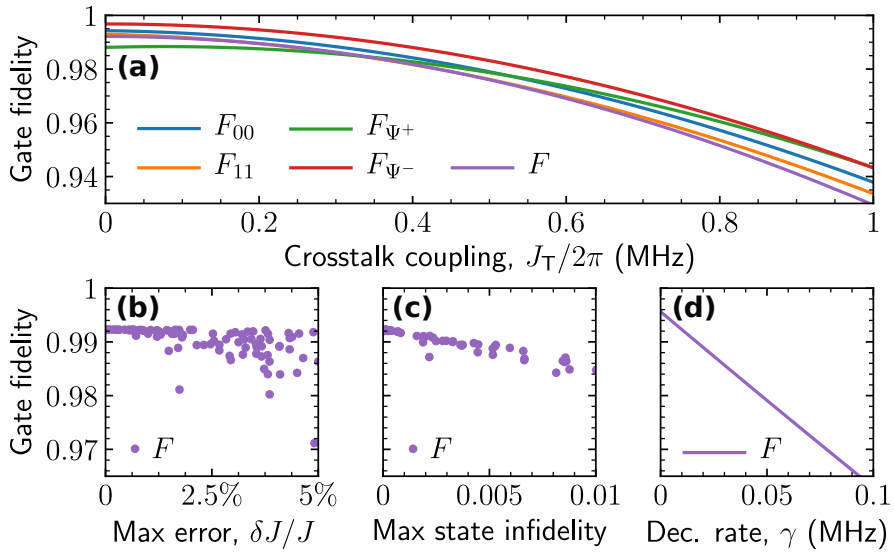


Figure 4.6: Investigating gate stability for the following system infidelities: (a) Crosstalk coupling between the target qubits. (b) Random asymmetric noise in the couplings between the target and control qubits. (c) Control state infidelity. (d) Qubit decoherence with rate  $\gamma$ . The figure is adapted from Ref. [8].

in Figure 4.5a–f. Except for the phase gate controlled by  $|\Psi^+\rangle_C$ , which is affected most strongly by couplings to other control states, the fidelities are above 0.99 over a wide range of parameters. Due to the mathematical equivalence between the two swapping gates controlled by  $|00\rangle_C$  and  $|11\rangle_C$ , the gate fidelities for these operations are very similar. We attribute the difference to qubit relaxation, which only affects  $|11\rangle_C$  and becomes more pronounced as the gate time increases. The identity gate controlled by  $|\Psi^-\rangle_C$  is only limited by decoherence, and its gate fidelity decreases linearly with the gate time.

With a superconducting circuit implementation in mind, we consider a variety of system infidelities and their impact on the gate fidelities, see Figure 4.6. Most harmful is a direct capacitive coupling between the target qubits (Figure 4.6a), which allows the target qubits to bypass the control qubits, thereby circumventing the interference condition set by the control qubits. The gate fidelities roughly de-

crease with the square of the cross-coupling strength  $J_T$ , leading to noticeable gate infidelities even for a relatively weak coupling. However, as we will show in the next section, crosstalk should not be suppressed, but rather utilized to combat another effect appearing in superconducting qubits: couplings to higher-energy states in the qubits' spectrum.

Figure 4.6b shows simulation results with random noise on the couplings between the target and control qubits emulating asymmetries present in an actual circuit due to fabrication limits. Each data point in the plot corresponds to a simulation with random deviations from the noiseless value,  $J$ , denoting by  $\delta J$  the maximum deviation over the four couplings. The gate performance is very robust towards this type of noise.

Bell state generation, which is required for the control states  $|\Psi^\pm\rangle_C$ , has been shown with a state infidelity of  $\sim 0.005$ [118]. We introduce control state infidelity in the following way. For each data point in Figure 4.6c we construct a random four-by-four Hermitian matrix  $M$ , from which we construct a unitary matrix  $V = e^{i\epsilon M}$ , where  $\epsilon$  is a small real parameter. In the simulations, we apply  $V$  to the initial state of the control qubits in order to model imperfect state preparation. The resulting gate fidelity is shown as a function of the maximum infidelity among the four control states. The diamond gate suffers a linear decrease in gate fidelity, but remains high-performing for realistic control state infidelity.

Qubit decoherence in the form of relaxation and dephasing is included in the master equation (4.37) with rate  $\gamma$ . In Figure 4.6d we see that the gate fidelity decreases linearly with  $\gamma$ . Even for qubits with  $\gamma = 0.05$  MHz, corresponding to a lifetime of  $\gamma^{-1} = 20$   $\mu$ s, the gate fidelity is  $\sim 0.98$ . We attribute this robustness to the relatively short gate time of 59.3 ns.

#### 4.2.4 Higher-energy states

In the previous section, we treated a model for four coupled qubits. In the superconducting circuit implementation of Figure 4.2, these qubits are comprised of the two lowest energy states of the each transmon,  $|0\rangle$  and  $|1\rangle$ . However, in an actual superconducting circuit, the qubits may couple to higher-energy states in the transmon spectrum, which is the spectrum of a slightly anharmonic oscillator[108]. In this

section, we analyse the effects from including the second excited state,  $|2\rangle$ , in the spectrum, thereby turning each qubit into a qutrit.

The full analysis of the circuit of Figure 4.2b is given in Appendix B.2. The resulting four-qutrit Hamiltonian is a sum of the non-interacting part

$$\tilde{H}_0 = -\frac{1}{2}\Omega_T(\tilde{\sigma}_z^{T1} + \tilde{\sigma}_z^{T2}) - \frac{1}{2}\Omega_C(\tilde{\sigma}_z^{C1} + \tilde{\sigma}_z^{C2}), \quad (4.40)$$

and the interaction terms

$$\tilde{H}_{\text{int}} = J_T\tilde{\sigma}_y^{T1}\tilde{\sigma}_y^{T2} + J_C\tilde{\sigma}_y^{C1}\tilde{\sigma}_y^{C2} + J(\tilde{\sigma}_y^{T1} + \tilde{\sigma}_y^{T2})(\tilde{\sigma}_y^{C1} + \tilde{\sigma}_y^{C2}), \quad (4.41)$$

which are analogous to Eqs. (4.28)–(4.29). The ‘Pauli z-operator’ on qutrit  $j$ , denoted  $\tilde{\sigma}_j$ , includes  $|2\rangle_j$  in such a way that it has an energy  $\Omega_j + \alpha_j$  above  $|1\rangle_j$ , with  $\Omega_j$  and  $\alpha_j$  the frequency and anharmonicity, respectively. Typically  $\alpha_j/\Omega_j \sim -0.05$ , yielding a small detuning of the second excited state compared to an equidistant spectrum (i.e. to vanishing anharmonicity). The operator is given as

$$\tilde{\sigma}_z^j = |0\rangle\langle 0|_j - |1\rangle\langle 1|_j - \left(3 + \frac{2\alpha_j}{\Omega_j}\right) |2\rangle\langle 2|_j, \quad (4.42)$$

The ‘Pauli y-operator’ on qutrit  $j$  is

$$\tilde{\sigma}_y^j = iT_0^j |1\rangle\langle 0|_j + iT_2^j |2\rangle\langle 1|_j + \text{H.c.}, \quad (4.43)$$

where  $T_0^j \approx 1$  and  $T_2^j \approx \sqrt{2}$  can be expressed in terms of  $\Omega_j$  and  $\alpha_j$  (see Appendix B.2). Hence, the coupling between the first and second excited state is as strong as the coupling between the two lowest (qubit) levels. Due to the small anharmonicity in transmons, i.e. that the energy separation between the qubit levels almost equals the separation between the first and second excited state, couplings that exchange a single excitation like  $|11\rangle \rightarrow |02\rangle$  are not strongly energetically suppressed. In fact, this transition is sometimes used for the CZ gate[107]. Notice that this lack of suppression holds for transmons in general, and is not a consequence of the specific model considered here.

This has two undesired consequences. Firstly, unless  $|J_C/\alpha_C| \ll 1$ , it allows the control state  $|11\rangle_C$  to mix with  $|02\rangle_C$  and  $|20\rangle_C$ , leading

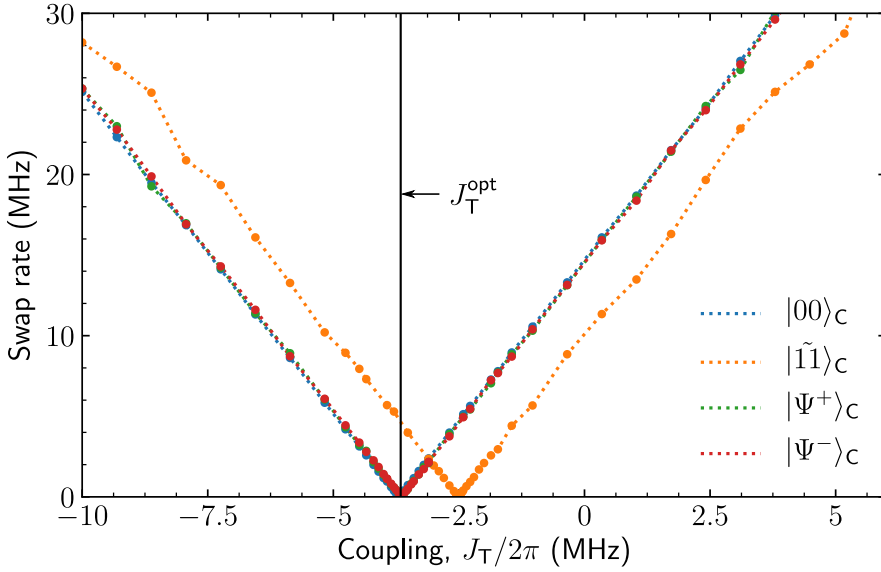


Figure 4.7: Swap rate, found as the inverse of the smallest time  $t$  where the swap fidelity (probability)  $|\langle \phi |_{\text{C}} \langle 01 |_{\text{T}} e^{-i(\tilde{H}_0 + \tilde{H}_{\text{int}})t} | 10 \rangle_{\text{T}} | \phi \rangle_{\text{C}}|^2$  becomes close to unity, versus crosstalk strength  $J_{\text{T}}$ . Data points are shown with the control state  $|\phi\rangle_{\text{C}}$  set to each of the displayed states. The parameters used in the simulation are  $J_{\text{C}}/2\pi = 20$  MHz,  $J/2\pi = 65$  MHz,  $\Omega_{\text{C}}/2\pi = 7$  GHz,  $\Omega_{\text{T}}/2\pi = 9$  GHz,  $\alpha_{\text{C}} = -270$  MHz and  $\alpha_{\text{T}} = -280$  MHz. The optimal value of Eq. (4.47) is marked with a vertical line,  $J_{\text{T}}^{\text{opt}}/2\pi = -3.66$  MHz. The figure is adapted from Ref. [8].

to a non-conserved control state during the gate operation. This can be resolved by redefining the control state as

$$|\tilde{11}\rangle_{\text{C}} = \cos \tilde{\theta} |11\rangle_{\text{C}} + \sin \tilde{\theta} \frac{1}{\sqrt{2}} (|02\rangle_{\text{C}} + |20\rangle_{\text{C}}), \quad (4.44)$$

with the mixing angle  $\tilde{\theta} = -\frac{1}{2} \arctan\left(2\sqrt{2}J_{\text{C}}T_1^{\text{C}}T_2^{\text{C}}/\alpha_{\text{C}}\right) \sim 0.5$ , such that it is an eigenstate of an effective control state Hamiltonian. This introduces a significant component of  $(|02\rangle_{\text{C}} + |20\rangle_{\text{C}})/\sqrt{2}$ , which is avoided if  $J_{\text{C}} = 0$ . Details are found in Appendix B.2.

Secondly, excitations to the second excited states allow unwanted processes which bypass the control. For instance, when the diamond

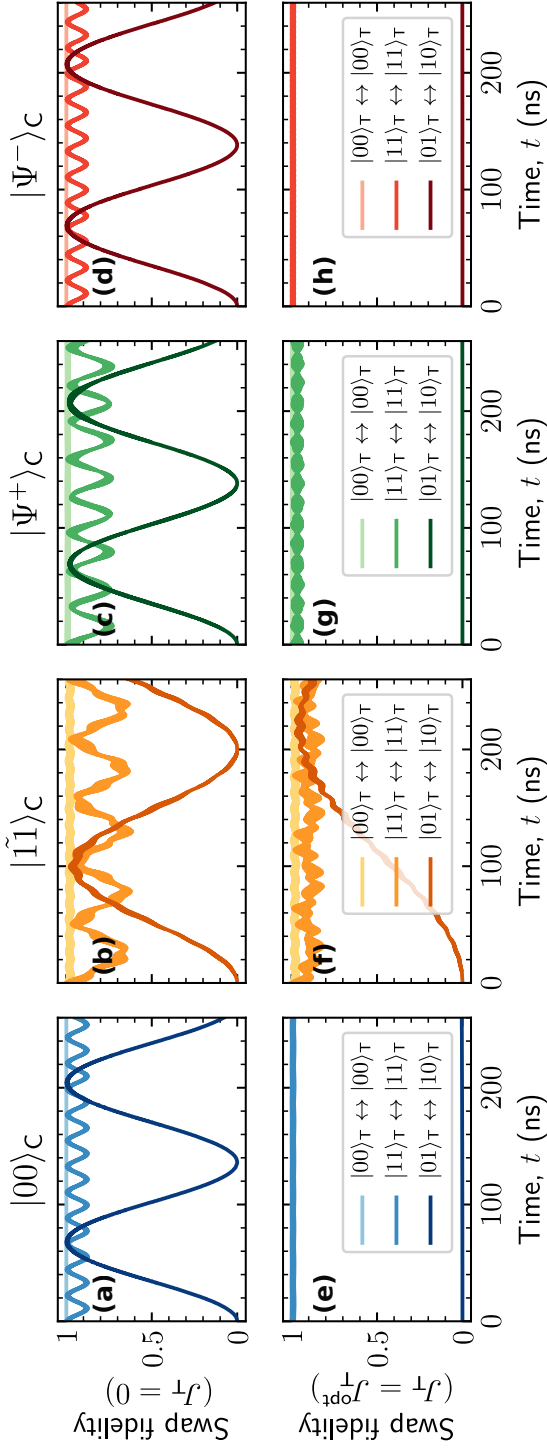


Figure 4.8: Fidelity for swapping  $|\psi\rangle_T \leftrightarrow |\psi'\rangle_T$  for the indicated processes, computed as  $|\langle\phi|_C \langle\psi'|_T e^{-i(\tilde{H}_0 + \tilde{H}_{\text{int}})t} |\psi\rangle_T |\phi\rangle_C|^2$ , with the control state  $|\phi\rangle_C$  indicated above each column. The parameters used in the simulation are  $J_C/2\pi = 20$  MHz,  $J/2\pi = 65$  MHz,  $\Omega_C/2\pi = 7$  GHz,  $\Omega_T/2\pi = 9$  GHz,  $\alpha_C = -270$  MHz and  $\alpha_T = -280$  MHz. (a)–(d) No crosstalk,  $J_T = 0$ . (e)–(h) Crosstalk is set to its optimal value of Eq. (4.47),  $J_T^{\text{opt}}/2\pi = -3.66$  MHz. The figure is adapted from Ref. [8].

gate is desired to be idle, leakage across the control can occur via:

$$|\Psi^-\rangle_C |10\rangle_T \rightarrow \frac{1}{\sqrt{2}}(|02\rangle_C - |20\rangle_C) |00\rangle_T \rightarrow |\Psi^-\rangle_C |01\rangle_T. \quad (4.45)$$

Since this is a second order process in the qutrit model Hamiltonian, it would not pose a threat to the functionality of the diamond gate if it only relied on (generally faster) first order processes. However, the swap operations of Eqs. (4.31)–(4.32) are also second order processes, leading to a failure of the idle diamond gate on the same time-scale as the operation of the swap gates. Similarly, the control state  $|\Psi^+\rangle$  fails to prevent excitation leakage across the control, corrupting the operation of Eq. (4.33).

However, these undesired processes can be mitigated by taking advantage of the effects of crosstalk. The circuit analysis in Appendix B.2 reveals a weak unavoidable crosstalk coupling of strength  $J_T$  in the interaction Hamiltonian (4.41), which by itself has a significant negative impact on the gate fidelities, c.f. Figure 4.6a. This leads directly to leakage across the control through processes of the type

$$|\Psi^-\rangle_C |10\rangle_T \rightarrow |\Psi^-\rangle_C |01\rangle_T. \quad (4.46)$$

This process has the same unwanted outcome as the one of Eq. 4.45. As we show below, we can therefore restore the gate functionality by tuning the value of  $J_T$  such that these two unwanted leakage processes cancel each other. Analyzing the problem with second order perturbation theory in order to calculate the amplitude of the leaked state (see Appendix B.2), we find destructive interference between these processes when the crosstalk strength takes the optimal value

$$J_T^{\text{opt}} = \frac{(JT_2^C)^2}{\Omega_C + \Omega_T + \alpha_C + J_C(T_1^C)^2} + \frac{(JT_2^C)^2}{\Omega_C - \Omega_T + \alpha_C + J_C(T_1^C)^2}. \quad (4.47)$$

Thus by tuning the crosstalk strength to  $J_T = J_T^{\text{opt}}$ , we expect the fidelity for the target qubit swap  $|01\rangle_T \leftrightarrow |10\rangle_T$  to diminish, or equivalently a vanishing swap rate, when the control state is  $|\Psi^\pm\rangle_C$ . Figure 4.7 shows the swap rate for varying  $J_T$ , with control qubits in each of the four control states. We find two distinct zero-points, one for the data related to the control states  $|00\rangle_C$  and  $|\Psi^\pm\rangle_C$  at

the expected value  $J_T^{\text{opt}}$  (vertical line), and one for  $|\tilde{11}\rangle_C$ . Thus, it is possible to prevent the unwanted swap operation for the control states  $|\Psi^\pm\rangle_C$ , but as a consequence also the swap operation controlled by  $|00\rangle_C$  is obstructed. On the other hand, the swap operation controlled by  $|\tilde{11}\rangle_C$  is preserved at  $J_T = J_T^{\text{opt}}$ , although the gate time is prolonged to around 220 ns. Remarkably, for  $J_T/2\pi \approx -2.5$  MHz the situation is reversed. Here, putting the control in  $|\tilde{11}\rangle_C$  prevents swapping, while the three remaining control states permit it. At each zero-point, the gate time (inverse swap rate) for the swapping gate(s) is prolonged compared to the results in the previous section. To reduce the gate time, one should pick parameters such that the zero-points are further apart, or such that the inclination of the graphs are steeper.

Figure 4.8 illustrates in more detail the cancellation of unwanted transfer by crosstalk engineering. Each subfigure shows the swap fidelity for different initial target qubit states. The control is initialized in the state indicated above each column. Figure 4.8a–d (the top row) show simulations for  $J_T = 0$ , while the crosstalk has been put to its optimal value,  $J_T = J_T^{\text{opt}}$ , in Figure 4.8e–h (the bottom row). As expected from Figure 4.7, the swap  $|01\rangle_T \leftrightarrow |10\rangle_T$  (dark lines) occurs for any control state when there is no crosstalk, but is controlled uniquely by  $|\tilde{11}\rangle_C$  when the crosstalk is at the optimal value. In the cases of  $|00\rangle_T$  and  $|11\rangle_T$ , we wish to maintain a unit fidelity across all control states, i.e. the states should acquire at most a phase. Tuning the crosstalk to  $J_T^{\text{opt}}$  also improves the gate operation in this regard.

Engineering crosstalk to mitigate unwanted leakage through higher-excited states is killing two birds with one stone: Each process is harmful to the functionality of the diamond gate, but letting them cancel each other preserves the ability to control the swap operation. The price is the loss of swap functionality in the gate controlled by  $|00\rangle_C$ , and an increased gate time for the model parameters considered here. Generally, the phases applied to each target state will be modified for all four controlled gates, but we do not pursue an analysis here, as other factors specific to the implementation will contribute to this as well. Rather, our main goal was to demonstrate a passive method for dealing with undesired leakage processes.

#### 4.2.5 Discussion

We have proposed a quantum interference device by coupling four qubits with exchange interactions. By analyzing the unitary dynamics

of the system, we have shown that it realizes the diamond gate: a four-way controlled two-qubit gate, with the ability to run two different entangling swap and phase operations, a (parity) phase operation, an idling gate with no dynamics, or an arbitrary superposition of these. We considered an implementation in superconducting qubits using transmon qubits, and found that it generally operated fast and with high fidelity using state-of-the-art model and noise parameters. When taking second excited states into account, we had to prevent leakage across the control by engineering crosstalk, demonstrating a general method to avoid leakage in superconducting qubit systems. The cost of this was a single redefined control state, one swap gate turning into a phase gate, altered phases on the gates, and a slower gate for the considered parameters. However, we only consider this analysis a starting point for an actual implementation, which might also include active microwave driving to optimize the operations or to prevent certain transitions. It might also be worthwhile to consider other types of superconducting qubits with larger anharmonicity, or entirely different platforms such as lattices of ultracold atoms or ions, where qubit encoded in hyperfine states or vibrational modes are far detuned from the rest of the spectrum.

We illustrated how the four-qubit diamond gate device can constitute an essential building block in an extensible quantum computer, and proposed a simple scheme where quantum algorithms are run on the computer by parallel processing on each four-qubit module interspersed with two-qubit operations spreading entanglement in the system, and single-qubit operations. Evidently, this scheme is adaptable to many different algorithms, and future work will investigate which algorithms are suitable to be implemented in the diamond-plaquette device.

### 4.3 Qubit-qutrit based gates

I will conclude this chapter with a very brief account of another superconducting gate project I was involved in. While the development of the superconducting quantum transistor and Heisenberg XXZ coupler described in Section 3.7 and 3.6 gave us a diamond-shaped qubit network, we were still interested in one-dimensional chains of coupled qubits. In particular, we knew that the original quantum transistor proposal of Ref. [106] of a four-qubit chain with

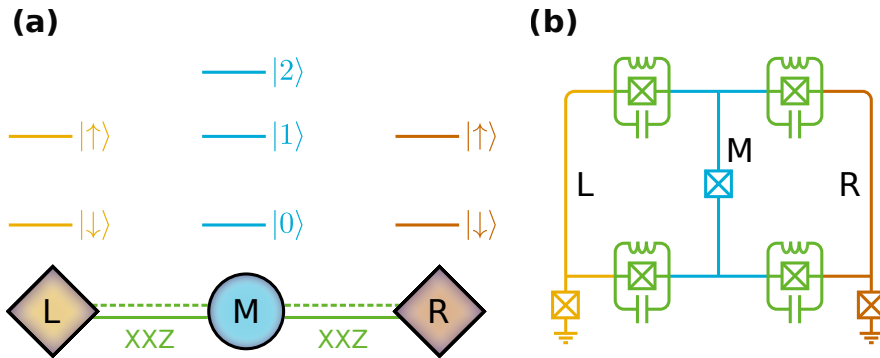


Figure 4.9: (a) System of two qubits (L and R) coupled to a qutrit (M) via Heisenberg XXZ couplings. (b) Superconducting circuit implementing the system.

Heisenberg XXZ couplings had interesting gate properties. Therefore, we became interested in realizing a slightly simpler system: a chain consisting of two qubits and one qutrit (a three-level system) coupled with Heisenberg XXZ couplings, as displayed in Figure 4.9a. Thomas Bækkegaard undertook the task of finding a superconducting circuit implementation of the system, resulting in the circuit in Figure 4.9b, and studying which quantum gates the system could facilitate using different driving schemes on the qubits and qutrit. Notice the XXZ coupler elements colored in green, also present in the designs in Section 3.7 and 3.6. The results were published in Ref. [7]. Since my role in the project was minor – confined to idea development, supervising and commenting on the manuscript – I will not say much about it here.

#### 4.3.1 Hardware supported gates

Any quantum algorithm must be compiled into a series of gates performed on the hardware. Since each gate operation takes precious time, during which the qubits may lose coherence, it is important to reduce the number of gate operations to a minimum. Naturally, the more gates the hardware supports natively, the better the chance for compilation into few gates. In Ref. [7] we show that a single superconducting hardware chip implementing the mentioned qubit-qutrit system supports a variety of quantum gates. Here, I give a

brief rundown of these gates, that are achieved only by detuning and driving the qubits and qutrit with different schemes. The discussion here is kept short and simplified; the interested reader may consult Ref. [7] for further details.

*Bell state preparation.* First, we make the qutrit transitions  $|0\rangle \leftrightarrow |1\rangle$  and  $|1\rangle \leftrightarrow |2\rangle$  non-resonant with both qubit transitions  $|\uparrow\rangle \leftrightarrow |\downarrow\rangle$  using microwave driving. A series of pulses on the qutrit takes it from the ground state,  $|0\rangle$ , to the superposition state  $(|0\rangle + |2\rangle)/\sqrt{2}$ . Assuming the qubits are initialized in their ground state,  $|\downarrow\rangle$ , the qutrit excitation will dissociate into two qubit excitations,  $|\downarrow\rangle (|0\rangle + |2\rangle) |\downarrow\rangle / \sqrt{2} \rightarrow (|\downarrow\rangle |0\rangle |\downarrow\rangle + |\uparrow\rangle |0\rangle |\uparrow\rangle) / \sqrt{2}$ , producing the Bell state,  $(|\downarrow\downarrow\rangle + |\uparrow\uparrow\rangle) / \sqrt{2}$ , on the qubits.

*Controlled-controlled-Z gate.* The CCZ gate transforms  $|\uparrow 0 \uparrow\rangle \rightarrow -|\uparrow 0 \uparrow\rangle$  and does nothing to the other computational states (the computational states for the qutrit is  $|0\rangle$  and  $|2\rangle$  for this gate). First, we make the qubit and qutrit states non-resonant. Next, microwave driving takes  $|\uparrow 0 \uparrow\rangle \leftrightarrow |\uparrow 1 \uparrow\rangle$ . Due to the ZZ-couplings a  $2\pi$  pulse provides the necessary overall sign change,  $|0\rangle \rightarrow i|1\rangle \rightarrow |0\rangle$ , giving rise to the double-conditional phase operation, CCZ.

*Toffoli gate.* The Toffoli gate (CCNOT) applies a ‘not’ operation (X gate) on qubit  $R$  only if the  $L$  qubit is in state  $|\uparrow\rangle$  and the qutrit is in state  $|0\rangle$ . A Hadamard gate can be applied on the target qubit,  $R$ , as a  $\pi/2$ -rotation about the  $y$ -axis, denoted  $\text{IIH}$ . Then, using the CCZ gate described above, the Toffoli gate can be implemented as  $\text{CCNOT} = \text{IIH} \cdot \text{CCZ} \cdot \text{IIH}$ .

*Fredkin gate.* The Fredkin gate (CSWAP) swaps the  $L$  and  $R$  qubits only if control qubit comprised of the qutrit states  $|0\rangle$  and  $|1\rangle$  is in the  $|1\rangle$  state. The remaining qutrit state,  $|2\rangle$ , is outside the computational subspace. First, we make  $|1\rangle \leftrightarrow |2\rangle$  resonant with  $|\uparrow\rangle \leftrightarrow |\downarrow\rangle$ , and far-detuned from  $|0\rangle \leftrightarrow |1\rangle$ . When the control qubit is in  $|0\rangle$ , no swap happens because there are no resonant states, however, when its state is  $|1\rangle$ , the swap  $|\uparrow 1 \downarrow\rangle \leftrightarrow |\downarrow 1 \uparrow\rangle$  occurs via the resonant intermediate state,  $|\downarrow 2 \downarrow\rangle$ . The state  $|\downarrow 1 \downarrow\rangle$  has trivial dynamics, but acquires a relative minus sign, which can be corrected for by applying the CCZ gate.

*Controlled-controlled holonomic gate.* This gate is a general single-qubit gate,  $U(\phi, \theta)$ , parametrized in the angles  $\phi$  and  $\theta$ , which is applied to the computational qubit comprised of  $|0\rangle$  and  $|2\rangle$  only if both  $L$  and  $R$  qubits are in  $|\uparrow\rangle$ . This can be achieved using a driving scheme inspired by Ref. [198]. First qubit and qutrit states

are made non-resonant. Then, we drive the transitions  $|0\rangle \leftrightarrow |1\rangle$  and  $|1\rangle \leftrightarrow |2\rangle$  with the same Gaussian envelopes, but different amplitudes,  $a$  and  $b$ , with  $|a|^2 + |b|^2 = 1$ . Depending on the choice of complex amplitudes, one can obtain the desired gate parameters,  $\phi$  and  $\theta$ , via  $e^{i\phi} \tan(\theta/2) = a/b$ .

---

# Geometric phases and holonomic gate

*In this final chapter, I present unpublished work I did on non-Abelian geometric phases in a system of two coupled qubits, and how this can realize quantum gates.*

After the work on the Bose polaron in the group of Georg M. Bruun we became interested in topological phase transitions in condensed matter and geometric phases; all properties of certain parameter-dependent Hamiltonians. In order to relate this to the work in the group of Nikolaj T. Zinner, we sought a superconducting qubit implementation of a specific ‘topological’ Hamiltonian.

The parameter-dependent Hamiltonian in mind was shown to accommodate a topological invariant – a so-called second Chern number – by Avron *et al.* in 1988[199, 200]. Furthermore, they also cast the Hamiltonian in terms of two interacting spin-1/2 particles, or for our purpose: two superconducting qubits. Kolodrubetz [201] had proposed a method for measuring the second Chern number, and we became interested in finding a specific protocol that would accomplish this in the superconducting system. At that time, the second Chern number had never been measured in any system. However, this changed in 2018, when Sugawa *et al.* simulated the Hamiltonian we also considered using an engineered driving between hyperfine states in an ultracold rubidium gas[202]. While this scheme

could likely be applied to a superconducting system, we turned our focus towards another geometric property of the Hamiltonian.

The Hamiltonian – or rather family of Hamiltonians – depends on five parameters; each being the coupling strength of a term in the Hamiltonian. The second Chern number is an integral over a closed surface in the five-dimensional parameter space, and thus requires access to all five couplings. However, a less demanding geometric property of the system is its non-Abelian geometric phase, which a state picks up while the parameters are varied. This only requires access to the parameter values – and associated couplings – along the path taken in parameter space. If the path is closed the states in the Hilbert space corresponding to the initial point in parameter space is transformed unitarily onto itself; a map known as a holonomic gate in the language of quantum computing. Designing a superconducting chip with the necessary couplings for an interesting (entangling) two-qubit gate would be a natural extension of the work presented in the preceding two chapters.

While a universal gate set based on holonomic gates has already been proposed in superconducting qubits[203], and holonomic single-qubit gates[198] and entangling operations has been demonstrated[204], the outcome of our project could have provided a useful addition.

Native couplings between superconducting qubits can be designed such that they are tunable through external fluxes. We saw this in the Heisenberg XXZ coupler in Section 3.7. Since the external fluxes always appear in trigonometric functions, the couplings are periodic in the fluxes. See for instance Eq. (3.41) or consider the effective Josephson energy for a SQUID[107],

$$E_J(\Phi_{\text{ext}}) \sim \left| \cos \left( \frac{\pi \Phi_{\text{ext}}}{\Phi_0} \right) \right|, \quad (5.1)$$

where  $\Phi_{\text{ext}}$  is the external flux through the SQUID loop. It is clear that increasing the external flux by a whole number of flux quanta would take the Josephson energy, and any coupling strengths depending on it, one round in a closed loop in circuit parameter space. One could then implement the holonomic gate by designing a superconducting chip with the necessary couplings and take the couplings strengths through a closed loop by means of the external fluxes.

During my stay at Massachusetts Institute of Technology in 2018, I discussed the possibility of implementing the five couplings of

the Hamiltonian experimentally with members of the Engineering Quantum Systems group. While some of the couplings were readily available, others would be exceedingly difficult to engineer. The first step would therefore be to identify which couplings would be necessary for a given gate. In this chapter, I present the general answer to this question. This answer also closes the chapter and the thesis, as the scientific impact was too uncertain compared to time a proper treatment of specific gate realizations and superconducting circuit designs required.

## 5.1 Geometric phases

It is well-known that a quantum state can pick up a geometric phase in addition to the usual dynamic phase when the parameters of the Hamiltonian are varied adiabatically. Given certain conditions, following a closed path in parameter space takes the initial state to itself:

$$|\psi\rangle \rightarrow \underbrace{e^{i\gamma}}_{\text{geometric}} \underbrace{e^{-\frac{i}{\hbar} \int_0^t dt' E(t')}}_{\text{dynamic}} |\psi\rangle . \quad (5.2)$$

The existence of the geometric phase was shown in 1984 by Berry[205], and is often called Berry's phase. It is given as an integral along the closed path,  $\Gamma$ , in parameter space

$$\gamma = \oint_{\Gamma} i \langle \psi | \nabla_{\mathbf{q}} | \psi \rangle \cdot d\mathbf{q} , \quad (5.3)$$

where  $\mathbf{q}$  is a vector of the Hamiltonian parameters.

Berry assumed that the state,  $|\psi\rangle$ , is a non-degenerate eigenstate along the path, and will continuously follow the parameter-dependent energy subspace due to the adiabatic theorem. If the assumption of non-degeneracy was relaxed somewhere along the path, the degenerate states could mix, resulting in a final state contaminated with components from other subspaces. However, if the initial state belongs to a  $N$ -fold degenerate subspace that is  $N$ -fold degenerate along the entire path, there is no leakage out of the subspace. Thus, the final state will belong to the same subspace as the initial state, however it may differ from the initial state by not just a phase, but an  $N$ -dimensional unitary transformation. This can be cast as a non-Abelian (non-commutative) geometric phase; a straightforward generalization of Berry's phase ( $N = 1$ ). In the following, we

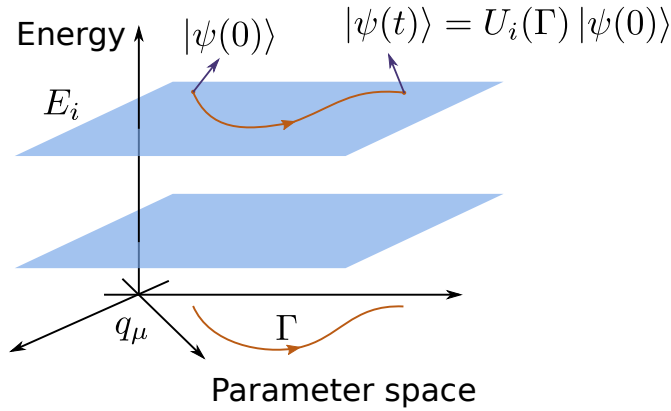


Figure 5.1: The evolution of an initial state,  $\psi(0)$ , in a parameter-dependent energy subspace (blue sheet) is dictated by the adiabatic evolution of the parameters along the path,  $\Gamma$ .

derive the non-Abelian geometric phase, which was first considered by Wilczek and Zee[206] immediately following Berry's paper.

### 5.1.1 Derivation of the geometric phase

Consider a continuous family of Hamiltonians,  $H(\mathbf{q})$ , parameterized by a vector of real parameters,  $\mathbf{q} = (q_1, q_2, \dots, q_N)$ , being the coordinates of a differentiable manifold  $M$ . Suppose that the family of Hamiltonians possesses a symmetry, such that each Hamiltonian  $H(\mathbf{q})$  has an  $N$ -fold degenerate energy subspace with energy  $E_i(\mathbf{q})$ . We focus on the unitary time-evolution operator in this subspace,  $U_i(\Gamma)$ , resulting from adiabatically changing the parameters along the path  $\Gamma$  in  $M$ , as illustrated in Figure 5.1. The Hilbert space can be separated into a number of such subspaces, the unitary operator on the entire Hilbert space is the product  $\mathcal{U}(\Gamma) = \prod_i U_i(\Gamma)$ .

Suppose the parameters  $\mathbf{q}(t')$  are varied adiabatically for times  $t' \in [0, t]$  along a path  $\Gamma$  (not necessarily closed). In a snapshot along the path, the local eigenstates of the  $N$ -fold degenerate subspace satisfy (we drop the subspace index  $i$  in this derivation)

$$H(t') |\psi_a(t')\rangle = E(t') |\psi_a(t')\rangle, \quad a = 1, \dots, N. \quad (5.4)$$

A state  $|\eta_a(t')\rangle$  with initial condition  $|\eta_a(0)\rangle = |\psi_a(0)\rangle$  evolves according to the Schrödinger equation,

$$i\hbar |\dot{\eta}_a(t')\rangle = H(t') |\eta_a(t')\rangle, \quad (5.5)$$

The state at a later time can be expanded in the local eigenbasis as

$$|\eta_a(t')\rangle = U_{ab}(t') |\psi_b(t')\rangle, \quad (5.6)$$

where  $U_{ab}(t')$  are matrix elements of the unitary time-evolution matrix, we wish to determine. This implies that the time-evolved states are themselves orthonormal (we drop the explicit time-dependence for better readability):

$$\langle \eta_b | \eta_a \rangle = \langle \psi_d | U_{bd}^* U_{ac} | \psi_c \rangle = U_{bd}^* U_{ac} \delta_{dc} = (UU^\dagger)_{ab} = \delta_{ab}. \quad (5.7)$$

Evidently, as  $|\eta_a\rangle$  belong to the degenerate subspace,  $i\hbar |\dot{\eta}_a\rangle = E |\eta_a\rangle$ , and hence  $\langle \eta_b | \dot{\eta}_a \rangle = -iE \delta_{ab} / \hbar$ . From Eq. (5.6) follows  $|\psi_c\rangle = (U^\dagger)_{ca} |\eta_a\rangle$  and  $\langle \psi_c | = \langle \eta_a | U_{ac}$ , which allows us to compute

$$A_{ab} \equiv i \langle \psi_b | \dot{\psi}_a \rangle = i(\dot{U}^\dagger U)_{ab} + E \delta_{ab} / \hbar \quad (5.8)$$

the matrix elements of the Hermitian gauge potential (or connection)  $A$ . This yields the matrix equation

$$\dot{U} = iU(A - E/\hbar), \quad (5.9)$$

where an identity matrix multiplied on  $E/\hbar$  is implicitly understood. Integrating this equation from times 0 to  $t$ , with the initial condition  $U(0) = \mathbb{1}$ , the solution is found in terms of a Dyson series producing the time-ordered exponential:

$$\begin{aligned} U(t) &= \sum_{n=0}^{\infty} \frac{1}{n!} \int_0^t dt_1 \int_0^{t_1} dt_2 \cdots \int_0^{t_{n-1}} dt_n T_t \{B(t_n) \cdots B(t_2) B(t_1)\} \\ &\equiv T_t \exp \left( \int_0^t dt' B(t') \right), \end{aligned} \quad (5.10)$$

where  $B \equiv i(A - E/\hbar)$ . Here  $T_t$  denotes the time-ordering operator placing the operators in order of increasing time arguments, i.e. earlier times to the left and later times to the right. By the Baker-Campbell-Hausdorff formula, the dynamical phase factor can be pulled out:

$$U(t) = \exp \left( -\frac{i}{\hbar} \int_0^t dt' E(t') \right) T_t \exp \left( i \int_0^t dt' A(t') \right). \quad (5.11)$$

Finally, let us rewrite the geometric part of  $U(t)$  as an integral in parameter space. Firstly, we see that (recall implied sum over  $\mu$ )

$$|\dot{\psi}_a\rangle = \frac{d}{dt} |\psi_a(\mathbf{q}(t))\rangle = \frac{dq_\mu}{dt} \frac{\partial}{\partial q_\mu} |\psi_a\rangle, \quad (5.12)$$

which means that the gauge potential can be expressed as

$$A = \frac{dq_\mu}{dt} A^\mu \quad (5.13)$$

where  $A^\mu$  is a time-independent matrix with elements

$$(A^\mu)_{ab} = i \langle \psi_b | \partial_\mu \psi_a \rangle, \quad (5.14)$$

where we introduced the short-hand notation  $\partial_\mu = \partial/\partial q_\mu$ . Inserting Eq. (5.13) allows us to express the geometric phase in a time-independent manner:

$$T_t \exp \left( i \int_0^t dt' A(t') \right) = \mathcal{P} \exp \left( i \int_\Gamma dq_\mu A^\mu \right), \quad (5.15)$$

where  $\mathcal{P}$  denotes the path-ordered integral along  $\Gamma$ , which inherits the ordering from the time-ordering, i.e. latest paths acts first. Notice that the adiabatic time-evolution has been derived for a general path. For a closed path  $U$  maps states from the degenerate subspace to itself; a map known in differential geometry as a *holonomy*. Combining Eq. (5.11) with Eq. (5.15) for a closed path, we arrive at the final expression for the holonomy,

$$U_i(\Gamma) = \underbrace{\exp \left( -i \int_0^t dt' E_i(t') \right)}_{\text{dynamic phase factor}} \underbrace{\mathcal{P} \exp \left( i \oint_\Gamma dq_\mu A_i^\mu \right)}_{\text{geometric holonomy}}, \quad (5.16)$$

where we have re-inserted the subspace index. Borrowing nomenclature from gauge theory, the  $N \times N$ -matrix  $A_i(\mathbf{q}) = dq_\mu A_i^\mu(\mathbf{q})$  is known as a gauge connection or gauge potential. In the case  $N = 1$ , the gauge potential is Abelian, and we recover the expression for Berry's phase of Eq. (5.3). However, in the general case, a non-Abelian gauge potential can lead to off-diagonal elements in the holonomy, which mixes the initial states in the subspace.

## 5.2 Two-qubit holonomic gate

The canonical example of a system with a non-Abelian gauge potential is a time-reversal invariant Fermi system, which by Kramer's theorem has a two-fold degenerate subspace for any point in  $M$ [199, 200, 206, 207]. Recently, Sugawa *et al.*[202] realized this system by simulating the four-level Hamiltonian

$$H = -\frac{\hbar}{2} \mathbf{q} \cdot \mathbf{\Gamma} = -\frac{\hbar}{2} (q_1 \Gamma_1 + q_2 \Gamma_2 + q_3 \Gamma_3 + q_4 \Gamma_4 + q_5 \Gamma_5), \quad (5.17)$$

where the  $\Gamma_j$ 's are the  $4 \times 4$  Dirac matrices.

Compare Eq. (5.17) to the Hamiltonian  $H = -\mu \mathbf{B} \cdot \boldsymbol{\sigma}$  of a spin-1/2 particle with magnetic moment  $\mu$  in a magnetic field  $\mathbf{B}$ , which is the textbook example of a system with a Berry's phase[208]. The spin-1/2 system has two eigenstates with energies  $\pm |\mu \mathbf{B}|$ , which are non-degenerate for  $\mu \mathbf{B} \neq \mathbf{0}$ . Thus, the gauge potential associated with each subspace is Abelian with matrix dimension  $N = 1$ .

The simplest system with a non-Abelian gauge potential must have a subspace with degeneracy  $N = 2$ . This can be achieved through Kramer's degeneracy[207] present in a time-reversal invariant Fermi system, such as a spin-3/2 particle in an electric quadrupole field[199, 200], for which the Hamiltonian can be cast on the form of Eq. (5.17). Here  $\mathbf{q}$  is a parameter vector that determine the quadrupole field matrix, and the Dirac matrices are certain combinations of spin-3/2 operators. The spin-3/2 system has four states grouped in two degenerate subspaces with energy  $\pm (\hbar/2) |\mathbf{q}|$ . The subspaces are separated in energy except when the quadrupole field is zero ( $\mathbf{q} = \mathbf{0}$ ), and all four states become degenerate with zero energy. This is reminiscent of the system of a spin-1/2 particle in a magnetic field, except that the gauge potential associated with each subspace is non-Abelian with matrix dimension  $N = 2$ . However, the physical interpretation of the Hamiltonian is irrelevant for the geometric properties, and in the following we will consider an implementation of Eq. (5.17) not as a spin-3/2 system, but as two coupled qubits.

We employ the definitions and conventions of Ref. [202] for the Dirac matrices and time-reversal operator, which can all be represented as two-qubit operators. The time-reversal operator is  $T = \Theta K$ , where  $K$  performs a complex conjugation, and  $\Theta = i\sigma_y^{(1)} \mathbb{1}^{(2)}$ , where the tensor product between the Pauli  $y$ -operator on qubit 1 and the

identity on qubit 2. Note that the time-reversal operator has the following effect on the computational two-qubit basis states:

$$T\{|00\rangle, |01\rangle, |10\rangle, |11\rangle\} = \{-|10\rangle, -|11\rangle, |00\rangle, |01\rangle\}. \quad (5.18)$$

We can therefore choose the following as our basis

$$\{|10\rangle, T|10\rangle, |11\rangle, T|11\rangle\}, \quad (5.19)$$

in which the Dirac matrices are:

$$\Gamma_1 = \begin{bmatrix} 0 & 0 & 0 & 1 \\ 0 & 0 & -1 & 0 \\ 0 & -1 & 0 & 0 \\ 1 & 0 & 0 & 0 \end{bmatrix} = \sigma_y^{(1)} \sigma_y^{(2)}, \quad (5.20)$$

$$\Gamma_2 = \begin{bmatrix} 0 & 0 & 1 & 0 \\ 0 & 0 & 0 & 1 \\ 1 & 0 & 0 & 0 \\ 0 & 1 & 0 & 0 \end{bmatrix} = \mathbb{1}^{(1)} \sigma_x^{(2)}, \quad (5.21)$$

$$\Gamma_3 = \begin{bmatrix} 0 & 0 & -i & 0 \\ 0 & 0 & 0 & i \\ i & 0 & 0 & 0 \\ 0 & -i & 0 & 0 \end{bmatrix} = -\sigma_z^{(1)} \sigma_y^{(2)}, \quad (5.22)$$

$$\Gamma_4 = \begin{bmatrix} 1 & 0 & 0 & 0 \\ 0 & 1 & 0 & 0 \\ 0 & 0 & -1 & 0 \\ 0 & 0 & 0 & -1 \end{bmatrix} = \mathbb{1}^{(1)} \sigma_z^{(2)}, \quad (5.23)$$

$$\Gamma_5 = \begin{bmatrix} 0 & 0 & 0 & -i \\ 0 & 0 & -i & 0 \\ 0 & i & 0 & 0 \\ i & 0 & 0 & 0 \end{bmatrix} = \sigma_x^{(1)} \sigma_y^{(2)}. \quad (5.24)$$

Since  $T^2 = -1$  and  $T$  commutes with the above Dirac matrices – and thus  $H$  of Eq. (5.17) – Kramer's theorem ensures doubly degenerate energy levels for every parameter vector  $\mathbf{q}$ . The time-reversal symmetry of the system is more explicit if we express the Hamiltonian as an operator on a quaternionic vector space instead of the usual complex Hilbert space. The formalism of quaternionic vector spaces is explained in Ref. [200], from which we borrow definitions and conventions such as right scalar multiplication.

### 5.2.1 Quaternionic representation

The quaternions  $\mathbb{H}$  is a non-commutative field generated by  $i, j$ , and  $k$  with the property  $i^2 = j^2 = k^2 = ijk = -1$ . A quaternionic scalar  $x = x_0 + x_1i + x_2j + x_3k \in \mathbb{H}$  has the conjugate  $\bar{x} = x_0 - x_1i - x_2j - x_3k \in \mathbb{H}$  and the norm  $|x| = \sqrt{\bar{x}x} \in \mathbb{R}$ . The fermionic time-reversal operator,  $T$ , can be interpreted as a quaternionic structure map, which means that scalar multiplication with  $j$  and  $k$  in the quaternionic vector space can be interpreted as a time-reversal operator in the complex vector space. This means that any state of the system can be expressed as a vector in four-dimensional complex vector space, or, equivalently, as a vector in a two-dimensional quaternionic vector space. We can use  $\{|10\rangle, |11\rangle\}$  as a basis for  $\mathbb{H}^2$ , noticing that the two quaternionic coefficients comprise the same amount of information (eight real numbers) as the four complex coefficients defining a vector in  $\mathbb{C}^4$ . This basis is chosen deliberately since our basis for  $\mathbb{C}^4$  in Eq. (5.19) can be derived from the quaternionic basis,  $\{|10\rangle, |11\rangle\}$ , by applying  $T$  to each basis state. Specifically, for a state  $|\psi\rangle \in \mathbb{C}^4$ , the (right) quaternionic action is defined by

$$|\psi\rangle i \equiv i |\psi\rangle, \quad (5.25)$$

$$|\psi\rangle j \equiv T |\psi\rangle, \quad (5.26)$$

$$|\psi\rangle k \equiv (|\psi\rangle i)j = T(i |\psi\rangle) = -iT |\psi\rangle. \quad (5.27)$$

We can write any state as a linear combination of  $|10\rangle$  and  $|11\rangle$  with quaternionic coefficients:

$$|\psi\rangle = \sum_{l=0,1} |1l\rangle (v_{l,0} + v_{l,1}i + v_{l,2}j + v_{l,3}k) \quad (5.28)$$

with  $v_{l,\alpha} \in \mathbb{R}$  for  $l = 0, 1$  and  $\alpha = 0, 1, 2, 3$ . Using the definitions above, this corresponds to the following decomposition in the complex vector space:

$$|\psi\rangle = \sum_{l=0,1} \left[ |1l\rangle (v_{l,0} + v_{l,1}i) + (T |1l\rangle)(v_{l,2} - v_{l,3}i) \right]. \quad (5.29)$$

Here the state is expressed as a linear combination of the four basis states of Eq. (5.19) with complex coefficients.

As a quaternionic operator on  $\mathbb{H}^2$ , the Hamiltonian of Eq. (5.17) is expressed as:

$$H = -\frac{\hbar}{2} \begin{bmatrix} q_4 & \bar{q} \\ q & -q_4 \end{bmatrix}, \quad (5.30)$$

with  $q = q_2 + q_3i + q_1j - q_5k \in \mathbb{H}$ . This expression can also be found from the representation of the quaternionic units in terms of Pauli matrices,  $i\sigma_z \sim i$ ,  $-i\sigma_y \sim j$  and  $-i\sigma_x \sim k$ , which are identified with the  $2 \times 2$  blocks in the Dirac matrices of Eqs. (5.20)–(5.24) and plugged into Eq. (5.17). The normalized quaternionic eigenvectors of  $H$  are

$$|\psi_{\pm}\rangle = N_{\pm}(\mathbf{q}) \begin{bmatrix} q_4 \pm |\mathbf{q}| \\ q \end{bmatrix}, \quad (5.31)$$

with eigenvalues  $E_{\pm}(\mathbf{q}) = (-\hbar/2)(\pm|\mathbf{q}|)$ , where the normalization factor is  $N_{\pm}(\mathbf{q}) = \left[|q|^2 + (q_4 \pm |\mathbf{q}|)^2\right]^{-1/2}$ . The degeneracy point  $\mathbf{q} = \mathbf{0}$  is known as a Yang monopole, but regarded as a quaternionic matrix,  $H$  is non-degenerate everywhere else in parameter space. However, as a complex matrix, we know it is everywhere two-fold degenerate. Mapping the eigenvectors of Eq. (5.31) to the complex vector space via Eq. (5.29) only gives us two four-dimensional complex vectors:

$$\begin{aligned} |\psi_{\pm}\rangle &= N_{\pm} [|10\rangle (q_4 \pm |\mathbf{q}|) + |11\rangle (q_2 + q_3i + q_1j - q_5k)] \\ &= N_{\pm} [|10\rangle (q_4 \pm |\mathbf{q}|) + |11\rangle (q_2 + q_3i) + (T|11\rangle)(q_1 + q_5i)] \\ &= N_{\pm} [|10\rangle (q_4 \pm |\mathbf{q}|) + |11\rangle (q_2 + q_3i) + |01\rangle (q_1 + q_5i)]. \end{aligned} \quad (5.32)$$

The remaining two orthogonal vectors are, by Kramer's theorem, found by application of  $T$  to each eigenvector:

$$T|\psi_{\pm}\rangle = N_{\pm} [|00\rangle (q_4 \pm |\mathbf{q}|) + |01\rangle (q_2 + q_3i) - |11\rangle (q_1 + q_5i)]. \quad (5.33)$$

### 5.2.2 Holonomy as a quantum gate

Adiabatically traversing a closed path,  $\Gamma$ , in parameter space produces the geometric holonomy,

$$U_{\pm}^G(\Gamma) = \mathcal{P} \exp \left( i \oint_{\Gamma} A_{\pm}(\mathbf{q}) \right), \quad (5.34)$$

where the superscript  $G$  reminds us, that we only consider the geometric part of the unitary operator of Eq. (5.16). In the following, we are not interested in the dynamic part, which only contributes a phase difference to states in different energy subspaces.

Let us now consider the Hilbert space as a four-dimensional complex vector space. Since  $\Gamma$  is closed, the unitary operation on the Hilbert space,  $U^G = U_-^G U_+^G$ , maps the states at the initial parameter point to itself. For example, if the system parameters are initially  $\mathbf{q} = (q_1, 0, 0, 0, 0)$ , with  $q_1 > 0$ , the four basis states are the Bell states:

$$|\psi_+\rangle = \frac{1}{\sqrt{2}}(|10\rangle + |01\rangle) = |\Psi^+\rangle, \quad (5.35)$$

$$T|\psi_+\rangle = \frac{1}{\sqrt{2}}(|00\rangle - |11\rangle) = |\Phi^-\rangle, \quad (5.36)$$

$$|\psi_-\rangle = \frac{1}{\sqrt{2}}(|01\rangle - |10\rangle) = |\Psi^-\rangle, \quad (5.37)$$

$$T|\psi_-\rangle = -\frac{1}{\sqrt{2}}(|00\rangle + |11\rangle) = -|\Phi^+\rangle. \quad (5.38)$$

From a quantum computational point of view,  $U^G$  is a gate operation, which can mix states in the same energy subspace, spanned by  $\{|\psi_+\rangle, T|\psi_+\rangle\}$  and  $\{|\psi_-\rangle, T|\psi_-\rangle\}$ , respectively, but is protected from mixing states from different subspaces. Suppose we pick  $\Gamma$  such that  $U_{\pm}^G(\Gamma) = \sigma_x$ , then

$$U_+^G(\Gamma) |\Psi^+\rangle = |\Phi^-\rangle, \quad (5.39)$$

$$U_-^G(\Gamma) |\Psi^-\rangle = -|\Phi^+\rangle. \quad (5.40)$$

This gate performs a time-reversal operation, which is equivalent to the simple Pauli  $y$ -gate on the first qubit. A more interesting example would be an entangling two-qubit gate. However, this simple example with Bell states illustrates the idea of a holonomic gate: the initial parameter points defines which states can be mapped onto which, and the path in parameter space defines the mapping. Due to the large freedom in these choices, there is a large search space for potentially interesting quantum gates.

### 5.2.3 Gauge potential and holonomy

In the quaternionic representation the gauge potential is a non-Abelian scalar,  $A_{\pm} = dq_{\mu} A_{\pm}^{\mu}$ , with components on the form

$$A_{\pm}^{\mu} = A_{0,\pm}^{\mu} + A_{1,\pm}^{\mu} i + A_{2,\pm}^{\mu} j + A_{3,\pm}^{\mu} k, \quad (5.41)$$

with real coefficients,  $A_{\alpha,\pm} \in \mathbb{R}$  for  $\alpha = 0, 1, 2, 3$ . The geometric holonomy of Eq. (5.34) becomes

$$U_{\pm}^G(\Gamma) = \mathcal{P} \exp \left( \oint_{\Gamma} dq_{\mu} (iA_{0,\pm}^{\mu} - A_{1,\pm}^{\mu} + kA_{2,\pm}^{\mu} - jA_{3,\pm}^{\mu}) \right). \quad (5.42)$$

Since  $U_{\pm}^G$  is unitary, the real part,  $A_{1,\pm}$ , cannot contribute to the integral. Inserting the Pauli matrix representation,  $i \sim i\sigma_z$ ,  $j \sim -i\sigma_y$  and  $k \sim -i\sigma_x$ , we get the expression for the operator on the complex vector space:

$$U_{\pm}^G(\Gamma) = \mathcal{P} \exp \left( i \oint_{\Gamma} dq_{\mu} (\sigma_z A_{0,\pm}^{\mu} - \sigma_x A_{2,\pm}^{\mu} + \sigma_y A_{3,\pm}^{\mu}) \right), \quad (5.43)$$

From this we see that  $A_{0,\pm}^{\mu}$  contributes to a phase operation, and  $A_{2,\pm}^{\mu}$  and  $A_{3,\pm}^{\mu}$  contribute to non-diagonal elements in  $U_{\pm}^G$ , which transforms the basis states, such as in Eqs. (5.39)–(5.40). The  $\mu$ 's component of the gauge potential is computed as

$$\begin{aligned} A_{\pm}^{\mu} &= i \langle \psi_{\pm} | \partial_{\mu} \psi_{\pm} \rangle \\ &= \underbrace{iN_{\pm}^{-1} \partial_{\mu} N_{\pm} + iN_{\pm} (q_4 \pm |\mathbf{q}|) \partial_{\mu} (q_4 \pm |\mathbf{q}|)}_{\text{purely imaginary}} + iN_{\pm} \bar{q} \partial_{\mu} q. \end{aligned} \quad (5.44)$$

The purely imaginary terms contribute to  $A_{1,\pm}^{\mu}$  and can be ignored. The only source of contributions to  $U_{\pm}^G$  is

$$i\bar{q} \partial_{\mu} q = \begin{cases} q_1 i + q_5 + q_2 k + q_3 j, & \mu = 1 \\ q_2 i + q_3 - q_1 k - q_5 j, & \mu = 2 \\ q_3 i - q_2 + q_5 k - q_1 j, & \mu = 3 \\ 0, & \mu = 4 \\ q_5 i - q_1 - q_3 k + q_2 j, & \mu = 5 \end{cases} \quad (5.45)$$

If, for instance,  $q_1$  is varied along  $\Gamma$ , i.e.  $dq_1 \neq 0$ , then the gauge potential would contain terms proportional to  $q_1 i + q_5 + q_2 k + q_3 j$ . In order to obtain, say,  $\sigma_y$  in the integrand of Eq. (5.43)  $q_2 \propto A_{\pm,3}^1$  must be non-zero along the part of  $\Gamma$  where  $dq_1 \neq 0$ . Similarly, a  $\sigma_x$  term can only appear if  $q_3 \propto A_{\pm,2}^1$  is non-zero when  $dq_1 \neq 0$ .

These observations are summarized in Table 5.1. From this we see that whenever we change a single parameter among  $\{q_1, q_2, q_3, q_5\}$ , the remaining three parameters control a Pauli matrix each. However,

Vary	$\sigma_z$	$\sigma_x$	$\sigma_y$
$q_1$	$q_5$	$q_3$	$q_2$
$q_2$	$q_3$	$q_5$	$q_1$
$q_3$	$q_2$	$q_1$	$q_5$
$q_4$	—	—	—
$q_5$	$q_1$	$q_2$	$q_3$

Table 5.1: If the parameter in the left column is varied along  $\Gamma$ , the right columns show which parameters are multiplied to each Pauli matrix in the path integral of Eq. (5.43).

the path-ordered integral cannot be computed analytically, except for special cases such as where the integrand only contains one Pauli matrix along each line segment of  $\Gamma$ .

#### 5.2.4 Final remarks

A further investigation into the holonomic quantum gates of the system would require a search of (i) the initial parameter points, which defines the Hilbert space the holonomy acts on, and (ii) the closed paths defining the gate itself. One could explore the Hilbert spaces analytically, as Eqs. (5.32)–(5.33) give the basis states in terms of computational states, but a general search for interesting quantum gates would be numerical. However, at this point it is not even clear if the system accommodates entangling two-qubit holonomic gates. If a desired gate or family of gates was found, the next step would be to design a superconducting chip that implements exactly the necessary coupling, and make sure they are sufficiently tunable through external fluxes.

This is a daunting task, and while the idea of using non-Abelian geometric phases to implement quantum gates is academically intriguing, it is likely that more efficient gates can be engineered by other means, for instance as discussed in the previous chapter.

# Mixed-dimensional Bose polaron

This appendix is quoted from Ref. [5] with minor changes to fit the context here.

First we derive expressions for  $\Sigma_0(\mathbf{k}_\perp, \omega)$  and  $\Sigma_1(\mathbf{k}_\perp, \omega)$  that sum to be the polaron self-energy  $\Sigma(\mathbf{k}_\perp, \omega)$ , the key ingredient in all further computations. From the self-energy we may directly evaluate the spectral function  $A(\mathbf{k}_\perp, \omega)$  from Eq. (2.73) and obtain the quasiparticle energy  $\varepsilon_{\mathbf{k}_\perp}$  as the solution to Eq. (2.70). The quasiparticle residue  $Z_{\mathbf{k}_\perp}$  and the effective mass  $m_{\mathbf{k}_\perp}^*$  given by Eqs. (2.71)–(2.72) require the derivatives of the self-energy.

## A.1 $\Sigma_0$ and its derivatives

Computation of  $\Sigma_0(\mathbf{k}_\perp, \omega)$  as given in Eq. (2.63) requires the pair propagator given in Eq. (2.68) with  $i\omega_m + \mu \rightarrow \omega + i0^+$ . In this section we consider the following:

$$\Sigma_0(\mathbf{0}, \omega) = \frac{n_B}{g^{-1} - \Pi(\mathbf{0}, \omega)} \quad (\text{A.1})$$

$$\partial_\omega \Sigma_0(\mathbf{0}, \omega) = \frac{1}{n_B} (\Sigma_0(\mathbf{0}, \omega))^2 \partial_\omega \Pi(\mathbf{0}, \omega) \quad (\text{A.2})$$

$$k_\perp^{-1} \partial_{k_\perp} \Sigma_0(\mathbf{k}_\perp, \omega)|_{k_\perp=0} = \frac{1}{n_B} (\Sigma_0(\mathbf{0}, \omega))^2 k_\perp^{-1} \partial_{k_\perp} \Pi(\mathbf{k}_\perp, \omega)|_{k_\perp=0}. \quad (\text{A.3})$$

We start by simplifying the pair propagator by taking the zero-temperature limit, i.e., by setting the Bose distribution function  $f_{\mathbf{p}} = 0$ . In spherical coordinates the pair propagator becomes:

$$\begin{aligned} \Pi(\mathbf{k}_{\perp}, \omega) &= \frac{2m_B}{(2\pi)^3} \int_0^{\infty} dp p^2 \int_0^{\pi} d\theta \sin\theta \int_0^{2\pi} d\phi \\ &\times \left[ \left( \frac{p^2 + \tilde{g}_B}{2\tilde{E}_p} + \frac{1}{2} \right) \frac{1}{2m_B\omega - \tilde{E}_p - \alpha^{-1}(p^2 \sin^2\theta + k_{\perp}^2 - 2pk_{\perp} \sin\theta \cos\phi) + i0^+} + \frac{1}{p^2(1 + \alpha^{-1} \sin^2\theta)} \right] \end{aligned} \quad (\text{A.4})$$

with  $\tilde{E}_p \equiv \sqrt{p^2(p^2 + 2\tilde{g}_B)}$  and  $\tilde{g}_B \equiv 2m_B g_B n_B$ . The integral over  $\phi$  is trivial when  $k_{\perp} = 0$ , but it can be performed also in the case  $k_{\perp} \neq 0$ . In the latter case, we let  $z_0 = (2m_B\omega - \tilde{E}_p - \alpha^{-1}(p^2 \sin^2\theta + k_{\perp}^2) + i0^+) / (2\alpha^{-1}pk_{\perp} \sin\theta)$  located in the upper half complex plane. The  $\phi$  integral takes the form  $\int_0^{2\pi} d\phi (z_0 + \cos\phi)^{-1} = 2\pi / (\sqrt{z_0 - 1}\sqrt{z_0 + 1})$ , where the complex square roots should be taken in the upper half plane. The integral over  $\theta$  can be simplified by defining  $x = -\cos\theta$  and substituting  $\int_0^{\pi} d\theta \sin\theta \rightarrow 2 \int_0^1 dx$ , yielding for the pair propagator:

$$\begin{aligned} \Pi(\mathbf{k}_{\perp}, \omega) &= \frac{2m_B}{2\pi^2} \int_0^{\infty} dp \int_0^1 dx \left[ \left( \frac{p^2 + \tilde{g}_B}{2\tilde{E}_p} + \frac{1}{2} \right) \frac{p^2}{\sqrt{z_+}\sqrt{z_-}} + \frac{1}{1 + \alpha^{-1}(1 - x^2)} \right] \\ &= \frac{2m_B}{2\pi^2} \int_0^{\infty} dp \left[ \left( \frac{p^2 + \tilde{g}_B}{2\tilde{E}_p} + \frac{1}{2} \right) \int_0^1 dx \frac{p^2}{\sqrt{z_+}\sqrt{z_-}} + \frac{\text{arcsinh}(\alpha^{-1/2})}{\sqrt{\alpha^{-1}(\alpha^{-1} + 1)}} \right] \end{aligned} \quad (\text{A.5})$$

with  $z_{\pm} = 2m_B\omega - \tilde{E}_p - \alpha^{-1}(p\sqrt{1 - x^2} \pm k_{\perp})^2 + i0^+$ . In the case  $k_{\perp} = 0$  the expression reduces to

$$\begin{aligned} \Pi(\mathbf{0}, \omega) &= \frac{2m_B}{2\pi^2} \int_0^{\infty} dp \left[ \left( \frac{p^2 + \tilde{g}_B}{2\tilde{E}_p} + \frac{1}{2} \right) \int_0^1 dx \frac{p^2}{2m_B\omega - \tilde{E}_p - \alpha^{-1}p^2(1 - x^2) + i0^+} + \frac{\text{arcsinh}(\alpha^{-1/2})}{\sqrt{\alpha^{-1}(\alpha^{-1} + 1)}} \right] \\ &= \frac{2m_B}{2\pi^2} \int_0^{\infty} dp \left[ \left( \frac{p^2 + \tilde{g}_B}{2\tilde{E}_p} + \frac{1}{2} \right) \mathcal{P} \int_0^1 dx \frac{p^2}{2m_B\omega - \tilde{E}_p - \alpha^{-1}p^2(1 - x^2)} + \frac{\text{arcsinh}(\alpha^{-1/2})}{\sqrt{\alpha^{-1}(\alpha^{-1} + 1)}} \right] \\ &- i\pi \frac{2m_B}{2\pi^2} \int_0^{\infty} dp p^2 \left( \frac{p^2 + \tilde{g}_B}{2\tilde{E}_p} + \frac{1}{2} \right) \int_0^1 dx \delta(2m_B\omega - \tilde{E}_p - \alpha^{-1}p^2(1 - x^2)). \end{aligned} \quad (\text{A.6})$$

The second equality separates the real and imaginary part of the integral. Here  $\mathcal{P}$  denotes the Cauchy principal value integral and  $\delta(x)$  is the Dirac delta function. In practice we use the first line in Eq. (A.6) to calculate the real part of the integral by setting  $0^+$  to a positive number which is sufficiently small. We let  $z_1 = (2m_B\omega - \tilde{E}_p - \alpha^{-1}p^2 + i0^+)\alpha/p^2$  and take the  $x$  integral as  $\int_0^1 dx (z_1 + x^2)^{-1} = \text{arccot}(\sqrt{z_1})/\sqrt{z_1}$  with the complex square root taken in the upper half plane. Hence

$$\begin{aligned} & \Re\epsilon\Pi(\mathbf{0}, \omega) \\ &= \frac{2m_B}{2\pi^2} \int_0^\infty dp \left[ \left( \frac{p^2 + \tilde{g}_B}{2\tilde{E}_p} + \frac{1}{2} \right) \Re\epsilon \left( \frac{\alpha \text{arccot}(\sqrt{z_1})}{\sqrt{z_1}} \right) + \frac{\text{arcsinh}(\alpha^{-1/2})}{\sqrt{\alpha^{-1}(\alpha^{-1}+1)}} \right]. \end{aligned} \quad (\text{A.7})$$

For the imaginary part of the pair propagator, we define a new variable  $u = 1 - x^2$  and the function  $u_\delta(p) = (2m_B\omega - \tilde{E}_p)\alpha/p^2$  which allows us to express

$$\Im\Pi(\mathbf{0}, \omega) = -\frac{2m_B}{2\pi} \int_0^\infty dp \left( \frac{p^2 + \tilde{g}_B}{2\tilde{E}_p} + \frac{1}{2} \right) \int_0^1 du \frac{\alpha}{2\sqrt{1-u}} \delta(u_\delta(p) - u). \quad (\text{A.8})$$

The Dirac delta function is only non-vanishing along the  $u$  integration interval for those values of  $p$  where  $0 < u_\delta(p) < 1$ . Notice that this implies that  $\Im\Pi(\mathbf{0}, \omega) = 0$  for  $\omega \leq 0$ . In the case  $\omega > 0$  we have to determine the values of  $p$  in the integration interval that fulfill  $0 < u_\delta(p) < 1$ . Formally we may define this set as  $\mathcal{V} = \{p \in (0; \infty) : u_\delta(p) \in (0; 1)\}$ . Since the Dirac delta function contributes only when  $p \in \mathcal{V}$ , we have

$$\Im\Pi(\mathbf{0}, \omega) = -\frac{2m_B}{2\pi} \int_{\mathcal{V}} dp \left( \frac{p^2 + \tilde{g}_B}{2\tilde{E}_p} + \frac{1}{2} \right) \frac{\alpha}{2\sqrt{1 - u_\delta(p)}}. \quad (\text{A.9})$$

We now prove that  $\mathcal{V}$  is an interval. First notice that  $u_\delta(p) \rightarrow \infty$  as  $p \rightarrow 0$  and  $u_\delta(p) \rightarrow -\alpha < 0$  as  $p \rightarrow \infty$ . Since  $u_\delta$  is continuous the inequality  $0 < u_\delta(p) < 1$  is indeed fulfilled somewhere along the  $p$  integration. Second we notice from explicit computation that the equation  $du_\delta/dp = 0$  has at most one real solution on  $(0; \infty)$  which must correspond to a global minimum. Thus  $u_\delta$  decreases monotonically in the region where  $0 < u_\delta(p) < 1$ . We conclude that

$\mathcal{V} = (p_{\min}; p_{\max})$  with the end points uniquely defined by  $u_\delta(p_{\min}) = 1$  and  $u_\delta(p_{\max}) = 0$ . Explicitly we have

$$p_{\min} = \begin{cases} \sqrt{\frac{-\tilde{g}_B \alpha^2 - \omega \alpha - \alpha \sqrt{(\tilde{g}_B^2 + \omega^2) \alpha^2 + 2\tilde{g}_B \omega \alpha}}{\alpha^2 - 1}} & \text{if } \alpha < 1 \\ \sqrt{\frac{\omega^2}{2(\tilde{g}_B + \omega)}} & \text{if } \alpha = 1 \\ \sqrt{\frac{-\tilde{g}_B \alpha^2 - \omega \alpha + \alpha \sqrt{(\tilde{g}_B^2 + \omega^2) \alpha^2 + 2\tilde{g}_B \omega \alpha}}{\alpha^2 - 1}} & \text{if } \alpha > 1 \end{cases} \quad (\text{A.10})$$

and

$$p_{\max} = \sqrt{-\tilde{g}_B + \sqrt{\tilde{g}_B^2 + \omega^2}}. \quad (\text{A.11})$$

The imaginary part of the pair propagator takes the final form:

$$\begin{aligned} \Im \Pi(\mathbf{0}, \omega) &= \begin{cases} 0 & \text{if } \omega \leq 0 \\ -\frac{2m_B}{2\pi} \int_{p_{\min}}^{p_{\max}} dp \left( \frac{p^2 + \tilde{g}_B}{2\tilde{E}_p} + \frac{1}{2} \right) \frac{\alpha}{2\sqrt{1 - (2m_B \omega - \tilde{E}_p) \alpha / p^2}} & \text{if } \omega > 0. \end{cases} \end{aligned} \quad (\text{A.12})$$

We now turn to the derivatives of the pair propagator appearing in Eqs. (A.2)–(A.3). From Eq. (A.5) we find

$$\begin{aligned} \partial_\omega \Pi(\mathbf{k}_\perp, \omega) &= \frac{(2m_B)^2}{2\pi^2} \int_0^\infty dp \left( \frac{p^2 + \tilde{g}_B}{2\tilde{E}_p} + \frac{1}{2} \right) \\ &\quad \times \int_0^1 dx \left[ \frac{-p^2}{2(z_+)^{3/2} \sqrt{z_-}} + \frac{-p^2}{2(z_-)^{3/2} \sqrt{z_+}} \right], \end{aligned} \quad (\text{A.13})$$

which simplifies in the case  $k_\perp = 0$  using  $z_- = z_+$  and  $\int_0^1 dx (z_1 + x^2)^{-2} = (\sqrt{z_1} / (z_1 + 1) + \operatorname{arccot}(\sqrt{z_1})) / (2z_1^{3/2})$ , where the complex square root should be taken in the upper half plane (note that  $z_1^{3/2} = z_1 \sqrt{z_1}$ ). We find

$$\begin{aligned} \partial_\omega \Pi(\mathbf{0}, \omega) &= -\frac{(2m_B)^2}{2\pi^2} \int_0^\infty dp \left( \frac{p^2 + \tilde{g}_B}{2\tilde{E}_p} + \frac{1}{2} \right) \\ &\quad \times \frac{\alpha^2}{2z_1^{3/2} p^2} \left[ \frac{\sqrt{z_1}}{z_1 + 1} + \operatorname{arccot}(\sqrt{z_1}) \right]. \end{aligned} \quad (\text{A.14})$$

Similarly we find

$$k_{\perp}^{-1} \partial_{k_{\perp}} \Pi(\mathbf{k}_{\perp}, \omega) = \frac{2m_B}{2\pi^2} \int_0^{\infty} dp \left( \frac{p^2 + \tilde{g}_B}{2\tilde{E}_p} + \frac{1}{2} \right) \times \int_0^1 dx \frac{-p^2 2\alpha^{-1} k_{\perp} (\alpha^{-1} (k_{\perp} - p\sqrt{1-x^2})(k_{\perp} + p\sqrt{1-x^2}) - 2m_B\omega + \tilde{E}_p - i0^+)}{z_+^{3/2} z_-^{3/2}}. \quad (\text{A.15})$$

Notice that we may safely put  $k_{\perp} = 0$  in the above expression and evaluate the  $x$  integral:

$$\begin{aligned} k_{\perp}^{-1} \partial_{k_{\perp}} \Pi(\mathbf{k}_{\perp}, \omega)|_{k_{\perp}=0} &= \frac{2m_B}{\pi^2} \int_0^{\infty} dp \left( \frac{p^2 + \tilde{g}_B}{2\tilde{E}_p} + \frac{1}{2} \right) \frac{p^2}{\alpha} \\ &\times \int_0^1 dx \frac{2m_B\omega - \tilde{E}_p + i0^+ + \alpha^{-1} p^2 (1-x^2)}{(2m_B\omega - \tilde{E}_p + i0^+ - \alpha^{-1} p^2 (1-x^2))^3} \\ &= \frac{2m_B}{4\pi^2 \alpha} \int_0^{\infty} dp \left( \frac{p^2 + \tilde{g}_B}{2\tilde{E}_p} + \frac{1}{2} \right) p^2 \left[ \frac{3}{(2m_B\omega - \tilde{E}_p + i0^+ - \alpha^{-1} p^2)^2} \right. \\ &\quad \left. + \frac{\sqrt{\alpha} (2m_B\omega - \tilde{E}_p + i0^+ + 2\alpha^{-1} p^2) \operatorname{arccot}(z_1)}{p (2m_B\omega - \tilde{E}_p + i0^+ - \alpha^{-1} p^2)^{5/2}} \right]. \quad (\text{A.16}) \end{aligned}$$

This concludes the derivations of the numerical integrals we implemented in order to compute Eqs. (A.1)–(A.3).

## A.2 $\Sigma_1$ and its derivatives

In this section we shall compute  $\Sigma_1(\mathbf{0}, \omega)$  and the derivatives  $\partial_{\omega} \Sigma_1(\mathbf{0}, \omega)$  and  $k_{\perp}^{-1} \partial_{k_{\perp}} \Sigma_1(\mathbf{k}_{\perp}, \omega)|_{k_{\perp}=0}$ . From Eq. (2.64), with  $i\omega_n + \mu \rightarrow \omega + i0^+$ , we have

$$\begin{aligned} \Sigma_1(\mathbf{k}_{\perp}, \omega) &= -T \sum_{\nu} \int \frac{d^3 p}{(2\pi)^3} \left( \frac{u_{\mathbf{p}}^2}{i\omega_{\nu} - E_{\mathbf{p}}} - \frac{v_{\mathbf{p}}^2}{i\omega_{\nu} + E_{\mathbf{p}}} \right) \\ &\times \frac{1}{g^{-1} - \Pi(\mathbf{p}_{\perp} + \mathbf{k}_{\perp}, i\omega_n + i\omega_{\nu})} \Big|_{i\omega_n + \mu \rightarrow \omega + i0^+} \\ &= \int \frac{d^3 p}{(2\pi)^3} \frac{v_{\mathbf{p}}^2}{g^{-1} - \Pi(\mathbf{p}_{\perp} + \mathbf{k}_{\perp}, \omega - E_{\mathbf{p}})}, \quad (\text{A.17}) \end{aligned}$$

where the last line is found from performing the sum over Matsubara frequencies and letting the temperature  $T \rightarrow 0$ . Here we exploit that

the chemical potential  $\mu$  is minus infinity such that any poles and branch cuts of the  $\mathcal{T}$ -matrix are pushed to infinity.

We have to simplify the expression above in order to get a numerical feasible implementation. Therefore we approximate the pair propagator by that for a non-interaction Bose gas at zero temperature  $\Pi_{\text{vac}}$ . This amounts to setting  $g_B = 0$  and  $f_{\mathbf{p}} = 0$  in Eq. (2.68). We now show that it reduces to the expression in Eq. (2.74). Notice that these approximations are only applied to the pair propagator, as setting the temperature to zero in the entire expression for  $\Sigma_1$  would make it vanish, and this we are definitely not interested in. The pair propagator takes the form

$$\begin{aligned} & \Pi_{\text{vac}}(\mathbf{p}_\perp, \omega - E_{\mathbf{p}}) \\ &= \int \frac{d^3 \tilde{\mathbf{p}}}{(2\pi)^3} \left[ \frac{1}{\omega - E_{\mathbf{p}} - \tilde{\mathbf{p}}^2/2m_B - (\mathbf{k}_\perp + \mathbf{p}_\perp + \tilde{\mathbf{p}}_\perp)^2/2m + i0^+} + \frac{2m_B}{\tilde{\mathbf{p}}^2 + \tilde{\mathbf{p}}_\perp^2/\alpha} \right]. \end{aligned} \quad (\text{A.18})$$

We shift  $\tilde{\mathbf{p}}$  in the first term in the integrand by adding the constant vector  $\mathbf{p}_\perp m_B/M$ . Then we scale  $\tilde{\mathbf{p}}_\perp$  in the entire integrand by the factor  $\sqrt{m/M}$  such that the integral, with  $z' = 2m_B(\omega - E_{\mathbf{p}} - (\mathbf{p}_\perp + \mathbf{k}_\perp)^2/2M + i0^+)$ , becomes

$$\begin{aligned} & \Pi_{\text{vac}}(\mathbf{p}_\perp + \mathbf{k}_\perp, \omega - E_{\mathbf{p}}) \\ &= \frac{2m_B}{1 + \alpha^{-1}} \int \frac{d^3 \tilde{\mathbf{p}}}{(2\pi)^3} \left[ \frac{1}{z' - \tilde{\mathbf{p}}^2} + \frac{1}{\tilde{\mathbf{p}}^2} \right] \end{aligned} \quad (\text{A.19})$$

$$= \frac{2m_B}{2\pi^2(1 + \alpha^{-1})} \int_0^\infty d\tilde{p} \frac{z'}{z' - \tilde{p}^2} \quad (\text{A.20})$$

$$= -\frac{2m_B z'}{4\pi^2(1 + \alpha^{-1})} \int_{-\infty}^\infty d\tilde{p} \frac{1}{(\tilde{p} + \sqrt{z'})(\tilde{p} - \sqrt{z'})}. \quad (\text{A.21})$$

Noting that the pole at  $\sqrt{z'}$  is located in the upper half complex plane, we perform the contour integral around the pole yielding  $\int_{-\infty}^\infty d\tilde{p} [(\tilde{p} + \sqrt{z'})(\tilde{p} - \sqrt{z'})]^{-1} = i\pi/\sqrt{z'}$ . The pair propagator simplifies to

$$\begin{aligned} & \Pi_{\text{vac}}(\mathbf{p}_\perp + \mathbf{k}_\perp, \omega - E_{\mathbf{p}}) \\ &= \begin{cases} -i \frac{\sqrt{m_B} m_r}{\sqrt{2\pi}} \sqrt{\left| \omega - E_{\mathbf{p}} - \frac{(\mathbf{p}_\perp + \mathbf{k}_\perp)^2}{2M} \right|} & \text{if } \omega - E_{\mathbf{p}} - \frac{(\mathbf{p}_\perp + \mathbf{k}_\perp)^2}{2M} \geq 0 \\ \frac{\sqrt{m_B} m_r}{\sqrt{2\pi}} \sqrt{\left| \omega - E_{\mathbf{p}} - \frac{(\mathbf{p}_\perp + \mathbf{k}_\perp)^2}{2M} \right|} & \text{if } \omega - E_{\mathbf{p}} - \frac{(\mathbf{p}_\perp + \mathbf{k}_\perp)^2}{2M} < 0 \end{cases} \end{aligned} \quad (\text{A.22})$$

which is equivalent to the expression in Eq. (2.74).

Returning to  $\Sigma_1$  from Eq. (A.17) we go to spherical coordinates  $(p, \theta, \phi)$  and substitute  $x = -\cos \theta$ :

$$\begin{aligned} \Sigma_1(\mathbf{k}_\perp, \omega) &= \frac{1}{2\pi^3} \int_0^\infty dp \int_0^1 dx \int_0^\pi d\phi \\ &\times \frac{p^2 v_{\mathbf{p}}^2}{g^{-1} - e^{i\psi} - \frac{\sqrt{m_B} m_r}{\sqrt{2\pi}} \sqrt{\left| \omega - E_{\mathbf{p}} - \frac{k_\perp^2 + p^2(1-x^2) + 2k_\perp p \sqrt{1-x^2} \cos \phi}{2M} \right|}}, \end{aligned} \quad (\text{A.23})$$

where  $e^{i\psi_\pm} \in \{1, -i\}$  are integration variable dependent phase factors given according to Eq. (A.22). In the case  $k_\perp = 0$  the  $\phi$  integration is trivial, and we get

$$\Sigma_1(\mathbf{0}, \omega) = \frac{1}{2\pi^2} \int_0^\infty dp \int_0^1 dx \frac{p^2 v_{\mathbf{p}}^2}{g^{-1} - e^{i\psi} - \frac{\sqrt{m_B} m_r}{\sqrt{2\pi}} \sqrt{\left| \omega - E_{\mathbf{p}} - \frac{p^2(1-x^2)}{2M} \right|}}. \quad (\text{A.24})$$

The derivate of  $\Sigma_1(\mathbf{0}, \omega)$  with respect to  $\omega$  is straight-forward to compute:

$$\begin{aligned} \partial_\omega \Sigma_1(\mathbf{0}, \omega) &= -\frac{\sqrt{m_B} m_r}{4\sqrt{2}\pi^3} \int_0^\infty dp \int_0^1 dx \\ &\times \frac{p^2 v_{\mathbf{p}}^2 e^{i\psi} \left( \omega - E_{\mathbf{p}} - \frac{p^2(1-x^2)}{2M} \right)}{\left| \omega - E_{\mathbf{p}} - \frac{p^2(1-x^2)}{2M} \right|^{3/2} \left( g^{-1} - e^{i\psi} - \frac{\sqrt{m_B} m_r}{\sqrt{2\pi}} \sqrt{\left| \omega - E_{\mathbf{p}} - \frac{p^2(1-x^2)}{2M} \right|} \right)^2}. \end{aligned} \quad (\text{A.25})$$

Finally we compute the limit of  $k_\perp^{-1} \partial_{k_\perp} \Sigma_1(\mathbf{k}_\perp, \omega)$  when  $k_\perp \rightarrow 0$  from Eq. (A.23). We notice that the integrand of  $k_\perp^{-1} \partial_{k_\perp} \Sigma_1(\mathbf{k}_\perp, \omega)$  consists of two term when  $k_\perp$  is small. One of the terms is proportional to  $k_\perp^{-1} \cos \phi$  and the integral over  $\phi$  vanishes. The other term is constant with respect to  $\phi$  and  $k_\perp$ , and the  $\phi$  integral just yields a factor of  $\pi$ . All taken together, we find that  $k_\perp^{-1} \partial_{k_\perp} \Sigma_1(\mathbf{k}_\perp, \omega)|_{k_\perp=0} = -M^{-1} \partial_\omega \Sigma_1(\mathbf{0}, \omega)$ , and so we do not have to implement this formula separately.

## Four-qubit diamond gate

This appendix is quoted from Ref. [8] with minor changes to fit the context here.

### B.1 Unitary dynamics in the qubit model

In this appendix we show that the Hamiltonian of Eq. (4.30) realizes the four-qubit quantum gate of Eq. (4.36) by analyzing the dynamics within Floquet theory. Typically in superconducting qubits  $|\Delta| \gg |J|, |J_C|$ , so if we think of the qubit detuning,  $\Delta$ , as a driving frequency, the system is driven rapidly compared to the time-scale set by the qubit interaction strengths. Consequently, on the gate operation time-scale, it is appropriate to consider the Magnus expansion for the Floquet Hamiltonian to first order in  $J/\Delta$ , which can be computed as[209]:

$$\begin{aligned}
 H_F = & J_C (\sigma_+^{C1} \sigma_-^{C2} + \sigma_-^{C1} \sigma_+^{C2}) \\
 & + \frac{J^2}{\Delta} (\sigma_-^{T1} + \sigma_-^{T2}) (\sigma_+^{T1} + \sigma_+^{T2}) (\sigma_z^{C1} + \sigma_z^{C2}) \\
 & - \frac{J^2}{\Delta} (\sigma_-^{C1} + \sigma_-^{C2}) (\sigma_+^{C1} + \sigma_+^{C2}) (\sigma_z^{T1} + \sigma_z^{T2}) \quad (B.1) \\
 & - \frac{J_C J}{\Delta} (\sigma_+^{C1} \sigma_z^{C2} + \sigma_+^{C2} \sigma_z^{C1}) (\sigma_-^{T1} + \sigma_-^{T2}) \\
 & - \frac{J_C J}{\Delta} (\sigma_-^{C1} \sigma_z^{C2} + \sigma_-^{C2} \sigma_z^{C1}) (\sigma_+^{T1} + \sigma_+^{T2}) .
 \end{aligned}$$

Within the Floquet formalism  $\exp(-iH_F T)$  takes the system from time zero through one driving cycle of period  $T = 2\pi/|\Delta|$ . Successive application  $n$  times yields the time-evolution operator,  $U(nT) = \exp(-iH_F nT)$ . Since the gate time is much larger than one period, we consider  $t = nT$  a continuous time variable, and the continuous time-evolution operator,  $U(t) = \exp(-iH_F t)$ .

Suppose we initialized the control qubits in one of the control basis states,  $\{|00\rangle_C, |11\rangle_C, |\Psi^+\rangle_C, |\Psi^-\rangle_C\}$ . Typically, one thinks of control qubits, or their state, as a catalyzer for a given gate operation performed on the target qubits. The control qubits are allowed to partake in the gate operation, for instance by facilitating state transfer between target qubits not directly coupled, as long as the control qubits return to their initial state after the completion of the gate operation. A priori we cannot guarantee that this is the case. In fact, we see by application of the Floquet Hamiltonian  $H_F$  of Eq. (B.1) to each control state (producing operators acting on the target qubits only) that they generally evolve in time:

$$H_F |00\rangle_C = |00\rangle_C \frac{2J^2}{\Delta} \left[ (\sigma_-^{T1} + \sigma_-^{T2})(\sigma_+^{T1} + \sigma_+^{T2}) - \sigma_z^{T1} - \sigma_z^{T2} \right] - |\Psi^+\rangle_C \frac{\sqrt{2}J_C J}{\Delta} (\sigma_-^{T1} + \sigma_-^{T2}), \quad (\text{B.2})$$

$$H_F |11\rangle_C = -|11\rangle_C \frac{2J^2}{\Delta} (\sigma_-^{T1} + \sigma_-^{T2})(\sigma_+^{T1} + \sigma_+^{T2}) + |\Psi^+\rangle_C \frac{\sqrt{2}J_C J}{\Delta} (\sigma_+^{T1} + \sigma_+^{T2}), \quad (\text{B.3})$$

$$H_F |\Psi^+\rangle_C = |\Psi^+\rangle_C \left[ J_C - \frac{2J^2}{\Delta} (\sigma_z^{T1} + \sigma_z^{T2}) \right] + |11\rangle_C \frac{\sqrt{2}J_C J}{\Delta} (\sigma_-^{T1} + \sigma_-^{T2}) - |00\rangle_C \frac{\sqrt{2}J_C J}{\Delta} (\sigma_+^{T1} + \sigma_+^{T2}), \quad (\text{B.4})$$

$$H_F |\Psi^-\rangle_C = |\Psi^-\rangle_C (-J_C). \quad (\text{B.5})$$

We see that  $H_F$  couples the triplet states  $|00\rangle_C$ ,  $|11\rangle_C$  and  $|\Psi^+\rangle_C$ , but that the singlet state  $|\Psi^-\rangle_C$  is unchanged in time. Notice that all control states decouples in the special case  $J_C = 0$ , i.e. when there is no direct coupling between the control qubits.

### B.1.1 The case of $J_C = 0$

In this case, each control state is perfectly preserved under the time-evolution, and we can simply determine the gate operation on the target qubits associated with each control state. However, the absence of a direct coupling between the control qubits makes it difficult to prepare the entangled Bell states,  $|\Psi^\pm\rangle_C$ . Ideally, the control-control coupling would be tunable and only on during control state preparation. On the other hand, since it does not couple to any of the target qubits, we do not expect the value of  $J_C$  to be of fundamental importance to the nature of the gate operations, which is our main focus here. Assuming  $J_C = 0$ , the Floquet Hamiltonian can be cast as

$$H_F = |00\rangle\langle 00|_C H_T^{00} + |11\rangle\langle 11|_C H_T^{11} + |\Psi^+\rangle\langle\Psi^+|_C H_T^{\Psi^+} + |\Psi^-\rangle\langle\Psi^-|_C H_T^{\Psi^-}, \quad (\text{B.6})$$

with the following Hamiltonians acting only on the target qubits:

$$H_T^{00} = \frac{2J^2}{\Delta} \left[ (\sigma_-^{T1} + \sigma_-^{T2})(\sigma_+^{T1} + \sigma_+^{T2}) - \sigma_z^{T1} - \sigma_z^{T2} \right], \quad (\text{B.7})$$

$$H_T^{11} = -\frac{2J^2}{\Delta} (\sigma_-^{T1} + \sigma_-^{T2})(\sigma_+^{T1} + \sigma_+^{T2}), \quad (\text{B.8})$$

$$H_T^{\Psi^+} = -\frac{2J^2}{\Delta} (\sigma_z^{T1} + \sigma_z^{T2}), \quad (\text{B.9})$$

$$H_T^{\Psi^-} = 0. \quad (\text{B.10})$$

In order to compute the time-evolution operator,  $U(t) = \exp(-iH_F t)$ , we notice that  $H_F$  is on the form

$$H_F = \sum_{i=1}^N P_i H_i, \quad (\text{B.11})$$

where  $P_i = |i\rangle\langle i|$  is the projector onto the  $i$ 'th orthonormal basis state of the  $N$ -dimensional subsystem  $A$ , and  $H_i$  is a Hamiltonian on a disjoint subsystem  $B$ , such that  $H_i$  commute with every  $P_j$ . Operators on this form has the property that the product of any two terms is zero,  $(P_i H_i)(P_j H_j) = 0$  for  $i \neq j$ , enabling an algebraic property known as "freshman's dream":  $(H_F)^n = \sum_{i=1}^N (P_i H_i)^n$  for any integer  $n > 0$ . This has the consequence that the operator exponential can be

written as a sum:

$$\begin{aligned}
 \exp(-iH_{\text{F}}t) &= \sum_{n=0}^{\infty} \frac{(-it)^n}{n!} (H_{\text{F}})^n \\
 &= 1 + \sum_{n=1}^{\infty} \frac{(-it)^n}{n!} \sum_{i=1}^N (P_i H_i)^n \\
 &= 1 - N + \sum_{i=1}^N \exp(-iP_i H_i t) .
 \end{aligned} \tag{B.12}$$

Since  $(P_i)^n = P_i$  for any integer  $n > 0$ , we can pull the projector out of each exponential in the sum:

$$\begin{aligned}
 \exp(-iP_i H_i t) &= \sum_{n=0}^{\infty} \frac{(-it)^n}{n!} (P_i H_i)^n \\
 &= 1 + \sum_{n=1}^{\infty} \frac{(-it)^n}{n!} P_i (H_i)^n \\
 &= 1 - P_i + P_i \exp(-itH_i) .
 \end{aligned} \tag{B.13}$$

Finally, utilizing  $\sum_{i=1}^N P_i = 1$ , we find that the time-evolution operator can be expressed as

$$\begin{aligned}
 U(t) &= \exp(-iH_{\text{F}}t) \\
 &= 1 - N + \sum_{i=1}^N [1 - P_i + P_i \exp(-itH_i)] \\
 &= \sum_{i=1}^N P_i \exp(-itH_i) .
 \end{aligned} \tag{B.14}$$

The above decomposition of the time-evolution can be used whenever one or more control qubits (subsystem  $A$ ) catalyze a unitary gate operation on a set of target qubits (subsystem  $B$ ) in the sense that the Hamiltonian does not mix the chosen control states. In our case, we can easily express the Hamiltonians (B.7)–(B.10) as matrices and find the unitary matrix exponentials. In the computational basis of the target qubits, they are as follows:

$$U_{\text{T}}^{00}(t) = \exp(-iH_{\text{T}}^{00}t) = \begin{pmatrix} 1 & 0 & 0 & 0 \\ 0 & \frac{1}{2}e^{-it\zeta} + \frac{1}{2} & \frac{1}{2}e^{-it\zeta} - \frac{1}{2} & 0 \\ 0 & \frac{1}{2}e^{-it\zeta} - \frac{1}{2} & \frac{1}{2}e^{-it\zeta} + \frac{1}{2} & 0 \\ 0 & 0 & 0 & e^{-it\zeta} \end{pmatrix} , \tag{B.15}$$

$$U_T^{11}(t) = \exp(-iH_T^{11}t) = \begin{pmatrix} e^{it\zeta} & 0 & 0 & 0 \\ 0 & \frac{1}{2}e^{it\zeta} + \frac{1}{2} & \frac{1}{2}e^{it\zeta} - \frac{1}{2} & 0 \\ 0 & \frac{1}{2}e^{it\zeta} - \frac{1}{2} & \frac{1}{2}e^{it\zeta} + \frac{1}{2} & 0 \\ 0 & 0 & 0 & 1 \end{pmatrix}, \quad (\text{B.16})$$

$$U_T^{\Psi^+}(t) = \exp(-iH_T^{\Psi^+}t) = \begin{pmatrix} e^{it\zeta} & 0 & 0 & 0 \\ 0 & 1 & 0 & 0 \\ 0 & 0 & 1 & 0 \\ 0 & 0 & 0 & e^{-it\zeta} \end{pmatrix}, \quad (\text{B.17})$$

$$U_T^{\Psi^-}(t) = \exp(-iH_T^{\Psi^-}t) = \begin{pmatrix} 1 & 0 & 0 & 0 \\ 0 & 1 & 0 & 0 \\ 0 & 0 & 1 & 0 \\ 0 & 0 & 0 & 1 \end{pmatrix}, \quad (\text{B.18})$$

with  $\zeta = 4J^2/\Delta$ . The time-evolution operator for the four-qubit system is then

$$U(t) = |00\rangle\langle 00|_C U_T^{00}(t) + |11\rangle\langle 11|_C U_T^{11}(t) + |\Psi^+\rangle\langle \Psi^+|_C U_T^{\Psi^+}(t) + |\Psi^-\rangle\langle \Psi^-|_C U_T^{\Psi^-}(t). \quad (\text{B.19})$$

Thus, each of the four unitaries (B.15)–(B.18) above is a gate operation performed on the target qubits, controlled entirely by the four control states, which are unaltered by the operation. The control states  $|00\rangle_C$  and  $|11\rangle_C$  induce oscillations between the target qubit states combined with a phase on either  $|00\rangle_T$  or  $|11\rangle_T$ , depending on the control state, and  $|\Psi^+\rangle_C$  controls a pure phase operation that distinguishes between the number of excitations in the target qubits. The singlet control state,  $|\Psi^-\rangle_C$ , on the other hand, does nothing to the target qubits, and this control state can therefore be used to turn off the gate between the target qubits. The gate is fully quantum mechanical, as superpositions of control states will run the corresponding computations on the target qubits in parallel. The system comprise a true four-qubit quantum interference device in the form of a four-way controlled two-qubit gate (the diamond gate).

Of particular interest is the gate operation at the time  $t = t_g \equiv \pi/|\zeta|$ , which results in the operations discussed in the main text. Setting  $t = t_g$  in Eq. (B.19) produces the four-qubit unitary gate  $U$  of Eq. (4.36).

As we shall see below, a non-zero  $J_C$  introduce infidelities, albeit only very small. We may therefore ask ourselves whether the control-qubit coupling is necessary at all. After all, if the control qubits are decoupled,  $J_C = 0$ , we may still initialize them in the computational basis states by driving each control qubit individually. Expressing the Bell states in the computational basis casts Eq. (B.19) as:

$$\begin{aligned}
 U(t) = & |00\rangle\langle 00|_C U_T^{00}(t) + |11\rangle\langle 11|_C U_T^{11}(t) \\
 & + (|01\rangle\langle 01|_C + |10\rangle\langle 10|_C) \frac{1}{2} (U_T^{\Psi^+}(t) + U_T^{\Psi^-}(t)) \\
 & + (|01\rangle\langle 10|_C + |10\rangle\langle 01|_C) \frac{1}{2} (U_T^{\Psi^+}(t) - U_T^{\Psi^-}(t)).
 \end{aligned} \tag{B.20}$$

Notice that the computational basis control states are unaltered if and only if  $U_T^{\Psi^+}(t) = U_T^{\Psi^-}(t)$ , or equivalently  $t = 0, 2t_g, 4t_g, \dots$ , which reduces  $U(t)$  to the identity operator on all qubits. This is not surprising, since  $J_C = 0$  and our choice of bases results in complete symmetry between the control and target qubits, and if we require no evolution of the control qubits, no evolution of the target qubits can occur either. On the other hand, the symmetry between control and target qubits when  $J_C = 0$  means that the role of control and target qubits is only a matter of choice of basis. This also means that the roles can be interchanged between operations, for instance in a larger quantum computer where the four-qubit diamond gate device is a subsystem.

### B.1.2 The case of non-zero $J_C$

When  $J_C$  is non-zero, we see from Eqs. (B.2)–(B.4) that the Floquet Hamiltonian couples the triplet control states  $\{|00\rangle_C, |11\rangle_C, |\Psi^+\rangle_C\}$ . In the following we study how strongly they mix during the gate operation, and we find that it only has a weak impact on the gate fidelity.

Before we proceed with the calculation, we notice from the first terms on the right-hand side of Eqs. (B.4)–(B.5) that the presence of  $J_C$  adds a global phase to the pure phase gates. Specifically, the gates of Eqs. (B.17)–(B.18) must be modified  $U_T^{\Psi^\pm}(t) \rightarrow e^{\mp itJ_C} U_T^{\Psi^\pm}(t)$ , leading to the expressions (4.33)–(4.34) in the main text at  $t = t_g$ . As the singlet state  $|\Psi^-\rangle_C$  remains uncoupled to other control states, this is the only modification of the identity gate, which thus suffers no infidelity due to the control qubit coupling.

Since  $|00\rangle_C$  and  $|11\rangle_C$  couples to  $|\Psi^+\rangle_C$  in a completely analogous way, it is enough to treat the case  $|11\rangle_C$ . Suppose we initialize the control qubits in  $|11\rangle_C$ , and consider the effect of  $H_F$  on each four-qubit state, expressing the target-qubit states in the basis  $\{|00\rangle_T, |11\rangle_T, |\Psi^+\rangle_T, |\Psi^-\rangle_T\}$ :

$$H_F |11\rangle_C |00\rangle_T = \frac{2J_C J}{\Delta} |\Psi^+\rangle_C |\Psi^+\rangle_T - \frac{4J^2}{\Delta} |11\rangle_C |00\rangle_T, \quad (\text{B.21})$$

$$H_F |11\rangle_C |11\rangle_T = 0, \quad (\text{B.22})$$

$$H_F |11\rangle_C |\Psi^+\rangle_T = \frac{2J_C J}{\Delta} |\Psi^+\rangle_C |11\rangle_T - \frac{4J^2}{\Delta} |11\rangle_C |\Psi^+\rangle_T, \quad (\text{B.23})$$

$$H_F |11\rangle_C |\Psi^-\rangle_T = 0. \quad (\text{B.24})$$

Starting with Eq. (B.23), we see that  $H_F$  couples  $|11\rangle_C |\Psi^+\rangle_T$  and  $|\Psi^+\rangle_C |11\rangle_T$ , and thus we consider the linear combinations  $|E_\pm\rangle$ ,

$$\begin{pmatrix} |E_+\rangle \\ |E_-\rangle \end{pmatrix} = \begin{pmatrix} \cos \vartheta & \sin \vartheta \\ -\sin \vartheta & \cos \vartheta \end{pmatrix} \begin{pmatrix} |\Psi^+\rangle_C |11\rangle_T \\ |11\rangle_C |\Psi^+\rangle_T \end{pmatrix} \quad (\text{B.25})$$

which are eigenstates with energies  $E_\pm = (J_C \pm \kappa)/2$ , where  $\kappa \equiv (1/\Delta)\sqrt{64J^4 + 16J^2J_C(J_C + \Delta) + J_C^2\Delta^2}$ , and the mixing angle,  $\vartheta$ , is defined through

$$\tan \vartheta = \frac{2J_C J}{E_+ \Delta + 4J^2}. \quad (\text{B.26})$$

Expanding  $|11\rangle_C |01\rangle_T$  and  $|11\rangle_C |10\rangle_T$  in eigenstates, the dynamics are

$$\begin{aligned} U(t) \begin{pmatrix} |11\rangle_C |01\rangle_T \\ |11\rangle_C |10\rangle_T \end{pmatrix} &= \frac{1}{\sqrt{2}} \begin{pmatrix} 1 \\ -1 \end{pmatrix} |11\rangle_C |\Psi^-\rangle_T \\ &+ \frac{1}{\sqrt{2}} \begin{pmatrix} 1 \\ 1 \end{pmatrix} \left( \sin \vartheta e^{-iE_+ t} |E_+\rangle + \cos \vartheta e^{-iE_- t} |E_-\rangle \right). \end{aligned} \quad (\text{B.27})$$

Since the time-evolution of  $|11\rangle_C |01\rangle_T$  and  $|11\rangle_C |10\rangle_T$  only differ by a sign on  $|11\rangle_C |\Psi^-\rangle_T$ , the states have swapped after a time  $t$  if the dynamical phases account for this relative sign. Under the assumption that  $\Delta$  is much larger than  $J$  and  $J_C$  (all assumed positive for simplicity), we can simplify the expressions for the energies by approximating  $\kappa \approx \sqrt{J_C^2 + 16J^2J_C/\Delta} \approx J_C + 8J^2/\Delta$ . We see from

Eq. (B.26) that  $\vartheta \ll 1$ . Therefore, the amplitude for the unwanted component  $|\Psi^+\rangle_C |11\rangle_C$  in the final state scales with

$$\sin \vartheta \approx \tan \vartheta \approx \frac{1/4J}{t_g/2\pi + 1/J_C}, \quad (\text{B.28})$$

which illustrates a trade-off between the gate fidelity and gate time. However, this unwanted state component only leads to small gate infidelities. Ignoring this small effect,

$$U(t) \begin{pmatrix} |11\rangle_C |01\rangle_T \\ |11\rangle_C |10\rangle_T \end{pmatrix} \approx \frac{1}{\sqrt{2}} \begin{pmatrix} 1 \\ -1 \end{pmatrix} |11\rangle_C |\Psi^-\rangle_T + \frac{1}{\sqrt{2}} \begin{pmatrix} 1 \\ 1 \end{pmatrix} e^{i4J^2t/\Delta} |11\rangle_C |\Psi^+\rangle_T \quad (\text{B.29})$$

leading to the desired state swap  $|01\rangle_T \leftrightarrow |10\rangle_T$  at the gate time  $t_g$ .

To conclude the discussion of the  $U_T^{11}$  gate of Eq. 4.32, we must consider the dynamic evolution of  $|11\rangle_C |11\rangle_T$  and  $|11\rangle_C |00\rangle_T$ . The former is a zero-energy eigenstate, cf. Eq. (B.22), unchanged by time, but the latter is not an eigenstate and mixes with other states. However, comparing Eqs. (B.23) and (B.21), we see that this mixing with unwanted states is essentially the same problem discussed above. Thus, up to similar small effects,  $|11\rangle_C |00\rangle_T$  picks up a phase factor of  $e^{i4J^2t_g/\Delta} = -1$  during the gate operation, as desired. From the numerical simulations of the average fidelity discussed in Section 4.2.3, we find that the average infidelity of the  $U_T^{11}$  gate is well-estimated by  $(2J/\Delta)^2 = \pi/(t_g\Delta)$ , which is in qualitative agreement with Eq. B.28 for the scaling of the unwanted states' amplitude.

The case where the control qubits are initialized in  $|00\rangle_C$  is analogous. On the other hand, both  $|00\rangle_C$  and  $|11\rangle_C$  couples equivalently to  $|\Psi^+\rangle_C$ , providing two channels for gate infidelities when the control is initialized in  $|\Psi^+\rangle_C$ , and hence a larger infidelity. Numerically, we indeed find that the average infidelity is twice as large,  $2\pi/(t_g\Delta)$ , for the  $U_T^{\Psi^+}$  compared to  $U_T^{00}$  and  $U_T^{11}$ .

### B.1.3 Equivalent gate diagram for the diamond gate

The four-qubit unitary of the diamond gate of Eq. (4.36),  $U \equiv U(t_g)$ , can be expressed in terms of simpler gates in a quantum gate circuit. One way to express the diamond gate is shown in Figure B.1.

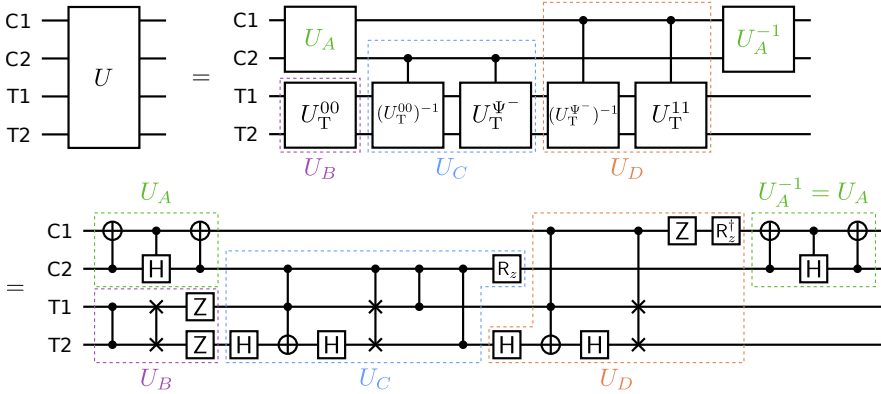


Figure B.1: Decomposition of the diamond gate in standard gates from the literature. The figure is adapted from Ref. [8].

This decomposition is found from the following considerations. We notice that the two-qubit operations performed on the target qubits have simple decompositions in well-known gates, cf. Eqs. (4.31)–(4.34), but writing these as conditional operations on the control qubits is not straight-forward due to the Bell states among the control states. As the first operation in our decomposition, we therefore apply the unitary  $U_A$  comprised of two CNOT gates and one controlled-H, which maps the control states to the computational basis:  $U_A \cdot \{|00\rangle_C, |11\rangle_C, |\Psi^+\rangle_C, |\Psi^-\rangle_C\} = \{|00\rangle_C, |11\rangle_C, |10\rangle_C, -|01\rangle_C\}$ . The diamond gate leaves the control states unaltered, and we therefore apply the inverse transformation,  $U_A^{-1}$ , as the last step in the decomposition. After the application of  $U_A$ , the two-qubit gates of Eqs. (4.31)–(4.34) are conditional on the computational control states, making a decomposition much more manageable.

The operations on the target qubits are decomposed in three unitary blocks:  $U_B$ ,  $U_C$  and  $U_D$ . The first operation,  $U_B = U_T^{00}$ , is unconditional on the control qubits, and is the only gate applied when both control qubits are in the  $|0\rangle$  state. Next, if only C2 is in  $|1\rangle$  (after  $U_A$ ), the target qubits must be subject to  $U_T^{\Psi^-}$ , which we implement in  $U_C$ . If both C1 and C2 are in  $|1\rangle$ , the gate  $U_T^{11}$  must be applied to the target qubits, which is implemented in  $U_D$ . Finally, if only C1 is in  $|1\rangle$ , the gate circuit performs  $U_T^{11}(U_T^{\Psi^-})^{-1}U_T^{00} = -ZZ e^{-it_g J_C} = U_T^{\Psi^+}$ , thereby verifying the diamond gate operation.

Expressing these unitary operations in standard gates leads us

to the final line in the figure. Here  $R_z = |0\rangle\langle 0| e^{-it_g J_C/2} + |1\rangle\langle 1| e^{it_g J_C/2}$  is z-rotation. This gate diagram can be further decomposed into e.g. CNOT gates and single-qubit rotations. Using the open-source Python toolbox Qiskit[210], we find such a decomposition into 42 CNOTs and 49 single-qubit rotations.

## B.2 Superconducting circuit analysis

In this appendix we analyse the superconducting circuit device of Figure 4.2, shown as a lumped element diagram in Figure B.2. We quantize the circuit using standard techniques [125] and truncate each anharmonic oscillator degree of freedom to qutrits (three-level systems), thus arriving at the Hamiltonian (4.40)–(4.41). From the qutrit Hamiltonian, the qubit Hamiltonian (4.28)–(4.29) follows readily by ignoring all terms involving the second excited transmon states,  $|2\rangle$ , and ignoring the small crosstalk term, i.e. putting  $J_T = 0$ . We study the control qubit subspace in the qutrit model and derive the redefined control state 4.44. Finally, we derive the optimal crosstalk strength,  $J_T^{\text{opt}}$  of Eq. 4.47, for countertacting unwanted leakage through the second-excited states.

### B.2.1 Derivation of the qutrit model Hamiltonian

The classical Lagrangian for the circuit of Figure B.2 is

$$\begin{aligned} \mathcal{L} = & \frac{C_C}{2} \dot{\phi}_2^2 + \frac{C}{2} (\dot{\phi}_3 - \dot{\phi}_2)^2 + \frac{C_T}{2} (\dot{\phi}_4 - \dot{\phi}_3)^2 + \frac{C}{2} (\dot{\phi}_1 - \dot{\phi}_2)^2 \\ & + \frac{C_T}{2} (\dot{\phi}_6 - \dot{\phi}_1)^2 + \frac{C}{2} (\dot{\phi}_5 - \dot{\phi}_6)^2 + \frac{C_C}{2} \dot{\phi}_5^2 + \frac{C}{2} (\dot{\phi}_4 - \dot{\phi}_5)^2 \quad (\text{B.30}) \\ & + \frac{C'}{2} (\dot{\phi}_2 - \dot{\phi}_5)^2 + E_{J_C} \cos(\phi_2) + E_{J_C} \cos(\phi_5) \\ & + E_{J_T} \cos(\phi_6 - \phi_1) + E_{J_T} \cos(\phi_4 - \phi_3) . \end{aligned}$$

Here  $\phi_i$ , for  $i = 1, \dots, 6$ , are node fluxes relative to ground at the positions displayed in Figure B.2. The capacitances and Josephson energies of the model are shown in Figure B.2 at their respective circuit elements. In the following we used units where the flux quantum is  $\Phi_0 = h/(2e) = 2\pi$ , in addition to  $\hbar = 1$ .

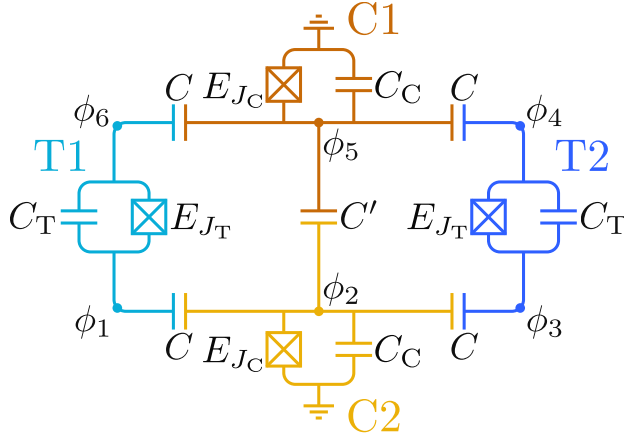


Figure B.2: Lumped circuit element diagram of the device from Figure 4.2 with the relevant circuit parameters marked. Node fluxes relative to ground are denoted  $\phi_i$  with  $i = 1, \dots, 6$ , capacitances are  $C$ ,  $C'$ ,  $C_T$  and  $C_C$ , and Josephson energies are  $E_{J_T}$  and  $E_{J_C}$ . The figure is adapted from Ref. [8].

We transform the node flux coordinates  $\vec{\phi}' = (\phi_1, \phi_2, \phi_3, \phi_4, \phi_5, \phi_6)^T$  using the transformation matrix

$$T = \begin{pmatrix} 0 & 0 & 0 & 0 & -1 & 0 \\ 0 & 1 & 0 & 0 & 0 & 0 \\ 1 & 0 & 0 & 0 & 0 & -1 \\ 0 & 0 & 1 & -1 & 0 & 0 \\ 1 & 0 & 0 & 0 & 0 & 1 \\ 0 & 0 & 1 & 1 & 0 & 0 \end{pmatrix}, \quad (\text{B.31})$$

into the new coordinate vector,

$$T\vec{\phi}' \equiv \vec{\phi} = (\phi_{C1}, \phi_{C2}, \phi_{T1}, \phi_{T2}, \phi_{CM,T1}, \phi_{CM,T2})^T, \quad (\text{B.32})$$

containing coordinates for each transmon C1, C2, T1, and T2, and two center-of-mass coordinates.

Defining the capacitance matrix

$$\mathcal{C} = \begin{pmatrix} C + C_T & -C & 0 & 0 & 0 & -C_T \\ -C & C_C + C' + 2C & -C & 0 & -C' & 0 \\ 0 & -C & C + C_T & -C_T & 0 & 0 \\ 0 & 0 & -C_T & C + C_T & -C & 0 \\ 0 & -C' & 0 & -C & C_C + C' + 2C & -C \\ -C_T & 0 & 0 & 0 & -C & C + C_T \end{pmatrix} \quad (\text{B.33})$$

and the transformed capacitance matrix  $K = (T^T)^{-1}\mathcal{C}T^{-1}$ , we can express the Lagrangian as

$$\begin{aligned} \mathcal{L} = & \frac{1}{2}\dot{\vec{\phi}}^T K \dot{\vec{\phi}} + E_{J_C} \cos(\phi_{C1}) + E_{J_C} \cos(\phi_{C2}) \\ & + E_{J_T} \cos(\phi_{T1}) + E_{J_T} \cos(\phi_{T2}) . \end{aligned} \quad (\text{B.34})$$

The generalized momenta (in the new coordinate system) is  $\vec{p} = \frac{\partial \mathcal{L}}{\partial \dot{\vec{\phi}}} = K \dot{\vec{\phi}}$ , and hence the classical Hamiltonian is

$$\begin{aligned} \mathcal{H} = & \vec{p}^T \dot{\vec{\phi}} - \mathcal{L} \\ = & \frac{1}{2}\vec{p}^T K^{-1} \vec{p} - E_{J_C} \cos(\phi_{C1}) - E_{J_C} \cos(\phi_{C2}) \\ & - E_{J_T} \cos(\phi_{T1}) - E_{J_T} \cos(\phi_{T2}) . \end{aligned} \quad (\text{B.35})$$

The capacitance matrix  $K$  can be inverted analytically:

$$K^{-1} = \begin{pmatrix} 8E_{C_C} & -\mathcal{E}_{CC} & \mathcal{E}_{CT} & \mathcal{E}_{CT} & -\mathcal{E}_{C,CM} & -\mathcal{E}_{C,CM} \\ -\mathcal{E}_{CC} & 8E_{C_C} & \mathcal{E}_{CT} & \mathcal{E}_{CT} & \mathcal{E}_{C,CM} & \mathcal{E}_{C,CM} \\ \mathcal{E}_{CT} & \mathcal{E}_{CT} & 8E_{C_T} & \mathcal{E}_{TT} & 0 & 0 \\ \mathcal{E}_{CT} & \mathcal{E}_{CT} & \mathcal{E}_{TT} & 8E_{C_T} & 0 & 0 \\ -\mathcal{E}_{C,CM} & \mathcal{E}_{C,CM} & 0 & 0 & 8E_{C_{CM}} & \mathcal{E}_{CM,CM} \\ -\mathcal{E}_{C,CM} & \mathcal{E}_{C,CM} & 0 & 0 & \mathcal{E}_{CM,CM} & 8E_{C_{CM}} \end{pmatrix} , \quad (\text{B.36})$$

where

$$E_{C_C} = \frac{1}{8} \frac{2C_T(C_C + C') + C(C_C + C' + 2C_T)}{C_C(2C_T(C_C + 2C') + C(C_C + 2C' + 4C_T))} , \quad (\text{B.37})$$

$$E_{C_T} = \frac{1}{8} \frac{2(C^2 + 2C_T(C_C + 2C') + C(C_C + 2C' + 4C_T))}{(C + 2C_T)(2C_T(C_C + 2C') + C(C_C + 2C' + 4C_T))} , \quad (\text{B.38})$$

$$E_{\text{CM}} = \frac{1}{8} \frac{2(C + C_C)}{CC_C}, \quad (\text{B.39})$$

$$\mathcal{E}_{\text{CC}} = \frac{2C'C_T + C(C' + 2C_T)}{C_C(2C_T(C_C + 2C') + C(C_C + 2C' + 4C_T))}, \quad (\text{B.40})$$

$$\mathcal{E}_{\text{CT}} = \frac{C}{2C_T(C_C + 2C') + C(C_C + 2C' + 4C_T)}, \quad (\text{B.41})$$

$$\mathcal{E}_{\text{TT}} = \frac{2C^2}{(C + 2C_T)(2C_T(C_C + 2C') + C(C_C + 2C' + 4C_T))}, \quad (\text{B.42})$$

$$\mathcal{E}_{\text{C,CM}} = \frac{1}{C_C}, \quad (\text{B.43})$$

$$\mathcal{E}_{\text{CM,CM}} = \frac{2}{C_C}. \quad (\text{B.44})$$

We assume that  $C_C, C_T \gg C, C'$  which means that each colored circuit area in Figure B.2 may be regarded as a well-defined transmon, and couplings between transmons as perturbations. In the weak coupling limit, the capacitive energies for the transmons are  $E_{C_C} \approx \frac{1}{8C_C}$  and  $E_{C_T} \approx \frac{1}{8C_T}$ , while the energy of the center-of-mass degrees of freedom is  $E_{\text{CM}} \approx \frac{1}{4C} \gg E_{C_C}, E_{C_T}$ . In analogy with classical particles, the transmons correspond to pendulums of mass  $C_C$  and  $C_T$ , while the center-of-mass degrees of freedom correspond to a very light free particle. We will therefore ignore the center-of-mass degrees of freedom, as their motion will primarily contribute a constant energy shift, which does not affect the dynamics of the transmons. Notice that the crosstalk coupling between T1 and T2,  $\mathcal{E}_{\text{TT}} \approx \frac{C^2}{2C_T^2 C_C}$ , is suppressed compared to the C1-C2 coupling  $\mathcal{E}_{\text{CC}} \approx \frac{C'+C}{C_C^2}$  and the control-target coupling  $\mathcal{E}_{\text{CT}} \approx \frac{C}{2C_T C_C}$ . This is expected, as the circuit has no direct capacitive coupling between T1 and T2.

Since we intend to operate the transmons near the ground state, we can assume that each transmon is near the vicinity of the potential minimum, thus allowing a fourth order expansion of the cosines in the Hamiltonian (B.35). Up to an irrelevant constant energy shift, we arrive at

$$\mathcal{H} = \sum_{v=\text{C,T}} \sum_{i=1,2} H_{\text{cl},vi} + \sum_{i,j=1,2} \mathcal{E}_{\text{CT}} p_{\text{Ci}} p_{\text{Tj}} - \mathcal{E}_{\text{CC}} p_{\text{C1}} p_{\text{C2}} + \mathcal{E}_{\text{TT}} p_{\text{T1}} p_{\text{T2}}, \quad (\text{B.45})$$

where the Hamiltonian for the non-interacting transmon  $vi$  is

$$\mathcal{H}_{vi} = 4E_{C_v} p_{vi}^2 + \frac{1}{2} E_{J_v} \phi_{vi}^2 - \frac{1}{24} E_{J_v} \phi_{vi}^4. \quad (\text{B.46})$$

The first two terms in  $\mathcal{H}_{vi}$  describe a harmonic oscillator, while the last term is a small anharmonic term.

We quantize the system by mapping the classical conjugate coordinates to the quantum operators:

$$\phi_{vi} \mapsto \left( \frac{2E_{C_v}}{E_{J_v}} \right)^{1/4} (b_{vi}^\dagger + b_{vi}) \quad (\text{B.47})$$

$$p_{vi} \mapsto i \left( \frac{E_{J_v}}{32E_{C_v}} \right)^{1/4} (b_{vi}^\dagger - b_{vi}), \quad (\text{B.48})$$

for  $\nu = C, T$  and  $i = 1, 2$ . Here  $b_{vi}$  is the usual bosonic annihilation operator, which diagonalizes the harmonic oscillator part of the Hamiltonian, such that the mapping for transmon  $vi$  to a quantum Hamiltonian is

$$\mathcal{H}_{vi} \mapsto H_{vi} = \sqrt{8E_{C_v}E_{J_v}} \left( b_{vi}^\dagger b_{vi} + \frac{1}{2} \right) - \frac{1}{12} E_{C_v} (b_{vi} + b_{vi})^4. \quad (\text{B.49})$$

In the basis of harmonic oscillator states,  $|n\rangle_{vi}^{\text{HO}}$  for  $n = 0, 1, 2, \dots$ , the annihilation operator is  $b_{vi} = \sum_{n=1}^{\infty} \sqrt{n} |n-1\rangle_{vi}^{\text{HO}}$ . We assume that the transmons are operated near their ground states, and we therefore truncate each single-transmon Hilbert space to the first three harmonic oscillator states. Up to a constant energy shift, this results in the single-qutrit Hamiltonian,

$$\begin{aligned} H_{vi} \mapsto \tilde{H}_{vi} = & (\sqrt{8E_{C_v}E_{J_v}} - E_{C_v}) |1\rangle\langle 1|_{vi}^{\text{HO}} \\ & + (2\sqrt{8E_{C_v}E_{J_v}} - 3E_{C_v}) |2\rangle\langle 2|_{vi}^{\text{HO}} \\ & - \frac{E_{C_v}}{\sqrt{2}} |0\rangle\langle 2|_{vi}^{\text{HO}} - \frac{E_{C_v}}{\sqrt{2}} |2\rangle\langle 0|_{vi}^{\text{HO}}. \end{aligned} \quad (\text{B.50})$$

We denote qutrit operators with tildes to distinguish them from, e.g., the qubit operators used in Sections 4.2.1–4.2.3. Notice that inclusion of the third state,  $|2\rangle_{vi}^{\text{HO}}$ , introduces mixing terms in the Hamiltonian. Thus, unlike the case of truncation to qubits, where the two lowest harmonic oscillator states become the qubit states, we

have to diagonalize the above Hamiltonian. Doing so, we find the qutrit states:

$$|0\rangle_{vi} = \frac{1}{\sqrt{\frac{1}{2}E_{C_v}^2 + \omega_{0,\nu}^2}} \left( \frac{E_{C_v}}{\sqrt{2}} |0\rangle_{vi}^{\text{HO}} - \omega_{0,\nu} |2\rangle_{vi}^{\text{HO}} \right) \quad (\text{B.51})$$

$$|1\rangle_{vi} = |1\rangle_{vi}^{\text{HO}} \quad (\text{B.52})$$

$$|2\rangle_{vi} = \frac{1}{\sqrt{\frac{1}{2}E_{C_v}^2 + \omega_{2,\nu}^2}} \left( -\frac{E_{C_v}}{\sqrt{2}} |0\rangle_{vi}^{\text{HO}} + \omega_{2,\nu} |2\rangle_{vi}^{\text{HO}} \right), \quad (\text{B.53})$$

where the corresponding energies can be expressed as

$$\omega_{0,\nu} = \sqrt{\left( \Omega_\nu + \frac{1}{2}\alpha_\nu \right)^2 - \frac{1}{2}\alpha_\nu^2} - \Omega_\nu - \frac{1}{2}\alpha_\nu, \quad (\text{B.54})$$

$$\omega_{1,\nu} = \omega_{0,\nu} + \Omega_\nu, \quad (\text{B.55})$$

$$\omega_{2,\nu} = \omega_{1,\nu} + \Omega_\nu + \alpha_\nu. \quad (\text{B.56})$$

Here  $\Omega_\nu$  is the qubit frequency, i.e. the energy difference between the qubit levels, and  $\alpha_\nu$  is the anharmonicity. In terms of circuit parameters, they are given as

$$\Omega_\nu = \frac{1}{2}E_{C_v} + \sqrt{\left( \sqrt{8E_{C_v}E_{J_\nu}} - \frac{3}{2}E_{C_v} \right)^2 + \frac{1}{2}E_{C_v}^2}, \quad (\text{B.57})$$

$$\alpha_\nu = -E_{C_v}. \quad (\text{B.58})$$

In the transmon regime,  $E_{C_v} \ll E_{J_\nu}$ , the anharmonicity is negative and much smaller than the qubit frequency,  $-\alpha_\nu \ll \Omega_\nu$ . We can write the qutrit Hamiltonian on the form

$$\tilde{H}_{vi} = -\frac{1}{2}\Omega_\nu \tilde{\sigma}_z^{vi} + \frac{1}{2}(\omega_{0,\nu} + \omega_{1,\nu}) \mathbb{1}_{vi}, \quad (\text{B.59})$$

which is a straightforward generalization of the typical single-qubit Hamiltonian. Here  $\mathbb{1}_{vi}$  is the identity operator and  $\tilde{\sigma}_z^{vi}$  is a generalized Pauli  $z$ -operator,

$$\tilde{\sigma}_z^{vi} = |0\rangle\langle 0|_{vi} - |1\rangle\langle 1|_{vi} - \left( 3 + \frac{2\alpha_\nu}{\Omega_\nu} \right) |2\rangle\langle 2|_{vi}. \quad (\text{B.60})$$

We now map the interaction terms of the Hamiltonian (B.45) to the qutrit model. Quantization of an interaction term yields

$$\mathcal{E}_{\nu\mu} p_{\nu i} p_{\mu j} \mapsto -\mathcal{E}_{\nu\mu} \left( \frac{E_{J_\nu}}{32E_{C_\nu}} \right)^{1/4} \left( \frac{E_{J_\mu}}{32E_{C_\mu}} \right)^{1/4} (b_{\nu i}^\dagger - b_{\nu i})(b_{\mu j}^\dagger - b_{\mu j}), \quad (\text{B.61})$$

where  $\nu, \mu \in \{\text{C}, \text{T}\}$  and  $i, j \in \{1, 2\}$ . Since the operator  $b_{\nu i}^\dagger - b_{\nu i} = \sum_{n=1}^{\infty} \sqrt{n}(|n\rangle\langle n-1|_{\nu i}^{\text{HO}} - |n-1\rangle\langle n|_{\nu i}^{\text{HO}})$ , we expect the coupling between the transmon states  $|n-1\rangle_{\nu i}$  and  $|n\rangle_{\nu i}$  to be roughly  $\sqrt{n}$ . However, if the transmons are initialized in the qubit subspace, spanned by the lowest two states, population of higher order states require higher-order processes and are limited by the number of excitations in the system. Truncating the Hilbert space to the lowest three harmonic oscillator states maps  $b_{\nu i}^\dagger - b_{\nu i} \mapsto -i\tilde{\sigma}_y^{\nu i}$ , where  $\tilde{\sigma}_y^{\nu i}$  is the generalized Pauli  $y$ -operator on qutrit  $\nu i$  defined as

$$\tilde{\sigma}_y^{\nu i} = iT_0^\nu |1\rangle\langle 0|_{\nu i} + iT_2^\nu |2\rangle\langle 1|_{\nu i} + \text{H.c.}, \quad (\text{B.62})$$

with

$$T_\beta^\nu = \sqrt{2} \frac{\omega_{\beta,\nu} - \frac{1}{2}\alpha_\nu}{\sqrt{\omega_{\beta,\nu}^2 + \frac{1}{2}\alpha_\nu^2}}, \quad \beta = 0, 2. \quad (\text{B.63})$$

In the transmon regime  $T_0^\nu \approx 1$  and  $T_2^\nu \approx \sqrt{2}$ , as expected.

Putting these results together and ignoring the constant off-set in Eq. (B.59), we find the final qutrit Hamiltonian:

$$\begin{aligned} \tilde{H} = & -\frac{1}{2}\Omega_{\text{T}}(\tilde{\sigma}_z^{\text{T1}} + \tilde{\sigma}_z^{\text{T2}}) - \frac{1}{2}\Omega_{\text{C}}(\tilde{\sigma}_z^{\text{C1}} + \tilde{\sigma}_z^{\text{C2}}) \\ & + J_{\text{T}}\tilde{\sigma}_y^{\text{T1}}\tilde{\sigma}_y^{\text{T2}} + J_{\text{C}}\tilde{\sigma}_y^{\text{C1}}\tilde{\sigma}_y^{\text{C2}} \\ & + J(\tilde{\sigma}_y^{\text{T1}} + \tilde{\sigma}_y^{\text{T2}})(\tilde{\sigma}_y^{\text{C1}} + \tilde{\sigma}_y^{\text{C2}}), \end{aligned} \quad (\text{B.64})$$

which is the sum of  $\tilde{H}_0$  and  $\tilde{H}_{\text{int}}$  from Eqs. (4.40)–(4.41) in the main text. In terms of circuit parameters, the couplings are

$$J_{\text{T}} = \mathcal{E}_{\text{TT}} \sqrt{\frac{E_{J_{\text{T}}}}{32E_{C_{\text{T}}}}}, \quad (\text{B.65})$$

$$J_{\text{C}} = -\mathcal{E}_{\text{CC}} \sqrt{\frac{E_{J_{\text{C}}}}{32E_{C_{\text{C}}}}}, \quad (\text{B.66})$$

$$J = \mathcal{E}_{\text{CT}} \left( \frac{E_{J_{\text{C}}}}{32E_{C_{\text{C}}}} \right)^{1/4} \left( \frac{E_{J_{\text{T}}}}{32E_{C_{\text{T}}}} \right)^{1/4}. \quad (\text{B.67})$$

### B.2.2 Redefinition of the control states

We wish to understand how the second excited states influence the dynamics of the control states. In order to make the problem more manageable, we reduce to system size to the control qubits only and consider the effective control Hamiltonian

$$\tilde{H}_C = -\frac{1}{2}\Omega_C(\tilde{\sigma}_z^{C1} + \tilde{\sigma}_z^{C2}) + J_C\tilde{\sigma}_y^{C1}\tilde{\sigma}_y^{C2}, \quad (\text{B.68})$$

which assumes the target qubits are far detuned from the control qubits, e.g. during state initialization. We expect this Hamiltonian to dominate the dynamics of the control qubits also when the full four-qubit diamond gate operates.

Let us consider the effect on each control state. First, we see that

$$\tilde{H}_C |00\rangle_C = -\Omega_C |00\rangle_C - J_C(T_0^C)^2 |11\rangle_C, \quad (\text{B.69})$$

$$\tilde{H}_C |\Psi^\pm\rangle_C = \pm J_C(T_0^C)^2 |\Psi^\pm\rangle_C - J_C T_0^C T_2^C \frac{1}{\sqrt{2}}(|12\rangle_C \pm |21\rangle_C). \quad (\text{B.70})$$

Since the  $\tilde{\sigma}_y$  operators only couples neighboring energy states, the zero excitation state  $|00\rangle_C$  does not couple to any second excited transmon levels. However, it does couple to  $|11\rangle_C$ , but being offset by two excitations, this coupling is energetically suppressed. The Bell states' couplings to second excited states, i.e. the second term on the right hand side of Eq. B.70, can be dismissed with the same argument. Effectively, the states  $|00\rangle_C$  and  $|\Psi^\pm\rangle_C$  exhibit no dynamics.

This does not hold for the  $|11\rangle_C$  state:

$$\begin{aligned} \tilde{H}_C |11\rangle_C &= \Omega_C |11\rangle_C + J_C T_0^C T_2^C (|02\rangle_C + |20\rangle_C) \\ &\quad - J_C (T_0^C)^2 |00\rangle_C - J_C (T_2^C)^2 |22\rangle_C, \end{aligned} \quad (\text{B.71})$$

The last two terms are energetically suppressed, but the coupling to  $(|02\rangle_C + |20\rangle_C)/\sqrt{2}$  can not be dismissed on this account. Noticing that the Hamiltonian only couples this state back to  $|11\rangle_C$ ,

$$\begin{aligned} \tilde{H}_C \frac{1}{\sqrt{2}}(|02\rangle_C + |20\rangle_C) &= (\Omega_C + \alpha_C) \frac{1}{\sqrt{2}}(|02\rangle_C + |20\rangle_C) \\ &\quad + \sqrt{2} J_C T_0^C T_2^C |11\rangle_C, \end{aligned} \quad (\text{B.72})$$

we can diagonalize the Hamiltonian in the subspace spanned by  $|11\rangle_C$  and  $(|02\rangle_C + |20\rangle_C)/\sqrt{2}$ , yielding two eigenstates. The redefined

control state,  $|\tilde{11}\rangle_C$  of Eq. (4.44), is the eigenstate that reduces to  $|11\rangle_C$  when  $J_C \rightarrow 0$ . When initializing the control in  $|\tilde{11}\rangle_C$  rather than  $|11\rangle_C$ , we suppress dynamics in the control state and hence gate infidelity.

### B.2.3 Engineering crosstalk

The presence of second excited states in the transmon spectrum allows quantum state transfer between the target qubits, which renders the swap operation unconditional on the control state. This has essentially the same consequences as a small direct coupling between the target qubits (crosstalk). Both effects are unavoidable in a superconducting transmon qubit implementation, but we can effectively avoid the state transfer by picking the crosstalk strength such that it cancels the state transfer occurring via the qutrit levels. The goal of this section is to derive a value of the crosstalk strength which optimally achieves this cancellation.

For our analysis here, we assume that the control qubits are initialized in  $|\Psi^-\rangle_C$ , which should ideally prevent any dynamics in the system, and that the target qubits are initialized in  $|01\rangle_T$ . The Hamiltonian  $\tilde{H}$  of Eq. (B.64) couples  $|\Psi^-\rangle_C |01\rangle_T$  to several other states, but we are only interested in processes that contribute significantly to the unwanted swap operation,

$$|\Psi^-\rangle_C |01\rangle_T \rightarrow |\Psi^-\rangle_C |10\rangle_T . \quad (\text{B.73})$$

Thus we truncate our analysis at second-order contributions, which leaves only the states shown in Figure B.3. These four states comprise an effective Hilbert space, where the swap can occur as a first-order crosstalk process (green), or a second-order process via the detuned states involving second-excited transmon states (magenta). The latter processes, being second-order occurring via detuned states, are relatively slow, which means that only a small amount of crosstalk is needed in order to match their transition rates.

In the basis

$$\left\{ |\Psi^-\rangle_C |10\rangle_T, \quad \frac{1}{\sqrt{2}}(|02\rangle_C - |20\rangle_C) |00\rangle_T, \right. \\ \left. \frac{1}{\sqrt{2}}(|02\rangle_C - |20\rangle_C) |11\rangle_T, \quad |\Psi^-\rangle_C |01\rangle_T \right\} \quad (\text{B.74})$$

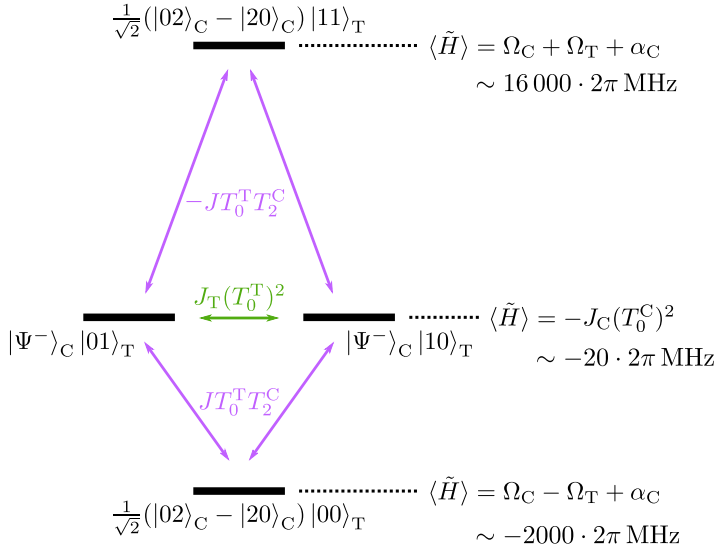


Figure B.3: Subspace relevant for the cancellation of unwanted swap between the target qubits. State couplings and their strengths are shown in green and magenta. The energy (expectation value) of the states are indicated, and estimates are given using the same parameters as in the simulations in Section. 4.2.4. The figure is adapted from Ref. [8].

the effective Hamiltonian is

$$\tilde{H}_{\text{eff}} = \begin{pmatrix} 0 & \delta & \delta & \kappa \\ \delta & \Delta_- & 0 & \delta \\ \delta & 0 & \Delta_+ & \delta \\ \kappa & \delta & \delta & 0 \end{pmatrix}, \quad (\text{B.75})$$

with

$$\Delta_{\pm} = \Omega_C \pm \Omega_T + \alpha_C + J_C(T_0^C)^2 \quad (\text{B.76})$$

$$\delta = JT_0^T T_2^C \quad (\text{B.77})$$

$$\kappa = J_T(T_0^T)^2. \quad (\text{B.78})$$

Thus, the goal is to find the relationship between  $\delta$  and  $\kappa$  such that the dynamics under the effective Hamiltonian is frozen for the initial state  $|\Psi^-\rangle_C |10\rangle_T$ . The transition probability, which we want to minimize,

is

$$P = \left| \langle 10 |_{\text{T}} \langle \Psi^- |_{\text{C}} e^{-i\tilde{H}_{\text{eff}}t} | \Psi^- \rangle_{\text{C}} | 01 \rangle_{\text{T}} \right|^2, \quad (\text{B.79})$$

We consider the problem perturbatively in the effective couplings, writing  $\tilde{H}_{\text{eff}} = \tilde{H}_{\text{eff},0} + \tilde{V}_{\text{eff}}$ , with  $\tilde{H}_{\text{eff},0}$  being the diagonal and  $\tilde{V}_{\text{eff}}$  the non-diagonal part of  $\tilde{H}_{\text{eff}}$ . This enables us to express the time-evolution operator in the interactionpicture,

$$U_I(t) = e^{i\tilde{H}_{\text{eff},0}t} e^{-i\tilde{H}_{\text{eff}}t} e^{-i\tilde{H}_{\text{eff},0}t}, \quad (\text{B.80})$$

as a Dyson series. Truncating the perturbative series at second-order contributions,

$$\begin{aligned} U_I(t) \approx & 1 - i \int_0^t dt' e^{i\tilde{H}_{\text{eff},0}t'} \tilde{V}_{\text{eff}} e^{-i\tilde{H}_{\text{eff},0}t'} \\ & + (-i)^2 \int_0^t dt' \int_0^{t'} dt'' e^{i\tilde{H}_{\text{eff},0}t'} \tilde{V}_{\text{eff}} e^{-i\tilde{H}_{\text{eff},0}(t'-t'')} \tilde{V}_{\text{eff}} e^{-i\tilde{H}_{\text{eff},0}t''}, \end{aligned} \quad (\text{B.81})$$

we find for the transition probability:

$$P = \left| \langle 10 |_{\text{T}} \langle \Psi^- |_{\text{C}} U_I(t) | \Psi^- \rangle_{\text{C}} | 01 \rangle_{\text{T}} \right|^2 \quad (\text{B.82})$$

$$= \left| -i \int_0^t dt' \kappa - \delta^2 \int_0^t dt' \int_0^{t'} dt'' \left( e^{i\Delta_-(t''-t')} + e^{i\Delta_+(t''-t')} \right) \right|^2 \quad (\text{B.83})$$

$$= \left| -it\kappa + \delta^2 \left( \frac{i\Delta_-t + e^{-i\Delta_-t} - 1}{\Delta_-^2} + \frac{i\Delta_+t + e^{-i\Delta_+t} - 1}{\Delta_+^2} \right) \right|^2 \quad (\text{B.84})$$

$$\approx t^2 \left| \kappa - \delta^2 \left( \frac{1}{\Delta_-} + \frac{1}{\Delta_+} \right) \right|^2, \quad (\text{B.85})$$

where we have ignored the terms of order  $\delta^2/\Delta_{\pm}^2 \ll 1$  in the last line. Thus, the condition for a vanishing transition probability is

$$\kappa = \delta^2 \left( \frac{1}{\Delta_-} + \frac{1}{\Delta_+} \right), \quad (\text{B.86})$$

which in terms of the crosstalk strength becomes  $J_{\text{T}} = J_{\text{T}}^{\text{opt}}$  of Eq. (4.47).

# Bibliography

- [1] N. J. S. Loft, L. B. Kristensen, A. E. Thomsen, A. G. Volosniev, and N. T. Zinner. “CONAN – The cruncher of local exchange coefficients for strongly interacting confined systems in one dimension”. In: *Computer Physics Communications* 209 (2016), pp. 171–182.
- [2] N. J. S. Loft, L. B. Kristensen, A. E. Thomsen, and N. T. Zinner. “Comparing models for the ground state energy of a trapped one-dimensional Fermi gas with a single impurity”. In: *Journal of Physics B Atomic Molecular Physics* 49.12, 125305 (June 2016), p. 125305.
- [3] N. J. S. Loft, O. V. Marchukov, D. Petrosyan, and N. T. Zinner. “Tunable self-assembled spin chains of strongly interacting cold atoms for demonstration of reliable quantum state transfer”. In: *New Journal of Physics* 18.4, 045011 (Apr. 2016), p. 045011.
- [4] C. W. Duncan, N. J. S. Loft, P. Öhberg, N. T. Zinner, and M. Valiente. “Spin Localization of a Fermi Polaron in a Quasirandom Optical Lattice”. In: *Few-Body Systems* 58.2 (2017), p. 50.
- [5] N. J. S. Loft, Z. Wu, and G. M. Bruun. “Mixed-dimensional Bose polaron”. In: *Physical Review A* 96.3 (2017), p. 033625.
- [6] N. J. S. Loft, L. B. Kristensen, C. K. Andersen, and N. T. Zinner. “Quantum spin transistors in superconducting circuits”. In: *arXiv preprint arXiv:1802.04292* (2018).
- [7] T. Bækkegaard, L. B. Kristensen, N. J. S. Loft, C. K. Andersen, D. Petrosyan, and N. T. Zinner. “Realization of efficient quantum gates with a superconducting qubit-qutrit circuit”. In: *Scientific Reports (accepted for publication)* (2019).
- [8] N. J. S. Loft, M. Kjaergaard, L. B. Kristensen, C. K. Andersen, T. W. Larsen, S. Gustavsson, W. D. Oliver, and N. T. Zinner. “Quantum interference device for controlled two-qubit operations”. In: *arXiv preprint arXiv:1809.09049 (submitted to npj Quantum Information)* (2018).

- [9] L. B. Kristensen, N. J. S. Loft, C. K. Andersen, and N. T. Zinner. *Quantum logic gate and quantum spin transistors*. European Patent Office application no. EPO 17185721.2–1879. Aug. 10, 2017.
- [10] N. J. S. Loft. *SonPy – Python interface for Sonnet*. Version 1.1. Available here: <https://github.com/QMIT/sonpy>. Sept. 16, 2018.
- [11] N. J. S. Loft, A. S. Dehkharghani, N. P. Mehta, A. G. Volosniev, and N. T. Zinner. “A variational approach to repulsively interacting three-fermion systems in a one-dimensional harmonic trap”. In: *The European Physical Journal D* 69 (2015).
- [12] A. S. Dehkharghani, N. J. S. Loft, and N. T. Zinner. “Kvantemagneter – Magneter når de er allermindst”. In: *Aktuel Naturvidenskab* 5-2016 (2016).
- [13] N. J. S. Loft. “På jagt efter computerens næste kvantespring”. In: *videnskab.dk* (Mar. 24, 2017).
- [14] N. J. S. Loft. “Vi får aldrig eksakt viden om verden”. In: *videnskab.dk* (Aug. 10, 2017).
- [15] N. J. S. Loft. “Tyngdekraften findes kun i dit hoved”. In: *videnskab.dk* (Jan. 27, 2018).
- [16] N. J. S. Loft. “Matematikken kan bryde sammen i morgen”. In: *videnskab.dk* (Jan. 6, 2019).
- [17] W. Heisenberg. “Mehrkörperproblem und Resonanz in der Quantenmechanik”. In: *Zeitschrift für Physik* 38.6-7 (1926), pp. 411–426.
- [18] P. A. M. Dirac. “On the theory of quantum mechanics”. In: *Proceedings of the Royal Society of London. Series A, Containing Papers of a Mathematical and Physical Character* 112.762 (1926), pp. 661–677.
- [19] L. Onsager. “Crystal statistics. I. A two-dimensional model with an order-disorder transition”. In: *Physical Review* 65.3-4 (1944), p. 117.
- [20] H. Bethe. “Zur theorie der metalle”. In: *Zeitschrift für Physik* 71.3-4 (1931), pp. 205–226.
- [21] M. Takahashi. *Thermodynamics of one-dimensional solvable models*. Cambridge University Press, 2005.
- [22] M. D. Girardeau. “Relationship between Systems of Impenetrable Bosons and Fermions in One Dimension”. In: *Journal of Mathematical Physics* 1.6 (1960), pp. 516–523.
- [23] E. H. Lieb and W. Liniger. “Exact analysis of an interacting Bose gas. I. The general solution and the ground state”. In: *Physical Review* 130.4 (1963), p. 1605.
- [24] L. Tonks. “The Complete Equation of State of One, Two and Three-Dimensional Gases of Hard Elastic Spheres”. In: *Physical Review* 50 (Nov. 1936), pp. 955–963.

- [25] H. Moritz, T. Stöferle, M. Köhl, and T. Esslinger. “Exciting collective oscillations in a trapped 1D gas”. In: *Physical review letters* 91.25 (2003), p. 250402.
- [26] T. Kinoshita, T. Wenger, and D. S. Weiss. “A quantum Newton’s cradle”. In: *Nature* 440 (Apr. 2006), pp. 900–903.
- [27] M. Lewenstein, A. Sanpera, V. Ahufinger, B. Damski, A. Sen, and U. Sen. “Ultracold atomic gases in optical lattices: mimicking condensed matter physics and beyond”. In: *Advances in Physics* 56 (Mar. 2007), pp. 243–379.
- [28] I. Bloch, J. Dalibard, and W. Zwerger. “Many-body physics with ultracold gases”. In: *Reviews of Modern Physics* 80 (July 2008), pp. 885–964.
- [29] E. Haller, M. Gustavsson, M. J. Mark, J. G. Danzl, R. Hart, G. Pupillo, and H.-C. Nägerl. “Realization of an Excited, Strongly Correlated Quantum Gas Phase”. In: *Science* 325 (Sept. 2009), p. 1224.
- [30] E. Haller, R. Hart, M. J. Mark, J. G. Danzl, L. Reichsöllner, M. Gustavsson, M. Dalmonte, G. Pupillo, and H.-C. Nägerl. “Pinning quantum phase transition for a Luttinger liquid of strongly interacting bosons”. In: *Nature* 466 (July 2010), pp. 597–600.
- [31] T. Esslinger. “Fermi-Hubbard Physics with Atoms in an Optical Lattice”. In: *Annual Review of Condensed Matter Physics* 1 (Apr. 2010), pp. 129–152.
- [32] G. Pagano et al. “A one-dimensional liquid of fermions with tunable spin”. In: *Nature Physics* 10 (Mar. 2014), pp. 198–201.
- [33] T. Kinoshita, T. Wenger, and D. S. Weiss. “Observation of a One-Dimensional Tonks-Girardeau Gas”. In: *Science* 305 (Aug. 2004), pp. 1125–1128.
- [34] B. Paredes, A. Widera, V. Murg, O. Mandel, S. Fölling, I. Cirac, G. V. Shlyapnikov, T. W. Hänsch, and I. Bloch. “Tonks-Girardeau gas of ultracold atoms in an optical lattice”. In: *Nature* 429 (May 2004), pp. 277–281.
- [35] H. Feshbach. “A unified theory of nuclear reactions. II”. In: *Annals of Physics* 19.2 (1962), pp. 287–313.
- [36] C. Chin, R. Grimm, P. Julienne, and E. Tiesinga. “Feshbach resonances in ultracold gases”. In: *Rev. Mod. Phys.* 82 (2 Apr. 2010), pp. 1225–1286.
- [37] T. Sowiński and M. Á. García-March. “One-dimensional mixtures of several ultracold atoms: a review”. In: *arXiv preprint arXiv:1903.12189* (2019).

- [38] M. Olshanii. "Atomic Scattering in the Presence of an External Confinement and a Gas of Impenetrable Bosons". In: *Physical Review Letters* 81 (Aug. 1998), pp. 938–941.
- [39] J. B. McGuire. "Interacting fermions in one dimension. I. Repulsive potential". In: *Journal of Mathematical Physics* 6.3 (1965), pp. 432–439.
- [40] J. McGuire. "Interacting fermions in one dimension. II. Attractive potential". In: *Journal of Mathematical Physics* 7.1 (1966), pp. 123–132.
- [41] C.-N. Yang. "Some exact results for the many-body problem in one dimension with repulsive delta-function interaction". In: *Physical Review Letters* 19.23 (1967), p. 1312.
- [42] E. H. Lieb and F. Y. Wu. "Absence of Mott transition in an exact solution of the short-range, one-band model in one dimension". In: *Physical Review Letters* 20 (1968), pp. 1445–1448.
- [43] M. D. Girardeau. "Ground and Excited States of Spinor Fermi Gases in Tight Waveguides and the Lieb-Liniger-Heisenberg Model". In: *Physical Review Letters* 97.21, 210401 (Nov. 2006), p. 210401.
- [44] S. E. Gharashi and D. Blume. "Correlations of the Upper Branch of 1D Harmonically Trapped Two-Component Fermi Gases". In: *Physical Review Letters* 111.4, 045302 (July 2013), p. 045302.
- [45] E. J. Lindgren, J. Rotureau, C. Forssén, A. G. Volosniev, and N. T. Zinner. "Fermionization of two-component few-fermion systems in a one-dimensional harmonic trap". In: *New Journal of Physics* 16.6, 063003 (June 2014), p. 063003.
- [46] A. G. Volosniev, D. V. Fedorov, A. S. Jensen, M. Valiente, and N. T. Zinner. "Strongly interacting confined quantum systems in one dimension". In: *Nature Communications* 5, 5300 (Nov. 2014), p. 5300.
- [47] F. Deuretzbacher, D. Becker, and L. Santos. "Momentum distributions and numerical methods for strongly interacting one-dimensional spinor gases". In: *Phys. Rev. A* 94 (2 Aug. 2016), p. 023606.
- [48] F. Deuretzbacher, D. Becker, J. Bjerlin, S. M. Reimann, and L. Santos. "Quantum magnetism without lattices in strongly interacting one-dimensional spinor gases". In: *Physical Review A* 90.1, 013611 (July 2014), p. 013611.
- [49] A. G. Volosniev, D. Petrosyan, M. Valiente, D. V. Fedorov, A. S. Jensen, and N. T. Zinner. "Engineering the dynamics of effective spin-chain models for strongly interacting atomic gases". In: *Physical Review A* 91.2, 023620 (Feb. 2015), p. 023620.
- [50] C. Duncan, F. Bellotti, P. Öhberg, N. Zinner, and M. Valiente. "Mobile spin impurity in an optical lattice". In: *New Journal of Physics* 19.7 (2017), p. 075001.

- [51] J. Decamp, J. Gong, H. Loh, and C. Miniatura. "Symmetry, Tan Contact and Spectral Gap in One-Dimensional Fermions: A Graph-Theory Treatment". In: *arXiv preprint arXiv:1907.13412* (2019).
- [52] L. Qizhong, W. Ye, W. Zhongqi, et al. "Numerical simulation of deep learning algorithm for gas explosion in confined space". In: *Journal of Physics: Conference Series*. Vol. 1187. 4. IOP Publishing, 2019, p. 042034.
- [53] A. N. Wenz, G. Zürn, S. Murmann, I. Brouzos, T. Lompe, and S. Jochim. "From Few to Many: Observing the Formation of a Fermi Sea One Atom at a Time". In: *Science* 342 (Oct. 2013), pp. 457–460.
- [54] G. E. Astrakharchik and I. Brouzos. "Trapped one-dimensional ideal Fermi gas with a single impurity". In: *Physical Review A* 88.2 (2013), p. 021602.
- [55] N. Oelkers, M. T. Batchelor, M. Bortz, and X.-W. Guan. "Bethe ansatz study of one-dimensional Bose and Fermi gases with periodic and hard wall boundary conditions". In: *Journal of Physics A: Mathematical and General* 39.5 (2006), p. 1073.
- [56] X.-W. Guan and Z.-Q. Ma. "One-dimensional multicomponent fermions with  $\delta$ -function interaction in strong- and weak-coupling limits: Two-component Fermi gas". In: *Phys. Rev. A* 85 (3 Mar. 2012), p. 033632.
- [57] M. Christandl, N. Datta, A. Ekert, and A. J. Landahl. "Perfect State Transfer in Quantum Spin Networks". In: *Phys. Rev. Lett.* 92 (18 May 2004), p. 187902.
- [58] M. Christandl, N. Datta, T. C. Dorlas, A. Ekert, A. Kay, and A. J. Landahl. "Perfect transfer of arbitrary states in quantum spin networks". In: *Phys. Rev. A* 71 (3 Mar. 2005), p. 032312.
- [59] G. M. Nikolopoulos, D. Petrosyan, and P. Lambropoulos. "Coherent electron wavepacket propagation and entanglement in array of coupled quantum dots". In: *Europhysics Letters* 65.3 (2004), p. 297.
- [60] G. M. Nikolopoulos, D. Petrosyan, and P. Lambropoulos. "Electron wavepacket propagation in a chain of coupled quantum dots". In: *Journal of Physics: Condensed Matter* 16.28 (2004), p. 4991.
- [61] M. Plenio, J. Hartley, and J. Eisert. "Dynamics and manipulation of entanglement in coupled harmonic systems with many degrees of freedom". In: *New Journal of Physics* 6.1 (2004), p. 36.
- [62] M. Bellec, G. M. Nikolopoulos, and S. Tzortzakis. "Faithful communication Hamiltonian in photonic lattices". In: *Optics letters* 37.21 (2012), pp. 4504–4506.

- [63] A. Perez-Leija, R. Keil, A. Kay, H. Moya-Cessa, S. Nolte, L.-C. Kwek, B. M. Rodríguez-Lara, A. Szameit, and D. N. Christodoulides. “Coherent quantum transport in photonic lattices”. In: *Physical Review A* 87.1 (2013), p. 012309.
- [64] R. B. Diener, G. A. Georgakis, J. Zhong, M. Raizen, and Q. Niu. “Transition between extended and localized states in a one-dimensional incommensurate optical lattice”. In: *Physical Review A* 64.3 (2001), p. 033416.
- [65] G. De Chiara, D. Rossini, S. Montangero, and R. Fazio. “From perfect to fractal transmission in spin chains”. In: *Physical Review A* 72.1 (2005), p. 012323.
- [66] D. Petrosyan, G. M. Nikolopoulos, and P. Lambropoulos. “State transfer in static and dynamic spin chains with disorder”. In: *Physical Review A* 81.4 (2010), p. 042307.
- [67] A. Zwick, G. A. Alvarez, J. Stolze, and O. Osenda. “Robustness of spin-coupling distributions for perfect quantum state transfer”. In: *Physical Review A* 84.2 (2011), p. 022311.
- [68] G. M. Nikolopoulos. “Statistics of a quantum-state-transfer Hamiltonian in the presence of disorder”. In: *Physical Review A* 87.4 (2013), p. 042311.
- [69] P. W. Anderson. “Absence of Diffusion in Certain Random Lattices”. In: *Phys. Rev.* 109 (5 Mar. 1958), pp. 1492–1505.
- [70] H. Hu, A.-B. Wang, S. Yi, and X.-J. Liu. “Fermi polaron in a one-dimensional quasiperiodic optical lattice: The simplest many-body localization challenge”. In: *Phys. Rev. A* 93 (5 May 2016), p. 053601.
- [71] S. N. Bose. “Plancks Gesetz und Lichtquantenhypothese”. In: *Zeitschrift für Physik* 26.1 (Dec. 1924), pp. 178–181.
- [72] E. Fermi. “Sulla quantizzazione del gas perfetto monoatomico”. In: *Rendiconti Lincei* 145 (1926).
- [73] A. Einstein. “Quantentheorie des einatomigen idealen Gases”. In: *Sitzungsberichte der Preussischen Akademie der Wissenschaften* 1 (1925), pp. 3–14.
- [74] M. H. Anderson, J. R. Ensher, M. R. Matthews, C. E. Wieman, and E. A. Cornell. “Observation of Bose-Einstein condensation in a dilute atomic vapor”. In: *science* (1995), pp. 198–201.
- [75] K. B. Davis, M.-O. Mewes, M. R. Andrews, N. J. van Druten, D. S. Durfee, D. Kurn, and W. Ketterle. “Bose-Einstein condensation in a gas of sodium atoms”. In: *Physical review letters* 75.22 (1995), p. 3969.
- [76] N. N. Bogoliubov. “On the theory of superfluidity”. In: *Izv. Akad. Nauk Ser. Fiz.* 11 (1947), pp. 23–32.

- [77] A. L. Fetter and J. D. Walecka. *Quantum theory of many-particle systems*. McGraw-Hill Book Company, 1971.
- [78] C. J. Pethick and H. Smith. *Bose–Einstein condensation in dilute gases*. Cambridge University Press, 2008.
- [79] H. Bruus and K. Flensberg. *Many-body quantum theory in condensed matter physics: an introduction*. Oxford University Press, 2004.
- [80] M. E. Peskin and D. Schroeder. *An Introduction to Quantum Field Theory*. 1995.
- [81] L. D. Landau. “Über die Bewegung der Elektronen in Kristallgitter”. In: *Phys. Z. Sowjetunion* 3 (1933), p. 644.
- [82] G. Baym and C. Pethick. *Landau Fermi-Liquid Theory: Concepts and Applications*. Wiley-VCH, 1991.
- [83] E. Dagotto. “Correlated electrons in high-temperature superconductors”. In: *Rev. Mod. Phys.* 66 (3 July 1994), pp. 763–840.
- [84] M. E. Gershenson, V. Podzorov, and A. F. Morpurgo. “Colloquium : Electronic transport in single-crystal organic transistors”. In: *Rev. Mod. Phys.* 78 (3 Sept. 2006), pp. 973–989.
- [85] R. Bishop. “On the ground state of an impurity in a dilute fermi gas”. In: *Annals of Physics* 78.2 (1973), p. 391.
- [86] P. W. Higgs. “Broken symmetries and the masses of gauge bosons”. In: *Physical Review Letters* 13.16 (1964), p. 508.
- [87] R. S. Christensen. “Polarons: Interacting Impurities In Ultracold Gases”. PhD thesis. Aarhus University, Feb. 2017.
- [88] S. P. Rath and R. Schmidt. “Field-theoretical study of the Bose polaron”. In: *Phys. Rev. A* 88 (5 Nov. 2013), p. 053632.
- [89] F. Chevy. “Universal phase diagram of a strongly interacting Fermi gas with unbalanced spin populations”. In: *Phys. Rev. A* 74 (6 2006), p. 063628.
- [90] N. Prokof’ev and B. Svistunov. “Fermi-polaron problem: Diagrammatic Monte Carlo method for divergent sign-alternating series”. In: *Phys. Rev. B* 77 (2 Jan. 2008), p. 020408.
- [91] C. Mora and F. Chevy. “Ground state of a tightly bound composite dimer immersed in a Fermi sea”. In: *Phys. Rev. A* 80 (3 Sept. 2009), p. 033607.
- [92] M. Punk, P. T. Dumitrescu, and W. Zwerger. “Polaron-to-molecule transition in a strongly imbalanced Fermi gas”. In: *Phys. Rev. A* 80 (5 Nov. 2009), p. 053605.
- [93] R. Combescot, S. Giraud, and X. Leyronas. “Analytical theory of the dressed bound state in highly polarized Fermi gases”. In: *EPL (Europhysics Letters)* 88.6 (2009), p. 60007.

- [94] P. Massignan and G. M. Bruun. “Repulsive polarons and itinerant ferromagnetism in strongly polarized Fermi gases”. In: *European Physical Journal D* 65 (Nov. 2011), pp. 83–89.
- [95] P. Massignan, M. Zaccanti, and G. M. Bruun. “Polarons, dressed molecules and itinerant ferromagnetism in ultracold Fermi gases”. In: *Reports on Progress in Physics* 77.3 (2014), p. 034401.
- [96] J. Levinsen, M. M. Parish, and G. M. Bruun. “Impurity in a Bose-Einstein Condensate and the Efimov Effect”. In: *Phys. Rev. Lett.* 115 (12 Sept. 2015), p. 125302.
- [97] Y. Nishida and S. Tan. “Liberating Efimov Physics from Three Dimensions”. In: *Few-Body Systems* 51.2 (2011), p. 191.
- [98] Y. Nishida. “Induced p-wave superfluidity in two dimensions: Brane world in cold atoms and nonrelativistic defect CFTs”. In: *Annals of Physics* 324.4 (2009), pp. 897–919.
- [99] Y. Nishida and S. Tan. “Universal Fermi gases in mixed dimensions”. In: *Phys. Rev. Lett.* 101.17 (2008), p. 170401.
- [100] N. B. Jørgensen, L. Wacker, K. T. Skalmstang, M. M. Parish, J. Levinsen, R. S. Christensen, G. M. Bruun, and J. J. Arlt. “Observation of Attractive and Repulsive Polarons in a Bose-Einstein Condensate”. In: *Phys. Rev. Lett.* 117 (5 July 2016), p. 055302.
- [101] Y. E. Shchadilova, R. Schmidt, F. Grusdt, and E. Demler. “Quantum Dynamics of Ultracold Bose Polarons”. In: *Phys. Rev. Lett.* 117 (11 Sept. 2016), p. 113002.
- [102] L. A. P. Ardila and S. Giorgini. “Impurity in a Bose-Einstein condensate: Study of the attractive and repulsive branch using quantum Monte Carlo methods”. In: *Phys. Rev. A* 92 (3 Sept. 2015), p. 033612.
- [103] F. Grusdt, R. Schmidt, Y. E. Shchadilova, and E. Demler. “Strong-coupling Bose polarons in a Bose-Einstein condensate”. In: *Phys. Rev. A* 96 (1 July 2017), p. 013607.
- [104] P. O. Fedichev, M. W. Reynolds, and G. V. Shlyapnikov. “Three-Body Recombination of Ultracold Atoms to a Weakly Bound  $s$  Level”. In: *Phys. Rev. Lett.* 77 (14 Sept. 1996), pp. 2921–2924.
- [105] D. S. Petrov. “Three-body problem in Fermi gases with short-range interaction”. In: *Phys. Rev. A* 67 (1 Jan. 2003), p. 010703.
- [106] O. V. Marchukov, A. G. Volosniev, M. Valiente, D. Petrosyan, and N. T. Zinner. “Quantum spin transistor with a Heisenberg spin chain”. In: *Nature Communications* 7.13070 (Oct. 2016).
- [107] P. Krantz, M. Kjaergaard, F. Yan, T. P. Orlando, S. Gustavsson, and W. D. Oliver. “A quantum engineer’s guide to superconducting qubits”. In: *Applied Physics Reviews* 6.2 (2019), p. 021318.

- [108] J. Koch, T. M. Yu, J. Gambetta, A. A. Houck, D. I. Schuster, J. Majer, A. Blais, M. H. Devoret, S. M. Girvin, and R. J. Schoelkopf. "Charge-insensitive qubit design derived from the Cooper pair box". In: *Phys. Rev. A* 76 (4 Oct. 2007), p. 042319.
- [109] G. Wendin. "Quantum information processing with superconducting circuits: a review". In: *Reports on Progress in Physics* 80.10 (2017), p. 106001.
- [110] A. Megrant, C. Neill, R. Barends, B. Chiaro, Y. Chen, L. Feigl, J. Kelly, E. Lucero, M. Mariantoni, P. J. O'Malley, et al. "Planar superconducting resonators with internal quality factors above one million". In: *Applied Physics Letters* 100.11 (2012), p. 113510.
- [111] A. Fruchtmann and I. Choi. "Technical roadmap for fault-tolerant quantum computing". In: *NQIT Technical Roadmap* (2016).
- [112] I. Buluta, S. Ashhab, and F. Nori. "Natural and artificial atoms for quantum computation". In: *Reports on Progress in Physics* 74.10 (2011), p. 104401.
- [113] S. Gustavsson, O. Zwiernik, J. Bylander, F. Yan, F. Yoshihara, Y. Nakamura, T. P. Orlando, and W. D. Oliver. "Improving quantum gate fidelities by using a qubit to measure microwave pulse distortions". In: *Physical review letters* 110.4 (2013), p. 040502.
- [114] M. Reagor, C. B. Osborn, N. Tezak, A. Staley, G. Prawiroatmodjo, M. Scheer, N. Alidoust, E. A. Sete, N. Didier, M. P. da Silva, et al. "Demonstration of universal parametric entangling gates on a multi-qubit lattice". In: *Science advances* 4.2 (2018), eaao3603.
- [115] M. Rol, C. Bultink, T. O'Brien, S. De Jong, L. Theis, X. Fu, F. Luthi, R. Vermeulen, J. de Sterke, A. Bruno, et al. "Restless tuneup of high-fidelity qubit gates". In: *Physical Review Applied* 7.4 (2017), p. 041001.
- [116] S. Sheldon, L. S. Bishop, E. Magesan, S. Filipp, J. M. Chow, and J. M. Gambetta. "Characterizing errors on qubit operations via iterative randomized benchmarking". In: *Physical Review A* 93.1 (2016), p. 012301.
- [117] Z. Chen, J. Kelly, C. Quintana, R. Barends, B. Campbell, Y. Chen, B. Chiaro, A. Dunsworth, A. Fowler, E. Lucero, et al. "Measuring and suppressing quantum state leakage in a superconducting qubit". In: *Physical review letters* 116.2 (2016), p. 020501.
- [118] R. Barends, J. Kelly, A. Megrant, A. Veitia, D. Sank, E. Jeffrey, T. C. White, J. Mutus, A. G. Fowler, B. Campbell, et al. "Superconducting quantum circuits at the surface code threshold for fault tolerance". In: *Nature* 508.7497 (2014), p. 500.

- [119] J. Kelly, R. Barends, B. Campbell, Y. Chen, Z. Chen, B. Chiaro, A. Dunsworth, A. G. Fowler, I.-C. Hoi, E. Jeffrey, et al. "Optimal quantum control using randomized benchmarking". In: *Physical review letters* 112.24 (2014), p. 240504.
- [120] Y. Chen et al. "Qubit Architecture with High Coherence and Fast Tunable Coupling". In: *Phys. Rev. Lett.* 113 (22 Nov. 2014), p. 220502.
- [121] M. Rol, F. Battistel, F. Malinowski, C. Bultink, B. Tarasinski, R. Vollmer, N. Haider, N. Muthusubramanian, A. Bruno, B. Terhal, et al. "A fast, low-leakage, high-fidelity two-qubit gate for a programmable superconducting quantum computer". In: *arXiv preprint arXiv:1903.02492* (2019).
- [122] M. Kjaergaard, M. E. Schwartz, J. Braumüller, P. Krantz, J. I.-J. Wang, S. Gustavsson, and W. D. Oliver. "Superconducting Qubits: Current State of Play". In: *arXiv preprint arXiv:1905.13641* (2019).
- [123] S. Sheldon, E. Magesan, J. M. Chow, and J. M. Gambetta. "Procedure for systematically tuning up cross-talk in the cross-resonance gate". In: *Phys. Rev. A* 93 (6 June 2016), p. 060302.
- [124] A. Blais, R.-S. Huang, A. Wallraff, S. M. Girvin, and R. J. Schoelkopf. "Cavity quantum electrodynamics for superconducting electrical circuits: An architecture for quantum computation". In: *Physical Review A* 69.6 (2004), p. 062320.
- [125] M. H. Devoret. "Quantum fluctuations in electrical circuits". In: *Les Houches, Session LXIII* 7.8 (1995).
- [126] L. B. Kristensen. "Superconducting Circuits in Quantum Computation". MA thesis. Aarhus University, Jan. 2017.
- [127] V. Bouchiat, D. Vion, P. Joyez, D. Esteve, and M. Devoret. "Quantum coherence with a single Cooper pair". In: *Physica Scripta* 1998.T76 (1998), p. 165.
- [128] Y. Nakamura, Y. A. Pashkin, and J. Tsai. "Coherent control of macroscopic quantum states in a single-Cooper-pair box". In: *nature* 398.6730 (1999), p. 786.
- [129] T. Orlando, J. Mooij, L. Tian, C. H. Van Der Wal, L. Levitov, S. Lloyd, and J. Mazo. "Superconducting persistent-current qubit". In: *Physical Review B* 60.22 (1999), p. 15398.
- [130] J. Mooij, T. Orlando, L. Levitov, L. Tian, C. H. Van der Wal, and S. Lloyd. "Josephson persistent-current qubit". In: *Science* 285.5430 (1999), pp. 1036–1039.
- [131] C. H. Van der Wal, A. Ter Haar, F. Wilhelm, R. Schouten, C. Harman, T. Orlando, S. Lloyd, and J. Mooij. "Quantum superposition of macroscopic persistent-current states". In: *Science* 290.5492 (2000), pp. 773–777.

- [132] J. Q. You, X. Hu, S. Ashhab, and F. Nori. “Low-decoherence flux qubit”. In: *Physical Review B* 75.14 (2007), p. 140515.
- [133] V. E. Manucharyan, J. Koch, L. I. Glazman, and M. H. Devoret. “Fluxonium: Single cooper-pair circuit free of charge offsets”. In: *Science* 326.5949 (2009), pp. 113–116.
- [134] F. Yan et al. “The flux qubit revisited to enhance coherence and reproducibility”. In: *Nature Communications* 7 (Nov. 2016).
- [135] P. B. Wigley et al. “Fast machine-learning online optimization of ultra-cold-atom experiments”. In: *Scientific Reports* 6 (May 2016), p. 25890.
- [136] E. Kapit. “The upside of noise: engineered dissipation as a resource in superconducting circuits”. In: *Quantum Science and Technology* 2.3 (2017), p. 033002.
- [137] D. P. DiVincenzo. “Two-bit gates are universal for quantum computation”. In: *Physical Review A* 51.2 (1995), p. 1015.
- [138] A. Barenco, C. H. Bennett, R. Cleve, D. P. DiVincenzo, N. Margolus, P. Shor, T. Sleator, J. A. Smolin, and H. Weinfurter. “Elementary gates for quantum computation”. In: *Phys. Rev. A* 52 (5 Nov. 1995), pp. 3457–3467.
- [139] M. A. Nielsen and I. L. Chuang. *Quantum Computation and Quantum Information: 10th Anniversary Edition*. Cambridge University Press, 2010.
- [140] N. D. Mermin. *Quantum computer science: an introduction*. Cambridge University Press, 2007.
- [141] A. W. Harrow, B. Recht, and I. L. Chuang. “Efficient discrete approximations of quantum gates”. In: *Journal of Mathematical Physics* 43.9 (2002), pp. 4445–4451.
- [142] D. Venturelli, M. Do, E. Rieffel, and J. Frank. “Compiling quantum circuits to realistic hardware architectures using temporal planners”. In: *Quantum Science and Technology* 3.2 (2018), p. 025004.
- [143] S. Khatri, R. LaRose, A. Poremba, L. Cincio, A. T. Sornborger, and P. J. Coles. “Quantum-assisted quantum compiling”. In: *Quantum* 3 (2019), p. 140.
- [144] D. Deutsch. “Quantum theory, the Church–Turing principle and the universal quantum computer”. In: *Proceedings of the Royal Society of London. A. Mathematical and Physical Sciences* 400.1818 (1985), pp. 97–117.
- [145] D. Deutsch and R. Jozsa. “Rapid solution of problems by quantum computation”. In: *Proceedings of the Royal Society of London. Series A: Mathematical and Physical Sciences* 439.1907 (1992), pp. 553–558.

- [146] R. Cleve, A. Ekert, C. Macchiavello, and M. Mosca. “Quantum algorithms revisited”. In: *Proceedings of the Royal Society of London. Series A: Mathematical, Physical and Engineering Sciences* 454.1969 (1998), pp. 339–354.
- [147] P. W. Shor. “Algorithms for quantum computation: Discrete logarithms and factoring”. In: *Proceedings 35th annual symposium on foundations of computer science*. Ieee. 1994, pp. 124–134.
- [148] L. K. Grover. “A fast quantum mechanical algorithm for database search”. In: *arXiv preprint quant-ph/9605043* (1996).
- [149] L. K. Grover. “Quantum mechanics helps in searching for a needle in a haystack”. In: *Physical review letters* 79.2 (1997), p. 325.
- [150] I. Kerenidis and A. Prakash. “Quantum recommendation systems”. In: *arXiv preprint arXiv:1603.08675* (2016).
- [151] E. Tang. “A quantum-inspired classical algorithm for recommendation systems”. In: *arXiv preprint arXiv:1807.04271* (2018).
- [152] E. Tang. “Quantum-inspired classical algorithms for principal component analysis and supervised clustering”. In: *arXiv preprint arXiv:1811.00414* (2018).
- [153] A. Gilyén, S. Lloyd, and E. Tang. “Quantum-inspired low-rank stochastic regression with logarithmic dependence on the dimension”. In: *arXiv preprint arXiv:1811.04909* (2018).
- [154] S. Lloyd, M. Mohseni, and P. Rebentrost. “Quantum principal component analysis”. In: *Nature Physics* 10.9 (2014), p. 631.
- [155] S. Lloyd, M. Mohseni, and P. Rebentrost. “Quantum algorithms for supervised and unsupervised machine learning”. In: *arXiv preprint arXiv:1307.0411* (2013).
- [156] A. W. Harrow, A. Hassidim, and S. Lloyd. “Quantum Algorithm for Linear Systems of Equations”. In: *Phys. Rev. Lett.* 103 (15 Oct. 2009), p. 150502.
- [157] S. Bravyi, D. Gosset, and R. Koenig. “Quantum advantage with shallow circuits”. In: *Science* 362.6412 (2018), pp. 308–311.
- [158] D. P. DiVincenzo. “The physical implementation of quantum computation”. In: *Fortschritte der Physik: Progress of Physics* 48.9-11 (2000), pp. 771–783.
- [159] L. S. Bishop, S. Bravyi, A. Cross, J. M. Gambetta, and J. Smolin. “Quantum volume”. In: *Quantum Volume. Technical Report* (2017).
- [160] C. H. Bennett, D. P. DiVincenzo, J. A. Smolin, and W. K. Wootters. “Mixed-state entanglement and quantum error correction”. In: *Physical Review A* 54.5 (1996), p. 3824.

- [161] A. Steane. "Multiple-particle interference and quantum error correction". In: *Proceedings of the Royal Society of London. Series A: Mathematical, Physical and Engineering Sciences* 452.1954 (1996), pp. 2551–2577.
- [162] D. Gottesman. "Stabilizer codes and quantum error correction". In: *arXiv preprint quant-ph/9705052* (1997).
- [163] A. R. Calderbank, E. M. Rains, P. Shor, and N. J. Sloane. "Quantum error correction via codes over  $GF(4)$ ". In: *IEEE Transactions on Information Theory* 44.4 (1998), pp. 1369–1387.
- [164] H. G. Katzgraber, H. Bombin, and M. Martin-Delgado. "Error threshold for color codes and random three-body Ising models". In: *Physical review letters* 103.9 (2009), p. 090501.
- [165] B. J. Brown, N. H. Nickerson, and D. E. Browne. "Fault-tolerant error correction with the gauge color code". In: *Nature communications* 7 (2016), p. 12302.
- [166] D. Gottesman. "The Heisenberg representation of quantum computers". In: *arXiv preprint quant-ph/9807006* (1998).
- [167] S. Aaronson and D. Gottesman. "Improved simulation of stabilizer circuits". In: *Phys. Rev. A* 70 (5 Nov. 2004), p. 052328.
- [168] R. Raussendorf and J. Harrington. "Fault-tolerant quantum computation with high threshold in two dimensions". In: *Physical review letters* 98.19 (2007), p. 190504.
- [169] A. D. Córcoles, E. Magesan, S. J. Srinivasan, A. W. Cross, M. Steffen, J. M. Gambetta, and J. M. Chow. "Demonstration of a quantum error detection code using a square lattice of four superconducting qubits". In: *Nature communications* 6 (2015), p. 6979.
- [170] T. O'Brien, B. Tarasinski, and L. DiCarlo. "Density-matrix simulation of small surface codes under current and projected experimental noise". In: *npj Quantum Information* 3.1 (2017), p. 39.
- [171] A. G. Fowler, M. Mariantoni, J. M. Martinis, and A. N. Cleland. "Surface codes: Towards practical large-scale quantum computation". In: *Physical Review A* 86.3 (2012), p. 032324.
- [172] K. Wright, K. Beck, S. Debnath, J. Amini, Y. Nam, N. Grzesiak, J.-S. Chen, N. Plesch, M. Chmielewski, C. Collins, et al. "Benchmarking an 11-qubit quantum computer". In: *arXiv preprint arXiv:1903.08181* (2019).
- [173] T. Harty, D. Allcock, C. Ballance, L. Guidoni, H. Janacek, N. Linke, D. Stacey, and D. Lucas. "High-fidelity preparation, gates, memory, and readout of a trapped-ion quantum bit". In: *Physical review letters* 113.22 (2014), p. 220501.

- [174] K. M. Itoh and H. Watanabe. "Isotope engineering of silicon and diamond for quantum computing and sensing applications". In: *MRS Communications* 4.4 (2014), pp. 143–157.
- [175] D. M. Zajac, A. J. Sigillito, M. Russ, F. Borjans, J. M. Taylor, G. Burkard, and J. R. Petta. "Resonantly driven CNOT gate for electron spins". In: *Science* 359.6374 (2018), pp. 439–442.
- [176] A. Sørensen and K. Mølmer. "Quantum computation with ions in thermal motion". In: *Physical review letters* 82.9 (1999), p. 1971.
- [177] A. Sørensen and K. Mølmer. "Entanglement and quantum computation with ions in thermal motion". In: *Phys. Rev. A* 62 (2 July 2000), p. 022311.
- [178] J. Benhelm, G. Kirchmair, C. F. Roos, and R. Blatt. "Towards fault-tolerant quantum computing with trapped ions". In: *Nature Physics* 4.6 (2008), p. 463.
- [179] J. P. Gaebler, T. R. Tan, Y. Lin, Y. Wan, R. Bowler, A. C. Keith, S. Glancy, K. Coakley, E. Knill, D. Leibfried, et al. "High-fidelity universal gate set for  $9+$  ion qubits". In: *Physical review letters* 117.6 (2016), p. 060505.
- [180] C. Ballance, T. Harty, N. Linke, M. Sepiol, and D. Lucas. "High-fidelity quantum logic gates using trapped-ion hyperfine qubits". In: *Physical review letters* 117.6 (2016), p. 060504.
- [181] A. Erhard, J. J. Wallman, L. Postler, M. Meth, R. Stricker, E. A. Martinez, P. Schindler, T. Monz, J. Emerson, and R. Blatt. "Characterizing large-scale quantum computers via cycle benchmarking". In: *arXiv preprint arXiv:1902.08543* (2019).
- [182] T. P. Harty, M. A. Sepiol, D. T. C. Allcock, C. J. Ballance, J. E. Tarlton, and D. M. Lucas. "High-Fidelity Trapped-Ion Quantum Logic Using Near-Field Microwaves". In: *Phys. Rev. Lett.* 117 (14 Sept. 2016), p. 140501.
- [183] C. Ballance, V. Schäfer, J. P. Home, D. Szwer, S. C. Webster, D. Allcock, N. M. Linke, T. Harty, D. A. Craik, D. N. Stacey, et al. "Hybrid quantum logic and a test of Bell's inequality using two different atomic isotopes". In: *Nature* 528.7582 (2015), p. 384.
- [184] S. Caldwell, N. Didier, C. Ryan, E. Sete, A. Hudson, P. Karalekas, R. Manenti, M. Reagor, M. da Silva, R. Sinclair, et al. "Parametrically activated entangling gates using transmon qubits". In: *arXiv preprint arXiv:1706.06562* (2017).

- [185] H. Paik, A. Mezzacapo, M. Sandberg, D. McClure, B. Abdo, A. Córcoles, O. Dial, D. Bogorin, B. Plourde, M. Steffen, et al. “Experimental demonstration of a resonator-induced phase gate in a multiqubit circuit-qed system”. In: *Physical Review Letters* 117.25 (2016), p. 250502.
- [186] S. Poletto, J. M. Gambetta, S. T. Merkel, J. A. Smolin, J. M. Chow, A. Córcoles, G. A. Keefe, M. B. Rothwell, J. Rozen, D. Abraham, et al. “Entanglement of two superconducting qubits in a waveguide cavity via monochromatic two-photon excitation”. In: *Physical review letters* 109.24 (2012), p. 240505.
- [187] D. C. McKay, S. Filipp, A. Mezzacapo, E. Magesan, J. M. Chow, and J. M. Gambetta. “Universal gate for fixed-frequency qubits via a tunable bus”. In: *Physical Review Applied* 6.6 (2016), p. 064007.
- [188] A. Dewes, F. R. Ong, V. Schmitt, R. Lauro, N. Boulant, P. Bertet, D. Vion, and D. Esteve. “Characterization of a Two-Transmon Processor with Individual Single-Shot Qubit Readout”. In: *Phys. Rev. Lett.* 108 (5 Feb. 2012), p. 057002.
- [189] Y. Salathé, M. Mondal, M. Oppliger, J. Heinsoo, P. Kurpiers, A. Potočnik, A. Mezzacapo, U. Las Heras, L. Lamata, E. Solano, et al. “Digital quantum simulation of spin models with circuit quantum electrodynamics”. In: *Physical Review X* 5.2 (2015), p. 021027.
- [190] A. Kandala, A. Mezzacapo, K. Temme, M. Takita, M. Brink, J. M. Chow, and J. M. Gambetta. “Hardware-efficient variational quantum eigensolver for small molecules and quantum magnets”. In: *Nature* 549.7671 (2017), p. 242.
- [191] F. Yan, P. Krantz, Y. Sung, M. Kjaergaard, D. L. Campbell, T. P. Orlando, S. Gustavsson, and W. D. Oliver. “Tunable Coupling Scheme for Implementing High-Fidelity Two-Qubit Gates”. In: *Phys. Rev. Applied* 10 (5 Nov. 2018), p. 054062.
- [192] N. Didier, E. A. Sete, M. P. da Silva, and C. Rigetti. “Analytical modeling of parametrically modulated transmon qubits”. In: *Phys. Rev. A* 97 (2 Feb. 2018), p. 022330.
- [193] A. Kandala, A. Mezzacapo, K. Temme, M. Takita, M. Brink, J. M. Chow, and J. M. Gambetta. “Hardware-efficient variational quantum eigensolver for small molecules and quantum magnets”. In: *Nature* 549 (Sept. 2017), pp. 242–246.
- [194] Z. Wang, S. Shankar, Z. Mineev, P. Campagne-Ibarcq, A. Narla, and M. Devoret. “Cavity Attenuators for Superconducting Qubits”. In: *arXiv preprint arXiv:1807.04849* (2018).

- [195] M. Kounalakis, C. Dickel, A. Bruno, N. Langford, and G. Steele. "Tuneable hopping and nonlinear cross-Kerr interactions in a high-coherence superconducting circuit". In: *npj Quantum Information* 4.1 (2018), p. 38.
- [196] J. R. Johansson, P. D. Nation, and F. Nori. "QuTip: An open-source Python framework for the dynamics of open quantum systems". In: *Comp. Phys. Comm.* 183.8 (2012), pp. 1760–1772.
- [197] M. A. Nielsen. "A simple formula for the average gate fidelity of a quantum dynamical operation". In: *Physics Letters A* 303.4 (2002), pp. 249–252.
- [198] A. A. Abdumalikov Jr, J. M. Fink, K. Juliusson, M. Pechal, S. Berger, A. Wallraff, and S. Filipp. "Experimental realization of non-Abelian non-adiabatic geometric gates". In: *Nature* 496.7446 (2013), p. 482.
- [199] J. E. Avron, L. Sadun, J. Segert, and B. Simon. "Topological Invariants in Fermi Systems with Time-Reversal Invariance". In: *Phys. Rev. Lett.* 61 (12 Sept. 1988), pp. 1329–1332.
- [200] J. Avron, L. Sadun, J. Segert, and B. Simon. "Chern numbers, quaternions, and Berry's phases in Fermi systems". In: *Communications in mathematical physics* 124.4 (1989), pp. 595–627.
- [201] M. Kolodrubetz. "Measuring the Second Chern Number from Nonadiabatic Effects". In: *Phys. Rev. Lett.* 117 (1 June 2016), p. 015301.
- [202] S. Sugawa, F. Salces-Carcoba, A. R. Perry, Y. Yue, and I. Spielman. "Second Chern number of a quantum-simulated non-Abelian Yang monopole". In: *Science* 360.6396 (2018), pp. 1429–1434.
- [203] Z.-Y. Xue, J. Zhou, and Z. Wang. "Universal holonomic quantum gates in decoherence-free subspace on superconducting circuits". In: *Physical Review A* 92.2 (2015), p. 022320.
- [204] D. J. Egger, M. Ganzhorn, G. Salis, A. Fuhrer, P. Mueller, P. K. Barkoutsos, N. Moll, I. Tavernelli, and S. Filipp. "Entanglement generation in superconducting qubits using holonomic operations". In: *Physical Review Applied* 11.1 (2019), p. 014017.
- [205] M. V. Berry. "Quantal phase factors accompanying adiabatic changes". In: *Proc. R. Soc. Lond. A* 392.1802 (1984), pp. 45–57.
- [206] F. Wilczek and A. Zee. "Appearance of gauge structure in simple dynamical systems". In: *Physical Review Letters* 52.24 (1984), p. 2111.
- [207] C. A. Mead. "Molecular Kramers degeneracy and non-Abelian adiabatic phase factors". In: *Physical review letters* 59.2 (1987), p. 161.
- [208] J. J. Sakurai, J. Napolitano, et al. *Modern quantum mechanics*. Vol. 185. Pearson Harlow, 2014.

- [209] M. Bukov, L. D'Alessio, and A. Polkovnikov. "Universal high-frequency behavior of periodically driven systems: from dynamical stabilization to Floquet engineering". In: *Advances in Physics* 64.2 (2015), pp. 139–226.
- [210] G. Aleksandrowicz et al. *Qiskit: An Open-source Framework for Quantum Computing*. 2019.